Energy Partitioning in Polyatomic Chemical Reactions: Quantum State Resolved Studies of Highly Exothermic Atom Abstraction Reactions from Molecules in the Gas Phase and at the Gas-Liquid Interface

by

Alexander M. Zolot

B.A., Colorado College, 2001

A thesis submitted to the

Faculty of the Graduate School of the

University of Colorado in partial fulfillment

of the requirements for the degree of

Doctor of Philosophy

Chemical Physics

2009

This thesis entitled:

Energy Partitioning in Polyatomic Chemical Reactions:

Quantum State Resolved Studies of Highly Exothermic Atom Abstraction Reactions from

Molecules in the Gas Phase and at the Gas-Liquid Interface

Written by Alexander M. Zolot

has been approved for the Chemical Physics program by

_____

David J. Nesbitt

_____

J. Mathias Weber

Date: _____

The final copy of this thesis has been examined by both the signatories, and we find that both the content and the form meet acceptable presentation standards of scholarly work in the above mentioned discipline.

Zolot, Alexander M. (Ph.D. Chemical Physics)

Energy Partitioning in Polyatomic Chemical Reactions:

Quantum State Resolved Studies of Highly Exothermic Atom Abstraction Reactions from Molecules in the Gas Phase and at the Gas-Liquid Interface

Thesis directed by Professor David J. Nesbitt

This thesis recounts a series of experiments that interrogate the dynamics of elementary chemical reactions using quantum state resolved measurements of gas-phase products. The gas-phase reactions F + HCl $\rightarrow$ HF + Cl and F + H_2O $\rightarrow$ HF + OH are studied using crossed supersonic jets under single collision conditions. Infrared (IR) laser absorption probes HF product with near shot-noise limited sensitivity and high resolution, capable of resolving rovibrational states and Doppler lineshapes. Both reactions yield inverted vibrational populations. For the HCl reaction, strongly bimodal rotational distributions are observed, suggesting microscopic branching of the reaction mechanism. Alternatively, such structure may result from a quantum-resonance mediated reaction similar to those found in the well-characterized F + HD system. For the H_2O reaction, a small, but significant, branching into $v = 2$ is particularly remarkable because this manifold is accessible only via the additional center of mass collision energy in the crossed jets. Rotationally hyperthermal HF is also observed. A*b initio* calculations of the transition state geometry suggest mechanisms for both rotational and vibrational excitation.

Exothermic chemical reaction dynamics at the gas-liquid interface have been investigated by colliding a supersonic jet of F atoms with liquid squalane ($C_{30}H_{62}$), a low vapor pressure hydrocarbon compatible with the high vacuum environment. IR spectroscopy provides absolute HF(*v,J*) product densities and Doppler resolved velocity component distributions perpendicular to the surface normal. Compared to analogous gas-phase F + hydrocarbon reactions, the liquid surface is a more effective “heat sink,” yet vibrationally

excited populations reveal incomplete thermal accommodation with the surface. Non-Boltzmann *J*-state populations and hot Doppler lineshapes that broaden with HF excitation indicate two competing scattering mechanisms: i) a direct reactive scattering channel, whereby newly formed molecules leave the surface without equilibrating, and ii) a partially accommodated fraction that shares vibrational, rotational, and translational energy with the liquid surface before returning to the gas phase.

Finally, a velocity map ion imaging apparatus has been implemented to investigate reaction dynamics in crossed molecular beams. Resonantly enhanced multiphoton ionization (REMPI) results in rotational, vibrational, and electronic state selectivity. Velocity map imaging measurements provide differential cross sections and information about the internal energy distribution of the undetected collision partner.

For my wife, Sabina, and my mom, Laurel. I have been inspired by your hard work, and I am eternally grateful for your boundless love, support, and patience.

Acknowledgements

A process as long and arduous as obtaining Ph.D. is impossible to complete without the help of an army of people who help along the way. This is my feeble attempt to recognize all those people explicitly, but I will no doubt leave many out, and to them I apologize.

I am particularly indebted to my advisor, David Nesbitt, whose depth of understanding and laser sharp intellect have made my graduate education a challenging and rewarding process. I have also had the opportunity to learn from visiting JILA fellow and Johns Hopkins Professor Paul Dagdigian, who gave the ion imaging experiment a shot in the arm and also seemed to finish another gas-liquid scattering model at home every night.

Thanks to the Nesbitt group members, past and present, for being there in a variety of ways. My lab partner, Danny Bell, who helped clean out a diffusion pump on multiple occasions, and helped me (or let me help him) build the ion imaging apparatus v.2.0. I've worked particularly closely with Brad Perkins, "the source" of all practical liquid scattering knowledge, Mike Ziemkiewicz, whose science and non-science insights have taught me much, and Mike Deskevich, whose tips on Unix scripting revolutionized my computer world. I've also enjoyed learning with and from Nesbitt group members Tom Baker, Julie Fiore, Melanie Roberts, Erin Sharp, Rob Roscioli, Larry Fiegland, Mike Wojcik, Oliver Monti, Christian Pluetzer, Jose Hodak, Richard Walters, Chandra Savage, Erin Whitney, Feng Dong, Vasiliy Fomenko, Thomas Haeber, and Warren Harper.

Outside the Nesbitt group, I have benefited greatly from the assistance of Mathias Weber, Anne McCoy, and Carl Lineberger. A special thanks for the technical advice at cookie time with JILA comrades Lenny Sheps, Elisa Miller, Django Andrews, Jeff Rathbone, and numerous other members of the Lineberger, Weber, and Ye groups. Nothing in my lab would work without the constant input from the JILA mechanical, electronic, and computer staff; a big thanks to Blaine Horner, Hans Green, Tom Foote, Tracy Buxkemper, Terry

Brown, James Fung-A-Fat, Paul Beckingham, Peter Ruprecht, and many others, whom I have not pestered as persistently as these poor souls.

Also, to my wonderful family, for their support and patience, and for providing much-needed distractions, thanks: Matt, Liza, Rachel, Isaac, Alayna, Gabe, Heidi, Mom, Jeanette, Lloyd, Doug, Sharon, Josh and Zach. I continued to be inspired by the memory of my Father, Herbert Zolot, who taught me to love learning.

I especially need to thank my beautiful wife Sabina, the only public relations / development expert who knows what it means to fill a Dewar. My love for you is boundless.

Contents

TABLES

FIGURES

Chapter I Introduction

The field of chemical reaction dynamics, as distinct from kinetics, originated with the advent of quantum mechanics in the 1920's. This revolution in physics established the laws governing the motion of electrons and atoms, enabling the building blocks of matter to be understood for the first time and theoretical chemistry to become a topic for exploration from first principles. The first steps toward comprehending elementary chemical reactions were taken by London,[1] who developed the idea of an electronically adiabatic potential energy surface (PES) for the simplest chemical reaction, $H + H_2$. Eyring, Polanyi, and Sato made further refinements,[2,3] leading to methods for constructing semi-empirical surfaces.[4] Significant computational hurdles prevented calculation of PESs from *ab initio* considerations until electronic computers made large-scale numerical calculations possible. At this early juncture, the only experimental measurements available for comparison were reaction rates, which shed little insight into the fundamental reaction process because of their highly thermally averaged nature.

Experimental methods capable of probing the nature of elementary reaction events began to be explored in the second half of the twentieth century. Taylor and Datz[5] initiated the use of crossed beams in their landmark study of the reaction $K + HBr \rightarrow KBr + H$, and advances in this technique lead to the so-called "alkali era" of reaction dynamics.[6] By the late 1960's, highly sophisticated angular scattering experiments arose, notably in Lee and Herschbach's "universal detection" crossed beam apparatus, which detected products with a rotatable electron-impact mass spectrometer.[7] Around the same time, product state distributions began to be probed, notably by Polanyi using chemiluminescence spectroscopy[8] and chemical laser studies by Pimentel and others.[9,10]

This experimental revolution was soon joined by a new era in theoretical studies, during which the first semi-empirical, and then purely *ab initio*, PESs were developed with the help of electronic computers in the 1970's. However, the tools needed to accurately predict the details of any arbitrary chemical reaction remain out of reach to this day. The fundamental difficulty in theoretical chemistry is obtaining sufficiently accurate solutions to many body problems in quantum mechanics, which are not analytically solvable. In contrast, two body problems are readily solved, as revealed by the analytical solutions to the hydrogen atom and harmonic oscillator, to name two chemically relevant examples. However, approximate numerical methods of solving many body problems arose by the 1930's, such as Hartree's treatment of atoms larger than hydrogen via the self consistent field method.[11,12]

Numerical solutions to the Schrödinger equation for reactive chemical systems awaited the development of electronic computers. These large systems are significantly more computationally demanding for many following reasons. First, the cost of *ab initio* calculations scales very quickly with the number of atoms and electrons in the system being modeled, such that high computational speed is absolutely crucial to obtain results. Secondly, meaningful results on chemically relevant systems require calculations accurate to less than about 1 kcal/mol, necessitating high-level theoretical methods[13-15] and better and more sophisticated electronic basis sets.[16] Such accuracy is particularly remarkable, as it represents only a small portion of the total system energy, which is 5–15 eV for loosely held electrons (i.e., 13.6 eV for a free H atom) to several thousand eV for core electrons in third row elements (almost 4,000 eV for a Cl 1s electron). Thirdly, accurate, and thus expensive, methods must be repeated at a large number of atomic coordinates to span the $3N$-6 dimensions describing a system with N atoms and construct the multidimensional PES. Fourthly, after a PES has been constructed, modeling the dynamical motion of the atoms adds computational expense, particularly when light hydrogen atoms necessitate sophisticated quantum wave packet methods.[17-19] Finally, single-surface methods fail

due to non- Born-Oppenheimer dynamics, requiring calculations of multiple electronic surfaces, the coupling elements between them, and multisurface dynamical methods.

Despite these challenges, advances in computer technology over the past two decades have enabled high-level *ab initio* PESs in 3*N*-6 dimensions with chemical accuracy to be produced for a handful of benchmark three-atom systems, including H + H_2,[20] O + H_2,[21] F + H_2,[22,23] Cl + H_2,[24] and F + HCl[25] reactions. This milestone achievement has already produced remarkable agreement with experiment, but significant challenges remain. In particular, as more advanced calculations are performed, one hopes to find the minimum level of sophistication needed to yield accurate predictions, necessitating close collaboration between experiment and theory. Additionally, because of the increasing computer costs associated with larger chemical systems, approximate theoretical methods will be needed for reactions with more atoms than the current state of the art, which can handle $N = 4$ atom systems in nearly full dimensionality.[26-28] In the foreseeable future, the vast majority of chemical reactions will not be accessible from first principles considerations. Such theoretical hurdles strongly motivate the continued experimental study of chemical reaction dynamics to provide detailed information on a large number of chemical reactions with which to rigorously test approximate and limited dimensional theoretical studies of larger systems.

Experimental studies of chemical reaction dynamics aim to measure as many observables as possible, to compare to detailed theoretical results. Using a quasi-classical description of the reaction event, the fundamental results may be expressed as an opacity function $O(b,E,\boldsymbol{N})$, which is the probability of reaction occurring with impact parameter b, collision energy E, and the set of reactant quantum states denoted by the vector $\boldsymbol{N}$. Kinetic rate constants hide many of these details by averaging over the thermal distribution of b, E, and $\boldsymbol{N}$, to provide the rate constant k, which depends only on temperature. Ideally, dynamical studies specify as many reactant parameters as possible, while measuring properties of the product, such as the product states $\boldsymbol{N'}$, and angular deflection Ω, defined with respect to the reactants' relative velocity. Since b cannot usually be

experimentally controlled, it is generally integrated over to provide the ideal experimental result: state-to-state differential cross section, $\sigma(E,\mathbf{N},\mathbf{N'},\Omega)$. Thus, a perfect experiment would utilize reactants with known E and $\mathbf{N}$, and measure the product state distribution $P(\mathbf{N'})$ and differential cross section $d\sigma/d\Omega$ into each solid angle Ω,. Such detailed measurements would reveal general features of the reaction dynamics and enable various theoretical methods to be critically evaluated.

Practical applications for understanding chemical reactivity from first principles abound. The physical insight gained from such studies may guide thinking about the nature of chemical processes, assisting in the emerging field of coherent control, which aims to manipulate chemical reactions using precisely constructed laser fields.[29] In spite of the apparent simplicity of elementary reactions, they have practical consequences in a number of regimes, including atmospheric chemistry, combustion processes, the design and use of chemical lasers, and the chemistry of the interstellar medium.[30-37]

Whether the goal is to increase understanding of fundamental physics that governs chemistry, or applying this to atomic level engineering, the field of chemical reaction dynamics depends critically on close interaction between theory and experiment. Thus, the study of chemical reaction dynamics has evolved into a highly complex field. Specialized experiments depend upon high-level theory for interpretation, and leading edge theoretical techniques use experimental results to vindicate novel methods.

Over the past few decades, the tools of experimental chemical reaction dynamics have progressed significantly. Skimmed supersonic beams provide cold, localized reactants with narrow velocity distributions, while pseudo-random chopping of such jets facilitates measurements of product speed distributions. For “universal” detection, products are ionized by electron impact, and such detectors have also utilized spectroscopic ionization techniques to provide state selectivity.[38] Concurrent developments in laser technology have enabled novel

methods of state resolved characterization of products, including laser induced fluorescence (LIF),[39] coherent anti-stokes Raman spectroscopy (CARS),[40] Rydberg time of flight detection of H atoms,[41] and resonantly enhanced multiphoton ionization (REMPI). REMPI detection has recently blossomed in conjunction with velocity map ion imaging (VMII) methods,[42-49] which enable sensitive velocity measurements to be made in conjunction with spectroscopically selective ionization. Each of these techniques presents unique advantages and problems with respect to sensitivity, resolution, and applicability to a given molecular system.

In the Nesbitt group, we have developed high-resolution, high-sensitivity direct detection of infrared (IR) laser absorption as a method for probing chemical reaction dynamics. IR measurements result in unambiguous chemical assignments and rovibrational quantum-state resolution. High-resolution measurements provide Doppler measurements of the product translational distributions projected onto the laser axis. High-sensitivity detection enables studies under low-density conditions, which preserve the nascent distributions formed in the reactive collision. Additionally, since all molecules other than homonuclear diatomics exhibit transition intensity in the IR, this detection method can, in principle, be used to detect almost any molecular species. Indeed, recent advances in high-power, high-resolution lasers, such as continuous wave optical parametric oscillators and quantum cascade sources, may lead to broader adoption of IR absorption techniques. Ch. II includes a detailed description of the ultra-high sensitivity IR spectrometer used for these dynamical studies.

Additional work has gone into constructing a VMII apparatus, as described in detail in Appendix B. This new capability builds on remarkable developments over past decade, which have enabled vastly improved velocity resolution.[50,51] Now, detailed velocity measurements can be made quickly, without a bulky and expensive rotatable detection apparatus. REMPI spectroscopy produces state selective generation of ions. Coupling this ion generation technique with VMII methods enables the parent ion's velocity vector to be measured, coming tantalizingly close to the perfect state resolved differential scattering cross section mentioned above.

Both IR spectroscopy and VMII techniques may be used to probe chemical reactions at a highly detailed level. To fully appreciate the contributions made with these techniques, an understanding of the past half-century of reaction dynamics and the current state of the art is needed. Three-atom systems provide some of the most rigorous tests to theory currently available, since existing methods enable the PES to be developed in full $3N\text{-}6 = 3$ dimensionality.[25,52,53] Reactions such as $H + H_2$,[54-57] $O + H_2$,[21,58-60] $F + H_2$,[17,61-71] and $Cl + H_2$,[24,72-75] have received particular attention because having only a single "heavy" (i.e. nonhydrogenic) atom makes then particularly approachable to high-level theoretical methods. More complicated three-atom systems have also been treated with high-level theory, such as the reaction of F with HCl, which is the subject of Ch. III.[25]

As one particularly well-studied example, the strongly exothermic reaction $F + H_2$ and its isotopic variants have proven to be an intensely productive focus of investigation from both theoretical and experimental perspectives. Extensive crossed-beam studies have revealed details of reactive scattering, including the differential and integral cross section as a function of collision energy,[66] as well as complete HF rovibrational quantum state distributions.[70] On the theoretical side, full-dimensional *ab initio* surfaces have been generated with global accuracy approaching a few tenths of a kcal/mol.[22,23] For three-atom system, rigorous quantum dynamical calculations of the reaction on one or more electronic surfaces are computationally accessible.[19] Indeed, the first definitive examples of elusive transition state resonance dynamics were identified experimentally in the isotopic variant reaction $F + HD \rightarrow HF + D$[68,76] and then confirmed in the $F + H_2$ reaction.[77] Calculation of non-adiabatic interactions between multiple spin-orbit surfaces has also become feasible, and such benchmark calculations on the $F(^2P_{3/2}, {}^2P_{1/2}) + H_2$ system have demonstrated the importance of including non-adiabatic processes.[19,78] These theoretical achievements are remarkable for the nearly quantitative agreement with experiment that has been obtained, and for demonstrating the importance of both i) nonadiabatic dynamics on multiple surfaces and ii) quantum resonances in the reaction dynamics using

wavepacket methods. Indeed, the ability to generate a PES from first principles and obtain results from numerically exact dynamical calculations that can be rigorously tested against experiment represents an important milestone achievement by the chemical physics community.

Advances in computational speed also enable existing methods to be tested on more complex systems. One such step is hydrogen exchange between two "heavy" atoms such as the reaction F + HCl → HF + Cl, which has been studied using the IR spectroscopy to probe the reaction dynamics, discussed in detail in Ch. III. While roughly analogous to the well-characterized F + H_2 reaction, this system poses significant challenges because it contains nearly three times as many electrons, which increase the cost of calculating the PES. Also, this system has low lying spin-orbit excited electronic states in both the entrance and exit channels, which necessitate high-level dynamically weighted multireference techniques to simulate.[25]

Although three-atom reaction systems continue to provide key challenges, entirely new phenomena arise in four-atom and larger systems, such as mode-specific chemistry[79-91] and energy transfer into "spectator" degrees of freedom.[92,93] However, as system size increases, so does the number of open channels, necessitating considerably more detailed experimental observations to characterize adequately the reaction channel and correlated product state distributions. Furthermore, theoretical studies become significantly more challenging as additional degrees of freedom dramatically increase the computational cost of i) exploring $3N$-6 molecular dimensions when generating the PES, and ii) dynamically simulating atomic motion on one or more electronic surfaces.

In spite of these challenges, the dynamics of polyatomic (i.e. $N \geq 4$) reactions have begun to be computationally feasible. In particular, remarkable advances have been made in developing an accurate *ab initio* PES and performing exact quantum reactive scattering calculations for the benchmark four-atom reaction system H + H_2O ↔ H_2 + OH.[26-28,92] The rate of recent progress in this dynamically rich reaction suggests that full-dimensional *ab initio* studies of four-atom

systems with more than one heavy (i.e., non-hydrogenic) atom will be feasible in the near future. Recent work by Bowman and coworkers[94] on the F + CH_4 system has demonstrated that chemical reactions with $N > 4$ are also beginning to be accessible, and accurate simulation of increasingly large systems is becoming attainable.

Of course, there are alternative methods to simulating chemical reactions that do not necessitate the exploration of the full PES. For instance, direct dynamics techniques enable classical trajectory simulations to be performed in arbitrary dimensions by calculating the PES energy and its derivatives "on the fly," at the nuclear coordinates traversed by a given trajectory.[95-98] However, computational costs in large systems restrict such calculations to relatively low levels of *ab initio* treatment. Furthermore, this method relies intrinsically on classical dynamics, making inherently quantum phenomena, such as zero point energy[99] and reactions promoted by tunneling through barriers,[68] difficult to model.

The current intractability of full dimensional studies for all but the simplest four-atom system emphasizes the need for further experimental efforts at the state-to-state level. Such work provides a crucial opportunity for benchmark testing of approximate theoretical methods against detailed experimental measurements and stimulates the development of progressively more rigorous multidimensional quantum computational techniques. Indeed, polyatomic reaction dynamics remain an active area of investigation. Notable examples include rotationally resolved studies of F + NH_3, F + CH_4,[100,101] and F + C_2H_6[102] performed by the Nesbitt group, and VMII studies of F + CH_4,[45-48] and Cl reacting with oxygenated[44] or halogenated[43] hydrocarbons. Theoretical investigations of F + CH_4 have been published, and this reaction is emerging as the benchmark atom plus penta-atom system.[94,103] Indeed, this six-atom system appears to be a fruitful testing ground for reduced dimensional studies, in part due to the large body of experimental measurements. Alternatively, the detailed experimental studies of F + H_2O presented in Ch. IV provide stimulus for comparison to more tractable lower dimensional systems, as reduced dimensional methods continue to be developed.

Moving further from the realm of full dimensionality and exact *ab initio* methods, the reaction of F atoms at the surface of a saturated liquid hydrocarbon (squalane, $C_{30}H_{62}$) is presented in Ch. V. Although bulk liquids may never be studied in full dimensions using *ab initio* treatments, methods for simulating self assembled monolayer surfaces (SAM) and bulk liquids using molecular mechanics (MM) methods have been developed by Hase and coworkers.[104-107] The MM technique enables hundreds of large molecules to be simulated by fitting interatomic forces to analytical two-body expressions. Meanwhile, Schatz and coworkers[108,109] have studied the scattering of open shell species with quantum mechanical (QM)[110] algorithms capable of describing reactive events, as an extension of the MM approach. This computational method has recently been extended to the study of bulk liquid interfaces, providing direct theoretical comparison to liquid scattering results.[108,109]

The development of theoretical tools capable of modeling such large chemical systems represents a significant step toward the goal of understanding all chemistry from first principles. Although simple three- and four-atom gas-phase reactions remain the only systems for which the full dimensional PES can be computed, the lessons learned on these systems are already providing insight into reactions at the interface of macroscopic systems. Nevertheless, these early models are likely to miss key elements of the true reaction dynamics, necessitating continued dialogue between experiment and theory to develop appropriate physical insight and theoretical tools that can accurately predict chemistry at the atomic level in a wide range of circumstances.

References for Chapter I

1 F. London, Z. Elektrochem. Angew. Phys. Chem. **35**, 552 (1929).

2 S. Sato, J. Chem. Phys. **23**, 2465 (1955).

3 H. Eyring and M. Polanyi, Z. Phys. Chem. B-Chem. Elem. Aufbau. Mater. **12**, 279 (1931).

4 S. Sato, J. Chem. Phys. **23**, 592 (1955).

5 E. H. Taylor and S. Datz, J. Chem. Phys. **23**, 1711 (1955).

6 K. R. Wilson, G. H. Kwei, D. R. Herschbach, J. A. Norris, J. H. Birely, and R. R. Herm, J. Chem. Phys. **41**, 1154 (1964).

7 Y. T. Lee, J. D. McDonald, P. R. Lebreton, and D. R. Herschbach, Rev. Sci. Instrum. **40**, 1402 (1969).

8 J. C. Polanyi and D. C. Tardy, J. Chem. Phys. **51**, 5717 (1969).

9 J. H. Parker and G. C. Pimentel, J. Chem. Phys. **51**, 91 (1969).

10 K. L. Kompa and G. C. Pimentel, J. Chem. Phys. **47**, 857 (1967).

11 D. R. Hartree, Proc. Camb. Philol. Soc. **24**, 111 (1928).

12 D. R. Hartree, Proc. Camb. Philol. Soc. **24**, 89 (1928).

13 H. J. Werner and P. J. Knowles, J. Chem. Phys. **89**, 5803 (1988).

14 R. J. Bartlett and G. D. Purvis, Phys. Scr. **21**, 255 (1980).

15 S. R. Langhoff and E. R. Davidson, Int. J. Quantum Chem. **8**, 61 (1974).

16 T. H. Dunning, J. Chem. Phys. **90**, 1007 (1989).

17 S. C. Althorpe, Chem. Phys. Lett. **370**, 443 (2003).

18 S. C. Althorpe and D. C. Clary, Annu. Rev. Phys. Chem. **54**, 493 (2003).

19 F. Lique, M. H. Alexander, G. L. Li, H. J. Werner, S. A. Nizkorodov, W. W. Harper, and D. J. Nesbitt, J. Chem. Phys. **128**, (2008).

20 Y. S. M. Wu, A. Kuppermann, and J. B. Anderson, Phys. Chem. Chem. Phys. **1**, 929 (1999).

21 S. Rogers, D. S. Wang, A. Kuppermann, and S. Walch, J. Phys. Chem. A **104**, 2308 (2000).

22 K. Stark and H. J. Werner, J. Chem. Phys. **104**, 6515 (1996).

23 C. X. Xu, D. Q. Xie, and D. H. Zhang, Chin. J. Chem. Phys. **19**, 96 (2006).

24 N. Balucani, D. Skouteris, G. Capozza, E. Segoloni, P. Casavecchia, M. H. Alexander, G. Capecchi, and H. J. Werner, Phys. Chem. Chem. Phys. **6**, 5007 (2004).

25 M. P. Deskevich, M. Y. Hayes, K. Takahashi, R. T. Skodje, and D. J. Nesbitt, J. Chem. Phys. **124**, 224303 (2006).

26 D. H. Zhang and J. Z. H. Zhang, J. Chem. Phys. **99**, 5615 (1993).

27 D. H. Zhang, J. Chem. Phys. **125**, 133102 (2006).

28 R. P. A. Bettens, M. A. Collins, M. J. T. Jordan, and D. H. Zhang, J. Chem. Phys. **112**, 10162 (2000).

29 E. B. W. Lerch, X. C. Dai, S. Gilb, E. A. Torres, and S. R. Leone, J. Chem. Phys. **124**, (2006).

30 R. A. Sultanov and N. Balakrishnan, Astrophys. J. **629**, 305 (2005).

31 S. Javoy, V. Naudet, S. Abid, and C. E. Paillard, Exp. Therm. Fluid Sci. **27**, 371 (2003).

32 D. Gerlich, E. Herbst, and E. Roueff, Planet Space Sci. **50**, 1275 (2002).

33 O. D. Krogh, D. K. Stone, and G. C. Pimentel, J. Chem. Phys. **66**, 368 (1977).

34 M. J. Berry, J. Chem. Phys. **59**, 6229 (1973).

35 C. Zhu, R. Krems, A. Dalgarno, and N. Balakrishnan, Astrophys. J. **577**, 795 (2002).

36 D. A. Neufeld, J. Zmuidzinas, P. Schilke, and T. G. Phillips, Astrophys. J. **488**, L141 (1997).

37 R. von Glasow and P. J. Crutzen, in *Treatise on Geochemistry*, edited by R. F. Keeling, H. D. Holland, and K. K. Turekian (Elsevier Pergamon, Amsterdam, 2003), Vol. 4, pp. 347.

38 P. Casavecchia, Rep. Prog. Phys. **63**, 355 (2000).

39 H. W. Cruse, P. J. Dagdigian, and R. N. Zare, Faraday Discuss. **55**, 277 (1973).

40 P. M. Aker, G. J. Germann, and J. J. Valentini, J. Chem. Phys. **96**, 2756 (1992).

41 X. M. Yang and D. H. Zhang, Accounts Chem. Res. **41**, 981 (2008).

42 J. K. Pearce, B. Retail, S. J. Greaves, R. A. Rose, and A. J. Orr-Ewing, J. Phys. Chem. A **111**, 13296 (2007).

43 R. L. Toomes, A. J. van den Brom, T. N. Kitsopoulos, C. Murray, and A. J. Orr-Ewing, J. Phys. Chem. A **108**, 7909 (2004).

44 C. Murray, A. J. Orr-Ewing, R. L. Toomes, and T. N. Kitsopoulos, J. Chem. Phys. **120**, 2230 (2004).

45 K. P. Liu, Phys. Chem. Chem. Phys. **9**, 17 (2007).

46 J. J. M. Lin, J. G. Zhou, W. C. Shiu, and K. P. Liu, Chin. J. Chem. Phys. **17**, 346 (2004).

47 J. G. Zhou, J. J. Lin, and K. P. Liu, J. Chem. Phys. **121**, 813 (2004).

48 W. Shiu, J. J. Lin, K. P. Liu, M. Wu, and D. H. Parker, J. Chem. Phys. **120**, 117 (2004).

49 J. G. Zhou, J. J. Lin, W. C. Shiu, S. C. Pu, and K. P. Liu, J. Chem. Phys. **119**, 2538 (2003).

50 D. W. Chandler and P. L. Houston, J. Chem. Phys. **87**, 1445 (1987).

51 A. Eppink and D. H. Parker, Rev. Sci. Instrum. **68**, 3477 (1997).

52 G. Capecehi and H. J. Werner, Phys. Chem. Chem. Phys. **6**, 4975 (2004).

53 J. F. Castillo, B. Hartke, H. J. Werner, F. J. Aoiz, L. Banares, and B. Martinez-Haya, J. Chem. Phys. **109**, 7224 (1998).

54 D. G. Truhlar and Kupperma.A, J. Chem. Phys. **56**, 2232 (1972).

55 R. D. Levine and S. F. Wu, Chem. Phys. Lett. **11**, 557 (1971).

56 S. C. Althorpe, F. Fernandez-Alonso, B. D. Bean, J. D. Ayers, A. E. Pomerantz, R. N. Zare, and E. Wrede, Nature **416**, 67 (2002).

57 R. E. Continetti, B. A. Balko, and Y. T. Lee, J. Chem. Phys. **93**, 5719 (1990).

58 P. F. Weck and N. Balakrishnan, J. Chem. Phys. **123**, 144308 (2005).

59 D. J. Garton, T. K. Minton, B. Maiti, D. Troya, and G. C. Schatz, J. Chem. Phys. **118**, 1585 (2003).

60 D. J. Garton, A. L. Brunsvold, T. K. Minton, D. Troya, B. Maiti, and G. C. Schatz, J. Phys. Chem. A **110**, 1327 (2006).

61 M. H. Alexander, D. E. Manolopoulos, and H. J. Werner, J. Chem. Phys. **113**, 11084 (2000).

62 M. Baer, M. Faubel, B. Martinez-Haya, L. Y. Rusin, U. Tappe, and J. P. Toennies, J. Chem. Phys. **108**, 9694 (1998).

63 M. Faubel, B. Martinez-Haya, L. Y. Rusin, U. Tappe, J. P. Toennies, F. J. Aoiz, and L. Banares, J. Phys. Chem. A **102**, 8695 (1998).

64 D. M. Neumark, A. M. Wodtke, G. N. Robinson, C. C. Hayden, and Y. T. Lee, J. Chem. Phys. **82**, 3045 (1985).

65 L. Y. Rusin and J. P. Toennies, Phys. Chem. Chem. Phys. **2**, 501 (2000).

66 F. Dong, S. H. Lee, and K. Liu, J. Chem. Phys. **113**, 3633 (2000).

67 Y. T. Lee, Science **236**, 793 (1987).

68 R. T. Skodje, D. Skouteris, D. E. Manolopoulos, S. H. Lee, F. Dong, and K. Liu, J. Chem. Phys. **112**, 4536 (2000).

69 W. B. Chapman, B. W. Blackmon, and D. J. Nesbitt, J. Chem. Phys. **107**, 8193 (1997).

70 W. B. Chapman, B. W. Blackmon, S. Nizkorodov, and D. J. Nesbitt, J. Chem. Phys. **109**, 9306 (1998).

71 W. W. Harper, S. A. Nizkorodov, and D. J. Nesbitt, J. Chem. Phys. **116**, 5622 (2002).

72 B. F. Parsons and D. W. Chandler, J. Chem. Phys. **122**, 174306 (2005).

73 M. H. Alexander, G. Capecchi, and H. J. Werner, Faraday Discuss. **127**, 59 (2004).

74 F. Dong, S. H. Lee, and K. Liu, J. Chem. Phys. **115**, 1197 (2001).

75 D. Skouteris, H. J. Werner, F. J. Aoiz, L. Banares, J. F. Castillo, M. Menendez, N. Balucani, L. Cartechini, and P. Casavecchia, J. Chem. Phys. **114**, 10662 (2001).

76 R. T. Skodje, D. Skouteris, D. E. Manolopoulos, S. H. Lee, F. Dong, and K. P. Liu, Phys. Rev. Lett. **85**, 1206 (2000).

77 M. H. Qiu, Z. F. Ren, L. Che, D. X. Dai, S. A. Harich, X. Y. Wang, X. M. Yang, C. X. Xu, D. Q. Xie, M. Gustafsson, R. T. Skodje, Z. G. Sun, and D. H. Zhang, Science **311**, 1440 (2006).

78 Y. R. Tzeng and M. H. Alexander, J. Chem. Phys. **121**, 5183 (2004).

79 R. B. Metz, J. D. Thoemke, J. M. Pfeiffer, and F. F. Crim, J. Chem. Phys. **99**, 1744 (1993).

80 M. Brouard, I. Burak, S. Marinakis, L. R. Lago, P. Tampkins, and C. Vallance, J. Chem. Phys. **121**, 10426 (2004).

81 A. Sinha, M. C. Hsiao, and F. F. Crim, J. Chem. Phys. **92**, 6333 (1990).

82 A. Sinha, M. C. Hsiao, and F. F. Crim, J. Chem. Phys. **94**, 4928 (1991).

83 S. Yan, Y. T. Wu, and K. P. Liu, Phys. Chem. Chem. Phys. **9**, 250 (2007).

84 J. B. Liu, B. Van Devener, and S. L. Anderson, J. Chem. Phys. **119**, 200 (2003).

85 J. R. Fair, D. Schaefer, R. Kosloff, and D. J. Nesbitt, J. Chem. Phys. **116**, 1406 (2002).

86 B. R. Strazisar, C. Lin, and H. F. Davis, Science **290**, 958 (2000).

87 C. Kreher, J. L. Rinnenthal, and K. H. Gericke, J. Chem. Phys. **108**, 3154 (1998).

88 K. Kudla and G. C. Schatz, Chem. Phys. **175**, 71 (1993).

89 M. J. Bronikowski, W. R. Simpson, B. Girard, and R. N. Zare, J. Chem. Phys. **95**, 8647 (1991).

90 J. M. Pfeiffer, R. B. Metz, J. D. Thoemke, E. Woods, and F. F. Crim, J. Chem. Phys. **104**, 4490 (1996).

91 J. D. Thoemke, J. M. Pfeiffer, R. B. Metz, and F. F. Crim, J. Phys. Chem. **99**, 13748 (1995).

92 D. H. Zhang, M. H. Yang, and S. Y. Lee, Phys. Rev. Lett. **89**, 283203 (2002).

93 M. C. Hsiao, A. Sinha, and F. F. Crim, J. Phys. Chem. **95**, 8263 (1991).

94 G. Czako, B. C. Shepler, J. B. Braams, and J. M. Bowman, J. Phys. Chem. A(in press) (2009).

95 K. Bolton, W. L. Hase, and G. H. Peslherbe, in *Modern Methods for Multidimensional Dynamics Computations in Chemistry*, edited by D. L. Thompson (World Scientific, River Edge, NJ, 1998), pp. 143.

96 W. Chen, W. L. Hase, and H. B. Schlegel, Chem. Phys. Lett. **228**, 436 (1994).

97 S. Rudic, C. Murray, J. N. Harvey, and A. J. Orr-Ewing, J. Chem. Phys. **120**, 186 (2004).

98 E. Uggerud and T. Helgaker, J. Am. Chem. Soc. **114**, 4265 (1992).

99 G. H. Peslherbe and W. L. Hase, J. Chem. Phys. **100**, 1179 (1994).

100 W. W. Harper, S. A. Nizkorodov, and D. J. Nesbitt, J. Chem. Phys. **113**, 3670 (2000).

101 W. W. Harper, S. A. Nizkorodov, and D. J. Nesbitt, Chem. Phys. Lett. **335**, 381 (2001).

102 E. S. Whitney, A. M. Zolot, A. B. McCoy, J. S. Francisco, and D. J. Nesbitt, J. Chem. Phys. **122**, 124310 (2005).

103 D. Troya, J. Chem. Phys. **123**, 214305 (2005).

104 S. A. Vazquez, J. R. Morris, A. Rahaman, O. A. Mazyar, G. Vayner, S. V. Addepalli, W. L. Hase, and E. Martinez-Nunez, J. Phys. Chem. A **111**, 12785 (2007).

105 T. Y. Yan and W. L. Hase, Phys. Chem. Chem. Phys. **2**, 901 (2000).

106 T. Y. Yan, W. L. Hase, and J. R. Barker, Chem. Phys. Lett. **329**, 84 (2000).

107 T. Y. Yan, N. Isa, K. D. Gibson, S. J. Sibener, and W. L. Hase, J. Phys. Chem. A **107**, 10600 (2003).

108 D. Kim and G. C. Schatz, J. Phys. Chem. A **111**, 5019 (2007).

109 B. K. Radak, S. Yockel, D. Kim, and G. C. Schatz, J. Phys. Chem. A (in press) (2009).

110 G. Li, S. B. M. Bosio, and W. L. Hase, J. Mol. Struct. **556**, 43 (2000).

Chapter II Experiment

2.1 Introduction

In the late 1960's, experimental advances in molecular jets, vacuum apparatus, and molecular detection via ionization and spectroscopy made measurements of molecular scattering dynamics possible, revolutionizing the field of chemical physics. Rapid growth in chemical reaction dynamics lead the Nobel Prize committee, in 1986, to honor Polanyi, Herschbach and Lee "for their contributions concerning the dynamics of chemical elementary processes."[1] On the experimental front, these luminaries instigated the study of chemical reaction dynamics using two complimentary techniques. Polanyi's infrared chemiluminescence method revealed internal state distributions of molecules immediately following chemical reaction.[2] Meanwhile, Herschbach and Lee obtained detailed angular scattering measurements using a crossed jet apparatus coupled with a rotatable mass analyzer.[3]

In the decades following these landmark achievements, the study of chemical reaction dynamics has progressed into a mature field, and extensive efforts have focused on revealing the details of molecular scattering with increasing resolution and sensitivity. Many techniques have been developed to measure one or more characteristics of the nascent products, though the "Holy Grail" of state-correlated differential cross sections remains elusive. However, recent developments in molecular beam and laser detection methods have come tantalizingly close to this ideal, with quantum-state resolution and highly detailed velocity distribution measurements. Two such methods have been utilized in my Ph.D. research, and will be described in this chapter.

Consider a bimolecular reaction of the form,

$$A + B \rightarrow C + D, \qquad (2.1)$$

with known collision energy and quantum states of A and B. The quantum state resolved velocity measurements of one fragment (C) enable the internal excitation of the unseen fragment (D) to be inferred from conservation of energy. One method capable of such state resolved velocity measurements is high-resolution IR laser spectroscopy, due to its inherent rovibrational selectivity, and the potential for Doppler resolution. Another method is velocity map ion imaging (VMII), which is considered in more detail in Appendix B. Briefly, VMII provides detailed measurements of ions' velocity vector distributions, while state selectivity results from resonantly enhanced multiphoton ionization (REMPI).

2.2 Infrared Laser Spectrometer

Infrared detection of nascent product molecules provides several unique capabilities. In addition to spectroscopic quantum-state resolution, IR absorption exhibits very narrow (≈ 1 MHz) homogeneous linewidths under low-density conditions, typically limited by residence time broadening in the continuous wave (CW) laser field. Thus, heterogeneous (Doppler) structure can elucidate product velocity distributions. Additionally, since most molecules are IR active, this technique can potentially be applied to detect almost any chemical species. Indeed, few other optical techniques can detect the HF molecule, the focus of the following work, because of the lack of a suitable fluorescent electronic state for LIF and particularly high energy electronic states, which complicate ionization spectroscopy.[4] Thus, IR detection provides a means of expanding the number of chemical species whose dynamics can be measured beyond those with suitable multiphoton transitions.

Key to the IR absorption method is the narrow bandwidth ($\Delta\nu \approx 3$ MHz) tunable light source. The F center laser, also commonly called the FCL or color center laser, used in the present work has been discussed elsewhere.[5,6] A detailed description of the Burleigh FCL-20 and

detailed realignment procedures comprises Appendix A. In practice, any narrow linewidth, continuous wave, tunable IR laser could be used to construct such a spectrometer. This section describes the IR source, the electro-optical diagnostic tools, and the components used to obtain absorption sensitivity near the fundamental "shot-noise" limit for counting photons.

The optical elements of the apparatus are illustrated in Fig. 2.1 and consist of the tunable IR source, a polarization stabilized HeNe reference laser (also used as a visible "tracer" beam), a wavelength measurement device (λ meter), scanning Fabry-Perot cavity, a reference gas absorption cell, the Herriot multipass cell, a pair of InSb detectors for high sensitivity differential absorption detection, and a number of other power-monitoring and noise-reducing optical elements. The following sections describe the electro-optical control of the laser frequency and intensity.

A. The F Center Laser:

The fundamental functioning of the FCL closely parallels that of a common CW dye laser. A short wavelength pump source, in this case the 647 nm light from a krypton ion laser, generates a population inversion which fluoresces at longer wavelength, i.e., the infrared. The gain medium is a salt crystal with Farbe center defects, commonly called color centers or F centers, which are lattice positions missing a monovalent anion, occupied instead by a single electron. The pumped transition is "vertical," i.e., an electronic excitation that occurs while nearby atoms remain in their ground state equilibrium positions. Following excitation, the atoms rapidly relax to a new equilibrium position for the excited state. IR fluorescence and stimulated emission occur via another vertical transition at large Stokes shift, forming a four state laser. The phonon broadening in the crystal results in a broad, homogeneous fluorescence and therefore a large tuning range for a narrow pump frequency.

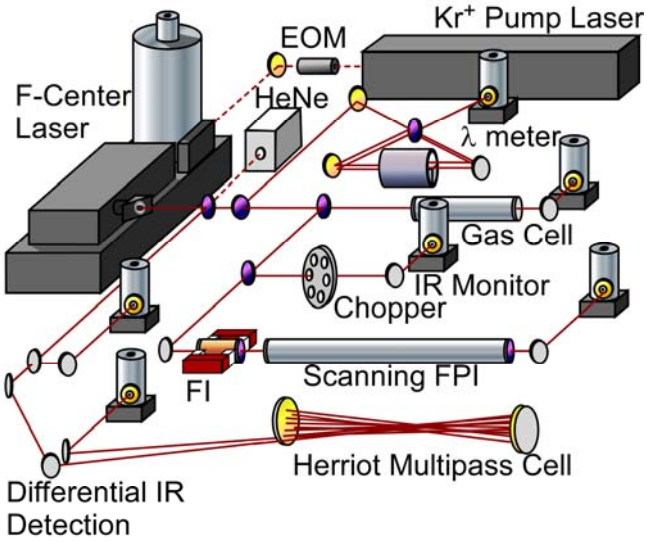

Figure 2.1 Optical elements of the infrared spectrometer. A 647 nm krypton ion laser optically pumps the F center laser through an electro-optical modulator (EOM). A polarization-stabilized helium neon laser (HeNe) overlaps with the IR laser beam. The infrared diagnostics include a wavelength (λ) meter, an absorption gas cell, a chopped-beam photovoltaic power meter, and scanning Fabry-Perot Interferometer (FPI). Optical feedback from the latter can be isolated with a Faraday Isolator (FI). Low density HF product is detected with increased path length in a Herriot multipass cell. Paired InSb detectors detect differential changes in probe power with sensitivity near the shot noise limit.

Despite this apparent simplicity, color center lasers are notorious for their fickle gain medium conditions. The salt crystals (primarily KCl or RbCl) are highly hygroscopic, such that prolonged exposure to moist air is likely to damage their surface polish. Additionally, crystal coloring occurs by exposing the crystals to a gas of alkali metal, resulting in the needed non-stoichiometric metal cation/chloride ratio and making the crystal reactive to adsorbed water. Thus, surface roughening results in reaction with water and the formation of OH^-, which absorbs in the IR and seriously degrades crystal performance.

Moisture problems are further complicated by crystal temperature and light constraints. The laser transition utilizes type II F centers, Cl^- vacancies with a neighboring Li atom dopant, which minimize the excited color centers' non-radiative rate. However, the F center–Li association is only one of many that may form, and it is somewhat less strongly bound than aggregates of two or more F centers, whose formation leads to the degradation of laser performance. Additionally, electronically excited F centers migrate more readily through the crystal, so aggregate F center formation must be prevented by never exposing the crystal to light when the crystal is warmer than -20 °C, below which temperature the migration of excited type II centers becomes adequately slow.

The combined constraints of cold and non-condensing conditions necessitate high vacuum as part of the laser apparatus. The crystals are mounted on a cold finger in a vacuum Dewar, such that they cryogenically cooled while being optically pumped. The crystal chamber has a built-in sorption pump and is also attached to an ion pump, such that a sufficiently outgassed chamber has a pressure of about $0.5–2\times10^{-10}$ Torr. Moving crystals in and out of the crystal chamber raises the largest hazard. The crystal chamber may only be vented to atmosphere after completely warming it to room temperature, a process that must be done with a cryogenically trapped mechanical pump to remove the sorption-pumped CO_2 and H_2O as the warming proceeds. The warmed crystals can only be handled in a darkened room with red

safelight illumination, preferably with less than 50% relative humidity. Following removal, crystals must be immediately transferred to a hermetically sealed container, surrounded by desiccant, and placed in a freezer for storage. Likewise, reinstalling the crystals involves thawing them before exposure to air and following the other precautions outlined in the Burleigh manual when preparing the crystal chamber for the gain media.

Two separate color center crystals span the 2.5–3.3 μm region, both conveniently pumped by the same 647 nm krypton ion wavelength. Crystal 3 (Li doped RbCl) covers the low energy portion of the spectrum (2.7–3.3 μm) but is used less frequently because monolayers of ice form on the crystal surface about 1–2 months after thermal cycling, absorbing at longer wavelengths and reducing the useable tuning range accessed without regular maintenance. Crystal 2, (Li doped KCl) has a tuning range of 2.5–2.8 μm, and is used on a more routine basis while searching for signal, aligning optics, or other wavelength independent tasks because it does not suffer as drastically from water absorption, has a higher peak power output, lower lasing threshold, and can be pumped with greater total power.

Alignment of the FCL must be performed regularly to attain optimal "single frequency" oscillation on a lone longitudinal mode of the laser cavity. The high gain crystals enable the cavity to support oscillation on several modes simultaneously, necessitating precise aligning of optical elements, illustrated in Fig. 2.2. This multi-line propensity is particularly significant on the *spatial hole burning mode* (SHBM), which originates as follows. The desired longitudinal mode attains the highest gain in the vicinity of its maximum electric field intensity, and the lowest gain at its nodes. Since the cavity modes are standing waves, the positions of the nodes are fixed in space. Thus, a mode with slightly different frequency (the SHBM) can receive high gain if its frequency shift is such that its nodes overlap the main mode's maxima, and vice versa. A short focal length cavity end mirror separates these two modes by the largest possible frequency, so the Burleigh design incorporates an $f = 0.71$ cm end mirror, resulting in an SHB displacement

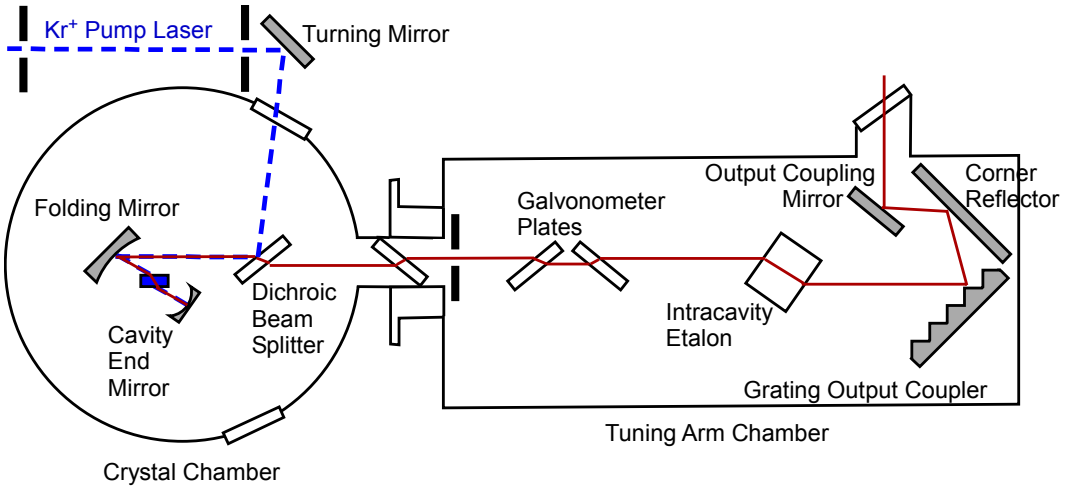

Figure 2.2 The F center laser (FCL), consisting of two independent vacuum regions. The crystal chamber is always under vacuum when the crystal is present and cooled with liquid nitrogen. The laser will operate without evacuating the tuning arm, though operation will be impeded in the vicinity of water lines.

of 0.18 cm^{-1}. For single-mode operation, a tunable "intracavity etalon" with a free spectral range (*FSR*) of 0.6 cm^{-1} is placed in the tuning arm. This *FSR* is about three times the frequency displacement of the SHBM, so it highly attenuates that component of the laser oscillation. To obtain single mode operation, the cavity end mirror must be carefully adjusted, helping eliminate the SHBM, and the intracavity iris should be partially closed, to selectively add the loss on transverse cavity modes other than the desired $TEM_{0,0}$ mode. Both of these adjustments are made along with the pump beam (via the input steering mirror) and grating vertical tilt to optimize the single mode laser power.

Particular difficulties may be encountered when scanning the laser continuously near the extreme red end of the RbCl crystal bandwidth, below about 3200 cm^{-1}. It was empirically found that mode-hopping instabilities in this region mimic those observed when the intracavity etalon has been tilted in its mount, away from optimal alignment. Specifically, the Burleigh manual describes tilting the intracavity etalon such that the remnant of the 647 nm beam in the tuning arm (used as a tracer) is reflected from the first etalon surface and positioned on the left edge of the tuning arm iris. This positioning, as viewed from within the tuning arm, is illustrated as point *A* in Fig. 2.3. For scanning the FCL below 3200 cm^{-1}, this rotation should be exaggerated by rotating the etalon further counterclockwise, placing the tracer reflection further to the left on the iris mount, point *B* in Fig. 2.3.

B. Infrared Diagnostics

Two diagnostic devices are used to monitor the IR frequency. The first is a traveling Michaelson interferometer, or λ meter, based on the design of Hall and Lee,[7] which enables absolute frequency calibration to within about 0.0005 cm^{-1}. A home-built Fabry-Perot Interferometer (FPI) provides an additional relative frequency calibration and real-time frequency

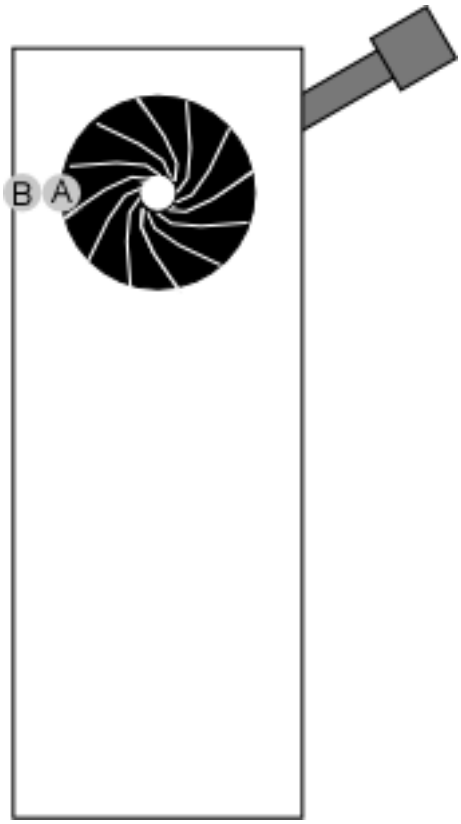

Figure 2.3 Position of the tracer beam reflected from the FCL etalon onto the intracavity iris, as viewed from the tuning arm. Location *A* indicates the recommended position according to the Burleigh manual, and location *B* is the position found to facilitate continuous tuning at the extreme red tuning range of the FCL.

stability measurement via piezoelectric scanning of its free spectral range. The details of these devices are described next.

The λ meter works by counting interference fringes from the unknown (IR) and a reference (polarization stabilized HeNe) lasers. Functionally, the IR laser and tracer HeNe are directed onto a beam splitter and the two resulting laser beams reflect from a moving corner cube cart, as illustrated in Fig. 2.4. The cart continuously translates on an air bearing, using solenoid "cart kickers" to counteract friction and maintain its back and forth motion without any user influence. The two beams recombine on the beam splitter and interfere on two photovoltaic devices, one for the IR and one for the visible beam.

The interference measurements relate to frequency as follows. A laser beam at frequency ν picks up a Doppler shift $\Delta\nu$ after reflecting off the corner cube with speed v_{cart}, according to,

$$\Delta\nu = \nu v_{cart}/c, \qquad (2.2)$$

where c is the speed of light. Because they reflect off the same cart, one laser channel picks up a blue shift of $\nu + \Delta\nu$, while the other is red shifted to $\nu - \Delta\nu$. These beams recombine on the beam splitter and interfere on a photodetector, producing a beat note (ν_b) at the difference between these two frequencies, i.e. $2\Delta\nu$. An equally valid analysis of this measurement is that when the cart moves by $\lambda/4$ ($\lambda = c/\nu$ is the laser wavelength) then the difference in path length between the two interferometer arms changes by $\lambda/2$, and the interference cycles 180°, i.e. from constructive to destructive interference. This cycle occurs every time the cart moves this distance, such that the photodetector signal oscillates at $\nu_b = 2v_{cart}/\lambda = 2\nu v_{cart}/c$, which is the same frequency predicted under the Doppler picture, above.

The need to know v_{cart} is removed by simultaneously measuring fringes generated by the unknown IR laser (ν_{IR}) and a reference laser beam (ν_{ref}) on separate detectors. The tracer HeNe beam provides a convenient reference, with precision better than the 1.5 GHz gain bandwidth[8] of

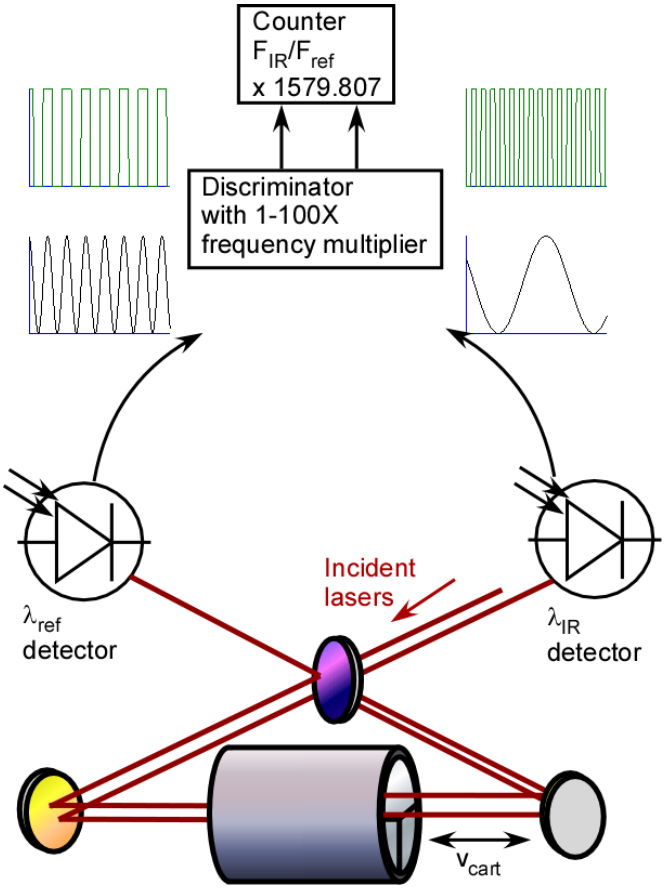

Figure 2.4 Schematic of the laser wavelength meter. A 50% beam splitter divides the incoming beam, containing both λ_{ref} (HeNe) and λ_{IR} (IR), in two. Each beam reflects from a traveling cart, recombines, and lands on two separate photodetectors. Interference fringes are detected and turned into square waves in the phase locked loop / discriminator / frequency multiplier. The resulting square wave is counted on the commercial waveform counter.

an unstabilized HeNe. Eq. 2.2 holds for the relation of each beat frequency and the corresponding laser frequency, such that the ratio of two such equations can be used to find

$$\nu_{IR} = \nu_{ref}\nu_{b\_IR}/\nu_{b\_ref}, \quad (2.3)$$

where ν_{b_IR} and ν_{b_ref} are the measured beat frequencies of the IR and reference channels, respectively.

The λ meter signal analysis electronics also appear in Fig. 2.4. The signal from each photodiode is AC coupled and sent though a discriminator, turning the interference waveform into a TTL pulse train. This square wave is used as the input to a phase lock loop, which servos to the input frequency, providing a square wave with frequency $F = X\nu_b$, where X is a knob-selectable frequency multiplier from 1–100. The output of the phase lock loop goes to a Hewlett Packard "universal counter," which counts the input square waves, and takes the ratio of the two channels' values. This value is multiplied by a calibration constant of 1579.807, corresponding to the frequency of the reference laser in cm^{-1}, divided by $X_{IR}/X_{ref} = 10$ for the relative discriminator multiplier constants, such that the counter displays the IR frequency in cm^{-1}. A typical cart speed of 7 cm/s and phase locked loop multiplication factors of 100 and 10 result in 2.8 and 1.1 million cycles for the IR and reference channels, respectively, in typical integration time of 0.5 s. Thus, the fractional frequency uncertainty is less than a part in a million, and the IR frequency can be measured with a precision of about 0.0005 cm^{-1}. The accuracy of this measurement varies across the FCL spectrum, but always suffices to locate 0.011 cm^{-1} Doppler broadened IR transitions.

This absolute wavelength measurement readily enables manual tuning of the FCL to any desired HF transition, and the second frequency measurement device, a scanning Fabry-Perot interferometer (FPI) schematically represented in Fig. 2.5, provides precise (1–2 MHz) relative frequency calibration over short continuous scans. The confocal optical arrangement provides a "bowtie" optical path, and a free spectral range (*FSR*, in cm^{-1}) given by

$$FSR = 1/(4L), \quad (2.4)$$

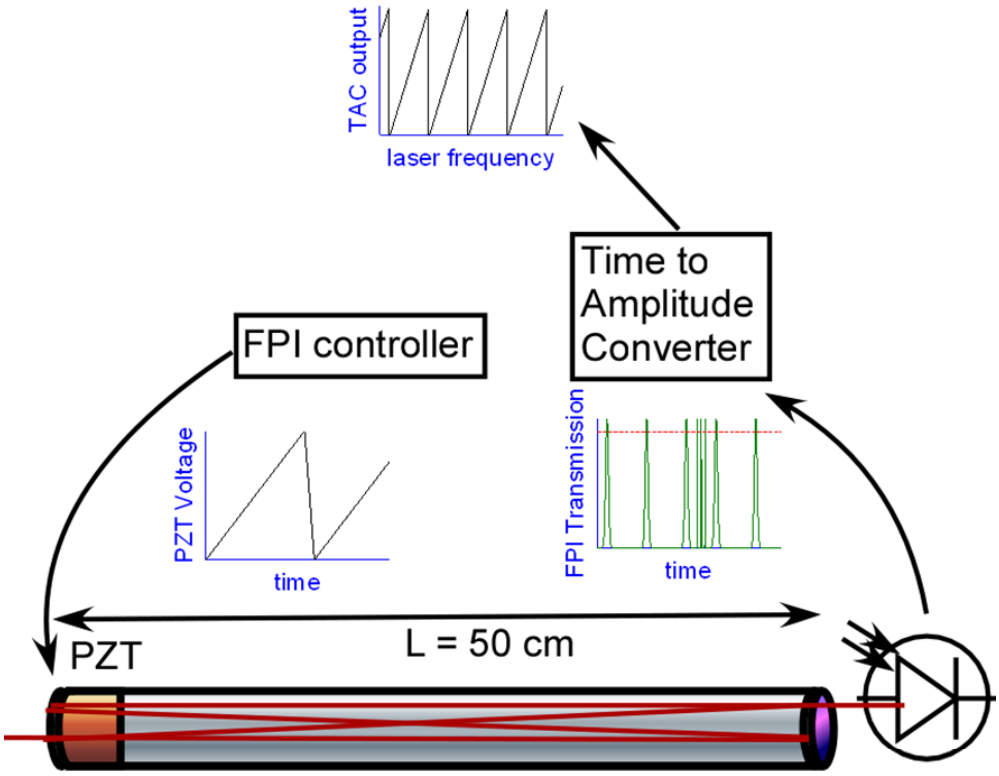

Figure 2.5 Schematic illustration of the scanning Fabry-Perot interferometer. A HV saw tooth wave, applied to the PZT on one end-mirror, results in a series of transmission fringes, which are monitored on a photodiode. The time delay between the beginning of the saw tooth wave and the arrival of the first transmission fringe is recorded on a time to amplitude converter, producing another saw tooth wave that can be used to calibrate the relative laser frequency.

where L is the distance between the cavity end mirrors. An L of 50 cm results in FSR of 0.005 cm^{-1}. The exact value of FSR can be calibrated to better than 1×10^{-5} cm^{-1} by monitoring the FPI output over short scans to get a good estimate of the FSR based on the λ meter reading. Following small scans, the FCL can be tuned in progressively larger steps, which enable this calibration to be extended over a very large frequency range and thereby increase the number of significant digits in the calibration.

For typical diagnostic use, the FPI cavity modulates with a ≈ 500 V saw tooth wave, applied to the cylindrical piezoelectric transducer (PZT) holding one of the cavity's optical elements. This voltage results in a mirror translation of about 2.5 μm, sufficient to make the FPI resonant with the IR frequency 2–3 times. The scanning cavity has a finesse of approximately 20, which is often sufficient to diagnose if the FCL is oscillating at one, or more than one, frequency at a time. However, the 0.005 cm^{-1} FPI FSR roughly corresponds to twice the FCL longitudinal mode spacing of about 0.01 cm^{-1}, so lasing on adjacent modes can be hard to identify using only the FPI. Fortunately, such multi-mode oscillation can also be identified by the modulation of the fringe envelope on the λ meter, caused by interference between laser modes. Thus, single frequency oscillation can be ascertained using the output of these two devices.

After recording short, continuous laser scans (0.3–10 GHz) the scanning FPI is used to calibrate the frequency axis as follows. As the laser frequency changes, a time to amplitude converter (TAC) measures the time from the start of the PZT translation to when the first fringe exceeds a certain threshold voltage on the photodiode, as illustrated in Fig. 2.5. With increasing laser frequency, the fringes are delayed and the TAC output increases. Thus, the rising edge of the saw tooth wave corresponds to an IR fringe moving with respect to the PZT driver pulse, followed by a very rapid falling edge as the next etalon fringe is detected. Advantages of this method are that laser instabilities (particularly "hopping" between longitudinal modes, as occurs with a poorly aligned FCL) are readily detected as discontinuities in the sloping side of the saw

tooth wave, and the abrupt "falling" edges of the TAC output provide markers for calibrating the Doppler scan with the $< 1\times10^{-5}$ cm^{-1} precision of the FPI *FSR* measurement.

C. Intensity Stabilization and High Sensitivity Detection

In order to measure nascent HF product distributions with sufficiently low density to maintain single collision conditions, absorption sensitivity close to the fundamental shot noise limit, i.e., the limit determined by the counting of discrete photons, must be attained. In practice, reaching this limit involves i) stabilizing the broad-band laser intensity fluctuations, ii) subtracting the remaining technical noise from the "signal" detector using a paired "reference" detector, and iii) carefully aligning optics such that non-common mode noise sources (such as clipping of the beam in the Herriot cell) are below the shot noise level in the detection bandwidth. This subsection describes how these three goals are attained.

The first bit of noise reduction results from stabilizing the laser output intensity. Instabilities in both the krypton ion pump laser and the FCL both contribute to the IR root mean square (RMS) noise of about 4% of the DC value without active stabilization. A commercially available "laser noise eater" [ConOptics electro-optic modulator (EOM)], positioned as illustrated in Fig. 2.1, reduces fluctuations on the 647 nm pump beam, reducing noise at acoustic frequencies (about 10 kHz and slower) to be unobservable, with most of the remaining (≈ 0.2% RMS) noise at 50 kHz and higher frequencies. However, since the EOM stabilizes the visible laser light passing through it, 2-3% RMS noise remains on the IR light. Thus, a custom electronic device, built by Terry Brown in the JILA electronics shop, has been inserted into the EOM servo loop, which allows the feedback signal to be toggled between the 647 nm intensity and the FCL IR power, as measured on the reference InSb detector. This servo operates synchronously with a number of other electro-optical loops, as described in more detail in Sect. 2.2(D). The complexity of the feedback loop necessitates a highly sophisticated circuit, containing proportional, integral,

differential (or PID) filtering. Adjustable frequency response for the feedback filters enables noise cancellation in the maximum possible bandwidth and finely adjustable servo gain, to maximize noise cancellation while maintaining servo loop stability. With this stabilization implemented, acoustic noise on the IR laser is unobservably small and approximately 0.3% noise remains, presumably caused by the servo loop because of its high frequency (100–500 kHz) approaching the ≈ 500 kHz EOM frequency response.

To obtain absorption sensitivity close to the shot noise limit, the remaining laser noise is subtracted from real "signal" fluctuations using a matched pair of low noise, liquid nitrogen cooled, InSb detectors. Small (0.25 mm^2) detectors result in fast (≈ 1 MHz) bandwidth, and very quiet detector electronics result in a 0.9 pA/√Hz noise floor. This contribution is dwarfed by shot noise on the detector's photocurrent (I_{SN}), given by

$$I_{SN} = \sqrt{2eI_{PC}B_W} \tag{2.5}$$

where e is the fundamental electron charge, I_{PC} is the total photocurrent, and B_W is the bandwidth of the measurement. For an IR power of 50 μW at 2.8 μm, I_{PC} = 100 μA, and $I_{SN}/\sqrt{B_W}$ = 5.9 pA/√Hz. Thus, the shot noise swamps technical noise by a factor of more than six. After subtraction of the common mode noise between the two detectors, the ultimate detection sensitivity is √2 times larger than I_{PC}/I_{SN}, about 7.6×10^{-8} Abs/√Hz.

The preceding argument suggests that increasing IR laser intensity $I(\nu)$ by a factor X should increase the signal to noise by $\sqrt{X}$. In practice, increasing laser intensity leads to saturation of the optical transition. Such saturation is quantified[9,10] by relating the number density (N_1 and N_2) in lower state 1 to upper state 2, via

$$N_2g_1/N_1g_2 = S/(1 + S). \tag{2.6}$$

Here, g_x is the degeneracy of state x, and the saturation parameter S is the ratio of the excitation rate to the relaxation rate when subjected to intensity $I(\nu)$. In the collision-free, transit time broadened conditions in the crossed jets, this ratio becomes

$$S = I(\nu)S_0/(\Delta\nu)^2, \quad (2.7)$$

where $S_0 = 4.5\times10^{-7}$ cm^{2}Hz^{11} is the HF integral cross section and $\Delta\nu$ is the transit time limited homogeneous linewidth. For an HF velocity of approximately 1000 m/s, and a beam diameter of 1 mm, $\Delta\nu$ = 1 MHz. Setting S = 1 provides the characteristic saturating intensity $I_{sat}(\nu)$,

$$I_{sat}(\nu) = \Delta\nu^2/S_0 = 2.2\times10^{16} \text{ photons/cm}^2\text{s} = 1.8 \text{ mW/mm}^2. \quad (2.8)$$

The probe beam is typically < 100 μW power in a 1 mm^2 beam, such that laser intensity remains more than a factor of ten below saturation. Significantly, the saturation parameter calculated via Eq. 2.7 is independent of tightness of the laser focus under these transit time broadened conditions, because $I(\nu)$ scales inversely with the square of the laser beam diameter, and so does $(\Delta\nu)^2$. Thus, all measurements are in a non-saturating regime and directly correlate to *absolute* HF densities in the laser path, as used to estimate absolute reaction cross sections in Sect. 2.3.

Next, common mode laser noise is removed from the measured IR signal by comparison of the laser intensity on the reference and signal InSb detectors. Approximately 40% of the power is diverted onto the reference detector, to measure the IR power and fluctuations. The remaining 60% passes through the Herriot cell, about half of which makes it onto the signal detector. A custom built "laser noise subtractor" scales the reference detector response to the DC level of the signal detector and subtracts common mode noise. The output of this device is amplified 10-fold, such that the IR shot noise swamps the electronic noise of subsequent electronic devices.

Experimentally realizable sensitivities of about twice the shot noise limit have been obtained, resulting in absorbance noise of $A_S = 3\times10^{-5}$ Abs in a 5 kHz bandwidth. The ultimate HF detection limit comes from Beer's law considerations of HF density and maximizing absorption path length through the Herriot cell. With practically realizable configurations of 16 passes through 5 cm of absorbing HF (l = 80 cm), and $\sigma = 1.4\times10^{-15}$ cm^2, (based on an integral line strength of 1.5×10^{-17} cm/# and a 0.011 cm^{-1} Doppler width) Beer's law produces a detection limit (ρ_{min}) of

$$\rho_{min} = A_N / \sigma l, \tag{2.9}$$

and a detection threshold of 4×10^8 HF/cm^3 per quantum state.

Additional sensitivity enhancement results from the redundant information obtained scanning the high-resolution laser in ≈ 3 MHz steps through a ≈ 300–900 MHz HF Doppler profile. At each frequency, an independent measurement of absorption is obtained to construct the Doppler profile, discussed in detail in Sect. 2.3(C). This scanning redundancy produces a large number of independent data points [N > 100–150 under a typical Doppler full width half maximum (FWHM)], providing a $\sqrt{N} \approx$ 10- to 12-fold gain in sensitivity. This effect is conclusively demonstrated in Ch. III and IV, where F atoms reacting with either HCl or H_2O result in signal intensities on par with this limiting noise. Nevertheless, robust results have been obtained via this Doppler averaging, as discussed in more detail in Ch. III. Statistics are further improved by a regimen of signal averaging, during which each IR transition is probed repeatedly over the course of the experiment. The 2.5–3.3 μm tunability of the IR source also enables many HF(v,J) states to be probed on both the P (ΔJ = -1) and R (ΔJ = + 1) branch transitions, further increasing the degree of data oversampling.

Finally, obtaining shot noise limited sensitivity also depends upon careful alignment of the IR laser. Several optical components are likely to attribute to absorbance noise. The HeNe tracer beam can weakly couple onto an InSb detector, but can be eliminated by placing an IR-transmitting germanium filter in the beam path. Also, transmission problems can occur when retroreflected IR beams overlap with incident ones and create standing waves along the beam path, which effectively become low finesse etalons. Such interference is readily identified by the sinusoidal noise pattern obtained when tapping on optical components that form one end of the etalon. Such optics are most likely detector windows and nearby fast-focusing lenses, because of their close proximity and weak sensitivity to lens alignment. This type of noise can be eliminated using irises and careful rotation of components to prevent back reflection.

Another likely culprit for laser noise is the FPI, which also readily produces optical feedback into the laser as it scans to modulate its transmission. However, this feedback is readily identified because it oscillates with the FPI PZT translation, is synchronous with the HV driver, and mimics the shape of the cavity transmission curve. Spatially filtering the FPI from the laser by closing an alignment aperture and/or by using a Faraday isolator (FI in Fig. 2.1) effectively eliminates this effect.

Partial clipping on the edge of the InSb detectors is another likely source of alignment noise. The fast InSb detectors are small (0.5 mm square), necessitating short (5 cm) focal length lenses to tightly focus the IR beam. The focus must be carefully centered on the detectors with a translation stage, such that small lens displacements or beam steering does not change the measured intensity. Remaining sources of loss along the laser path can cause intensity noise, as small motions result in differential changes between the detected reference and signal levels. However, stable optical mounts suppress such motion, which also tends to be in 100 Hz and lower "acoustic" frequencies that are far removed from the faster signal bandwidth.

Finally, the Herriot cell[12] is the most sensitive optical element to align for two reasons. First, the long distance (60 cm) between the Herriot cell mirrors amplifies any mirror motion, such that clipping noise readily becomes detectible. Secondly, the spherical mirrors enable laser divergence to be manipulated, but an understanding the laser propogation is needed to utilize this effect to prevent clipping on the laser beam on the edges of the mirrors. Specifically, the Herriot cell consists of two spherical mirrors with 30 cm radius of curvature, positioned in a nearly concentric fashion, i.e., they share an axis, but are somewhat less than $d = 60$ cm away from each other. The laser beam produces an elliptical pattern on the Herriot cell mirrors, as illustrated in Fig. 2.6. Careful choice of input spot position readily eliminates clipping on the entering beam, focused into the Herriot cell via a 50 cm lens. However, subsequent spots reflecting from the mirror increase in size, as the concave mirrors alter the beam divergence. Gaussian optics

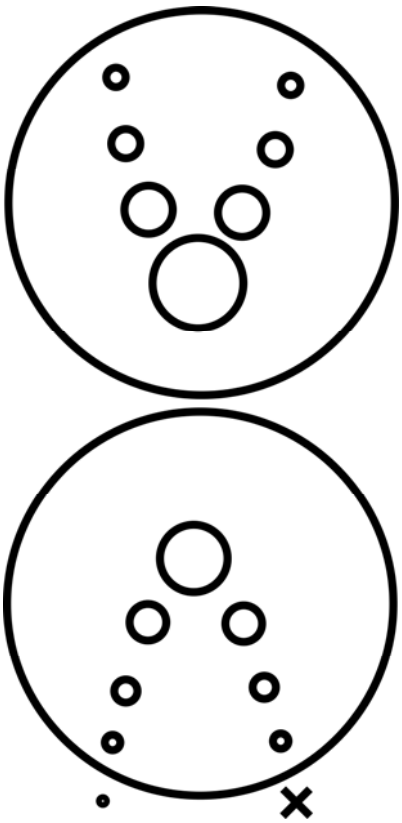

Figure 2.6 Illustration of the elliptical laser spot positions on the Herriot cell mirrors. The beam divergence changes following each reflection from the curved optics. For optimal mirror spacing, the output beam is highly collimated to prevent clipping as it passes by the mirror and travels to the signal detector.

considerations[13] reveal how laser spot size (ω, the $1/e$ electric field radius) changes as it passes through the Herriot cell, as shown in Fig. 2.7. In this figure, the spot size is plotted as a function of laser propagation distance. Reflections off the curved optics are readily identified as local maxima in beam size, i.e., where the diverging beam becomes converging. The spot sizes on the mirrors increase and then decrease for mirror spacing d less than twice the mirrors' radius of curvature. For the 16 pass cell modeled in Fig. 2.7, the spacing in panel b) leads to the most collimated output spot, and therefore the least clipped beam. In practice, this alignment can be attained by measuring the outgoing laser's spot size with a translatable iris near the chamber output while "walking" the mirror spacing to minimize this beam diameter.

The importance of laser collimation and alignment cannot be overemphasized, since light fluctuations of ten parts per million will quickly dominate the detection noise. Indeed, an attempted variation of the Herriot cell failed for this exact reason. Specifically, a triangular multipass configuration was implemented in which the laser beam traveled from one curved mirror to the other, off a flat mirror, and then returned to the first curved mirror. Thus, the jets could be positioned such that the laser passed in only one direction through the intersection region, parallel to the plane of the two jets' axes. This arrangement was designed to produce asymmetric Doppler shifts capable of distinguishing between forward and backward scattering of the HF product. However, tilting of the curved mirrors into the triangular configuration effectively changed the radius of curvature for one axis relative to the other, producing astigmatism. Thus, the mirror spacing needed to collimate the output spot, as illustrated in Fig. 2.7 was different for the horizontal versus vertical beam dimensions and the outgoing spot diverged on at least one axis, producing elliptical spots with different confocal beam parameters on two perpendicular axes. In principle, this effect could be corrected using an astigmatic optic (e.g., a cylindrical lens) in the triangular beam path. However, this additional complication to the

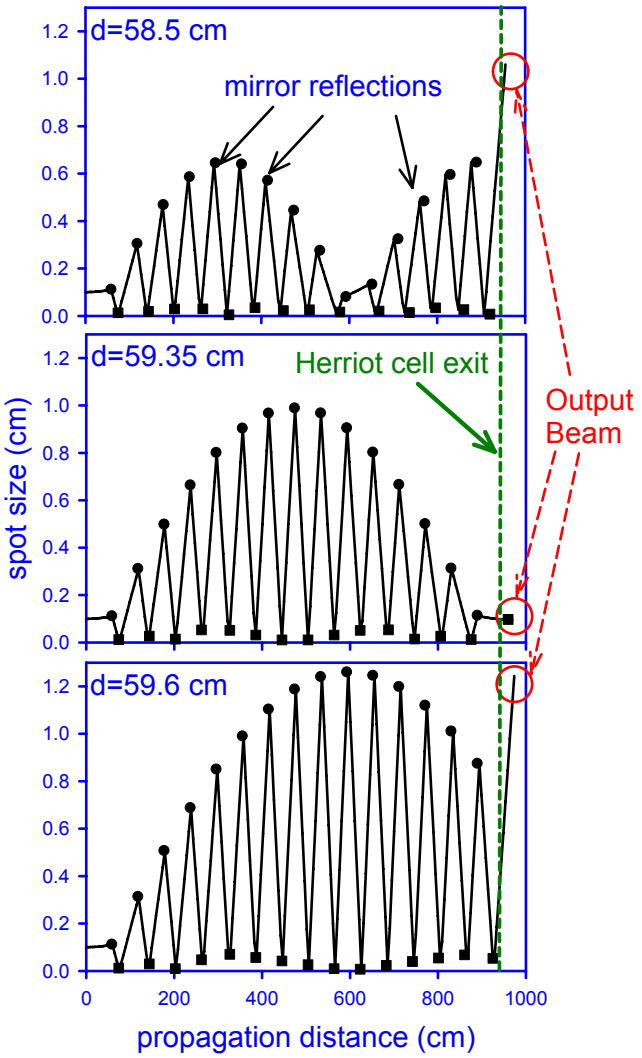

Figure 2.7 Gaussian optics predictions for the IR spot size in the Herriot cell. Mirror reflections are located at the circles, where local maxima of beam diameter occur. Minima are approximately at the squares, the locations of beam waists. After exiting the Herriot cell, the laser beam can only propagate to its waist and then continue to diverge. For the top panel, the mirrors are too close and the maximally collimated beam occurs prior to the outgoing pass. For the bottom panel, they are too far apart and the outgoing pass also diverges rapidly The middle panel, with mirror spacing d = 59.35 cm, produces a well-collimated output beam.

vacuum alignment was not attempted, and all of the reported results utilize a traditional Herriot cell.

D. Continuous and Automated Frequency Scanning

A pair of Brewster windows, mounted on a galvanometer (or galvo for short) as drawn in Fig. 2.2, enables continuous tuning of the FCL, while maintaining single mode operation. Functionally, these calcium fluoride windows displace the laser path by a small amount and change the cavity's free spectral range without changing the output path of the laser. Applying a current to the galvo tilts the plates in opposite directions, refractively displacing the laser beam and tuning the free spectral range of the cavity. To vary the IR frequency continuously, the intracavity etalon must track the moving longitudinal mode as the galvo plates scan. Thus, both the galvo and etalon PZT stacks must be calibrated for frequency tuned per volt applied. The ratio of these values determines the relative feed forward voltage applied to these devices to continuously scan the FCL frequency.

The single mode FCL output is monitored on the scanning FPI cavity to calibrate the feed forward calibration as follows. With the etalon unplugged and therefore static, scanning the galvo plates continuously changes the laser frequency until an adjacent longitudinal mode of the cavity experiences lower loss through the etalon and the IR frequency "hops" to oscillate on this mode instead. A plot of galvo monitor voltage versus the number of hops reveals the displacement of the original longitudinal mode in units of cavity $FSR = 0.01\ \text{cm}^{-1}$, resulting in a feed forward value of $7.23\ \text{V/cm}^{-1}$. Although *FSR* is technically changing with the galvo scan, it only does so in proportion to the number of observed hops out of the cavity mode number that is oscillating ($n \approx 350{,}000$), such that it can be treated as constant.

A similar process is used to calibrate the etalon PZT feed forward with the galvo plates stationary, except that in this case the laser frequency remains constant until the etalon transmission shifts enough to transfer lasing to the adjacent longitudinal mode. Measuring these

transitions as a function of etalon feed forward provides a similar calibration curve, and a value of –6.98 V/cm^{-1}, as measured on the PZT HV driver output monitor. Unfortunately, the etalon PZT responds nonlinearly to applied voltage over its 0–1000 V range, so this calibration is best performed at about 500 V to obtain a median value of the tuning response.

To compensate for laser frequency drift and nonlinearities in the galvo and etalon feed forward calibration, an servo loop prevents hopping between longitudinal modes as the cavity scans. This servo loop, illustrated in Fig. 2.8, functions by continuously "dithering" the etalon PZTs by applying a sinusoidal modulation voltage at frequency $\omega \approx 2$ kHz on top of the DC voltage applied to maintain the proper intracavity etalon mode spacing. Thus, the etalon mirrors oscillate at ω, but with low enough amplitude to avoid mode hops, resulting in a slight modulation of the output IR intensity as the etalon transmission moves relative to the longitudinal mode on which the cavity is oscillating. If the etalon is perfectly centered on the longitudinal mode, the modulation frequency will be at 2ω, while any average frequency mismatch results in some intensity modulation at the dither frequency, ω. Thus, synchronous detection of the error signal at ω provides feedback to the etalon servo.

The feedback signal comes from one of two places. If the krypton ion pump laser intensity is constant, then the reference InSb detects the IR modulation directly, as illustrated by the short dashed line in Fig. 2.8. Alternatively, under data acquisition conditions, the FCL power is actively constrained to be constant by the laser intensity servo described in Sect. 2.2(C). In this case, the EOM transmits higher pump laser power to maintain the same IR power as the etalon dithers. Thus, the EOM error signal contains the dither feedback information at frequency ω, and the FCL servo loop is completed according to the long dashed line in Fig. 2.8.

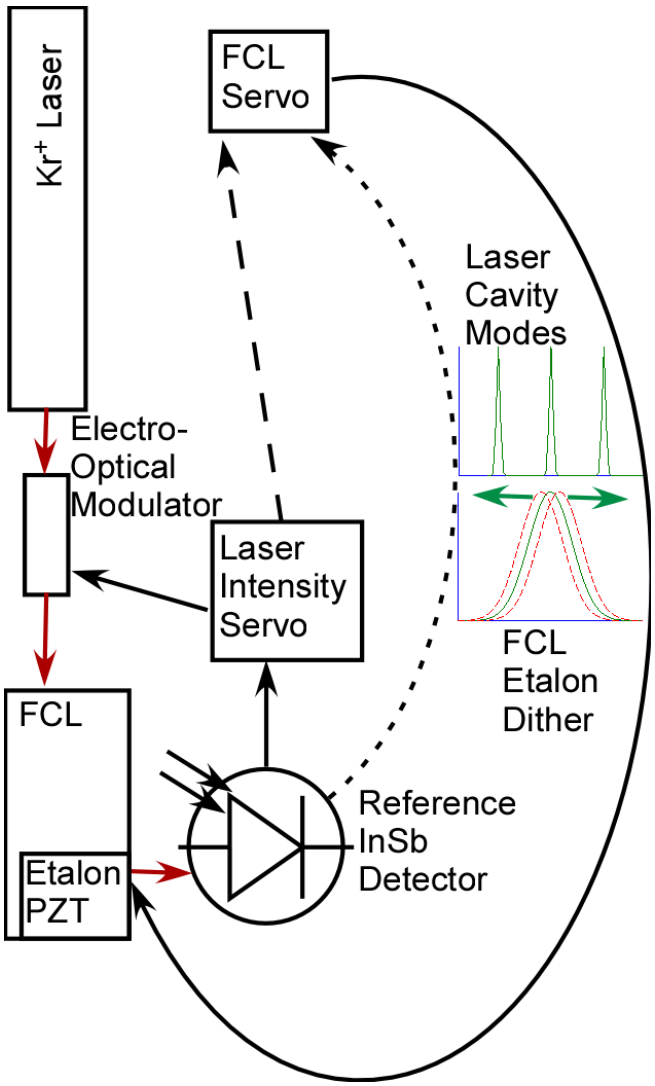

Figure 2.8 Schematic for the laser frequency servo loop. The FCL servo dithers the intracavity etalon voltage and monitors the error signal at the applied frequency. In the first servo mode (short dashed line), the IR intensity varies and is directly monitored. However, when the IR laser intensity servo is used, the EOM modulates the pump laser power changes to maintain constant IR power. In this mode, the error signal from the laser intensity servo (long dashed line) contains the information about the etalon dither.

2.3 Crossed Jet Apparatus

For the gas-phase reaction dynamics studies, reactants enter the ≈ 100 L diffusion-pumped vacuum chamber via two supersonic molecular jets. The jet axes are oriented at 90° angles and intersect 2.5–5.0 cm downstream from their orifices, as illustrated in Fig. 2.9. One jet emanates from a custom-built Proch-Trickl[14] valve, which uses a PZT disc actuator to generate 200–500 μs gas pulses. This valve delivers about 8×10^{13} molecules/cm^3 to the jet intersection region at typical backing pressures of 200 Torr for a 500 μm pinhole orifice. The radical source, described in detail below, uses a HV plasma (50–500 μs duration) to dissociate F_2 into reactive F atoms during an approximately 2 ms gas pulse. This valve has an approximately 0.03 by 0.3 cm orifice and typically operates with a stagnation pressure of 70 Torr, resulting in an additional 1.0×10^{14} #/cm^3 in the probe region. With the valves pulsing at 10.1 Hz, the average pressure in the chamber rises to ≈ 1.0×10^{-4} Torr, corresponding to a mean free path of λ ≈ 50 cm between molecular collisions, i.e., considerably greater than the distance to the chamber walls.

Low-density conditions ensure that the probability for secondary molecular collisions is on the order of 1 % prior to leaving the ≈ 0.5 cm detection volume. Most collisions are with helium and other rare carrier gas atoms which have small cross sections for rovibrationally inelastic scattering;[15] hence, this represents an upper limit for redistribution of the HF(*v,J*) population. Nevertheless, possible inelastic relaxation is a concern that has been explicitly tested for each system, as discussed in subsequent chapters. In general, such single collision conditions are readily satisfied, as only 0.04% of the approximately 1×10^{12} #/cm^3 F atoms present in the probe region need to react and form HF in a given (*v,J*) state to exceed the detection threshold computed in Sect. 2.2(C). Thus, the IR detection technique has enabled the study of reaction dynamics of systems with rate constants up to about ten times lower than the gas kinetic rate (i.e., cross sections of about 1 Å^2). The cross section for do-able experiments will scale with the

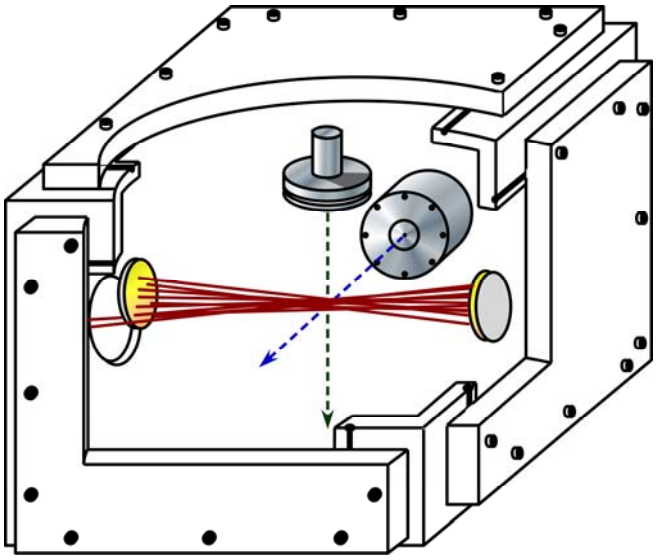

Figure 2.9 Illustration of the reaction vessel. Unskimmed molecular jets intersect at a 90° angle, centered on the IR multipass cell, whose axis is perpendicular to the plane defined by the central axes of the jets.

reactant densities, the absorption path length probed by the IR laser, and the RMS absorbance noise, while scaling inversely with the IR line strength and the number of populated product quantum states. Since the HF IR transition is a particularly strong one, and the present densities have been pushed close to the limits of single collision conditions, probable areas for improvement include lower noise (i.e., faster) data acquisition techniques, different probe geometries (such as cavity ring down), and different jet sources, such as crossed slit jets or higher efficiency radical sources.

In addition to providing a convenient source for directed, low density molecules, the supersonic jets also cool the reactants, with rotational temperatures of ≈ 30 K observed for the hydrides considered here, and colder distributions likely for species with smaller rotational constants. Jets also provide a means to vary translational energy via choice of carrier gas. These effects narrow the number of states and make kinetic energy dependent studies possible. The jets can be characterized a number of ways. First, the measured velocities closely match the predicted terminal velocities anticipated by fluid dynamics,[16] indicating efficient cooling of the expansion gases. Additionally, direct IR observations of HCl and the naturally present $H_2{}^{18}O$ isotopologue (whose low atmospheric concentration makes it easy to probe in low rotational states) also confirm efficient cooling.

A major new capability has also been developed for studying the nature of chemical reaction events at the vacuum interface of bulk liquid surfaces. These gas-liquid scattering experiments utilize the same F atom source as the crossed jet studies, but otherwise introduce a number of novel features. The use of bulk liquids in vacuum raises a number of interesting points. First, low vapor pressure (≈ 10^{-7} Torr) liquids are used to prevent loss of reactant and maintain long mean free paths. Secondly, the probability of a molecule incident upon the liquid colliding with the surface is essentially unity, and reaction probabilities are similarly high. However, checks against jet shocks at the surface and other nonlinear effects are also necessary. Finally,

issues of surface cleanliness in vacuum must be confronted by continuously refreshing the surface. These issues and further experimental details of the gas-liquid scattering studies can be found along with the experimental results in Ch. V.

A. Radical Source:

The F atom source is a standard solenoid fuel injector modified to generate radicals in an electrical discharge at the throat of the supersonic expansion, as shown in Fig. 2.10. The F atoms are produced as follows. The solenoid pulses 50–100 Torr of a 10% F_2 / 90% rare gas excimer pre-mix into a small (≈ 0.025 mL) volume defined by a slotted hole in a 0.5 mm inert (polychlorotrifluoroethylene) disk insulator, sandwiched between two metal electrodes. A miniature slit (300 μm × 0.3 cm) in the downstream electrode forms the limiting orifice, from which the gas expands past two slit-jet expansion-defining "jaws" and into the chamber. This source utilizes a slit expansion geometry because it prolongs the time between routine cleaning and sanding of the electrodes, presumably because the elongated orifice provides more electrode surface area for a given nozzle area, such that plasma wear is diluted over more electrode material. At the peak of the 2 ms gas pulse, a 500 μs HV pulse (≈ -1 kV) is applied to the lower electrode, striking an electrical discharge through the gas mixture to the grounded upper electrode on the valve body. Measuring HF densities produced in crossed jet studies of F + H_2, with known reaction cross section,[17] enables F densities of approximately 2.6×10^{12} atoms/cm^3 to be inferred. Such densities correlate to ≈ 2×10^{16} F atoms/cm^3 at the limiting orifice, or ≈ 10% of the F_2 dissociating into F atoms in the plasma. These measurements have also been used to estimate the reaction cross section for several systems, as discussed in detail in the next subsection.

Very recently, a similar plasma source has been designed for use with a Proch-Trickl pulsed valve, based on a design borrowed from the Ye group at JILA. For this valve, a pinhole source replaces the slit, and either ceramic or plastic insulators may be used. Based on the advice

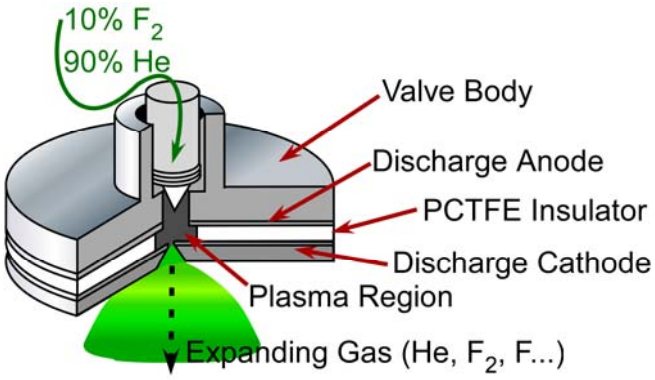

Figure 2.10 Drawing of the radical jet source. High voltage applied to the cathode strikes a plasma upstream of the limiting orifice, generating reactive F atoms.

of the Ye group, the electrodes were finely polished using a series of progressively finer sand paper grits, a fine paste polish, and then electro polishing, to remove surface roughness and extend the stable lifetime of the electrodes between servicing. This valve has been briefly used in the ion imaging apparatus described in Appendix B, and radical Cl production efficiency is comparable to that found for F atoms, above.

Because of the harsh environment in the radical atom source, the high voltage electrode surfaces physically and chemically degrade, leading to unstable plasma current and F atom production efficiency. Erratic performance generally arises after about a week of regular operation, but sanding and polishing the electrodes restores stability. This wear results in drift of the F atom density on an inverse day time scale, necessitating normalization of the data set with respect to F atom density. Thus, a strong reference transition is observed every 2–3 hours during data acquisition, such that the entire data set can be normalized and data collected over many weeks meaningfully compared and signal averaged.

The high sensitivity to HF product density also necessitates compensation for trace amounts of background HF contamination. This background originates from the F source, presumably via pre-reaction with impurities in the gas mixture at part per million concentrations. Fortunately, efficient cooling in the supersonic jet (even with the discharge on) confines all such background to HF $v = 0$, with a rotational temperature of ≈ 60 K, as shown in Fig. 2.11. This background is explicitly measured by re-scanning each transition originating in HF($v = 0$) without the second jet, such that the differential increase in integrated absorption can be attributed to the HF reactive product channel. This procedure works well but often generates significant uncertainties for the lowest [HF($v = 0$,$J < 6$)] states arising from subtraction of weak and nearly equivalent populations. Nevertheless, the plasma source and IR technique enable the HF populations to be observed, and provide direct measurement of population in the ground vibrational state, inaccessible via IR chemiluminescence methods.[2,18-29]

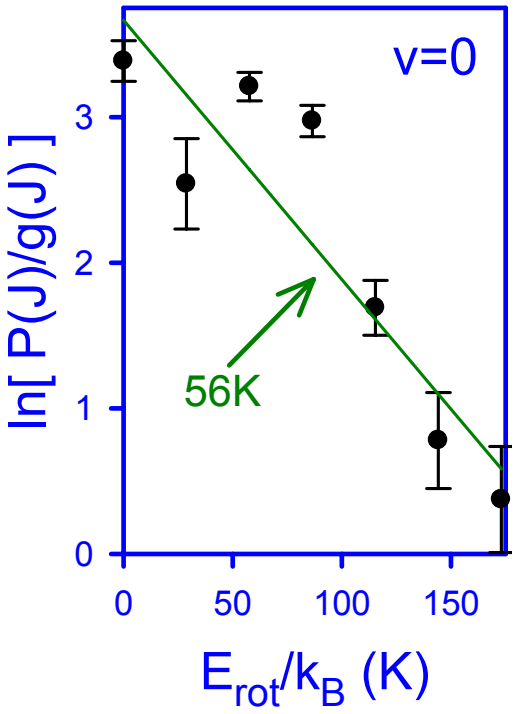

Figure 2.11 Boltzmann plot of the HF background produced in the F atom plasma source. The density of HF background is much smaller than that reactively produced in the crossed jets. Supersonic cooling confines the background to low J in the $v = 0$ manifold, as indicated by the ≈ 60 K fit to the rotational distribution.

B. Data acquisition

HF produced via reaction at the intersection of the pulsed jets results in a transient change in the intensity of the IR probe when the frequency lies within the Doppler profile of a populated HF(v,J) transition. A transient recorder (or, in a recent upgrade, a computer digital acquisition board) digitizes this transient absorption waveform, and it is analyzed in real time. Specifically, the absorption pulse is numerically averaged under a 100–500 μs window, coinciding with the peak absorption signal and resulting in a 2–10 kHz detection bandwidth. Additional time gates, preceding and/or following the signal gate by several hundred microseconds, are also averaged in order to correct for pulse-to-pulse changes in the absorption baseline and eliminate slow noise fluctuations. The net absorption is plotted as a function of laser frequency to construct Doppler profiles such as those presented in Fig. 3.3, 4.4, 5.5, and 5.10.

A digital to analog converter provides a voltage ramp used to automate the laser tuning as described in Sect. 2.2(D). Typically, the laser tunes about 3 MHz between jet pulses, and the process is repeated ≈ 1000 times over a 3 GHz window, sufficient to resolve the entire Doppler profile. However, it is also necessary to calibrate the frequency axis during the scan. For this purpose, the TAC output is also recorded, providing a measure of the FPI output at each laser step, as described in Sect. 2.2(B) and depicted in the top panel of Fig. 2.5. The TAC saw tooth wave contains sharp falling edges, spaced by the FSR of the FPI, such that a simple edge finding routine can be used to calibrate the frequency axis with the precision of the scanning etalon. Additional DC data are acquired, including the signal InSb detector DC level, used to convert measured waveforms into absorbance units, and the transmission of a reference gas cell, which provides absolute frequency calibration.

When acquiring data, the Doppler profiles are typically scanned at least three times in succession. This redundancy improves the statistical uncertainty of the measurements and also helps reveal systematic changes (e.g., poor plasma reproducibility in the F atom source), which

can be missed during long average scans. Some degree of redundancy is warranted, as Doppler measurements require only about one hundred seconds of acquisition time, and a similar amount of time goes into manually tuning the laser and preparing it when transitioning between spectral lines. Repeat measurements also statistically decrease uncertainties, an important effect for low signal experiments.

2.4 Data Analysis and Experimental Modeling

A. Spectral Analysis

Sample Doppler measurements are presented in each chapter for the reaction being studied. Figs. 3.3 and 5.5 illustrate the types of signal to noise and spectral features obtained for the various studies. Because chemical reaction readily produces vibrationally excited HF product, the measured absorption profiles, $A(\nu)$, contain structure according to the density of HF absorbing from the lower state j and emitting from the upper state i at each Doppler detuning $\nu-\nu_0$ according to the Beer-Lambert law, expressed as

$$A_{ij}(\nu-\nu_0) = \int dx \int d\nu' \, [\sigma_{i\rightarrow j}(\nu-\nu')\kappa_i(x,\nu'-\nu_0) - \sigma_{i\leftarrow j}(\nu-\nu')\kappa_j(x,\nu'-\nu_0)]. \qquad (2.10)$$

Here $\kappa_{i/j}(x,\nu'-\nu_0)$ is the spectral density (i.e., molecules/cm^3/cm^{-1}) of absorbers in states i or j, at a position x along the absorption path with Doppler shifted center frequency $\nu'-\nu_0$. $\sigma_{j\leftarrow i}(\nu-\nu')$ and $\sigma_{j\rightarrow i}(\nu-\nu')$ are the homogeneously broadened absorption/emission cross sections between states i and j centered on ν'. Since the homogeneous lineshape is much narrower than the inhomogeneous Doppler profile, it can be approximated as a delta function such that integrating over ν' yields

$$A_{ji}(\nu-\nu_0) = S_{i\rightarrow j}\int dx\ \kappa_i(x,\nu-\nu_0) - S_{i\leftarrow j}\int dx\ \kappa_j(x,\nu-\nu_0). \qquad (2.11)$$

Thus, the net absorption at $\nu-\nu_0$ is related to the difference in HF *column-integrated spectral density* $\int dx\ \kappa_{i/j}(x,\nu-\nu_0)$, weighted by the appropriate line strengths ($S_{i\leftrightarrow j}$).

To simplify the discussion of the quantum-state distributions, measured Doppler profiles are numerically integrated, and more detailed analysis of the absorption lineshapes is postponed until Sect. 2.4(C). Integrating Eq. 2.11 with respect to ν relates the integral absorbance to the total HF column-integrated density $\int dx\, \rho_{i/j}(x) = \int dx \int d\nu\, \kappa_{i/j}(x, \nu - \nu_0)$

$$\int A(\nu - \nu_0)\, d\nu = S_{i \rightarrow j} \int dx\, \rho_i(x) - S_{i \leftarrow j} \int dx\, \rho_j(x). \qquad (2.12)$$

Eq. 2.12 permits the *difference* in *column-integrated densities* (CIDs) for the lower and upper probe states to be extracted using the absorption line strengths ($S_{i \leftrightarrow j}$), well known from the analysis of Arunan, Setser and Ogilvie.[11]

For the excited vibrational populations observed following reactive scattering, significant HF density often forms in both *upper*, *j*, and *lower*, *i*, states, resulting in a competition between stimulated *emission* and *absorption* signals. Such non-equilibrium conditions are readily anticipated following chemical reaction, and form the basis of chemical lasers.[30] The presence of two unknown CIDs in Eq. 2.12 leads to correlation between upper and lower state populations in a least-squares fit to the spectral data. However, observation of lines originating from the highest energetically accessible (v_{max}) manifold effectively breaks this correlation, since the population in the (v_{max} + 1) upper state can be set to zero. Furthermore, the tunability of the IR laser permits observation of both P and R branch transitions out of many HF(v,J) lower states, increasing the number of measurements probing each state.

The network of accessible HF transitions in Fig. 2.12 illustrates the redundancy of the IR spectral measurements. This presentation emphasizes that more than one transition is measured for a large number of HF(v,J) states, and that the population in a given state is linked to that in every other. Fitting the entire spectrum simultaneously produces the set of HF(v,J) CIDs from the measured spectrum without any *ad hoc* assumptions. States whose energy exceeds the available energy can also be probed, and the absence of measurable population justifies fixing the density in these states to zero in the least squares fit. However, since the HF density in each manifold

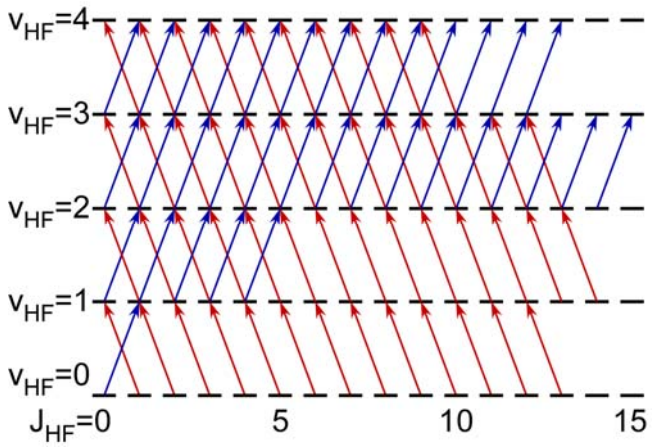

Figure 2.12 The network of accessible HF transitions in the 2.5–3.3 μm tuning range of the IR laser. A large number of *J* states in the $v = 0$–3 manifolds are accessible, many of them via both P and R branch transitions.

depends upon measurements in every higher populated manifold, illustrated in Fig. 2.12, the fitted uncertainties tend to increase in lower vibrational manifolds. This trend has been observed in every data set presented here. Nevertheless, robust measurements of HF density have generally been obtained down to the ground vibrational manifold.

B. Density-to-flux Transformation and Monte Carlo Simulation of the Crossed Molecular Jets

The measured IR spectrum yields HF state resolved column-integrated *densities* via least squares fitting of the spectrum described in the previous section. However, under crossed jet conditions the *flux* of product molecules, not the density, is directly proportional to the state resolved reaction cross section. Obtaining product fluxes requires consideration of the well-known *density-to-flux* transformation,[31-33] i.e. correctly taking into account the velocity-dependent detection sensitivity intrinsic in any density-based measurement technique, such as IR spectroscopy.

The single-collision conditions and excited Doppler measurements, discussed in more detail in Sect. 2.4(D), emphasize the need for the density-to-flux transformation. Essentially, if HF product is observed under single collision conditions it cannot be considered *translationally equilibrated*, and by simple energy conservation, lower energy product states can be expected to have higher recoil energies and spend less time in the detection volume. Conversely, translational equilibration necessarily entails post-reaction collisions, which may also cause inelastic redistribution of energy. Benchmark chemiluminescence studies[2,18-22,24-27,29,34-38] were performed under such translationally equilibrated conditions, further emphasizing the present interest in revisiting these reactions under lower density.

The relationship between reaction cross section and product density can be found via considerations based on those of Sonnenfroh and Liu.[31] Fundamentally, the probability P_F of an F

atom reacting following a displacement dl in the center of mass frame in the vicinity of a point $\boldsymbol{r}$, with density $\rho_{HX}(\boldsymbol{r})$ of reactant HX is given by the Beer's law-type expression,

$$P_F = \sigma_j \rho_{HX}(\boldsymbol{r}) dl, \tag{2.13}$$

where σ_j is the total reaction cross section for forming HF in state j, treated as a constant for the current discussion. Shifting to the laboratory frame requires the substitution $dl = (v_{rel}/v_F)dx$, where $v_{rel} = dl/dt$ is the relative velocity in the center of mass frame, and $v_F = dx/dt$ is the laboratory-frame F velocity, defined to be along the x axis. Thus, P_F becomes

$$P_F = \sigma_j \rho_{HX}(\boldsymbol{r})(v_{rel}/v_F)dx. \tag{2.14}$$

Thus, the rate of F loss $R_F(\boldsymbol{r})$ (in #/cm^3/s) at $\boldsymbol{r}$ is given by $-P_F$ times the density of F at $\boldsymbol{r}$, $\rho_F(\boldsymbol{r})$, divided by the time spent at $\boldsymbol{r}$, $dt = dx/v_F$. The rate of formation of HF is $R_{HF} = -R_F$, such that

$$R_{HF}(\boldsymbol{r}) = P_F \rho_F(\boldsymbol{r}) v_F/dx = \sigma_j \rho_F(\boldsymbol{r}) \rho_{HX}(\boldsymbol{r}) v_{rel}, \tag{2.15}$$

Note that the $\rho_F(\boldsymbol{r})$ and $\rho_{HX}(\boldsymbol{r})$ terms appear symmetrically in this expression, as they must, since it also could have been derived from identical considerations of the HX jet.

The local HF density $\rho_{HF}(\boldsymbol{r})$ results from the HF formation rate at $\boldsymbol{r}$ and the flux of HF passing through $\boldsymbol{r}$, due to reaction elsewhere. Mathematically, the density ρ_{HF} and the laboratory-frame velocity $\boldsymbol{v}_{HF}$ are related via the continuity equation of fluid dynamics,

$$d\rho_{HF}(\boldsymbol{r})/dt = R_{HF}(\boldsymbol{r}) - \boldsymbol{\nabla}\cdot\rho_{HF}(\boldsymbol{r})\boldsymbol{v}. \tag{2.16}$$

Integrating Eq. 2.16 over a finite volume V, $\iiint_V dV$, emphasizes the physical interpretation that the rate of change of HF molecules in V [$\iiint_V dV\, d\rho_{HF}(\boldsymbol{r})/dt$] must be equal to the rate at which they are formed [$\iiint_V dV\, R_{HF}(\boldsymbol{r})$] minus the net flux leaving V through its bounding surface A. This last term is made explicit by substituting $\iiint_V \boldsymbol{\nabla}\cdot\rho_{HF}(\boldsymbol{r})\boldsymbol{v}_{HF} = \iint_{Ac} \rho_{HF}(\boldsymbol{r})\boldsymbol{v}_{HF}\cdot d\boldsymbol{A}$, where $\iint_{Ac}$ denotes integral over a closed area A bounding V, according to Gauss' divergence theorem.

When $\rho_{HF}(\boldsymbol{r})$ is probed for a short time after the reaction begins in the crossed jets, the explicit time dependence of $\rho_{HF}(\boldsymbol{r})$ must be taken into account according to Eq. 2.16 in a detailed model of the experimental conditions. For the present experiment, the *steady state limit* is valid,

since the approximately 10–50 μs HF travel time from anywhere in the reaction region the probe laser is much smaller than i) the > 200 μs signal gate for averaging IR absorption data and ii) the even longer (> 0.5 ms) pulsed jet durations. Thus, time-dependent models can be avoided and setting the left hand side of Eq. 2.16 to zero results in

$$\iiint_V R_{HF}(\boldsymbol{r})dV = \iint_{Ac} \rho_{HF}(\boldsymbol{r})\boldsymbol{v}_{HF}\cdot d\boldsymbol{A}, \tag{2.17}$$

which states that the HF flux away from $\boldsymbol{r}$ must be equal to the rate of HF production at $\boldsymbol{r}$ for steady state conditions. Integrating over a sufficiently small region around $\boldsymbol{r}$, the velocity vector points normal to $\boldsymbol{dA}$ at all points. Denoting the small volume ΔV and surface area ΔA, dividing by ΔA, and substituting in for $R_{HF}(\boldsymbol{r})$ using Eq. 2.15, one finds an expression for the localized flux per unit area Φ,

$$\Phi(\boldsymbol{r}) = \sigma_j \rho_F \rho_{HX} v_{rel} \Delta V/\Delta A = \rho(\boldsymbol{r}) v_{HF}. \tag{2.18}$$

Here, the explicit $\boldsymbol{r}$ dependence of ρ_F, ρ_{HX}, and v_{rel} has been dropped because ΔV is assumed to be small enough that they are nearly constant.

Eq. 2.18 is too simple to accurately represent the conditions in the crossed jet apparatus, where a distribution of fluxes exist at each position, due to the generation of HF at every other position, and with a velocity distribution depending upon the HF point of origin and location of the flux in question. However, the total flux is a superposition of various flux components (labeled with subscript i), each of which still obey

$$\Phi_i = \rho_i v_i. \tag{2.19}$$

The total flux, $\Phi_{Tot} = \Sigma_i \Phi_i$, is still directly proportional to the state resolved cross section σ_j, in the limit that any changes in collision energy are small and do not result in dramatically different reaction cross section for portions of Φ_i originating from regions with significantly different mean collision energies. The relationship between Φ_{Tot} and $\rho_{Tot} = \Sigma_i \rho_i$ can be found by dividing both sides of Eq. 2.19 by v_i and summing over i,

$$\rho_{Tot} = \Sigma_i \Phi_i / v_i. \tag{2.20}$$

Dividing this expression by Φ_{Tot}, one finds that the right hand side is $\langle 1/v \rangle$ the flux-weighted expectation value of the inverse speed, which rigorously connects Φ_{Tot} to ρ_{Tot} according to,

$$\rho_{j\_Tot}/\langle 1/v \rangle_j = \Phi_{j\_Tot}. \quad (2.21)$$

For fixed probe geometry $\langle 1/v \rangle$ is also directly proportional to $\langle \tau \rangle$, which is used as the density to flux conversion factor in Ch. III and IV, and Appendix E, since the flux is subsequently normalized to provide the relative magnetude of σ_j for various j. This substitution is also intuitively appealing because $\langle \tau \rangle$ weighting reveals an enhanced detection probability for molecules in states that recoil such that they spend more time in the probe region.

In principle, the sum represented in Eq. 2.20 could be converted to an integral and evaluated for the explicit experimental conditions. In practice, such integration is cumbersome and is replaced by numerical Monte Carlo (MC) simulation instead. Specifically, the simulation models the explicit HF formation and absorption events for each of the crossed jet systems in order to directly approximate this sum. The details of the MC routine are as follows and are illustrated in Fig. 2.13. The program randomly samples "reaction locations" $\boldsymbol{r}$ within the cubic simulation volume with side $2d$, where d is the distance from the jet orifices to the probe axis. The product center of mass (COM) recoil direction is also randomly sampled within user-chosen i) differential scattering constraints and ii) change in kinetic energy corresponding to formation of a given product state. The reactant velocities are also randomly sampled from within the known speed distribution, while constraining the velocity vector to be parallel to the line connecting $\boldsymbol{r}$ to the corresponding reactants' nozzle orifice.

Thus, the MC routine simulates the distribution of speeds, densities, collision angles, and scattering angles present under the experimental conditions. The inputs to the model are as follows: i) probe and jet geometries, ii) and product masses, iii) reaction exothermicity, iv) jet

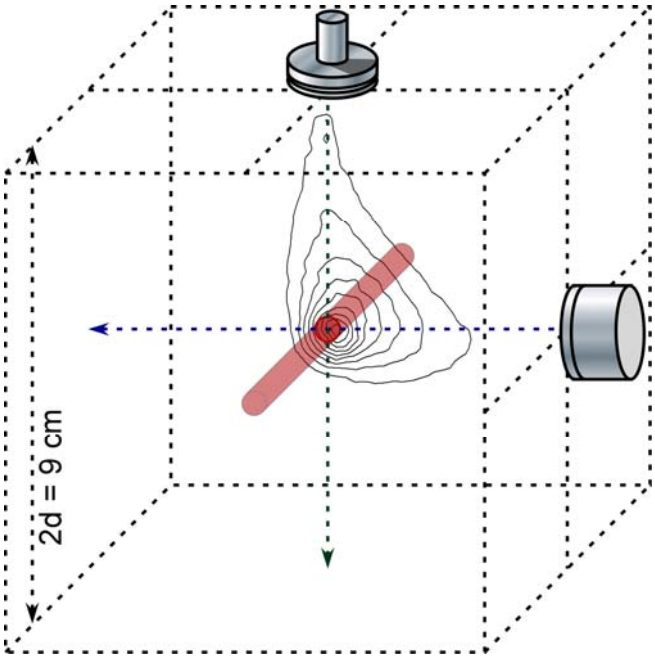

Figure 2.13 Illustration of the Monte Carlo computational volume used to simulate the F + HCl reaction conditions. The jet sources define two edges of the cubic volume, located d = 4.5 cm from their intersection point. The Herriot cell probe volume, shaded red, is centered at this point and simulated by a 0.5 cm diameter cylinder, perpendicular to the plane of the jets. The contours are the detection probability for HF formed with ΔE_{trans} = 0.0 kcal/mol, also presented in Fig. 2.14.

angular and speed distributions [measured experimentally via high-resolution Dopplerimetry on IR chromophores doped in the incident beams in a separate experiment], and v) the adiabatic, zero-point corrected transition-state barrier heights obtained from high-level *ab initio* calculations,[39,40] below which the reaction can not proceed classically. These parameters and a random sampling of the recoil dynamics enable the laboratory-frame trajectory of the HF product to be computed. If a randomly generated trajectory intersects the detection volume V (a cylinder with 0.5 cm radius, whose long axis is perpendicular to the plane of the jets), then such scattering trajectories contribute to the detected signal. The relative importance of the detected trajectory is found by histogramming the results according to the right hand side of Eq. 2.18, i.e., the product flux, numerically proportional to the product of $\rho_F(r)$, $\rho_{HX}(r)$, and v_{rel}. The histogrammed results provide information on the distribution of HF residence times in the probe region, the spatial distribution of detected reactions, the Doppler projection of the HF product, and the collision energies. Sampling a million MC trajectories produces good convergence, and the process is repeated for various differential scattering limits. A separate calculation is performed for each value of recoil translational energy change, ΔE_{trans}, based on specific HF(v,J) states and assumed coproduct (X radical from HX reacant) internal energy.

In general, the MC results are relatively insensitive to the assumed differential cross section largely because spatial averaging within the unskimmed jets blurs the details of the recoil dynamics. Nevertheless, different angular scattering limits are considered for each reaction system, as discussed in more detail in Appendix E. The density-to-flux transformation results in a modest increase in product branching into low-energy HF(v,J) states, when compared to the raw HF column-integrated densities. This effect arises from the higher average laboratory-frame velocities resulting for HF formed in lower internally excited states. Indeed, this physical picture predicts that the computed $\langle \tau \rangle$ values should scale inversely with the recoil speed, i.e., with the

average energy available to products to the negative one-half power, $\langle E_{avail} \rangle^{-1/2}$, as observed for sufficiently large E_{avail}, regardless of assumed differential cross section, as shown in Fig. A.13(b).

Of course, the exact values of the calculated $\langle \tau \rangle$ values are dependent on the chosen detection volume shown in Fig. 2.13. However, only the ratios of the HF residence times influence the final results, since the normalized HF populations are ultimately reported. Additionally, small changes in the shape or position of the probe volume are unlikely to perturb the ratios of the $\langle \tau \rangle$ values. This conclusion is expected because an average time was used as a conveniently calculated value, versus the true $\langle 1/v \rangle$ scaling factor derived from Eq. 2.20.

In addition to providing $\langle \tau \rangle$ values, the MC model provides a number of other insights into the experimental conditions. Specifically, the collision energy distribution is obtained from the computation, and found to be somewhat higher than expected for the jets intersecting at 90°. This increase results from the spatial distribution of detected products presented in Fig. 2.14, which reveals that "head on" collisions, i.e., those occurring closer to the line connecting the two jets, are somewhat likely to be detected, increasing the mean collision energy. This figure reveals that in every recoil energy regime, the highest sensitivity is for products formed near the detection volume, and collisions downstream with respect to the laboratory-frame center-of-mass velocity have negligible detection probability. However, products formed closer to the valve orifices have a reasonable probability of passing through the detection volume because the laboratory-frame velocity of the collision partners points that direction. The top left panel in Fig. 2.14 reveals that particularly endothermic processes that absorb kinetic energy ($\Delta E_{trans} < 0$) preferentially sample the region connecting the two jets. This effect occurs because this region corresponds to the highest energy "head-on" collisions, and excessively energetic collisions are not likely elsewhere. Thus, the Monte Carlo results match simple expectations based on and product flow.

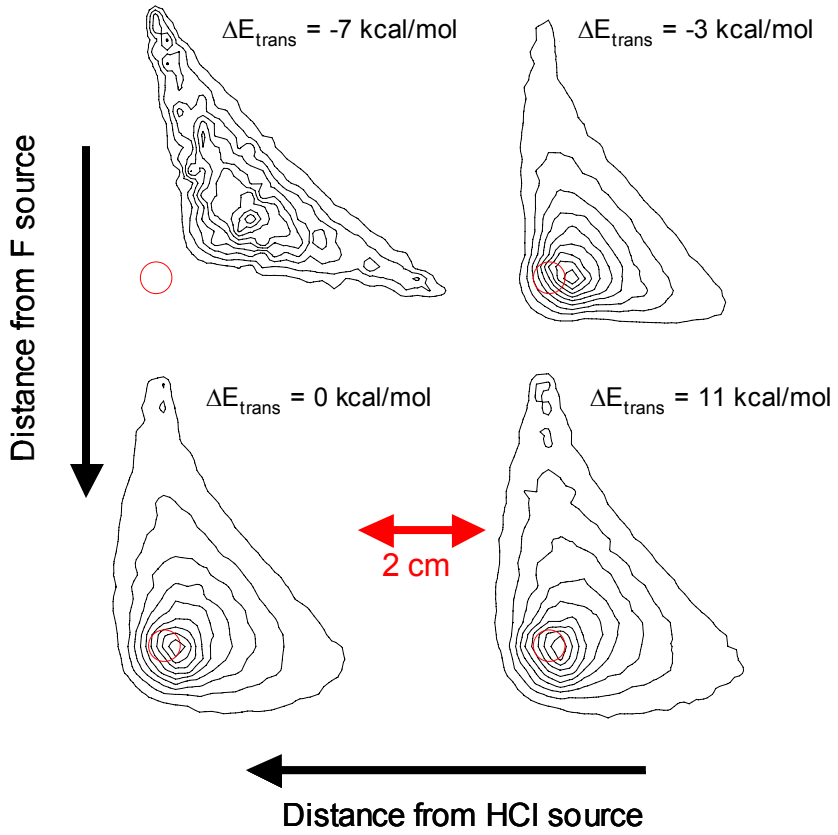

Figure 2.14 The relative detection sensitivity to HF formed following the reaction F + HCl, integrated with respect to the coordinate perpendicular to the plane of the jets. Representative results are shown for varying amounts of energy released into kinetic energy (ΔE_{trans}) by the reaction event. The distance from the HCl and F sources are the horizontal and vertical axes, respectively, as illustrated in Fig. 2.13. Contours are linearly spaced from 10% to 90% detection probability. The red circle denotes the location of the detection region.

Additionally, the MC model predicts detailed HF Doppler distributions for a given angular scattering distribution. However, the signal to noise ratio obtained in the F + H_2O and F + HCl reactions described in Ch. III and IV is too low to enable detailed comparison to the predictions. Geometric averaging of laboratory-frame COM and relative velocities under unskimmed jet conditions tends to blur detailed information about HF product recoil in the COM frame. Nevertheless, observed Doppler widths do directly report on the average energy released into translational energy following the reactive event, as discussed in more detail Sect. 2.4(D).

C. Reactive Cross Section Estimates

The IR absorption technique also enables absolute measurement of HF density, from which the reaction cross section σ can be estimated. Specifically, Eqs. 2.18 and 2.20 reveal that σ scales with ρ_{HF} and inversely with ρ_F, ρ_{HX}, v_{rel}, and $\langle\tau\rangle$. Since ρ_{HF} varies with the discharge conditions, it must be calibrated against a system with known reaction cross section. For the present studies, F + H_2 serves as a convenient reference, well characterized by Dong's[17] measured cross section of σ_{rxn}(F + H_2) = 3.0 Å^2 and Chapman's[41] HF quantum-state distribution at 2.3 kcal/mol collision energy. Since the total density of HF has been measured previously, it is only necessary to measure a single quantum state, j, and relate the fractional population f_j in that state to the total density via $\rho_{HF} = \rho_{HF,j}/f_j$.

Thus, the relative cross sections for two reactions (denoted 1 and 2) can be expressed according to parameters known experimentally or via MC simulation

$$\frac{\sigma_1}{\sigma_2} \approx \frac{\rho_{HF1}}{\rho_{HX1} v_{rel1} \tau_1} \frac{\rho_{HX2} v_{rel2} \tau_2}{\rho_{HF2}}. \qquad (2.22)$$

The values obtained in this way are somewhat approximate, since they depend critically upon the modeling of the reaction conditions that produce the average $\langle\tau\rangle$ values, as discussed in section

2.4(B). Nevertheless, cross sections calculated in this way for F + HCl and F + H_2O agree with the approximate values obtained from temperature-dependent rate constant measurements.[42,43]

D. Doppler Analysis

Doppler measurements obtained from the IR spectrometer can be considered "orthogonal" information about the reaction dynamics when compared to the quantum-state distributions. The observed Doppler profiles directly reveal laboratory-frame HF velocities, projected along the probe axis, following the reaction event. However, as mentioned in the previous section, the detailed information about the angular scattering dynamics of the F + H_2O and F + HCl systems is difficult to obtain with the signal to noise resulting from these relatively low cross section reactions. Given the signal to noise shown in the sample Doppler measurements in Fig. 3.3, and 4.4, we have been unable to disentangle velocity distributions for upper and lower states (according to Eq. 2.11) from the experimental noise. Instead, we have fit a number of selected states, whose upper state population have been found to be negligible, to a simple Gaussian lineshape according to

$$A(\nu) = A_0 \exp(-4\ln(2)[(\nu-\nu_0)/\Delta\nu]^2), \qquad (2.23)$$

where $A(\nu)$ is the measured Doppler profile, and the fitted parameters are the overall amplitude A_0, the line center ν_0, and the Gaussian FWHM $\Delta\nu$. The $\Delta\nu$ values are presented in the following chapters, and measured values exceed the room temperature HF Doppler width ($\Delta\nu_{thermal}$ = 330 MHz) and vary explicitly as a function of HF(v,J) rovibrational state. These observations strongly indicate that HF distributions remain translationally excited following the reactive encounter, direct evidence for single collision conditions at the jet intersection region. Additional Doppler analysis was possible for the large signals obtained following reaction at the gas-liquid interface. More precise modeling was performed in this case, as described in detail in Ch. V.

References for Chapter II

1 From, pp. http://nobelprize.org/nobel_prizes/chemistry/laureates/1986/.

2 J. C. Polanyi and D. C. Tardy, J. Chem. Phys. **51**, 5717 (1969).

3 Y. T. Lee, J. D. McDonald, P. R. Lebreton, and D. R. Herschbach, Rev. Sci. Instrum. **40**, 1402 (1969).

4 L. M. Tashiro, W. Ubachs, and R. N. Zare, J. Mol. Spectrosc. **138**, 89 (1989).

5 W. Gellermann, J. Phys. Chem. Solids **52**, 249 (1991).

6 J. V. V. Kasper, C. R. Pollock, R. F. Curl, and F. K. Tittel, Appl. Optics **21**, 236 (1982).

7 J. L. Hall and S. A. Lee, Appl. Phys. Lett. **29**, 367 (1976).

8 T. M. Niebauer, J. E. Faller, H. M. Godwin, J. L. Hall, and R. L. Barger, Appl. Optics **27**, 1285 (1988).

9 J. T. Verdeyen, *Laser Electronics*, 3rd ed. (Prentice Hall, Upper Saddle River, NJ, 1995).

10 W. Demtroder, *Laser Spectroscopy*. (Springer, Berlin, 1996).

11 E. Arunan, D. W. Setser, and J. F. Ogilvie, J. Chem. Phys. **97**, 1734 (1992).

12 D. Herriot, H. Kogelnik, and R. Kompfner, Appl. Optics **3**, 523 (1964).

13 A. Yariv, *Quantum electronics*, 3rd ed. (Wiley, New York, 1989).

14 D. Proch and T. Trickl, Rev. Sci. Instrum. **60**, 713 (1989).

15 W. B. Chapman, M. J. Weida, and D. J. Nesbitt, J. Chem. Phys. **106**, 2248 (1997).

16 D. R. Miller, in *Atomic and molecular beam methods*, edited by G. Scoles (Oxford University Press, New York, 1988), pp. 14.

17 F. Dong, S. H. Lee, and K. Liu, J. Chem. Phys. **113**, 3633 (2000).

18 D. Brandt and J. C. Polanyi, Chem. Phys. **35**, 23 (1978).

19 D. Brandt and J. C. Polanyi, Chem. Phys. **45**, 65 (1980).

20 A. M. G. Ding, L. J. Kirsch, D. S. Perry, J. C. Polanyi, and J. L. Schreiber, Faraday Discuss. **55**, 252 (1973).

21 L. J. Kirsch and J. C. Polanyi, J. Chem. Phys. **57**, 4498 (1972).

22 J. C. Polanyi and K. B. Woodall, J. Chem. Phys. **57**, 1574 (1972).

23 P. Beadle, M. R. Dunn, N. B. H. Jonathan, J. P. Liddy, and J. C. Naylor, J. Chem. Soc., Faraday Trans. II **74**, 2170 (1978).

24 P. Beadle, M. R. Dunn, N. B. H. Jonathan, J. P. Liddy, J. C. Naylor, and S. Okuda, J. Chem. Soc., Faraday Trans. II **74**, 2158 (1978).

25 D. Bogan and D. W. Setser, in *Fluorine-containing free radicals: kinetics and dynamics of reactions: based on a symposium sponsored by the Division of Physical Chemistry at the 169th meeting of the American Chemical Society, Philadelphia, Pennsylvania, April 7-11, 1975*, edited by J. W. Root (American Chemical Society, Washington, 1978), pp. 237.

26 D. J. Bogan and D. W. Setser, J. Chem. Phys. **64**, 586 (1976).

27 N. Jonathan, Melliars.Cm, D. Timlin, and D. H. Slater, Appl. Optics **10**, 1821 (1971).

28 N. Jonathan, Melliar-Smith Cm, S. Okuda, D. H. Slater, and D. Timlin, Mol. Phys. **22**, 561 (1971).

29 K. Tamagake, D. W. Setser, and J. P. Sung, J. Chem. Phys. **73**, 2203 (1980).

30 K. L. Kompa and G. C. Pimentel, J. Chem. Phys. **47**, 857 (1967).

31 D. M. Sonnenfroh and K. P. Liu, Chem. Phys. Lett. **176**, 183 (1991).

32 H. W. Cruse, P. J. Dagdigian, and R. N. Zare, Faraday Discuss. **55**, 277 (1973).

33 C. Naulin, M. Costes, A. Benseddik, and G. Dorthe, Laser Chem. **8**, 283 (1988).

34 J. C. Polanyi, Accounts Chem. Res. **5**, 161 (1972).

35 M. A. Wickramaaratchi, D. W. Setser, H. Hildebrandt, B. Korbitzer, and H. Heydtmann, Chem. Phys. **94**, 109 (1985).

36 W. H. Duewer and D. W. Setser, J. Chem. Phys. **58**, 2310 (1973).

37 H. W. Chang, D. W. Setser, M. J. Perona, and R. L. Johnson, Chem. Phys. Lett. **9**, 587 (1971).

38 J. P. Sung and D. W. Setser, Chem. Phys. Lett. **48**, 413 (1977).

39 M. P. Deskevich, D. J. Nesbitt, and H. J. Werner, J. Chem. Phys. **120**, 7281 (2004).

40 M. P. Deskevich, M. Y. Hayes, K. Takahashi, R. T. Skodje, and D. J. Nesbitt, J. Chem. Phys. **124**, 224303 (2006).

41 W. B. Chapman, B. W. Blackmon, S. Nizkorodov, and D. J. Nesbitt, J. Chem. Phys. **109**, 9306 (1998).

42 E. Wurzberg and P. L. Houston, J. Chem. Phys. **72**, 5915 (1980).

43 P. S. Stevens, W. H. Brune, and J. G. Anderson, J. Phys. Chem. **93**, 4068 (1989).

Chapter III Reaction dynamics of F + HCl → HF(*v*,*J*) + Cl: experimental measurements and quasi-classical trajectory calculations

3.1 Introduction

Elementary chemical reactions play a pivotal role in the foundations of chemical reaction dynamics.[1,2] Three-atom hydrogen exchange reactions in the form X + HY → HX + Y have been particularly important because of the theoretical tractability of developing potential energy surfaces (PES) in full 3*N*-6 = 3 dimensionality.[3-5] Intense effort has been focused toward reactions such as O + H_2,[6-9] Cl + H_2,[10-14] H + H_2,[15-18] and F + H_2,[19-28] due to the accessibility of high-level theoretical methods to systems with only a single "heavy" (i.e. nonhydrogenic) atom. In spite of the apparent simplicity of such systems, the dynamics of these three-atom reactions have proven to be extremely rich, with important roles in fields such as atmospheric, combustion, chemical laser, and interstellar chemistry.[29-35]

As one particularly well-studied example, the strongly exothermic reaction F + H_2 and its isotopic variants has proven to be an intensely productive focus of investigation from both theoretical and experimental perspectives.[19-28]

Extensive crossed-beam studies have revealed details of reactive scattering, including the differential and integral cross section as a function of collision energy,[22] as well as complete HF rovibrational quantum state distributions.[36] On the theoretical side, a full-dimensional *ab initio* potential energy surface (PES) has been generated[4,37] with global accuracy approaching a few tenths of a kcal/mol. For such a three-atom system, rigorous quantum reaction dynamics on one or more electronic surfaces are computationally accessible.[38] Indeed, the first definitive examples of elusive transition state resonance dynamics were identified experimentally in the isotopic

variant reaction F + HD → HF + D[27] and then confirmed in the F + H_2 reaction.[39] Calculation of non-adiabatic interactions between multiple spin-orbit surfaces has also become recently feasible, with such benchmark calculations performed on the F($^2P_{3/2}$, $^2P_{1/2}$) + H_2 system.[40] These theoretical achievements are remarkable for their nearly quantitative agreement with experiment. Indeed, the ability to generate a PES from first principles and obtain results from numerically exact dynamics calculations that can be rigorously tested against experiment represents an important milestone achievement by the chemical physics community.

Advances in computational speed also enable existing methods to be tested on more complex systems. One such step is hydrogen exchange between two "heavy" atoms such as the reaction F + HCl → HF + Cl, which forms the subject of this chapter. Although the Cl atom's added electrons (when compared to F + H_2) significantly increases the cost of *ab initio* calculations, the F + HCl reaction offers a number of desirable features. First, it involves the two lightest halogen atoms, each of which have already been studied through their respective reactions with molecular hydrogen.[10-14,20-23,25,26] Secondly, open shell halogen reactants and products necessarily result in multiple, low-lying spin orbit surfaces and the possibility of non-adiabatic dynamics. These surfaces can be explored in all 3*N*-6 reaction dimensions using multireference *ab initio* techniques at achievable computational cost. Thirdly, from a purely energetic perspective, the reaction can be viewed as a "substitution" for the spectator H atom in the F + H_2 system. Indeed, the nearly equal reaction exothermicity for these reactions [F + HCl → HF + Cl ΔH^0 = -33.059(14) kcal/mol,[41,42] F + H_2 → HF + Cl ΔH^0 = -32.001(14) kcal/mol[43]] provides an interesting opportunity for probing mass related changes in reaction dynamics without significantly different energetics. Finally, dynamical studies of such surfaces can help elucidate both classical and quantum dynamical contributions along the progression F + H_2, F + HD, and F + HCl, a perspective which proves particularly useful in light of the large body of work on heavy-light-heavy (HLH) mass combinations in chemical reactions.[44] Indeed, based on

the understanding of F + HD, such HLH systems may be expected to exhibit quantum transition state resonance dynamics, roughly corresponding to rapid "chattering" motion of the light atom between the two heavy atoms.[28,45,46] The convergence of theoretical and experimental techniques capable of identifying such phenomena[15,16,18,28,39,45-47] further motivates renewed studies of the F + HCl system.

Further clarification of this broad analogy between F + H_2 and F + HCl reaction systems necessitates detailed comparison of their theoretical PES. Two F + HCl surfaces have been recently reported, hereafter referred to as the SHHG PES[48], and the DHSN PES.[5] Both surfaces exhibit strongly bent transition-state geometries with an F−H−Cl angle of 131.2° and 123.1° for the SHHG and DHSN surfaces, respectively. This reaction geometry is surprisingly close to the ≈119° F–H–H angle found using multireference calculations on F + H_2.[4,37] There is general agreement between experiment and theory about the low F + H_2 classical barrier height (≈ 2 kcal/mol). In contrast, single reference variational methods used to generate the SHHG PES revealed a classical barrier of 4.01 kcal/mol. This value was empirically scaled to 1.12 kcal/mol on the SHHG surface, in light of the ≈ 1 kcal/mol activation energies inferred from temperature dependent kinetic studies.[49-51] However, the larger value is in much better agreement with that found on the more recent DHSN surface (3.75 kcal/mol), developed using high level multireference *ab initio* methods. By way of support, the present study requires high speed, helium carrier gases in crossed molecular jets, with the HF product not detectable under lower collision energy conditions. This qualitative observation lends credence to the appreciable barriers predicted by theoretical treatment.

Other differences between F + HCl and F + H_2 are readily evident, such as the ≈ 1–2 kcal/mol F–HCl and HF–Cl van der Waals wells visible in Fig. 3.1. These wells have been experimentally characterized via spectroscopy in argon-matrices[52] and helium nanodroplets,[53]

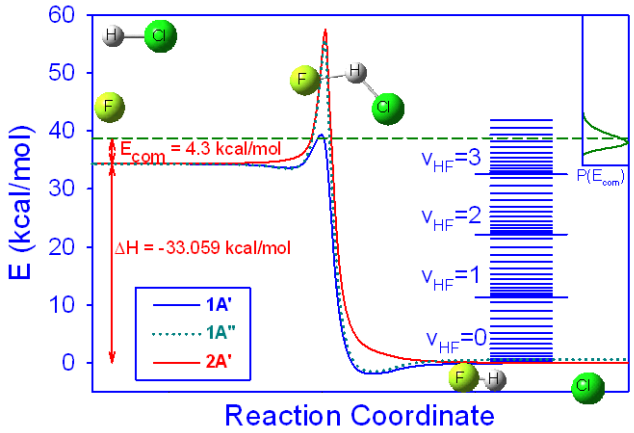

Figure 3.1 Reaction coordinate for the reaction F(^{2}P) + HCl → HF(v,J) + Cl(^{2}P), on the ground 1A' and excited surfaces, reported in Ref. 5. The dashed line represents the total energy available in the center of mass frame, with the collision energy distribution shown in inset.

and via molecular beam-scattering studies.[54] A new exit-well PES has recently been reported and bound states of the Cl–HF complex characterized on this surface.[55,56] Such strong attraction between the HX permanent dipole moment and the polarizability/quadrupole of the corresponding halogen atom create significant interaction that are not present on the F + H_2 surface. Several studies have provided a theoretical framework for characterizing van der Waals potentials in such open-shelled systems.[57-59] However, the influence of these wells on highly exothermic reactive dynamics has yet to be determined, further motivating the present work.

Previous studies of F + HCl $\rightarrow$ HF + Cl reveal a number of noteworthy features that suggest rich dynamic processes underlie this three-atom reaction. Temperature-dependent kinetic studies by Houston and coworkers have revealed strongly non-Arrhenius behavior, which was interpreted as evidence of microscopic branching through direct versus complex-mediated reaction mechanisms.[49,50] Pioneering studies by Beadle, Polanyi, Setser and others[60-65] exploited fast flow arrested-relaxation conditions to measure highly inverted HF vibrational branching ratios consistent with early barrier dynamics.[66] The influence of collisions in these studies on HF state distribution was carefully monitored and not found to perturb vibrational populations; however, the measured rotational populations were significantly bimodal and thought to be partially relaxed.[60,61,67] As a result, the Boltzmann-looking *low J* state populations were attributed to rotational thermalization prior to IR detection and hence neglected, with only the higher *J* states considered truly nascent.

As will be described more fully herein, the present direct absorption experimental results offer an alternative and intriguing analysis. Specifically, our results reveal a *bimodal* formation pathway into both low *J* and high *J* states, even under reaction conditions with approximately a 1000-fold reduction in relaxation probability (i.e., residence time × density) when compared to arrested relaxation studies.[60,63,68-70] The observation of bimodal HF rotational distributions in HF(v = 1, 2) therefore resurrects the possibility of *microscopic branching*, as first proposed to explain non-Arrhenius kinetics. Interestingly, no indication of either microscopic branching or

bimodal HF rotational distributions has been found in previous theoretical studies of F + HCl, including QCT calculations on a LEPS surface,[71] and QCT[66] and wave-packet[72] studies on the SHHG PES. Along with interest in both i) HLH resonance mediated and ii) nonadiabatic hopping dynamics in chemical reactions, this has provided additional incentive for recent work[5] in developing and fitting a new high level *ab initio* potential for F + HCl, along with the corresponding nonadiabatic matrix elements coupling these surfaces.[73] It is our hope that the availability of such benchmark surfaces will further facilitate theoretical investigations necessary for unraveling the reaction dynamics in this fundamental, albeit dynamically rich, bond-breaking and bond-making event.

3.2 Experiment

A crossed molecular-beam apparatus has been used to resolve the nascent product state distributions in the reaction F + HCl $\rightarrow$ HF + Cl under rigorous single collision conditions. An illustration of the crossed-jet–direct-infrared-absorption apparatus appears in Fig. 3.2 (a). The experimental details have been described in detail previously.[74-76] Here we present a brief overview of the experiment, emphasizing the specific apparatus modifications and operating conditions used in the present work.

Reactants are introduced into a 100 L diffusion-pumped vacuum chamber via two supersonic molecular jets. The jet expansion axes are oriented at 90° to each other and the laser probe axis. The F atom source is a standard solenoid fuel injector modified to generate radicals in an electrical discharge at the throat of the supersonic expansion, as illustrated in Fig. 3.2 (b). The F atoms are produced as follows. A pulsed solenoid valve releases 65 Torr (133.3 Pa/Torr) of a 10% F_2 / 90% He gas mixture into a small ($\approx$ 0.025 mL) volume defined by a slotted hole in a 0.5 mm inert (polychlorotrifluoroethylene) disk insulator sandwiched

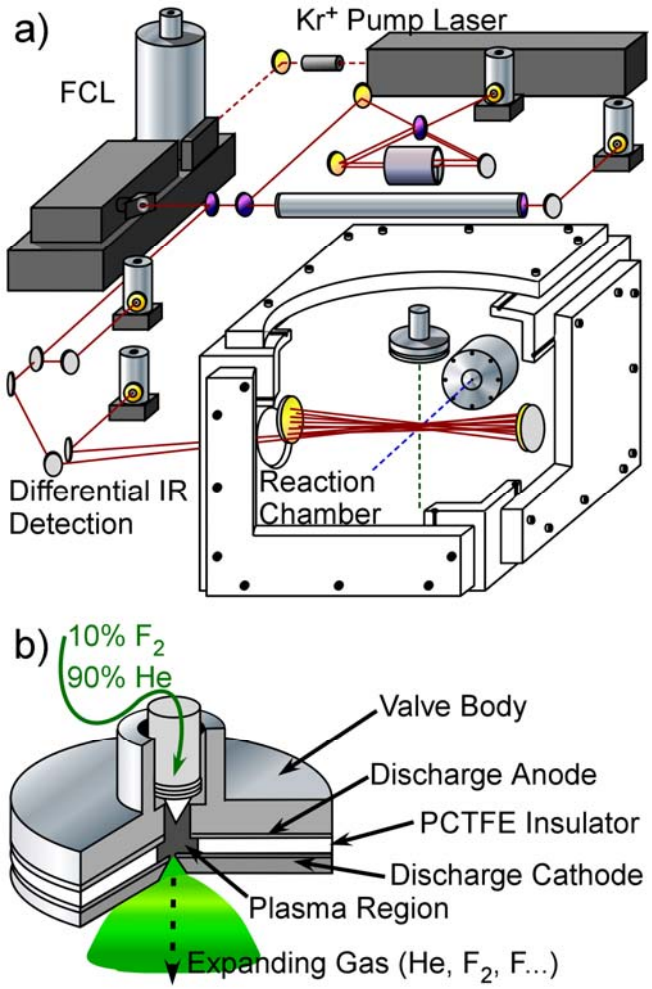

Figure 3.2 (a) Diagram of the crossed molecular jet apparatus used to study the reaction $F(^2P) + HCl \rightarrow HF(v,J) + Cl(^2P)$. HF product is detected via absorption of infrared laser light multipassed orthogonal to the plane containing the jet axes. Low jet densities enable the reaction to be studied under rigorously single collision conditions. See text for details. (b) Schematic of the modified solenoid valve, which generates $F(^2P)$ radicals in a plasma discharge between the limiting orifice and the valve body.

between two flat nickel electrodes. A miniature slit (300 μm×0.3 cm) in the downstream electrode forms the limiting orifice from which the gas expands past two slit-jet expansion-defining "jaws" and into the chamber. At the peak of the 2 ms gas pulse, a 500 μs HV pulse (≈ -1 kV) is applied to the lower electrode, striking an electrical discharge through the gas mixture to the grounded upper electrode on the valve body. A resulting radical density of approximately 2.6×10^{12} F atoms/cm^3 in the probe region has been measured against other H abstraction systems with known reaction cross sections (e.g., F + H_2). Such densities correlate to ≈ 2×10^{16} F atoms/cm^3 at the limiting orifice, or ≈ 10% of the F_2 dissociating into F atoms in the plasma. The relative HF density produced in the reaction F + H_2 can also be used to crudely estimate the reaction cross section (at E_{com} ≈ 4.3(1.3) kcal/mol) for F + HCl. Based on Dong's[22] measured cross sections [σ_{rxn}(F + H_2) = 3.0 Å^2] at the F + H_2 collision energy of 2.3 kcal/mol and the quantum-state distribution reported by Chapman[74], the relative density in HF(v = 3,J = 3) and the F + HCl branching ratios reported herein is consistent with a total F + HCl reaction cross section of σ_{rxn}(F + HCl) ≈ 0.2–0.5 Å^2 at our experimental collision energy. This value is slightly smaller than, but in reasonable agreement with, the ≈ 1 Å^2 value from temperature-dependent rate constant measurements.[49]

The second jet is a 1:1 mixture of HCl:He emanating from a custom-built Proch-Trickl[77] valve, which uses a PZT disc actuator to generate 500 μs pulses. 200 Torr of the gas mixture expands from a 500 μm pinhole to yield ≈ 4×10^{13} HCl molecules/cm^3 at the jet intersection region. The unskimmed jets intersect at a 90° angle, 4.5 cm downstream from each of the nozzle orifices. With the valves pulsing at 10.1 Hz, the average pressure in the chamber rises to ≈ 1.0×10^{-4} Torr. This pressure corresponds to a mean free path of λ ≈ 50 cm between molecular collisions, i.e., considerably greater than the distance to the chamber walls and well outside the 1 cm laser probe region.

To increase signal size, both jet expansions employ helium carrier gases, which results in jet velocities of 1.3×10^5 cm/s (10% F_2/He) and 9.2×10^4 cm/s (50% HCl/He), as directly measured by translating a small hearing aid microphone along each expansion axis. The measured velocities closely match the predicted terminal velocities anticipated by fluid dynamics,[78] indicating efficient cooling of the expansion gases. High collision energies are also necessary to surmount the anticipated ≈ 4 kcal/mol barrier to reaction.[5,48,79] Computational modeling of the experimental conditions yields the collision energy distribution [$P(E_{com})$], inset in Fig. 3.1. The average collision energy is 4.3(1.3) kcal/mol, such that most F + HCl collisions are expected to exceed the barrier. Modeling of the experimental conditions, discussed in more detail in Sect. 3.4, takes into account the velocity and angular distributions of gas in the supersonic expansions, as measured experimentally via high-resolution Dopplerimetry on IR chromophores doped in the incident beams in a separate experiment. Such measurements reveal translational velocity distributions with widths corresponding to a temperature of 30–50 K, caused by incomplete jet cooling and velocity slip relative to He carrier gas. Nevertheless, the reactant speed distribution makes a relatively small contribution to the width of the experimental collision energy distribution when compared to the wide range of lab-frame collision geometries available at the intersection of the unskimmed jets, which is primarily responsible for the broad collision energy distribution.

Product HF is detected via direct laser absorption on the $\Delta v = +1$ fundamental ($v = 1\leftarrow0$) and successive rovibrational "hot" bands ($v = 2\leftarrow1$, $v = 3\leftarrow2$, $v = 4\leftarrow3$) in the near infrared. The tunable IR source is a single mode ($\Delta\nu \approx 3$ MHz) continuous wave (CW) F-center laser (FCL) outfitted for continuous scanning by the addition of tunable galvo plates and a servo-loop-controlled intracavity etalon. The product HF is probed with < 50 μW infrared power, kept intentionally low to eliminate nonlinear effects due to optical saturation. Thus, high-sensitivity IR intensity changes can be attributed to the interaction with HF product in a linear regime, such that measurements can be directly correlated to *absolute* HF densities in the laser path length. The

absolute IR laser wavelength is measured with a traveling Michaelson interferometer[80] referenced to a polarization stabilized HeNe laser. This calibration is accurate to ≈ 15 MHz, more than sufficient to locate individual HF rovibrational transitions. The relative frequencies during each Doppler resolved scan are measured to much higher (1–2 MHz) precision via transmission fringes from a scanning Fabry-Perot cavity.[81]

A sample Doppler measurement for the HF product absorbing on the transition HF(v' = 4, J' = 4) ← HF(v'' = 3, J'' = 3) is shown in Fig. 3.3(a). Typical HF(v,J) signal strengths correspond to densities of about 5×10^7 HF molecules/cm^3/quantum state in the intersection region, which approaches the current detection sensitivity for the direct absorption technique. Indeed, these absorption signals are comparable to the fundamental peak-to-peak noise limit of ≈ 2×10^7 HF molecules/cm^3/state [double-dashed lines in Fig. 3.3(a)] created by the IR "photon counting" shot-noise.

A number of experimental improvements are therefore vital to attaining sensitivities approaching the shot-noise floor. First, the signal is increased via long absorption path length by multipassing the IR light through the reaction chamber 16 times using a modified Herriot cell.[82,83] Second, IR intensity fluctuations are minimized and removed from signal with the use of several custom electronic devices. Specifically, the CW IR intensity fluctuations are reduced via electro optical modulation and servo feedback control of the FCL's pump laser intensity. Remaining intensity noise is eliminated by electronic subtraction of common-mode noise observed on two liquid nitrogen-cooled InSb detectors. The resulting "difference signal" is obtained with sufficient sensitivity to reveal small (≈ 1 part in 10^5) intensity fluctuations on the signal detector caused by the transient absorption of HF(v,J) product. On typical transitions, such methods yield a signal to noise ratio (S/N) of ≈ 2:1 under conditions used in the current study.

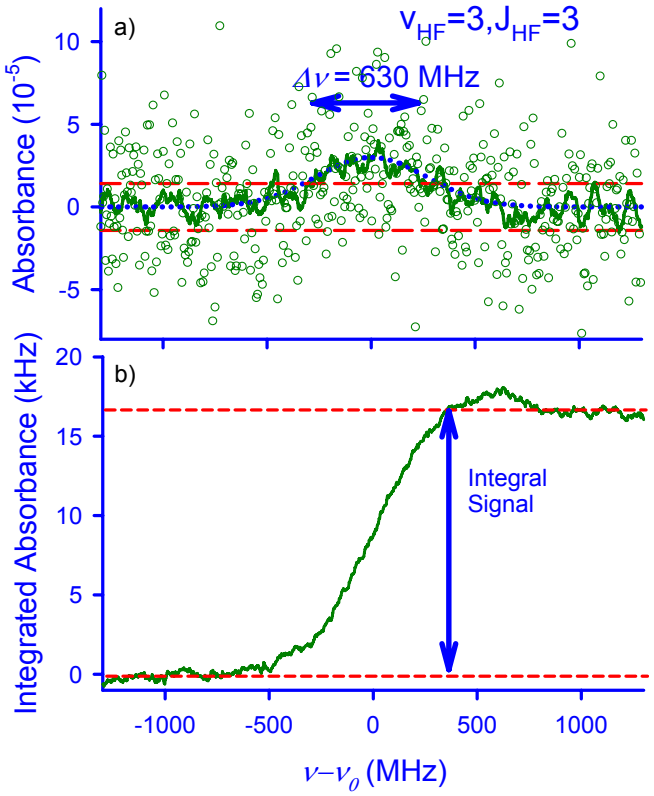

Figure 3.3 Sample infrared absorption data on the line HF(v' = 4, J' = 4) ← HF(v'' = 3, J'' = 3). (a) Absorption as a function of laser frequency. Open circles: raw data at 3 MHz frequency resolution. Dashed lines: theoretical peak-to-peak quantum shot-noise limit. Solid line: Savitzky-Golay (55 point, 4th order) smoothed data. Dotted line: Gaussian fit of the raw data, with indicated FWHM width of 630 MHz. (b) Integral of the raw data as a function of frequency, yielding the column-integrated absorbance for the transition.

Additional sensitivity enhancement is obtained by scanning the high resolution laser in ≈ 3 MHz steps through a ≈ 400–900 MHz HF Doppler profile. At each frequency, we obtain an independent measure of absorption by digitally recording the signal wave form and numerically integrating over 330 μs. The step size, approximately equal to the laser bandwidth, results in a large number of independent data points [$N > 100$ under a typical Doppler full width half maximum (FWHM)], providing a $\sqrt{N} \approx$ 10- to 12- fold gain in sensitivity. The solid line in Fig. 3.3(a) presents the raw data smoothed by a 55-point, 4th-order Savitzky-Golay algorithm,[84] which better represents the uncertainty of the measurement. Indeed, profiles for significantly populated states can even be least-squares fitted to a simple Gaussian lineshape. Such a fit to the *unsmoothed* data is shown as the dotted curve in Fig. 3.3(a). The Doppler width from this least-squares fit yields approximate information on HF recoil velocities in the lab frame, which are clearly hotter than room temperature ($\Delta\nu_{thermal}$ = 330 MHz) and indeed vary explicitly as a function of HF(v,J) rovibrational state.

By way of example, the inferred Doppler widths are plotted in Fig. 3.4 for several transitions originating in the $v = 2$ and $v = 3$ manifold. The plot abscissa is the enthalpy released in the reaction ($-\Delta H^0$) minus the internal energy of the HF product formed ($E^{HF\ internal}_{(v,J)}$), i.e., the *translational* energy release upon reaction ($\Delta E^{trans}_{(v,J)}$). These widths are ≥ 2-fold broader than that expected for room temperature HF, shown in Fig. 3.4 as a dashed line. Indeed, the observed Doppler widths increase systematically with $\Delta E^{trans}_{(v,J)}$, as expected from conservation of energy. Such excess translational Doppler excitation in the laboratory frame is consistent with exothermic energy release into the HF(v,J) products and represents additional confirmation of nascent, single collision conditions.

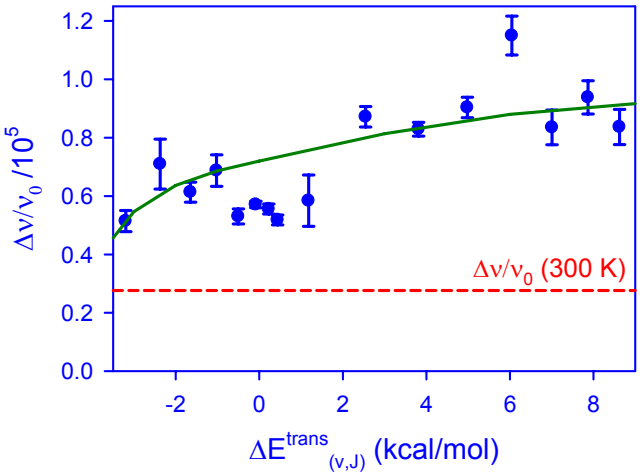

Figure 3.4 Observed HF Doppler width (FWHM) distributions projected along the laser axis as a function translational energy released [$\Delta E^{trans}_{(v,J)} = -\Delta H^0 - E^{HF\ internal}_{(v,J)}$]. The solid curve represents expected values based on a Monte Carlo simulation of the experimental conditions. The horizontal dashed line is a 300 K HF Doppler distribution.

Nascent column-integrated HF(v,J) product densities (reported in Sect. 3.3) are obtained from the total area under the various Doppler profiles. A representative analysis is presented in Fig. 3.3(b), where the *integral* of the raw data is plotted as a function of laser frequency. The smoothness of the plot underscores that the *integral absorption* values also benefit from a $\sqrt{N}$ improvement over N independent Doppler-resolved absorption measurements. Statistics of the integral absorption measurements are further improved by a regimen of signal averaging during which each IR transition is probed in at least three independent sets of triplicate scans (i.e., nine times) during the course of the experiment. The 2.3–3.3 μm tunability of the IR source also enables many HF(v,J) states to be probed on both the P ($\Delta J = -1$) and R ($\Delta J = +1$) branch transitions, further increasing the degree of oversampling of the data set. Data are also collected on a strong reference transition [i.e., HF($v' = 4, J' = 4$) ← HF($v'' = 3, J'' = 3$)] every 2–3 hours during data acquisition. By normalizing the entire data set to concurrent reference line observations, day-to-day fluctuations in the electrical discharge and F atom densities are eliminated from the analysis, so data acquired over multiple weeks can be meaningful compared.

Background HF($v = 0, J$) in the ground vibrational state is present at trace levels, due to pre-reaction with impurities in the fluorine source at the parts per million level. Fortunately, efficient cooling in the supersonic jet confines all such background to HF $v = 0$, low J levels. To take this into account, each transition out of the HF($v = 0,J$) manifold is scanned with and without the HCl reactant jet; the differential increase in integrated absorption is attributed to the HF reactive product channel. This procedure works well but generates significant uncertainties for the lowest (HF($v = 0, J < 6$)) states arising from subtraction of weak and nearly equivalent populations. Nevertheless, the present results provide first direct measurement of population in the ground vibrational state, which had been inaccessible via previous IR chemiluminescence methods.[60-65]

As noted previously, the experiment is conducted under rigorous single-collision conditions, obtained from low reactant pulsed flow densities, but at the expense of product signal strength. Based on our experimental conditions described above and an estimated[49] reaction cross section for F + HCl scattering of ≈ 1 Å^2, fewer than 1% of the F atoms suffer a reactive collision while transiting the secondary HCl jet. Of these 1% reactive events, the probability for elastic and/or inelastic collisions prior to IR detection is predicted to be down by an order of magnitude. Most collisions are with helium carrier gas, which is known to have small cross sections for rovibrationally inelastic scattering;[36] hence, this represents an upper limit for redistribution of the HF(v,J) population. By way of explicit verification, nascent HF(v,J) has been monitored on several rovibrational transitions as a function of backing pressure in the HCl jet. The resulting rotational distributions are summarized as a density ratio between two J states in the v = 3 and v = 2 manifolds, as shown in Fig. 3.5. The observed ratio is much larger than the value for a room temperature rotational distribution (dashed lines, Fig. 3.5), which furthermore remains constant within experimental uncertainty over more than a fourfold increase in gas density. This measurement represents explicit verification of the nascent character of the quantum-state populations. The lack of rotational redistribution is also consistent with the Doppler translational excitation plotted in Fig. 3.4, further validating that the quantum state distributions can be attributed to a single reactive collisional event.

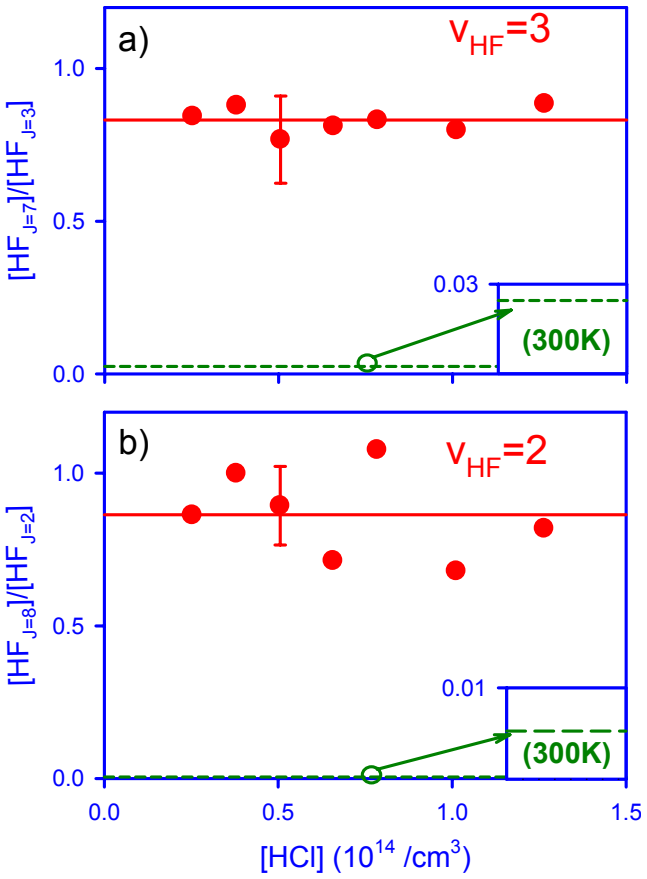

Figure 3.5 HF(v,J) density ratios observed in two rotational states versus the HCl density in the intersection region. (a) HF(v = 3) density ratio for J = 7 versus J = 3. (b) HF(v = 2) density ratio for J = 8 and J = 2. Dashed line is the ratio of densities at T_{rot} = 300 K. The solid line indicates the average ratio, with no systematic shift toward thermalization as HCl density increases. Representative error bars are shown at the ρ_{HCl} value used for full HF quantum-state distribution measurements.

3.3 Results

The data set consists of a series of high-resolution HF absorption Doppler profiles, recorded on each HF line within the tuning range (2.5–3.3 μm) of the FCL. Mathematically, the absorbance is related to differences in absolute HF densities by the Beer-Lambert law, i.e.

$$A_{ji}(\nu - \nu_0) = \int dx \int d\nu' \left[\sigma_{j\to i}(\nu - \nu')\kappa_j(x, \nu' - \nu_0) - \sigma_{j\leftarrow i}(\nu - \nu')\kappa_i(x, \nu' - \nu_0)\right], \quad (3.1)$$

where $\kappa_{i/j}(x, \nu' - \nu_0)$ is the spectral density (i.e., molecules/cm^3/cm^{-1}) of absorbers in states i or j, at a position x along the absorption path with Doppler shifted center frequency $\nu' - \nu_0$. $\sigma_{j\leftarrow i}(\nu - \nu')$ and $\sigma_{j\to i}(\nu - \nu')$ are the homogeneous absorption/emission lineshapes between states i and j, centered around ν'. Since the homogeneous lineshape is much narrower than the inhomogeneous Doppler profile, the integral over ν' can be readily performed to yield

$$A_{ji}(\nu - \nu_0) = S_{j\to i} \int dx\ \kappa_j(x, \nu - \nu_0) - S_{j\leftarrow i} \int dx\ \kappa_i(x, \nu - \nu_0), \quad (3.2)$$

whereby the net absorption at a given Doppler detuning, $\nu - \nu_0$, is related to the difference in HF *column-integrated spectral density* between states i and j at $\nu - \nu_0$, weighted by the appropriate line strength $S_{i\leftrightarrow j}$. We integrate over the absorption profile to obtain,

$$\int A(\nu - \nu_0)\, d\nu = S_{j\to i} \int dx\ \rho_j(x) - S_{j\leftarrow i} \int dx\ \rho_i(x), \quad (3.3)$$

which, based on well-known absorption line strengths ($S_{i\leftrightarrow j}$)[85], permits the *difference* in *column-integrated densities* for the lower and upper probe states to be extracted.

For the highly inverted vibrational populations observed in F + HCl reactive scattering, significant HF density is often formed in both j and i, resulting in competition between stimulated *emission* and *absorption* signals. By Eq. 3.3, this leads to correlation between upper and lower state densities in a least-squares fit to the data. However, the correlation is effectively broken by transitions out of the highest energetically accessible $v = 3$ manifold, for which there is zero population in the upper state. Furthermore, the tunability of the IR laser permits observation of both P and R branch transitions out of many HF(v,J) lower states, adding further redundancy to

the data set. By employing a network of such expressions as Eq. 3.3, the full spectrum of integrated intensities has been fitted using linear least-squares analysis. The results of the fit provide experimental values and uncertainties for the quantum state resolved HF(v,J) column-integrated densities, as displayed in Fig. 3.6 and presented in Table 3.1.

The nascent population densities shown in Fig. 3.6 (discussed further in Sect. 3.4.) immediately raise several interesting points. First, HF product is observed in a wide variety of states, from low J states in the $v = 0$ manifold to $v = 3$ states with high rotational excitation. The measured uncertainty increases uniformly from the highest vibrational manifold to the ground state because of the coupling of the observed absorption/emission lines in the least-squares fit to the observed spectrum. Thus, the number of observations that influence any given state grows with the number of upper state densities that also must be known, up to the highest energy, unpopulated, state in a series of transitions that are related according to Eq. 3.3. Nevertheless, even densities in the lower vibrational manifolds are determined with repeatedly low uncertainties.

The data reveal a strong propensity for vibrational population inversion. The maximum HF densities are observed in the HF($v = 2$) manifold, a somewhat smaller fraction in HF($v = 1$), and a yet smaller, but still significant, population in HF($v = 3$). This trend is consistent with Polanyi rules for strongly exothermic reactions with early barriers, which predict the formation of the nascent HF population predominantly in high vibrational levels. In fact, the F + HCl reaction is one of many systems studied by Polanyi and contemporaries[60-65] via IR chemiluminescence under arrested-relaxation conditions. The present study's vibrational branching and that reported in various chemiluminescence studies are compared in Fig. 3.7. The present HF densities are in excellent agreement with the various arrested-relaxation studies. We note for later discussion, however, that this level of agreement does not extend to rotational distributions in each HF(v) manifold.

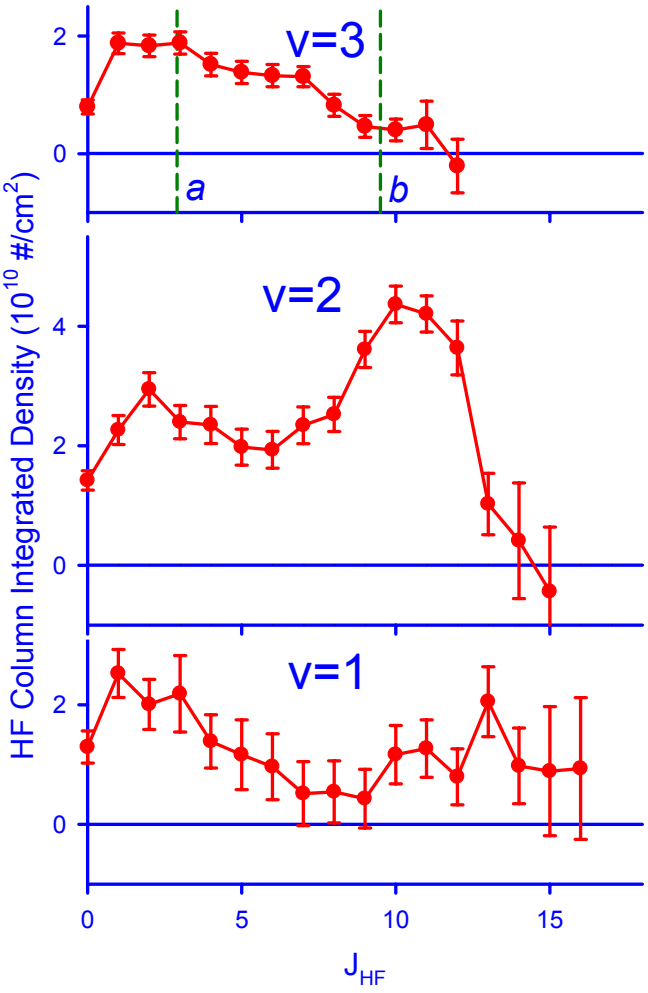

Figure 3.6 Column-integrated density distribution of nascent HF product formed from the reaction F + HCl. Values are obtained by least-squares fitting of the observed HF IR spectrum to a network of transitions, as discussed in the text. Vertical dashed line *a* reflects the reaction exothermicity (near $v = 3$, $J = 3$); *b* includes the 4.3 kcal/mol collision energy (near $v = 3$, $J = 9$).

Table 3.1 HF column-integrated densities (10^{10} molecules/cm^2) for F + HCl $\rightarrow$ HF(v,J) + Cl. Product fluxes have been inferred from detailed simulation of the reaction conditions. See text for details.

v	J	$\int dx\, \rho_{HF}(x)$	error	Normalized Flux (%)	error
0	6	-0.1	(1.2)	-0.3	(2.3)
	7	1.0	(1.3)	1.8	(2.4)
	8	0.6	(1.2)	1.1	(2.1)
	9	-0.1	(1.7)	-0.2	(3.1)
	10	0.5	(2.3)	0.8	(4.0)
	11	1.3	(2.2)	2.2	(3.8)
	12	1.4	(1.6)	2.3	(2.7)
	13	0.9	(2.1)	1.4	(3.5)
	14	2.2	(2.1)	3.5	(3.3)
1	0	1.3	(0.3)	2.1	(0.5)
	1	2.5	(0.4)	4.1	(0.9)
	2	2.0	(0.4)	3.2	(0.8)
	3	2.2	(0.6)	3.5	(1.1)
	4	1.4	(0.4)	2.2	(0.8)
	5	1.2	(0.6)	1.8	(0.9)
	6	1.0	(0.6)	1.5	(0.9)
	7	0.5	(0.5)	0.8	(0.8)
	8	0.5	(0.5)	0.8	(0.7)
	9	0.4	(0.5)	0.6	(0.7)
	10	1.2	(0.5)	1.7	(0.7)
	11	1.3	(0.5)	1.8	(0.7)
	12	0.8	(0.5)	1.1	(0.6)
	13	2.1	(0.6)	2.6	(0.8)
	14	1.0	(0.6)	1.2	(0.8)
	15	0.9	(1.1)	1.0	(1.2)
	16	0.9	(1.2)	1.0	(1.3)
2	0	1.4	(0.16)	1.8	(0.3)
	1	2.3	(0.2)	2.8	(0.5)
	2	2.9	(0.3)	3.6	(0.6)
	3	2.4	(0.3)	2.9	(0.5)
	4	2.3	(0.3)	2.8	(0.5)
	5	2.0	(0.3)	2.3	(0.5)
	6	1.9	(0.3)	2.2	(0.5)
	7	2.3	(0.3)	2.6	(0.5)
	8	2.5	(0.3)	2.7	(0.5)
	9	3.6	(0.3)	3.7	(0.6)
	10	4.4	(0.3)	4.3	(0.7)
	11	4.2	(0.3)	3.8	(0.6)
	12	3.6	(0.5)	3.0	(0.6)
	13	1.0	(0.5)	0.7	(0.4)
	14	0.4	(1.0)	0.2	(0.6)
	15	-0.4	(1.1)	-0.2	(0.4)
3	0	0.79	(0.12)	0.5	(0.2)
	1	1.88	(0.17)	1.3	(0.4)
	2	1.83	(0.18)	1.2	(0.4)
	3	1.88	(0.19)	1.2	(0.4)
	4	1.51	(0.19)	0.8	(0.3)
	5	1.38	(0.19)	0.7	(0.3)
	6	1.33	(0.19)	0.6	(0.2)
	7	1.31	(0.17)	0.5	(0.2)
	8	0.82	(0.19)	0.3	(0.2)
	9	0.46	(0.18)	0.2	(0.14)
	10	0.40	(0.18)	0.1	(0.12)
	11	0.5	(0.4)	0.1	(0.2)
	12	-0.2	(0.5)	-0.1	(0.2)

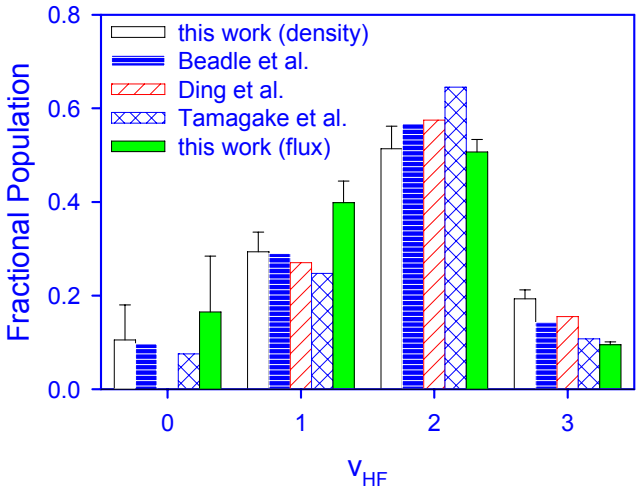

Figure 3.7 Vibrational HF product branching from F + HCl → HF(v) + Cl. The results of arrested-relaxation studies from Ref. 60,62,65 are as indicated. Population in v = 0 is directly observed for the first time; previous values are based on information theory predictions. Data are normalized to HF(v = 1–3) summed populations, enabling meaningful comparison of measurements with and without HF(v = 0) information.

Interestingly, direct absorption methods provide a first indication of finite nascent population in the HF($v = 0, J$) manifold, which does not emit in the near IR and thus had been invisible to early chemiluminescence studies. Any rotational structure within the small $v = 0$ signals is masked by the scatter between points because of the conjunction of low signal levels, subtraction of trace HF background, and uncertainty propagation with decreasing v. However, the HF $v = 0$ densities comprise 9.5(67)% of the total HF density observed, with the total population clearly exceeding this value due to exclusion of $J \leq 5$ background. Interestingly, the observed $v = 0$ density is consistent with the 7–9% surprisal predictions reported by several of the chemiluminescence studies[60,65]. This qualitative agreement between information theory and direct measurements of ground state HF confirms a dynamical propensity for a sizeable population in low energy states following reaction of F with HCl.

On the other hand, significant HF density is clearly also produced in high-energy rovibrational states. The dashed lines in Fig. 3.6 indicate the energetic limits for HF quantum states accessible via the 33 kcal/mol reaction exothermicity [$\approx E_{HF}(v = 3, J = 3)$] and those with the addition of the 4.3 kcal/mol average center-of-mass collision energy [$\approx E_{HF}(v = 3, J = 9)$]. For HF produced in states exceeding the lower limit, the center of mass recoil energy of the products is actually *less* than that of the reactant collision energy. Thus, the F + HCl reactive encounter favors excitation of the nascent HF molecule to such an extent that some fraction of the products are formed with all of the reaction energy plus some of the reactant translational energy sequestered in the HF internal energy. Indeed, finite density is observed above the upper energetic threshold, only dropping off to zero above $v = 3, J = 11$. Populating these highest states requires an additional 1.9 kcal/mol of collision energy, most likely arising from the significant width (σ = 1.3 kcal/mol, see inset of Fig. 3.1) in the crossed jet distributions. In principle, there may be an additional energy contribution from reaction of spin orbit excited ($^2P_{1/2}$) versus ground state ($^2P_{3/2}$) F atoms ($E_{spin\ orbit}$ = 1.1 kcal/mole) formed in a nearly statistical (2:4) ratio in the discharge

source. Evidence for such nonadiabatic reaction dynamics has been demonstrated in previous quantum state resolved F + H_2 and F + HD collision studies,[76,86] where E_{com} had negligible uncertainties with respect to spin orbit excitation energy. However, the high transition state barrier and collision energies necessary for the present study preclude any definitive implication of nonadiabatic dynamics.

A high degree of HF rotational excitation in lower vibrational manifolds is also evident from the state distributions in Fig. 3.6. Of considerable dynamic interest is the highly *nonmonotonic* structure apparent in the rotational distributions. This structure is particularly evident in the $v = 2$ manifold, which demonstrates a clear peaking at both low ($J \approx 2$) and high ($J \approx 10$) states. A qualitatively similar pattern of low ($J \approx 1$–3) and high ($J \approx 11$–13) state peaking is also evident in the HF($v = 1$) populations, though there appears to be additional structure in that manifold. Raw data from early arrested-relaxation studies[60,61] also indicate HF formation in low J levels of $v = 2$ and $v = 1$. However, these low-J population components were previously ascribed to rotational relaxation as a result of non-single-collision conditions and removed from the analysis.[60,61,67]

The current results suggest grounds for reinterpretation. Data for the $v = 1$ and $v = 2$ manifolds are replotted in Fig. 3.8 along with the raw and "corrected" results from arrested-relaxation studies.[60,62] The crossed-jet studies, performed under much lower-density single-collision conditions (see discussion in Sect. 3.1), clearly indicate the presence of a significant bifurcation into *both low and high J* states. In principle, discrepancies between these studies could arise from differences in thermal ($E_{com} \approx kT = 0.6$ kcal/mol) versus crossed supersonic jet ($E_{com} =$ 4.3 kcal/mol) collision energies. However, a much more likely interpretation is that the early studies were in fact less rotationally relaxed than originally suspected, with partial rotational relaxation simply adding to the true fraction of nascent product formed in low rotational states.

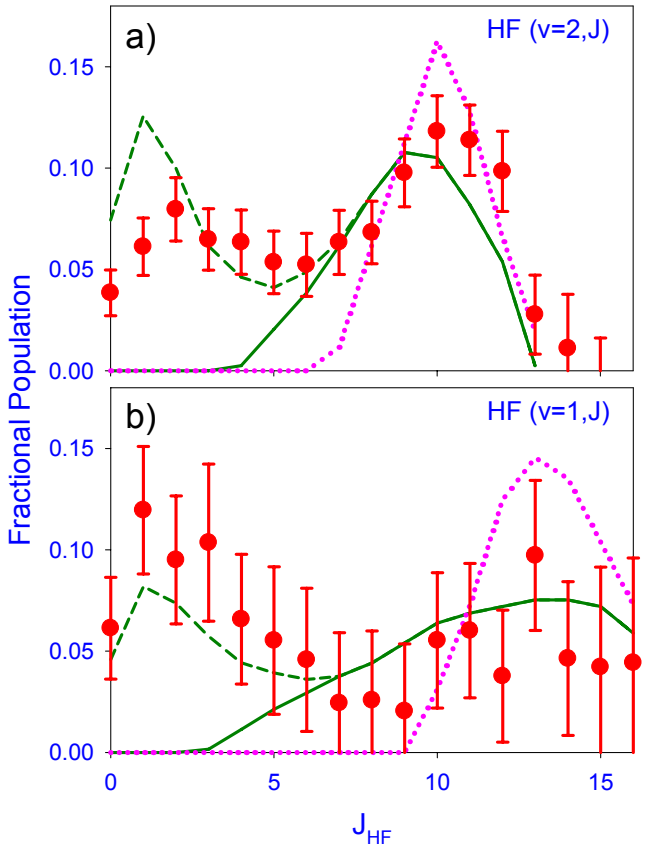

Figure 3.8 Rotational distributions for HF products in (a) $v = 2$ and (b) $v = 1$ manifolds, obtained from arrested relaxation (solid, dotted lines)[60,62] and the present crossed jet experiments (circles with error bars). Distributions reported from previous studies have been modified for presumed rotational relaxation, as illustrated by raw (dashed line) and corrected (solid line) results of Ref. 60.

It is also conceivable that the rotational distributions reported in arrested-relaxation studies of F + HBr and F + HI[60,65,87] may also suffer from overcompensation for rotational relaxation and may warrant study under lower density conditions.

It is apparent from Fig. 3.6 that the HF(v = 1,2; J) product distributions can not be adequately described by any simple statistical model. Indeed, these populations are remarkable for both the wide number of J states populated and the significant bifurcation of the population into low-versus-high rotational states in HF(v = 1) and HF(v = 2). By comparison, the reaction of F with H_2,[74] CH_4,[75] or C_2H_6,[88] each with comparable ≈ 30 kcal/mol exothermicities, produces similar degree of vibrational inversion but with a much more modest amount of HF rotation. Specifically, the rotational distributions peak at J_{max} ≈ 2 for F + CH_4 and F + C_2H_6, and at J_{max} ≈ 6 for F + H_2. In each case, the population decays *monotonically* for $J > J_{max}$. The current results are qualitatively different, with a relatively flat rotational distribution in HF(v = 3) extending out to J ≈ 5–6. The HF(v = 1) and HF(v = 2) manifolds are even broader, with local maxima occurring around J = 10. One intriguing interpretation of these double maxima may be microscopic branching in the reaction dynamics. For example, if reaction occurs through two dynamical pathways, one producing HF in low rotational states and the other with a propensity for rotational excitation, a bimodal distribution such as seen in Fig. 3.6 could arise naturally. One precedent for such bimodal and extensive rotational structure is the quantum transition-state resonance-mediated reactions of F + HD, which will be discussed further in the following section.

3.4 Analysis

The results in Fig. 3.6 show nascent column-integrated *densities* for HF(v,J) produced from the F + HCl reaction, as directly measured from the IR spectrum at the intersection of the reactant jets. However, it is the state resolved *fluxes* that represent the experimental quantity of interest; this requires consideration of the well-known[89-91] *density-to-flux* transformation, i.e.

correctly taking into account the velocity-dependent detection sensitivity intrinsic in any density based measurement technique. Modeling the effect of recoil energy on detection sensitivity requires a detailed Monte Carlo (MC) simulation of the collision and absorption events based on the explicit experimental geometry. Such a simulation has been described previously,[92] is briefly summarized here, and more completely detailed in Sect. 2.4(B) and Appendix E. The procedure statistically calculates the relative signal contribution for a particular HF(*v,J*) quantum state detected in some differential volume (*dV*) and Doppler detuning ($d\nu$) with respect to the probe laser axis. This absorption signal arises from HF formation at another volume (*dV'*) in the jet intersection region, with recoil energy and angular direction consistent with incident reactant velocities, reaction energetics and conservation of linear momentum for limiting forms of the differential cross section. The statistical averaging uses MC routines that simulate the distribution of reactant speeds, densities, collision angles, and scattering angles present under the experimental conditions. The inputs to the model are as follows: i) probe and jet geometries, ii) known reactant and product masses, iii) reaction exothermicity, iv) reactant jet angular distributions and speeds, and v) the adiabatic, zero-point corrected transition-state barrier height (3.75 kcal/mol) obtained from high-level *ab initio* calculations,[5,48,79] below which the reaction can not proceed classically.

The key function of the MC simulation is to predict the probability distribution of velocities for HF detected in state (*v,J*) as a function of HF–Cl recoil energy. These distributions, projected onto to the IR probe axis, also can be used to predict Doppler widths plotted as the dashed line in Fig. 3.4. The agreement between predicted and measured Doppler widths serves as an independent measure of model reliability, and increases confidence in the quantity of interest from the MC simulation. The *density-to-flux* transformation is obtained from

$$\Phi_{(v,J)} = \int dx\, \rho_{HF(v,J)}(x) \,/\langle \tau \rangle_{(v,J)}, \tag{3.4}$$

where $\Phi_{(v,J)}$ is the state resolved flux per unit area (in HF molecules/cm^2/s), $\int dx\, \rho_{HF(v,J)}(x)$ is the column-integrated density plotted in Fig. 3.6 and tabulated in Table 3.1, and $\langle \tau \rangle_{(v,J)}$ is the average time HF(v,J) spends in the probe laser volume. Due to spatial averaging within the unskimmed jets, the MC results are relatively insensitive to the assumed differential cross section, which is taken simply as isotropic. By way of support, MC simulations for extreme limits of i) sideways and ii) forward/backward scattering yield ratios of density-to-flux transformation factors and quantum state resolved populations that differ less than experimental uncertainties for a given vibrational manifold. The state resolved flux values calculated via Eq. 3.4 have been normalized to yield branching ratios into a given HF(v,J) state, as also summarized in Table 3.1. The density-to-flux transformation results in a modest increase in product branching into low-energy HF(v,J) states, yielding essentially identical trends for distributions of *rotational* HF column-integrated densities discussed in Sect. 3.3. Net *vibrational* populations can be obtained by summing over rotational states for a given vibrational state, as shown by the *flux* and *density* branching ratios illustrated in Fig. 3.7. This comparison generally provides very good agreement with previous studies, supporting expectations that chemiluminescence conditions were indeed sufficient to completely arrest vibrational ineleastic collisions.

3.5 Discussion

Recent theoretical studies have reported the vibrational branching of HF product, resulting in populations in [v = 0, 1, 2, 3] of [0.03, 0.31, 0.68, 0.01] on Kornweitz's LEPS surface[71] and [0.01, 0.12, 0.72, 0.16] on the SHHG PES.[66] Each of these studies consistently overestimates the population in the highest (v = 2,3) manifolds compared to experimental measurements, a trend continued by Hayes' study[73] on the new DHSN surface [0.001, 0.03, 0.43, 0.54]. Of particular importance, these calculations all reveal little or no population in the v = 0 manifold and a relatively insignificant fraction of v = 1 population. Such consistent over-

prediction of HF vibrational excitation with respect to experiment may signal the need to address remaining deficiencies in these QCT calculations, arising from either i) pure quantum effects such as transition state resonances, ii) non-adiabatic surface hopping dynamics, or iii) deficiencies in the previous ground state *ab initio* surfaces.

In light of the discrepancies in vibrational branching, it is not surprising that theoretical studies of the F + HCl reaction also fail to reproduce the highly structured rotational distributions reported herein. Sayos' QCT calculations[66] found HF product almost exclusively in high J (J = 10–16) v = 2. As discussed in the introduction, Sayos' SHHG PES and the more recent DHSN PES both contain highly bent transition states. Such bent reaction geometry is likely to significantly torque on the nascent HF diatom and constrain motion across the transition state.[73] The inability to explain lower-energy rotational populations has prompted us to further explore the DHSN surface via QCT, as described below.

To help interpret the observed trends in HF product state distributions and address remaining discrepancies with theory, a series of QCT calculations have been performed on the DHSN surface using a fourth-order Runge-Kutta integration method.[84] Using a time step of 5 atomic units = 0.12 fs, energy is conserved to better than 0.03 and 0.0002 kcal/mol for reactive and non-reactive events, respectively, with typical trajectories of 1–2 ps duration. The surface has been explored using trajectories starting in the entrance channel with an initial F–HCl distance of ≈10 Å, collision energies of 4–10 kcal/mol, initial HCl angular momenta of J = 0–5, and impact parameters of 0–4 Å. Representative calculations resulting from 50,000 trajectories starting in the F + HCl channel at E_{com} = 7 kcal/mol and J_{HCl} = 2 are plotted in Fig. 3.9. The choice of collision energy enhances reaction probability; however, the qualitative aspects of the HF product quantum-state distributions for reactive events prove relatively insensitive to collision conditions. Specifically, product HF is found exclusively in the v = 3 and v = 2 manifolds, with highest-energy rotational states primarily correlating with v = 2, as anticipated from conservation of

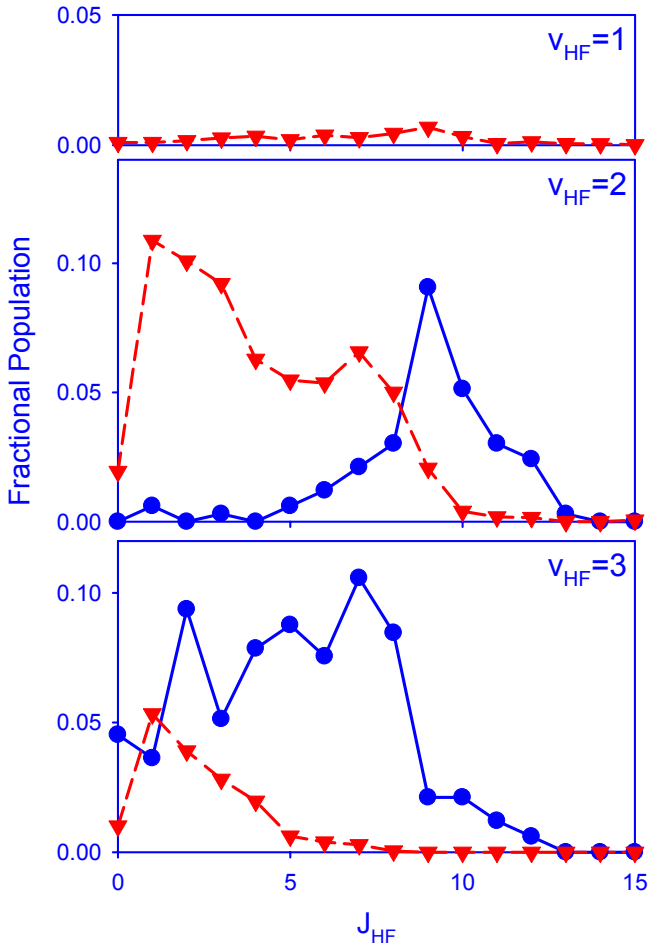

Figure 3.9 QCT results on the DHSN potential energy surface. Rovibrational distributions in $v = 1$, $v = 2$, and $v = 3$ are shown for trajectory calculations beginning far in the entrance channel (circles), and for trajectories beginning in the van der Waals well (triangles).

energy. The results are qualitatively similar to those reported by Sayos *et al*.,[48] who also found only rotationally excited HF in $v = 2$. The results of Sayos *et al*. are less vibrationally excited than the present DHSN calculations, but are performed on the SHHG PES, which has an empirically lowered barrier that enabled study at lower collision energies. Nevertheless, trajectories on both surfaces predict high vibrational excitation and, more specifically, only high rotational excitation in $v = 2$.

As a further test of these trends, a second set of trajectories has been performed, starting simply in the transition state (TS) region of the DHSN surface with total energy 0.2 kcal/mol above the classical barrier. Although these TS calculations have not been chosen to accurately reflect a distribution of reactive trajectories, they do reproduce the same propensity for i) exclusive population in the $v = 2$ and (to a lesser extent) $v = 3$ manifolds, and ii) peaking of high J state rotational excitation in $v = 2$. Thus, the DHSN surface clearly confirms results from earlier surfaces, in which only the high-J HF($v = 2$) and lower J HF($v = 3$) products are predicted via classical trajectory methods.

We have also used QCT methods to briefly explore the possible influence of the deep van der Waals well in the HF + Cl exit channel. These trajectories are motivated by the wealth of vibrational predissociation studies of van der Waals complexes, as well as the possibility of long lived resonance states that explore portions of the exit well not extensively visited by classical reaction path. Exit-well trajectories are started in the vicinity of the HF–Cl van der Waals minimum, in an initial distribution of HF rovibrational states obtained from full trajectory calculations shown in Fig. 3.9 and with zero kinetic energy in the HF–Cl coordinate. In essence, these conditions mimic what might be expected if nascent reactive products were to become trapped in the HF–Cl van der Waals well following reaction. The trajectories with non-rotating but vibrationally excited HF were found to be nondissociative on the time scales explored; this corresponds roughly to vibrational predissociation, which is known to be exquisitely sensitive to the hard inner wall of the PES and poorly modeled by QCT.[93] However, the dissociation

probability of the HF–Cl complex does rise rapidly with increasing HF internal rotation, in effect, rotationally predissociating to yield HF with reduced internal energy. The results of such trajectories are shown in Fig. 3.9, where the product HF fragments retain most of their vibrational energy while being "cooled" into lower angular momentum states. Thus, the Van der Waals exit well may play a significant role in the formation of the low-*J* HF observed experimentally and may even contribute to HF population in lower vibrational manifolds. Indeed, previous studies of exit-channel dynamics by Orr-Ewing and coworkers in reactive trajectories found that rotationally cold products with strong dipole moments can torque on recoiling fragments and thereby rotationally "heat up" in the exit channel.[94] It would seem equally dynamically plausible in the F + HCl system for highly rotationally excited HF to be "cooled" by angular forces in the van der Waals exit channel, which would be an interesting direction for further theoretical exploration.

As a final comment, we note that the broad bimodal rotational distributions observed in the F + HCl system are not entirely novel. In fact, the resonance-mediated reaction F + HD produces a similarly broad, highly structured distribution of rotational states in HF(v = 2), as measured at E_{com} = 0.6 kcal/mol by Harper *et al.*,[76] and predicted by the quantum dynamical calculations of Skodje et al.[27] To facilitate comparison, the F + HD results for HF(v = 2, J) are reproduced in Fig. 3.10 along with the distribution of HF(v = 2,J) fluxes from the present F + HCl work. The distributions from each reaction share a number of qualitative features, including highly nonstatistical populations, broad nearly constant intensities at low J and a sudden drop off to zero population at high J. The calculations of Skodje *et al.* interpret the F + HD distribution as the result of a transition state resonance due to H atom vibrational motion across the barrier, as first observed in elegant differentially resolved scattering measurements by Liu and coworkers. The qualitative similarity between rotational distributions in these two HLH systems therefore suggest the presence of transition state resonance dynamics also playing an important role in

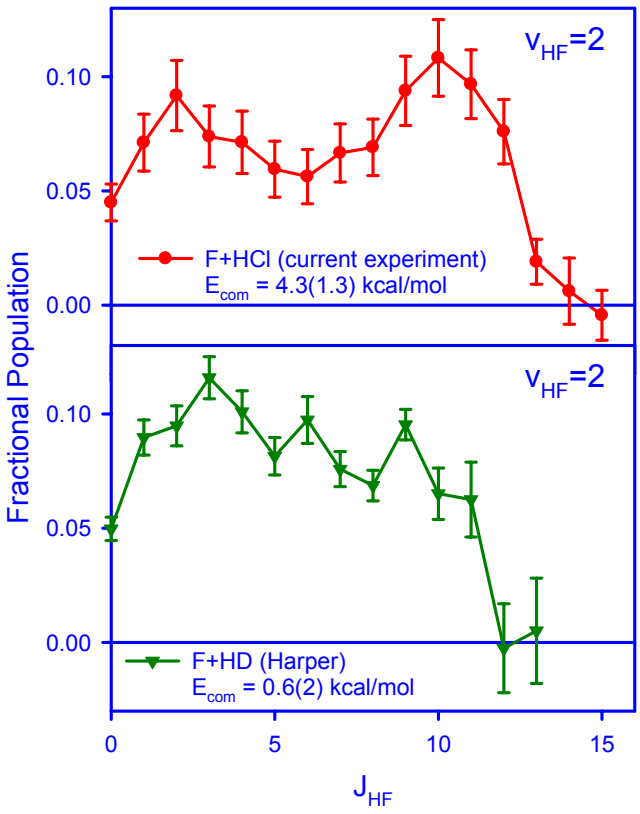

Figure 3.10 HF($v = 2$,J) rotational distributions from F + HCl (circles), in comparison with the F + HD reaction (triangles) from Ref. 76. The broad and structured populations from F + HD are dominated by a reactive transition state resonance at ≈ 0.5 kcal/mol.

F + HCl reactive scattering. At the very least, this is an intriguing result worthy of further experimental and theoretical attention. From an experimental perspective, we have constructed a velocity map ion imaging apparatus, which should permit reactive studies of F + HCl by probing the Cl($^2P_{1/2}$,$^2P_{3/2}$) product with energy and angular scattering resolution. From a theoretical perspective, this has motivated our development of a full set of high-level multireference (MRCI + Q), spin-orbit corrected potentials along with non-adiabatic terms coupling each of the surfaces. It is our hope that such efforts will help further elucidate the dynamical richness clearly still present in such a classic yet deceptively "simple" atom + diatomic reaction.

3.6 Summary and Conclusion

The reaction F + HCl $\rightarrow$ HF + Cl has been observed under rigorous single-collision conditions for the first time, based on high resolution direct absorption IR laser spectroscopy on the HF(v,J) product. The increased sensitivity of the direct absorption method permits operation under much lower reactant densities, resulting in many orders of magnitude reduction in time window for collisions of the nascent product. The absence of collisional relaxation is validated by studies as a function of reactant backing pressure, as well as high resolution of Doppler profiles of translationally "hot" product species. The HF vibrational distributions are in excellent agreement with results reported in early arrested-relaxation IR emission studies. The IR laser absorption technique also permits branching into the HF(v = 0) manifold to be observed directly for the first time. The HF rotational distribution reveals significant structure, with strongly bimodal populations evident in both the v = 2 and v = 1 manifolds. The presence of both low and high J nascent rotational structure under single collision conditions is qualitatively similar to raw data from early IR emission studies, for which the low J component was inferred to be due to "unarrested" rotational relaxation processes. The current studies offer indications that some

fraction of this low *J* component may have been truly nascent, which might warrant reanalysis of similar IR emission data from other X + HY systems.

This novel bifurcation in *J* state distributions highlights the possible presence of microscopic branching in the reaction, which might signal the presence of more complex dynamics due to quantum effects and/or non-adiabatic coupling between electronic surfaces. By way of example, the bimodal rotational distributions observed in F + HCl are qualitatively quite similar to what is seen in the F + HD system, for which the presence of a FH(v = 3)–D quantum transition state scattering resonance has been confirmed by both experiment and theory. In analogy to the work of Orr-Ewing on more nearly thermoneutral systems, we propose a possible alternate mechanism for microscopic branching between low *J* and high *J* rotational distributions that involves partial internal HF rotor relaxation in the outgoing exit-channel due to the HF–Cl van der Waals well. High-level multireference potentials will soon be available to permit full 3D quantum reactive scattering on multiple non-adiabatic surfaces, and thereby stimulate more rigorous comparison between theory and experiment and promote understanding of the underlying reaction dynamics.

References for Chapter III

1 G. B. Moore and I. W. M. Smith, J. Phys. Chem. **100**, 12848 (1996).

2 P. J. Kuntz, E. M. Nemeth, J. C. Polanyi, S. D. Rosner, and C. E. Young, J. Chem. Phys. **44**, 1168 (1966).

3 G. Capecehi and H. J. Werner, Phys. Chem. Chem. Phys. **6**, 4975 (2004).

4 J. F. Castillo, B. Hartke, H. J. Werner, F. J. Aoiz, L. Banares, and B. Martinez-Haya, J. Chem. Phys. **109**, 7224 (1998).

5 M. P. Deskevich, M. Y. Hayes, K. Takahashi, R. T. Skodje, and D. J. Nesbitt, J. Chem. Phys. **124**, 224303 (2006).

6 P. F. Weck and N. Balakrishnan, J. Chem. Phys. **123**, 144308 (2005).

7 S. Rogers, D. S. Wang, A. Kuppermann, and S. Walch, J. Phys. Chem. A **104**, 2308 (2000).

8 D. J. Garton, A. L. Brunsvold, T. K. Minton, D. Troya, B. Maiti, and G. C. Schatz, J. Phys. Chem. A **110**, 1327 (2006).

9 D. J. Garton, T. K. Minton, B. Maiti, D. Troya, and G. C. Schatz, J. Chem. Phys. **118**, 1585 (2003).

10 B. F. Parsons and D. W. Chandler, J. Chem. Phys. **122**, 174306 (2005).

11 M. H. Alexander, G. Capecchi, and H. J. Werner, Faraday Discuss. **127**, 59 (2004).

12 F. Dong, S. H. Lee, and K. Liu, J. Chem. Phys. **115**, 1197 (2001).

13 D. Skouteris, H. J. Werner, F. J. Aoiz, L. Banares, J. F. Castillo, M. Menendez, N. Balucani, L. Cartechini, and P. Casavecchia, J. Chem. Phys. **114**, 10662 (2001).

14 N. Balucani, D. Skouteris, G. Capozza, E. Segoloni, P. Casavecchia, M. H. Alexander, G. Capecchi, and H. J. Werner, Phys. Chem. Chem. Phys. **6**, 5007 (2004).

15 D. G. Truhlar and Kupperma.A, J. Chem. Phys. **56**, 2232 (1972).

16 R. D. Levine and S. F. Wu, Chem. Phys. Lett. **11**, 557 (1971).

17 R. E. Continetti, B. A. Balko, and Y. T. Lee, J. Chem. Phys. **93**, 5719 (1990).

18 S. C. Althorpe, F. Fernandez-Alonso, B. D. Bean, J. D. Ayers, A. E. Pomerantz, R. N. Zare, and E. Wrede, Nature **416**, 67 (2002).

19 M. H. Alexander, D. E. Manolopoulos, and H. J. Werner, J. Chem. Phys. **113**, 11084 (2000).

20 S. C. Althorpe, Chem. Phys. Lett. **370**, 443 (2003).

21 M. Baer, M. Faubel, B. Martinez-Haya, L. Y. Rusin, U. Tappe, and J. P. Toennies, J. Chem. Phys. **108**, 9694 (1998).

22 F. Dong, S. H. Lee, and K. Liu, J. Chem. Phys. **113**, 3633 (2000).

23 M. Faubel, B. Martinez-Haya, L. Y. Rusin, U. Tappe, J. P. Toennies, F. J. Aoiz, and L. Banares, J. Phys. Chem. A **102**, 8695 (1998).

24 Y. T. Lee, Science **236**, 793 (1987).

25 D. M. Neumark, A. M. Wodtke, G. N. Robinson, C. C. Hayden, and Y. T. Lee, J. Chem. Phys. **82**, 3045 (1985).

26 L. Y. Rusin and J. P. Toennies, Phys. Chem. Chem. Phys. **2**, 501 (2000).

27 R. T. Skodje, D. Skouteris, D. E. Manolopoulos, S. H. Lee, F. Dong, and K. Liu, J. Chem. Phys. **112**, 4536 (2000).

28 R. T. Skodje, D. Skouteris, D. E. Manolopoulos, S. H. Lee, F. Dong, and K. P. Liu, Phys. Rev. Lett. **85**, 1206 (2000).

29 R. A. Sultanov and N. Balakrishnan, Astrophys. J. **629**, 305 (2005).

30 S. Javoy, V. Naudet, S. Abid, and C. E. Paillard, Exp. Therm. Fluid Sci. **27**, 371 (2003).

31 D. Gerlich, E. Herbst, and E. Roueff, Planet Space Sci. **50**, 1275 (2002).

32 O. D. Krogh, D. K. Stone, and G. C. Pimentel, J. Chem. Phys. **66**, 368 (1977).

33 M. J. Berry, J. Chem. Phys. **59**, 6229 (1973).

34 C. Zhu, R. Krems, A. Dalgarno, and N. Balakrishnan, Astrophys. J. **577**, 795 (2002).

35 D. A. Neufeld, J. Zmuidzinas, P. Schilke, and T. G. Phillips, Astrophys. J. **488**, L141 (1997).

36 W. B. Chapman, B. W. Blackmon, and D. J. Nesbitt, J. Chem. Phys. **107**, 8193 (1997).

37 C. X. Xu, D. Q. Xie, and D. H. Zhang, Chin. J. Chem. Phys. **19**, 96 (2006).

38 S. C. Althorpe and D. C. Clary, Annu. Rev. Phys. Chem. **54**, 493 (2003).

39 M. H. Qiu, Z. F. Ren, L. Che, D. X. Dai, S. A. Harich, X. Y. Wang, X. M. Yang, C. X. Xu, D. Q. Xie, M. Gustafsson, R. T. Skodje, Z. G. Sun, and D. H. Zhang, Science **311**, 1440 (2006).

40 Y. R. Tzeng and M. H. Alexander, J. Chem. Phys. **121**, 5183 (2004).

41 J. D. D. Martin and J. W. Hepburn, J. Chem. Phys. **109**, 8139 (1998).

42 W. T. Zemke, W. C. Stwalley, J. A. Coxon, and P. G. Hajigeorgiou, Chem. Phys. Lett. **177**, 412 (1991).

43 B. P. Stoicheff, Can. J. Phys. **79**, 165 (2001).

44 R. T. Skodje, Annu. Rev. Phys. Chem. **44**, 145 (1993).

45 W. Jakubetz, D. Sokolovski, J. N. L. Connor, and G. C. Schatz, J. Chem. Phys. **97**, 6451 (1992).

46 I. M. Waller, T. N. Kitsopoulos, and D. M. Neumark, J. Phys. Chem. **94**, 2240 (1990).

47 F. Fernandez-Alonso and R. N. Zare, Annu. Rev. Phys. Chem. **53**, 67 (2002).

48 R. Sayos, J. Hernando, J. Hijazo, and M. Gonzalez, Phys. Chem. Chem. Phys. **1**, 947 (1999).

49 E. Wurzberg and P. L. Houston, J. Chem. Phys. **72**, 5915 (1980).

50 C. M. Moore, I. W. M. Smith, and D. W. A. Stewart, Int. J. Chem. Kinet. **26**, 813 (1994).

51 I. W. M. Smith and D. J. Wrigley, Chem. Phys. Lett. **70**, 481 (1980).

52 B. S. Ault, J. Chem. Phys. **68**, 4012 (1978).

53 J. M. Merritt, J. Kupper, and R. E. Miller, Phys. Chem. Chem. Phys. **7**, 67 (2005).

54 V. Aquilanti, D. Cappelletti, F. Pirani, L. Y. Rusin, M. B. Sevryuk, and J. P. Toennies, J. Phys. Chem. **95**, 8248 (1991).

55 A. V. Fishchuk, G. C. Groenenboom, and A. van der Avoird, J. Phys. Chem. A **110**, 5280 (2006).

56 A. V. Fishchuk, P. E. S. Wormer, and A. van der Avoird, J. Phys. Chem. A **110**, 5273 (2006).

57 J. Klos, M. M. Szczesniak, and G. Chalasinski, Int. Rev. Phys. Chem. **23**, 541 (2004).

58 M. L. Dubernet and J. M. Hutson, J. Phys. Chem. **98**, 5844 (1994).

59 M. Meuwly and J. M. Hutson, J. Chem. Phys. **119**, 8873 (2003).

60 P. Beadle, M. R. Dunn, N. B. H. Jonathan, J. P. Liddy, and J. C. Naylor, J. Chem. Soc., Faraday Trans. II **74**, 2170 (1978).

61 D. Bogan and D. W. Setser, in *Fluorine-containing free radicals: kinetics and dynamics of reactions: based on a symposium sponsored by the Division of Physical Chemistry at*

the 169th meeting of the American Chemical Society, Philadelphia, Pennsylvania, April 7-11, 1975, edited by J. W. Root (American Chemical Society, Washington, 1978), pp. 237.

62 A. M. G. Ding, L. J. Kirsch, D. S. Perry, J. C. Polanyi, and J. L. Schreiber, Faraday Discuss. **55**, 252 (1973).

63 N. Jonathan, Melliar-Smith Cm, S. Okuda, D. H. Slater, and D. Timlin, Mol. Phys. **22**, 561 (1971).

64 J. P. Sung and D. W. Setser, Chem. Phys. Lett. **48**, 413 (1977).

65 K. Tamagake, D. W. Setser, and J. P. Sung, J. Chem. Phys. **73**, 2203 (1980).

66 R. Sayos, J. Hernando, R. Francia, and M. Gonzalez, Phys. Chem. Chem. Phys. **2**, 523 (2000).

67 D. S. Perry, Private Communication (2006).

68 D. Brandt and J. C. Polanyi, Chem. Phys. **35**, 23 (1978).

69 L. J. Kirsch and J. C. Polanyi, J. Chem. Phys. **57**, 4498 (1972).

70 J. C. Polanyi and K. B. Woodall, J. Chem. Phys. **57**, 1574 (1972).

71 H. Kornweitz and A. Persky, J. Phys. Chem. A **108**, 140 (2004).

72 B. Y. Tang, B. H. Yang, K. L. Han, R. Q. Zhang, and J. Z. H. Zhang, J. Chem. Phys. **113**, 10105 (2000).

73 M. Y. Hayes, M. P. Deskevich, D. J. Nesbitt, K. Takahashi, and R. T. Skodje, J. Phys. Chem. A **110**, 436 (2006).

74 W. B. Chapman, B. W. Blackmon, S. Nizkorodov, and D. J. Nesbitt, J. Chem. Phys. **109**, 9306 (1998).

75 W. W. Harper, S. A. Nizkorodov, and D. J. Nesbitt, J. Chem. Phys. **113**, 3670 (2000).

76 W. W. Harper, S. A. Nizkorodov, and D. J. Nesbitt, J. Chem. Phys. **116**, 5622 (2002).

77 D. Proch and T. Trickl, Rev. Sci. Instrum. **60**, 713 (1989).

78 D. R. Miller, in *Atomic and molecular beam methods*, edited by G. Scoles (Oxford University Press, New York, 1988), pp. 14.

79 I. Last and M. Baer, J. Chem. Phys. **80**, 3246 (1984).

80 J. L. Hall and S. A. Lee, Appl. Phys. Lett. **29**, 367 (1976).

81 A. S. Pine, J. Opt. Soc. Am. **66**, 97 (1976).

82 D. Herriot, H. Kogelnik, and R. Kompfner, Appl. Optics **3**, 523 (1964).

83 D. Kaur, A. M. Desouza, J. Wanna, S. A. Hammad, L. Mercorelli, and D. S. Perry, Appl. Optics **29**, 119 (1990).

84 W. H. Press, S. A. Teukolsky, W. T. Vetterling, and B. P. Flannery, *Numerical recipes in C: the art of scientific computing*, 2 ed. (Cambridge University Press, New York, 1992).

85 E. Arunan, D. W. Setser, and J. F. Ogilvie, J. Chem. Phys. **97**, 1734 (1992).

86 S. A. Nizkorodov, W. W. Harper, W. B. Chapman, B. W. Blackmon, and D. J. Nesbitt, J. Chem. Phys. **111**, 8404 (1999).

87 D. Brandt and J. C. Polanyi, Chem. Phys. **45**, 65 (1980).

88 E. S. Whitney, A. M. Zolot, A. B. McCoy, J. S. Francisco, and D. J. Nesbitt, J. Chem. Phys. **122**, 124310 (2005).

89 H. W. Cruse, P. J. Dagdigian, and R. N. Zare, Faraday Discuss. **55**, 277 (1973).

90 C. Naulin, M. Costes, A. Benseddik, and G. Dorthe, Laser Chem. **8**, 283 (1988).

91 D. M. Sonnenfroh and K. P. Liu, Chem. Phys. Lett. **176**, 183 (1991).

92 W. W. Harper, S. A. Nizkorodov, and D. J. Nesbitt, Chem. Phys. Lett. **335**, 381 (2001).

93 E. Tannenbaum, K. J. Higgins, W. Klemperer, B. Segev, and E. J. Heller, J. Phys. Chem. B **106**, 8100 (2002).

94 S. Rudic, C. Murray, J. N. Harvey, and A. J. Orr-Ewing, J. Chem. Phys. **120**, 186 (2004).

Chapter IV $F + H_2O \rightarrow HF(v,J) + OH$: $HF(v,J)$ nascent product state distributions formed in crossed molecular jets

4.1 Introduction

As demonstrated in the previous chapter, significant progress has been made in understanding gas-phase reaction dynamics in three-atom systems. However, significant hurdles remain for larger systems because additional degrees of freedom dramatically increase the computational cost of characterizing the PES and performing quantum dynamical calculations on such surfaces in full dimensionality. Yet, even with the relatively modest increase from three to four atoms, entirely new phenomena become feasible, such as mode-specific chemistry[1-13] and energy transfer into "spectator" degrees of freedom.[14,15] Additionally, increasing system size and number of open channels necessitate considerably more detailed experimental observations to characterize adequately the product distributions at the quantum state-to-state level.

Recent work has demonstrated that the study of polyatomic (i.e. $N \geq 4$) reaction dynamics is on the horizon of computational feasibility. In particular, remarkable advances have been made in developing an accurate *ab initio* PES and performing exact quantum reactive scattering calculations for the benchmark four-atom reaction system $H + H_2O \leftrightarrow H_2 + OH$.[16-18] Recent progress in this dynamically rich reaction suggests that full-dimensional *ab initio* studies of four-atom systems with more than one heavy (i.e., non-hydrogen) atom will be feasible in the near future, and chemical systems with $N > 4$ are likely to become the outstanding computational challenge in $3N$-6 dimensions.

Direct dynamics methods present one interesting alternative to completely exploring dynamics on a high-dimensional PES. This technique enables classical trajectory simulations to

be performed in arbitrary dimensions by calculating the PES energy and its derivatives "on the fly," at the nuclear coordinates traversed by a given trajectory.[19-22] However, computational costs in systems of high dimensionality restrict such calculations to relatively low levels of *ab initio* treatment. Furthermore, this method relies intrinsically on classical dynamics, making inherently quantum phenomena, such as zero point energy[23] and reactions promoted by tunneling through barriers,[24] difficult to model. The current intractability of full dimensional studies for all but the simplest four-atom system emphasizes the need for further experimental efforts at the state-to-state level. Such work provides a crucial opportunity for benchmark testing of approximate theoretical methods against detailed experimental measurements and stimulates the development of progressively more rigorous multidimensional quantum computational techniques.

The $F + H_2O \rightarrow HF + OH$ reaction represents an ideal candidate for detailed comparison between experiment and novel theoretical techniques. In addition to fundamental interest in 4-atom bond-making and bond-breaking, this reaction plays an important role in Earth's atmosphere, where it is primarily responsible for scavenging F atoms introduced into the troposphere by photolysis of partially fluorinated compounds.[25] In astronomy this reaction may be important in determining the fate of F atoms in the interstellar medium.[26] The dynamics of this atom + triatom abstraction process are dominated by a relatively low transition state barrier ($\Delta E \approx$ 5 kcal/mol[27]) and yet a moderately high exothermicity (ΔH^0 = -17.61(2) kcal/mol[28,29]). Interestingly, these values are quite close to those found in the current state-of-the-art 4-atom reaction system, $H_2 + OH$, which features a similarly exothermic (ΔH^0 = -14.4 kcal/mol[28,30]) reaction path and low barrier ($\Delta E \approx$ 6 kcal/mol)[16] for formation of H_2O product.

As shown in Fig. 4.1, many rovibrational quantum states of HF and OH products are energetically accessible from reaction of F with H_2O. From an experimental perspective, quantum state resolved spectroscopic techniques have been developed that are capable of sensitively probing reactive scattering and energy flow into both diatomic species.[31-33] Alternatively, high-

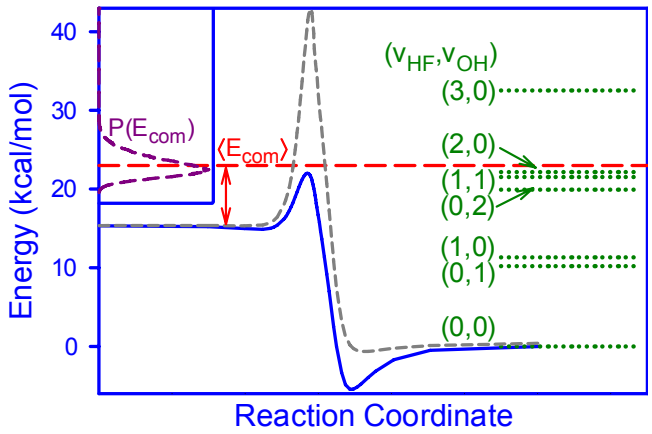

Figure 4.1 Reaction coordinate for F + $H_2O \rightarrow$ HF + OH on the two lowest adiabatic potential energy surfaces, from calculation in Ref. 27. Both surfaces asymptotically correlate to F($^2P_{3/2}$) reactant, but result in ground OH($^2P_{3/2}$) (solid line) and spin-orbit excited OH($^2P_{1/2}$) (short dashes) in the product channel. The inset plot is the calculated experimental collision energy distribution, whose average value, E_{com} = 5.4(1.3) kcal/mol above the reactant energy, is plotted as the long dashed line. Various vibrational levels of HF and OH products are shown as dotted lines.

level theoretical treatment may hope to attain chemically accurate *ab initio* results, while still using acceptably small basis sets to describe the second row atoms in this system. Recent multireference configuration interaction studies of the F + H_2O PES revealed that reaction on the two lowest electronic PESs occurs over barriers of $\Delta E \approx 5$ kcal/mol and 25 kcal/mol, which correlate adiabatically with the formation of ground ($^2\Pi_{3/2}$) and spin orbit excited ($^2\Pi_{1/2}$) product OH.[27] Although these two surfaces exhibit quite different *adiabatic* barriers to reaction, they can cross via multidimensional "seams" of conical intersections, including nuclear configurations close to the reactive transition state.

The importance of such non-adiabatic reaction considerations is emphasized by recent crossed jet studies of F + H_2O and F + D_2O performed in our group.[33,34] Though laser induced fluorescence (LIF) measurements revealed that only OD(v = 0,N) is produced, with an average rotational energy of $E_{rot} \approx 1$ kcal/mol, the reaction produces *ground* ($^2\Pi_{3/2}$) and *spin-orbit excited* ($^2\Pi_{1/2}$) OD products in roughly a 2:1 ratio. This result is surprising since spin-orbit excited radical adiabatically correlates to reaction on the first *excited* electronic surface, whose ≈ 25 kcal/mol barrier exceeds the collision energy by five-fold. Thus, multiple theoretical surfaces and non-adiabatic dynamical treatments will clearly be necessary to account for the apparent "surface hopping" dynamics leading to OH($^2\Pi_{1/2}$). The importance of such *non-adiabatic* dynamics underlying this relatively simple four-atom reaction further motivates quantum-state resolved studies of the HF(v,J) cofragment.

Both kinetic and dynamic studies of F + H_2O have been performed previously. Temperature dependent rates of the F + H_2O/D_2O reactions were reviewed by Stevens *et al.*,[35] inferring a tunneling mechanism and a $\Delta E \approx 4$ kcal/mol estimate for the transition state barrier height, in close agreement with the $\Delta E \approx 5$ kcal/mol value from *ab initio* theory.[27] In a series of pioneering dynamical studies, Setser and coworkers obtained rotationally resolved IR chemiluminescence spectra of HF in the v = 1 manifold and inferred cold OH vibrations.[36-38]

Recent photodetachment studies of the anionic cluster FH_2O^- have also shed insight upon the title reaction. Partial overlap between the FH_2O^- anion geometry and the F + H_2O transition state allows the reactive region of the PES to be accessed directly, resulting in a low energy tail attributed to formation of product HF + OH.[39] Direct dynamics simulations of the photodetachment process found substantial branching into the product channel, yielding rovibrationally excited HF products and vibrationally cold OH with modest amounts of rotational excitation.[40] These studies stimulate further study of this fundamental four-atom reaction under crossed beam conditions to resolve completely the energy partitioning in the HF fragment.

The following sections of this chapter describe the complete HF(v,J) product state distribution following the reaction F + $H_2O \rightarrow$ HF + OH, measured using the high-sensitivity laser spectrometer and crossed jet apparatus described in detail in Ch. I. Crossed supersonic jets enable the reaction to be studied with ≈ 1000-fold reduction in gas density compared to chemiluminescence studies. Furthermore, reverse seeding in a He diluent permits the supersonic jet reactants to more easily surmount the barrier by increasing the collision energy. Sensitive IR laser absorption methods provide i) complete rovibrational state resolution, ii) high resolution Dopplerimetry measurements along the probe axis, and iii) the first experimental measure of total product branching into each of the v = 0, 1 and 2 vibrational manifolds.

4.2 Experiment

Detailed descriptions of the crossed jet experimental apparatus appear in Ch. II. The specific conditions used in the present study are described here and illustrated in Fig. 4.2. The H_2O jet contains ≈ 30 Torr H_2O, produced by bubbling He through liquid water heated to 30 °C at a total pressure of 200 Torr. The remainder of the gas line, including the pulsed valve, is heated to 60 °C to prevent condensation. Fig. 4.3 displays IR measurements of $H_2{}^{18}O$ concentration, present

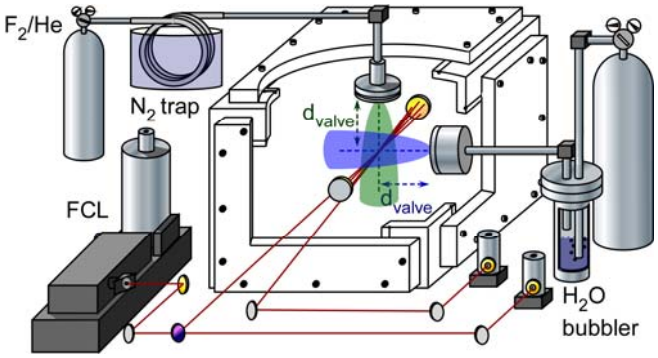

Figure 4.2 Schematic of the crossed jet apparatus, containing pulsed molecular jets of F and H_2O intersecting at 90° in a vacuum chamber. Product HF(v,J) is probed by quantum state resolved, high resolution IR laser absorption using a multipass cell oriented perpendicular to the plane defined by the jets axes.

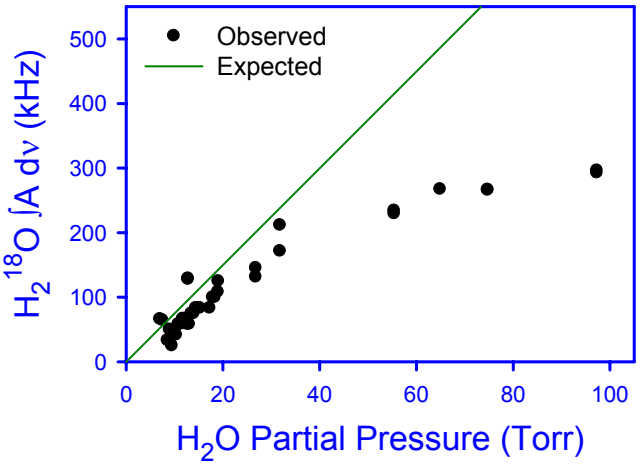

Figure 4.3 Measured spectral intensity of a isotopically substituted $H_2{}^{18}O$ line present in nature abundance in the reactant water jet. The jet's stagnation pressure is constant at 200 Torr with helium carrier gas. Partial pressure of water is varied by changing the liquid temperature.

in natural isotopic abundance. These measurements match the expected linear curve of growth as H_2O partial pressure increases up to the 30 Torr value used, confirming the absence of significant H_2O clustering in the reactant jet.

Given its high sensitivity, the IR probe detects trace HF gas produced in the radical source by impurities in the 10% F_2 90% He mixture passed through the high voltage plasma jet source. Detailed characterization of this background was presented in Ch. 2.3(B). The measured HF density corresponds to 1.0 ppm generated in the plasma source. Placing a liquid nitrogen cold trap in the F_2 gas line reduces this background approximately two-fold while leaving the reactive scattering intensity unchanged. Background corrections are made by measuring the HF spectrum in the presence and absence of H_2O reactant, and correcting the reactively scattered results for the background HF densities. This correction is most important in the $v = 0$ manifold at low J, as demonstrated by the ≈ 60 K HF background temperature shown in Fig. 2.11. As a result, background HF can be confidently eliminated from the reactive product distributions, although product signals in the very lowest HF($v = 0, J \leq 4$) rotational states are not measured reliably and thus not reported. However, HF branching into these states is not expected to be dynamically favored and does not change any of the conclusions drawn from the present results.

Doppler-resolved absorption measurements, such as those presented in Fig. 4.4(a,b), are recorded for all HF($v'' \leq 2$) IR transitions[41] within 2.5–3.3 μm, for a total of about 500 observations of 42 lines. Fitting the lineshapes, such as that in Fig. 4.4(b), to a simple Gaussian profile reveals translationally excited profiles (full width at half maximum [FWHM] of 880 MHz) following the reaction, corresponding to HF recoil speeds of ≈ 2.20 km/s. This value exceeds the 1.25 km/s FWHM of the F + H_2O center of mass (COM) velocity distribution. For states originating in the $v = 2$ manifold [Fig. 4.4(a)], less energy is available for product translation, and the observed Doppler widths decrease accordingly. However, the observed Doppler widths

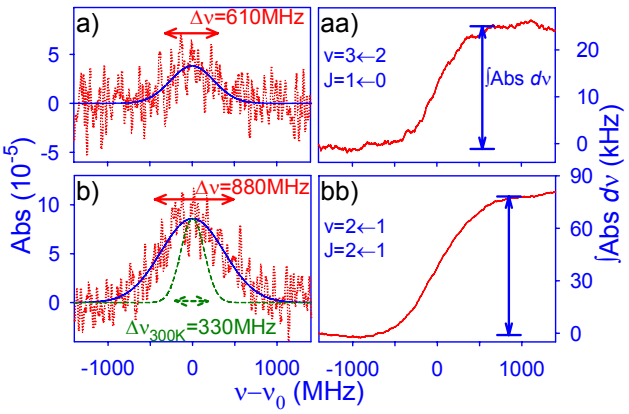

Figure 4.4 Sample Doppler-resolved absorption measurements originating from (a) HF (v = 3←2; J = 1←0) and (b) HF (v = 2←1; J = 2←1) transitions, with total integrated intensities with respect to laser detuning in (aa) and (bb) and indicated by solid arrows. Solid lines in the left hand plots are least squares fits to Gaussian lineshapes, with $\Delta\nu$ (FWHM) well in excess of the 300 MHz room temperature HF linewidth [dashed line in (b)]. Doppler profiles have been smoothed with Savitzky-Golay methods (4th order 25 point) relative to the high resolution measurements; fits and integrals have been obtained from the raw data.

strongly indicate that the nascent HF remains translationally excited following the reactive encounter, providing evidence for single collision conditions at the reactant jet intersection region.

Reaction cross sections and experimental conditions for the present study result in HF densities of $< 2\times10^{9}$ #/cm^3 per quantum state, requiring highly sensitive measurements of HF transient absorption. As shown by the raw data in Fig. 4.4(a,b), the IR absorption at these low densities is on the order of the fundamental photon shot noise limit of $\approx 1\times10^{-5}$ absorbance in the experimental 4.0 kHz bandwidth. Even at nearly shot-noise limited sensitivity, signals profit from integrating each Doppler profile to improve the signal to noise as described in Ch. III. This treatment reduces uncertainty by the square root of the 200–300 measurements under the Doppler FWHM, as reflected in the ≈ 5 kHz integral absorbance uncertainty in Fig. 4.4(aa,bb), and results in a detection sensitivity of $\approx 1\times10^{-8}$ HF/cm^3.

Since *absolute* HF densities are obtained from the IR absorption technique, the total reaction cross section of $\sigma \approx 0.8(0.5)$ Å^2 for F + H_2O at 5.4(1.3) kcal/mol collision energy has been obtained by calibrating the F atom density against F + H_2 as described in Ch. 2.4(C). This result agrees with measured thermal rate constant, which is approximately ten times lower than the molecular collision rate[35] and suggests that the collision energy does not efficiently couple into the reaction coordinate according to an intermediate- rather than early-barrier scenario. *Ab initio* calculations support this conclusion, with the breaking O–H bond extended to $r^{\dagger}(O–H^{A})$ = 1.031 Å at the transition state, significantly longer than the 0.958 Å bond length in H_2O, and the non-reactive O–H bond only mildly stretched to $r^{\dagger}(O–H^{B})$ = 0.971 Å.[27,42] This comparison suggests that vibrational excitation of OH stretching modes in water may selectively increase the reaction probability, an interesting area for future exploration.

As customary with the present experimental apparatus, nascent HF state distributions have been directly confirmed experimentally. Absorption measurements originating in the HF(v =

1) manifold have been observed over a tenfold change in the collision rate, obtained by simultaneously varying the distance d_{valve} from both jet sources to the intersection region on the laser probe axis (see Fig. 4.2). Integral absorbances are scaled by their transition strengths to produce a quantity roughly proportional to the HF rotational populations. These values have been normalized and plotted in Fig. 4.5, from which HF rotations are found to be significantly excited following the reaction event, since all three data sets appear significantly hotter than the 300 K line in Fig. 4.4(b). This excitation remains unperturbed under the density conditions probed, except perhaps at the highest collision densities explored (d_{valve} = 2.5 cm), which appears slightly colder than the lower density measurements. Thus, the remainder of this study, including the sample data in Fig. 4.4, has been carried out at the middle density conditions (d_{valve} = 3.5 cm, with densities of $\approx 5\times10^{14}$ #/cm^3 in the probe region), yielding sufficient signal for reasonable measurement uncertainties and maintaining rotationally unrelaxed conditions.

4.3 Results and Analysis

The observed HF spectral features are highly structured, as shown in the stick spectrum of measured integral intensities in Fig. 4.6. Specifically, both *absorption* and *stimulated emission* result from the nascent HF state distribution. Indeed, most of the nascent HF population is formed in the v = 1 manifold, resulting in net emission signals in the fundamental (v = 1←0) band and *absorption* on the v = 2←1 and v = 3←2 "hot bands". No HF absorption signals are observable in the v = 4←3 band, as expected based on the energy levels presented in Fig. 4.1.

The least squares analysis, described in detail in Ch. 2.4(A), has been performed using the known HF(v,J) transition line strengths[43] to obtain the nascent HF state resolved densities. All 500 observed HF line intensities are included in the fit, which matches experiment within uncertainty, as shown in Fig. 4.6. The resulting HF densities for the 42 states whose population

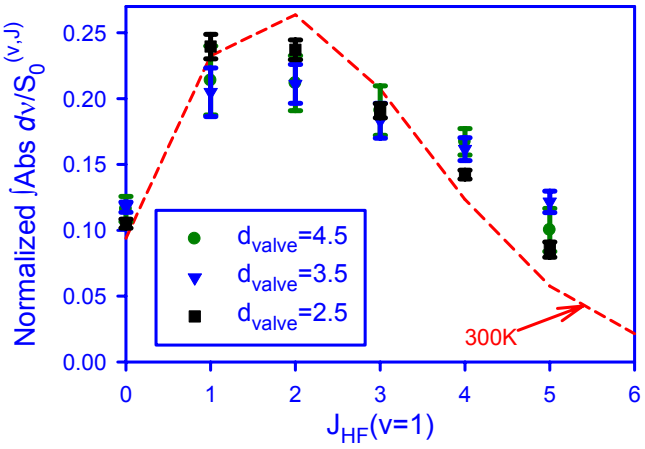

Figure 4.5 Normalized HF $v = 1$ integral absorbance measurements, scaled to the transition linestrength [$S_0(v,J)$] at three different source geometries. Both F and H_2O jet nozzle distances (d_{valve}) are varied relative to the laser probe axis to change the reactant density in the intersection region. The dashed line represents a room temperature rotational distribution, noticeably colder than the measured data. Measurements confirm negligible rotational redistribution of HF population with increasing gas density. Conditions used for all reported data in this study correspond to $d_{valve} = 3.5$ cm.

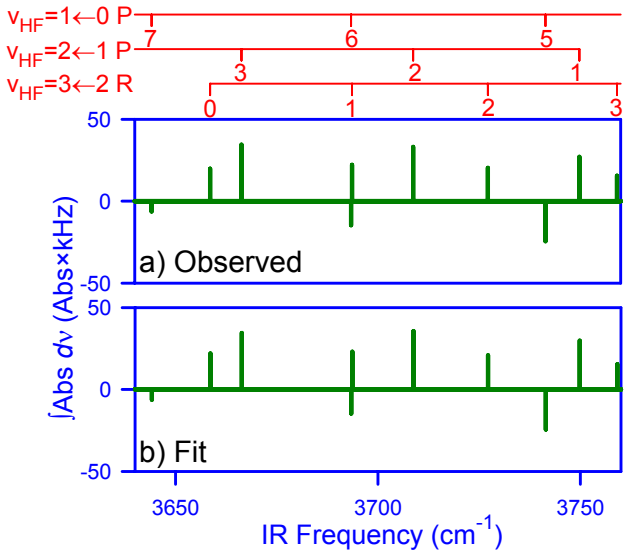

Figure 4.6 A portion of the a) observed and b) fitted IR stick spectra for HF(v,J) formed by the F + H_2O reaction. Transition intensities are found by locally integrating each Doppler-resolved measurement, as plotted in Fig. 4.4(aa) and (bb). Absorption features have positive amplitude, while negative absorption intensities result from stimulated emission on transitions originating from the $v_{HF} = 0$ manifold due to inverted vibrational populations in $v_{HF} = 1$.

has been measured in the current experiment are presented in Table 4.1.

Also presented in Table 4.2 and plotted in Fig. 4.7 are the HF rovibrational branching ratios, $P_{HF}(v,J)$, obtained by consideration of the *density-to-flux transformation*,[40] described in Ch. 2.4(B) and discussed in more detail in Appendix E. This transformation is necessary since laser absorption methods measure the HF *density*, whereas branching ratios are proportional to the state resolved product *flux* leaving the reaction volume. Based on detailed Monte Carlo (MC) modeling of the experimental apparatus,[34,35] the expected residence time $\langle \tau \rangle_{(v,J)}$ an HF molecule in state (v,J) spends in the detection volume can be predicted. This set of $\langle \tau \rangle_{(v,J)}$values represents proportionality constants for converting column-integrated HF density (#/cm^2) to flux (#/s/cm^2), which are then normalized to yield branching ratios. The MC model also provides a detailed picture for the distribution of collision energies in the crossed jet apparatus, presented in the inset of Fig. 4.1.

Table 4.1 HF column-integrated densities [$\int dx\ \rho_{HF}(x)$] observed following the reaction F + H_2O → HF(v,J) + OH, in units of 10^9 HF/cm^2. Uncertainties in parenthesis are one standard deviation from the least squares fit.

J	v = 0	v = 1	v = 2
0	--	64 (4)	21 (2)
1	--	109 (5)	16 (3)
2	--	112 (5)	13 (3)
3	--	105 (7)	7 (3)
4	--	78 (7)	0 (3)
5	3 (14)	51 (6)	0 (3)
6	7 (13)	38 (6)	0 (3)
7	28 (12)	23 (7)	--
8	15 (12)	22 (7)	--
9	21 (12)	7 (5)	--
10	6 (11)	0 (4)	--
11	8 (10)	9 (5)	--
12	4 (10)	3 (4)	--
13	4 (9)	7 (4)	--
14	22 (9)	6 (4)	--
15	10 (8)	0 (4)	--
16	3 (9)	--	--
17	8 (7)	--	--
18	-3 (7)	--	--

Table 4.2 HF state resolved flux (normalized to 100 %) following the reaction F + H_2O → HF(v,J) + OH. Uncertainties in parenthesis are one standard deviation from the least squares fit.

J	v = 0	v = 1	v = 2
0	--	7.9 (4)	2.5 (2)
1	--	13.5 (5)	2.0 (3)
2	--	13.9 (6)	1.6 (4)
3	--	13.0 (8)	0.9 (3)
4	--	9.7 (8)	0.0 (3)
5	0.4 (15)	6.3 (6)	0.0 (3)
6	0.9 (14)	4.6 (6)	0.0 (4)
7	3.5 (13)	2.8 (7)	--
8	1.8 (13)	2.8 (7)	--
9	2.6 (13)	0.8 (5)	--
10	0.8 (12)	0.0 (5)	--
11	1.0 (11)	1.1 (5)	--
12	0.5 (11)	0.4 (5)	--
13	0.5 (10)	0.9 (5)	--
14	2.8 (10)	0.7 (5)	--
15	1.2 (9)	0.0 (4)	--
16	0.4 (10)	--	--
17	0.9 (8)	--	--
18	-0.4 (8)	--	--

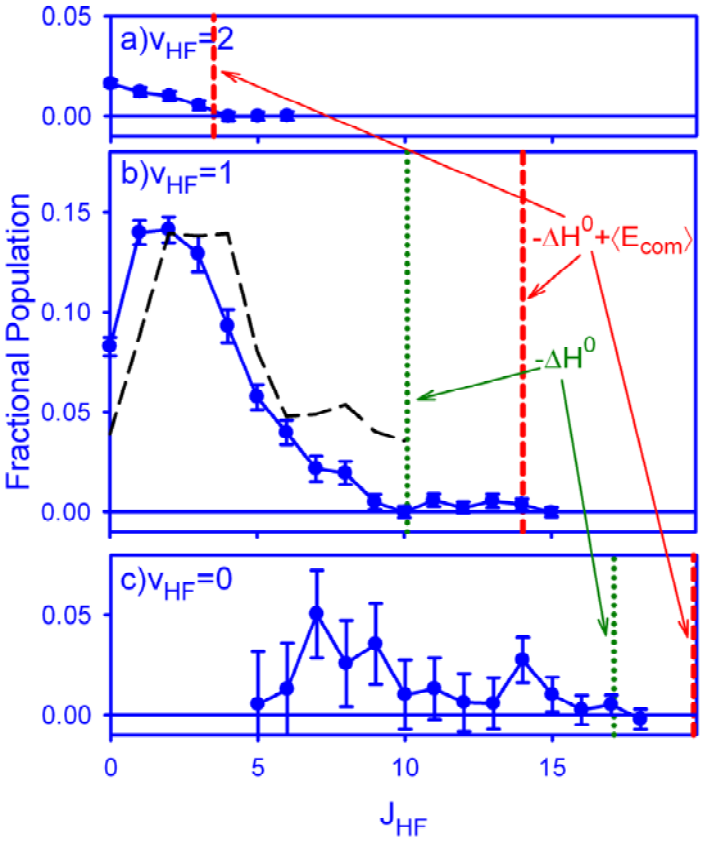

Figure 4.7 Observed nascent HF(v,J) populations produced by the F + H_2O reaction. Vertical lines represent the energetic limit based on the reaction energy (dotted) and the reaction energy plus the experimental collision energy (dashed). Long dashed line in (b) represents a scaled HF(v = 1) distribution from the arrested relaxation study in Ref. 28.

4.4 Discussion

The HF product distribution, summarized in Fig. 4.8, reveals significant rovibrational excitation of the nascent HF fragment following the reaction F + H_2O. The most populated manifold is v = 1, and significant rotational excitation is observed in the v = 0 and v = 1 populations. The general trends in the observed population distribution are discussed in this section.

Summing over the rotational levels produces HF vibrational branching ratios into v = [0, 1, 2] of [0.21(6), 0.75(2), 0.046(6)]. Predominant formation in the highest thermochemically accessible vibrational manifold, HF(v = 1), is in agreement with Polanyi rules[48,49] for exoergic reactions with early barriers, i.e. reactions characterized by reactant-like geometries (large F–H distance) at the transition state. The high proportion of vibrationally excited HF confirms the spectator nature of the OH fragment, which acts as an insignificant heat sink when compared to the highly excited HF. The present results are also in good agreement with the [0.24, 0.76, 0.00] vibrational branching estimates of Wickramaaratchi *et al*.,[38] who used a surprisal analysis of the F + D_2O reaction to infer the v = 0 population for F + H_2O. The agreement between predicted and observed branching ratios reflects favorably on the use of information theoretic treatments to predict qualitatively vibrational partitioning into the nascent HF bond.

Interestingly, the present experimental conditions result in about 5% of the observed HF population being formed in v = 2, which represents the first experimental observation of HF product in this manifold. Earlier reactive studies[36-38] at thermal collision energies ($kT \approx 0.6$ kcal/mol) found no detectable v = 2 product, consistent with total available energy constraints. However, recent estimates place the barrier for reaction at 4–5 kcal/mol,[27,35] so any reactions seen previously must have occurred either i) due to the "tail" of the thermal collision energy distribution or ii) via quantum tunneling through the barrier. If tunneling were the dominant

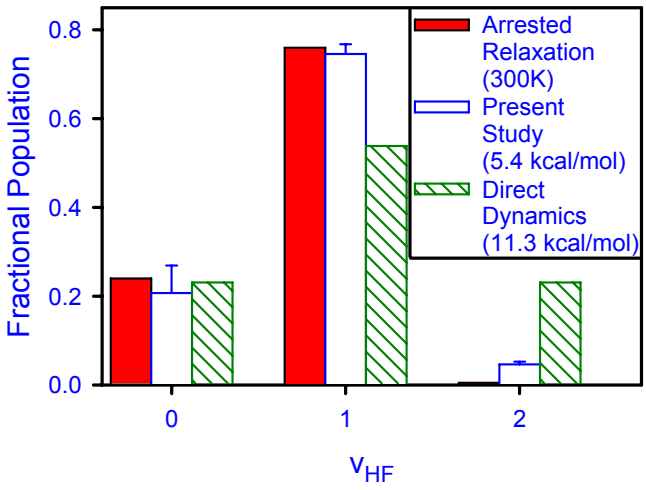

Figure 4.8 The vibrational branching for HF product found via: i) information theory estimates in the arrested relaxation experiments in Ref. 38 (solid bars), ii) measured in the present study (unfilled bars), and iii) calculated using direct dynamics from the F–H_2O anion geometry in Ref. 40 (striped bars). The energy in excess of the F + H_2O reactant asymptote due to experimental collision energy or initial theoretical geometry is indicated in parenthesis.

channel under thermal conditions, then the $v = 2$ manifold would *not* have been energetically inaccessible. Alternatively, thermal reactions may be dominated by improbably energetic collisions, in which case branching into the HF($v = 2$, J) manifold may have been present below the previous detection sensitivity.

In the present study, the higher crossed jet collision energies guarantee a high probability of exceeding the classical barrier. Since the energetic threshold for formation of HF($v = 2$) exceeds the reaction enthalpy by $\Delta E \approx 4.5$ kcal/mol, the extra energy needed to create $v = 2$ population in the present study arises from the reactant's $E_{com} \approx 5.4(1.3)$ kcal/mol COM collision energy. Such efficient coupling of reactant translational energy into product internal degrees of freedom has been observed previously in the reaction of F + HCl $\rightarrow$ HF + Cl,[46] another system characterized by a moderately large ($E^{\dagger} \approx 4$ kcal/mol) and early barrier. A simple physical picture for the coupling of reactant translational energy into product internal energy is based on the shifting nature of the reaction coordinate, which enables the barrier to be accessed via reactant translation and closely resembles H–F vibration after the saddle point. Thus, the energy used to overcome the barrier can readily couple into product internal energy, in accordance with early barrier expectations.[48,49]

Supporting theoretical evidence for significant formation into HF($v = 2$) population at these higher energies has previously been reported via direct dynamics studies by Ishikawa *et al*.[40] These trajectory simulations were started near the FH_2O^- ion complex minimum-energy geometry (found to be near the transition state region) in order to simulate dynamics following electron photodetachment from the negative ion complex. Starting geometries were found to be 11.3 kcal/mol above the reactant asymptote, corresponding to an additional 5–6 kcal/mol more incident collision energy than available in the present experimental study. As expected, these higher energies lead to a larger proportion of HF forming in the ($v = 2$) manifold, reported as HF [$v = 0, 1, 2$] branching ratios of [0.23, 0.54, 0.23].

Trends for HF(v) branching in the three vibrationally resolved studies of the F + H_2O reaction are summarized in Fig. 4.8. With increasing energy with respect to the transition state (due to either E_{com} or photodetachment starting geometry), the HF(v = 2) fractional population grows, primarily at the expense of HF(v = 1). This trend is easily rationalized by the near thermoneutral energetics for HF (v = 2) formation; small increases in the total energy enable the channel to open, with population efficiently coupled into this manifold by early barrier dynamics.

As mentioned previously, total vibrational branching ratios in the F + D_2O and F + H_2O arrested relaxation studies could only be inferred from surprisal analysis of the data, which permitted the IR non-emitting DF(v = 0) and HF(v = 0) populations to be estimated indirectly. Indeed, we have performed a similar statistical analysis (as described in Ref. 50,51) on the three different vibrationally resolved data sets (the present study, direct dynamical calculations,[40] and the F + D_2O chemiluminescence study[38]). The results yield linear plots with essentially identical slopes, consistent with vibrational ratios matching a simple one-parameter surprisal model at each of the various total energies. A more detailed description of these information theory analyses is presented in Appendix D.

The degree of rovibrational excitation of the HF product measured in the present experiment provides some information on the corresponding quantum states populated in the OH cofragment. For example, based on the energy level diagram in Fig. 4.1, HF (v = 2) population can only be accessed for the corresponding OH in its ground vibrational state. Similarly, formation of both OH(v = 1) and HF(v = 1) is just barely energetically allowed, which would leave insufficient energy for the high rotational excitation noted in HF(v = 1). Additionally, such a channel would also be inconsistent with the broad Doppler lineshapes observed in the HF (v = 1) manifold, which reveal a significant fraction of the remaining reaction exothermicity flowing into product translational recoil. Thus, a conservative upper limit of the 21(5)% product branching into OH (v = 1) can be attributed to co-formation of HF (v = 0). This estimate greatly exceeds the < 1% OD (v = 1):OH(v = 0) vibrational populations observed in F + D_2O/H_2O via

LIF.[33,34] Such results match Frank-Condon considerations of the *ab initio* transition state geometry for F–H_2O, where the non-reactive OH bond length of 0.971 Å closely matches the 0.970 Å bond length of the OH radical product,[27] such that the unbroken OH bond is anticipated to be a spectator to the reaction.

The HF rotational distributions presented in Fig. 4.7 reveal several features of dynamical interest. First of all, in comparison with the *hot* vibrational branching into HF vibrational states, the rotational populations are *relatively* cool but still quite energetically excited. Indeed, of the 23 kcal/mol energy available, 41% or $\langle E_{vib} \rangle \approx 9.5(0.3)$ kcal/mol is deposited in HF vibration, while the average rotational excitation is only $\langle E_{rot} \rangle \approx 2.1(0.4)$ kcal/mol. Secondly, appreciable population is observed in rovibrational states *higher* than the 17.61(2) kcal/mol exothermicity, due to efficient funneling of the incident collision energy ($E_{com} \approx 5$ kcal/mol) into internal energy of the products. Specifically, the thermochemical limit can only populate HF in the $v = 1$ manifold up to $J = 10$, above which finite population is observed up to the total energy limit above $J = 14$. Indeed, such collision-energy assisted, endoergic reactions are responsible for all population found in the HF($v = 2$) manifold, as discussed above. The $v = 2$ rotational populations are quite cold and decrease rapidly with increasing J, up to $J = 4$, which is inaccessible at the average collision energy employed. Conversely, the observed HF ($v = 0$, J) rotational states are quite hyperthermal, with progressions extending up to the energetic limit at HF($v = 0$,$J = 17$). These trends match simple energetic expectations for populating *higher* rotationally excited states in *lower* vibrational manifolds (and *vice versa*).

Interestingly, the current HF($v = 1$, J) rotational distribution is remarkably similar to, though slightly colder than, what was observed previously using IR chemilluminescence,[37] reproduced as the long dashed lines in Fig. 4.7. The main difference between the two distributions is that the crossed jet population decreases rapidly above $J \approx 5$, resulting in a lower average rotational energy of 1.3(0.2) kcal/mol versus > 1.6 kcal/mol for the previous study, whose

population is not reported above $J = 10$. This similarity seems to vindicate earlier studies. However, the level of agreement is also surprising, since these arrested relaxation measurements were performed at rather different thermal ($E_{com} \approx 0.6$ kcal/mol) versus crossed jet [$E_{com} \approx$ 5.4(1.3) kcal/mol] collision energies, and with an approximately 1000-fold increase in gas density and secondary collision probability. Thus, the quite similar, yet slightly cooler, HF($v = 1$) rotational distributions may simply be the dynamical signature of the threshold HF($v = 2$) channel opening up energetically in the crossed beam and not observed via arrested relaxation methods. More theoretical work will clearly be useful to help confirm or refute such a possible mechanism.

The nascent HF($v = 1,2$) rotational distributions are found to be significantly non-thermal, as revealed by the Boltzmann plots in Fig. 4.9. On one hand, the HF($v = 2$) rotational distribution shown in Fig. 4.9(a) appears quite cold, with most of the populated states falling on a 150 K slope preceding a sudden increase for the $J = 0$ state. Cold rotations in HF($v = 2$) are to be anticipated because accessing this manifold requires translationally *endoergic* reactive collisions and the additional energy needed to populate high J states is not available. On the other hand, the strongly non-thermal HF($v = 1$) rotational distribution contains significantly hotter components, as shown in the Boltzmann plot in Fig. 4.9(b). The curvature of this plot is qualitatively reproduced by a two-temperature fit to the data, corresponding to components with 180 K at low J and ≈ 1200 K at high J.

Similar rotational distributions, characterized by a near-thermal component at low J and hyperthermal decaying populations at high J, have previously been observed in polyatomic scattering dynamics.[21,47,52-54] In the present study, 33% of the HF population is found in states with more than 400 cm^{-1} rotational energy, due to the slowly decaying distribution in HF($v = 1$) and the broad HF($v = 0$) distribution peaked near $J = 7$–9. Indeed, HF rotation contains dynamical signatures that are not readily anticipated from statistical considerations, as shown by the nonlinear surprisal plots presented in Appendix D.

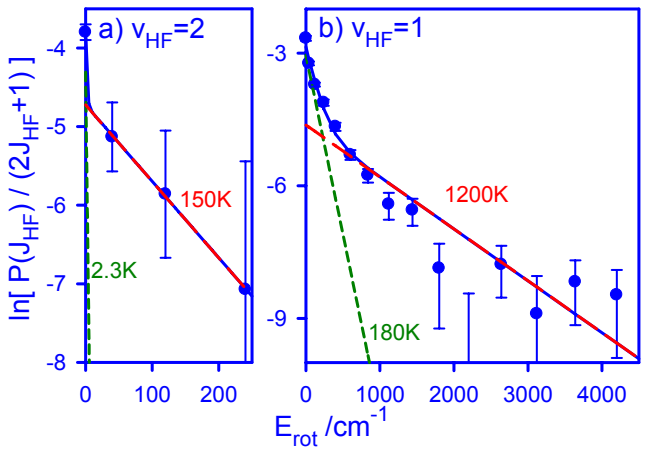

Figure 4.9 Boltzmann analysis of the HF product rotational populations in a) the $v_{HF} = 2$ and b) $v_{HF} = 1$ manifolds. Dashed lines represent thermal distributions, as labeled. Significant curvature in the observed distributions motivates fitting to the sum of two such thermal distributions, the total fit indicated by the solid line.

The structured rotational distributions may indicate multiple dynamical constraints, as opposed to a single constraint that might lead to a linear surprisal plot. Alternatively, the curvature in Fig. 4.9(b) may be caused by dynamical branching in the reaction mechanism, for example, between ground ($^2\Pi_{3/2}$) and excited ($^2\Pi_{1/2}$) states of the OH product. Both of these electronic states have been observed via LIF studies of the OH and OD products following the reactions F + D_2O/H_2O, and it is conceivable that branching between electronic channels might also correlate with hotter and cooler rotational distributions of the HF coproduct. However, future work will clearly be necessary to further elucidate possible non-adiabatic dynamics on the HF fragment's energy distribution.

Nonetheless, several physically motivated models anticipate highly rotationally excited HF. We consider two mechanisms, differing by when, during the course of reaction, the HF bond receives the torque necessary to create $J > 9$ states with more than 5 kcal/mol rotational energy. One possible answer is that the torque occurs near the transition state. Highly bent transition state geometries, such as the 103° F–H–O bond in the present reaction system,[56] offer one efficient mechanism for coupling reaction exothermicity into rotation of the nascent diatomic bond.[49] An alternative interpretation arises from the large dipole moments of both OH and HF fragments, which result in strong dipolar forces between diatoms in the ≈ 5.5 kcal/mol product channel well. Previous direct dynamical studies[21] have found sufficient dipole-dipole interaction in polyatomic exit channel dynamics to excite significantly product rotations well past the transition state region of the PES. Distinguishing between these two mechanisms would be an interesting avenue for future theoretical study and a clear step toward fundamental understanding of four-atom polyatomic reaction dynamics.

4.5 Conclusions

The F + $H_2O \rightarrow HF(v,J)$ + OH reaction has been studied by probing the nascent HF rovibrational distribution under single-collision crossed molecular jet conditions using IR laser spectroscopy. The results are summarized and discussed in light of recent *ab initio* characterization of the reaction path and transition state geometry. This study represents the first directly measured HF vibrational populations for this reaction, which are found to be highly inverted, consistent with a large F–H distance comparable to "early barrier" transition state geometry. These results generally agree with previous predictions, with branching into the threshold HF(v = 2) manifold highly sensitive to the total system energy. HF rotational energy increases monotonically as vibrational quanta decrease. The HF(v = 2,J) rotational distributions prove to be quite cold, reflecting endothermic formation of v = 2 made possible by additional incident kinetic energy in the crossed beam. The HF(v = 1,J) state distributions also exhibit hyperthermal rotational structure that extends out to the energetic limit. Two possible mechanisms, one due to energy release away from a strongly bent F–H_2O transition state geometry and the other induced by strong dipole-dipole interactions in the product well, are proposed to explain the propensity toward high J.

References for Chapter IV

1 R. B. Metz, J. D. Thoemke, J. M. Pfeiffer, and F. F. Crim, J. Chem. Phys. **99**, 1744 (1993).

2 M. Brouard, I. Burak, S. Marinakis, L. R. Lago, P. Tampkins, and C. Vallance, J. Chem. Phys. **121**, 10426 (2004).

3 A. Sinha, M. C. Hsiao, and F. F. Crim, J. Chem. Phys. **92**, 6333 (1990).

4 A. Sinha, M. C. Hsiao, and F. F. Crim, J. Chem. Phys. **94**, 4928 (1991).

5 S. Yan, Y. T. Wu, and K. P. Liu, Phys. Chem. Chem. Phys. **9**, 250 (2007).

6 J. B. Liu, B. Van Devener, and S. L. Anderson, J. Chem. Phys. **119**, 200 (2003).

7 J. R. Fair, D. Schaefer, R. Kosloff, and D. J. Nesbitt, J. Chem. Phys. **116**, 1406 (2002).

8 B. R. Strazisar, C. Lin, and H. F. Davis, Science **290**, 958 (2000).

9 C. Kreher, J. L. Rinnenthal, and K. H. Gericke, J. Chem. Phys. **108**, 3154 (1998).

10 K. Kudla and G. C. Schatz, Chem. Phys. **175**, 71 (1993).

11 M. J. Bronikowski, W. R. Simpson, B. Girard, and R. N. Zare, J. Chem. Phys. **95**, 8647 (1991).

12 J. M. Pfeiffer, R. B. Metz, J. D. Thoemke, E. Woods, and F. F. Crim, J. Chem. Phys. **104**, 4490 (1996).

13 J. D. Thoemke, J. M. Pfeiffer, R. B. Metz, and F. F. Crim, J. Phys. Chem. **99**, 13748 (1995).

14 M. C. Hsiao, A. Sinha, and F. F. Crim, J. Phys. Chem. **95**, 8263 (1991).

15 D. H. Zhang, M. H. Yang, and S. Y. Lee, Phys. Rev. Lett. **89**, 283203 (2002).

16 R. P. A. Bettens, M. A. Collins, M. J. T. Jordan, and D. H. Zhang, J. Chem. Phys. **112**, 10162 (2000).

17 D. H. Zhang, J. Chem. Phys. **125**, 133102 (2006).

18 D. H. Zhang and J. Z. H. Zhang, J. Chem. Phys. **99**, 5615 (1993).

19 K. Bolton, W. L. Hase, and G. H. Peslherbe, in *Modern Methods for Multidimensional Dynamics Computations in Chemistry*, edited by D. L. Thompson (World Scientific, River Edge, NJ, 1998), pp. 143.

20 W. Chen, W. L. Hase, and H. B. Schlegel, Chem. Phys. Lett. **228**, 436 (1994).

21 S. Rudic, C. Murray, J. N. Harvey, and A. J. Orr-Ewing, J. Chem. Phys. **120**, 186 (2004).

22 E. Uggerud and T. Helgaker, J. Am. Chem. Soc. **114**, 4265 (1992).

23 G. H. Peslherbe and W. L. Hase, J. Chem. Phys. **100**, 1179 (1994).

24 R. T. Skodje, D. Skouteris, D. E. Manolopoulos, S. H. Lee, F. Dong, and K. P. Liu, Phys. Rev. Lett. **85**, 1206 (2000).

25 R. von Glasow and P. J. Crutzen, in *Treatise on Geochemistry*, edited by R. F. Keeling, H. D. Holland, and K. K. Turekian (Elsevier Pergamon, Amsterdam, 2003), Vol. 4, pp. 347.

26 D. A. Neufeld, J. Zmuidzinas, P. Schilke, and T. G. Phillips, Astrophys. J. **488**, L141 (1997).

27 M. P. Deskevich, D. J. Nesbitt, and H. J. Werner, J. Chem. Phys. **120**, 7281 (2004).

28 S. A. Harich, D. W. H. Hwang, X. F. Yang, J. J. Lin, X. M. Yang, and R. N. Dixon, J. Chem. Phys. **113**, 10073 (2000).

29 W. T. Zemke, W. C. Stwalley, J. A. Coxon, and P. G. Hajigeorgiou, Chem. Phys. Lett. **177**, 412 (1991).

30 B. P. Stoicheff, Can. J. Phys. **79**, 165 (2001).

31 A. Schiffman, W. B. Chapman, and D. J. Nesbitt, J. Phys. Chem. **100**, 3402 (1996).

32 W. B. Chapman, B. W. Blackmon, S. Nizkorodov, and D. J. Nesbitt, J. Chem. Phys. **109**, 9306 (1998).

33 M. Ziemkiewicz, M. Wojcik, and D. J. Nesbitt, J. Chem. Phys. **123**, 224307 (2005).

34 M. Ziemkiewicz and D. J. Nesbitt, manuscript in preparation.

35 P. S. Stevens, W. H. Brune, and J. G. Anderson, J. Phys. Chem. **93**, 4068 (1989).

36 H. W. Chang, D. W. Setser, M. J. Perona, and R. L. Johnson, Chem. Phys. Lett. **9**, 587 (1971).

37 W. H. Duewer and D. W. Setser, J. Chem. Phys. **58**, 2310 (1973).

38 M. A. Wickramaaratchi, D. W. Setser, H. Hildebrandt, B. Korbitzer, and H. Heydtmann, Chem. Phys. **94**, 109 (1985).

39 X. Yang, X. B. Wang, and L. S. Wang, J. Chem. Phys. **115**, 2889 (2001).

40 Y. Ishikawa, T. Nakajima, T. Yanai, and K. Hirao, Chem. Phys. Lett. **363**, 458 (2002).

41 R. B. Leblanc, J. B. White, and P. F. Bernath, J. Mol. Spectrosc. **164**, 574 (1994).

42 G. Herzberg, *Infrared and Raman Spectra of Polyatomic Molecules*. (D. Van Nostrand Company, New York, 1945).

43 E. Arunan, D. W. Setser, and J. F. Ogilvie, J. Chem. Phys. **97**, 1734 (1992).

44 D. M. Sonnenfroh and K. P. Liu, Chem. Phys. Lett. **176**, 183 (1991).

45 H. W. Cruse, P. J. Dagdigian, and R. N. Zare, Faraday Discuss. **55**, 277 (1973).

46 A. M. Zolot and D. J. Nesbitt, J. Chem. Phys. **127**, 114319 (2007).

47 W. W. Harper, S. A. Nizkorodov, and D. J. Nesbitt, J. Chem. Phys. **113**, 3670 (2000).

48 J. C. Polanyi and W. H. Wong, J. Chem. Phys. **51**, 1439 (1969).

49 J. C. Polanyi, Accounts Of Chemical Research **5**, 161 (1972).

50 R. D. Levine and R. B. Bernstein, *Molecular Reaction Dynamics and Chemical Reactivity*. (Oxford University Press, New York, 1987).

51 J. T. Muckerman, J. Phys. Chem. **93**, 179 (1989).

52 D. Troya, J. Chem. Phys. **123**, 214305 (2005).

53 J. F. Castillo, F. J. Aoiz, L. Banares, E. Martinez-Nunez, A. Fernandez-Ramos, and S. Vazquez, J. Phys. Chem. A **109**, 8459 (2005).

54 E. S. Whitney, A. M. Zolot, A. B. McCoy, J. S. Francisco, and D. J. Nesbitt, J. Chem. Phys. **122**, 124310 (2005).

55 J. J. Valentini, J. Phys. Chem. A **106**, 5745 (2002).

56 M. P. Deskevich, M. Y. Hayes, K. Takahashi, R. T. Skodje, and D. J. Nesbitt, J. Chem. Phys. **124**, 224303 (2006).

Chapter V Reactive scattering dynamics at the gas-liquid interface: Studies of F + squalane ($C_{30}H_{62}$) (liquid) via high-resolution infrared absorption of product HF(*v,J*)

5.1 Introduction

Many practical chemical processes depend upon interactions at the gas-liquid interface, including distillation, gas chromatography, biological respiration, and atmospheric chemistry on aerosols and in bulk liquids. Despite such broad implications, relatively little is known about elementary processes at the gas-liquid interface. In contrast, a much deeper level of understanding has been established for gas-phase collision dynamics, where fundamental processes can be studied in isolation and compared to high-level theoretical models. Molecular dynamics at the surface of crystalline solids have also been probed in detail, largely motivated by interest in processes such as heterogeneous catalysis and corrosion. Dynamics in both gas phase and at gas-solid interfaces have proven more accessible due to their inherent compatibility with vacuum and relative theoretical accessibility via computational methods. Despite these additional challenges, there remains a keen motivation for study of comparable inelastic and reaction dynamics at the gas-liquid interface.

Fenn and coworkers[1] were the first to study the dynamics of gases scattering from liquid surfaces using low vapor pressure liquids for molecular beam scattering studies. Nathanson and coworkers have spearheaded the next generation of liquid scattering dynamics via flight-time measurements of scattered species with mass spectroscopic detection.[2-6] Minton and coworkers used similar methods to investigate reactive and inelastic scattering of Cl and O atoms from liquid hydrocarbon surfaces.[7-10] The first quantum-state resolved studies were performed by

McCaffery and coworkers, who detected I_2 scattered from various liquids by laser induced fluorescence (LIF).[11-14] McKendrick and coworkers have also utilized LIF to study reactions of O atoms with liquid hydrocarbon surfaces.[15-22] Our group has developed the use of high resolution IR absorption methods to probe *inelastic* scattering of CO_2 from a series of perfluorinated, hydrocarbon and hydrogen bonded liquids.[23-28] In this chapter, similar methods have been applied to reactive scattering dynamics, using a modification of the crossed jet apparatus that was the focus of the previous two chapters.

From these efforts, a general picture for scattering dynamics at the gas-liquid interface has begun to emerge. The observations fit broadly into one of two mechanisms: *trapping desorption* (TD), characterized by Boltzmann velocity and rotational state distributions matching the liquid temperature, and *impulsive/direct reactive scattering* (DRS), in which recoiling molecules retain a large fraction of their incident rotational and translational energy. Significantly, molecular vibrations are largely decoupled from the surface temperature in either TD or DRS scattering channels, indicating poor equilibration and suggesting an upper limit for surface interaction on the 10–100 ps time scale for intermolecular vibrational energy transfer.

In comparison to inelastic scattering, reactions at the gas-liquid interface have only recently begun to be characterized. Minton and coworkers used mass spectrometry to study the reactions of Cl, O, and O_2 with liquid squalane at 5–125 kcal/mol collision energies.[7-10] McKendrick and coworkers found modest vibrational excitation of OH formed by reaction of O atoms with various hydrocarbons,[15-22] and the $v = 1$ rotational temperature was found to be colder than that for $v = 0$, particularly when the fast moving products were selectively probed.[22] Excited vibrational population was found to increase with surface temperature[19] and depend on the particular liquid reactant,[18] trends ascribed to changes in the surface structure that influences secondary collisions with the liquid following reaction. Thus, both vibrational and rotational excitation strongly depends upon the degree to which product-surface interactions lead to energy transfer into the surface.

Previous studies of nearly thermoneutral full[7-10,15-20,22,29] or half[30-33] reactions at the gas-liquid interface have exploited either high incident translational energy or photolysis energy, respectively, and revealed that product molecules generally retained some fraction of the initial excitation. By way of contrast, the present study of H atom abstraction by F atoms at the liquid squalane surface is conducted at approximately thermal collision energies, though the reaction is highly exothermic. Fig. 5.1 schematically represents possible mechanisms for producing gas-phase HF following reaction at the gas-liquid interface. The important features are that incident or adsorbed F atoms (a, c in Fig. 5.1) may react and immediately eject product HF (b, c), or they may suffer one or more collisions with the surface (d, e) before desorbing (f). Competition between such direct or multiple encounters directly impacts the translational and internal energy of the recoiling products, as can be characterized spectroscopically using Doppler resolved infrared absorption spectroscopy.

The multitude of reactive sites in the liquid reactant complicates discussion of the reaction energetics, as summarized in Fig. 5.2 and Table 5.1. For H atom abstraction from any of the three types of C–H bonds present (primary, secondary or tertiary) HF product may be formed anywhere from v = 0–3, with correspondingly higher rotational levels accessible for the lower vibrational manifolds. The energetic threshold for HF(v = 4) formation exceeds the reaction exothermicity even for the most weakly bound tertiary C–H site, though these products become accessible with an additional 2.3 kcal/mol excitation. Based on the corresponding gas-phase dynamics (i.e., "Polanyi rules"[36]), one would anticipate DRS to couple energy most efficiently into the newly formed HF bond. In the TD mechanism, HF may remain trapped on the surface long enough to accommodate thermally with the bulk prior to desorption, in which case the nascent reaction dynamics may be obscured. The present study reveals an energetic partitioning *between* the DRS and TD extremes, interpreted with respect to the time-scale for desorption following reactions at the gas-liquid interface.

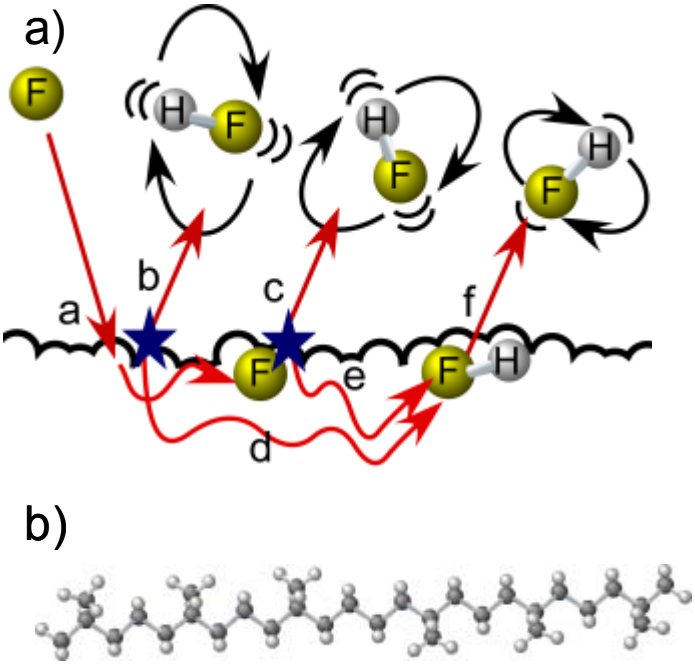

Figure 5.1 a) Possible reactive encounters between reactant F atoms and a liquid hydrocarbon interface. Incident F atoms (a) may react immediately upon contact (b), or after absorbing at the interface (c). HF product may recoil directly into the gas phase (b,c), or may remain trapped (d,e) before desorbing (f). b) The chemical structure of squalane, a saturated hydrocarbon with a 24-carbon backbone and six symmetrically placed methyl side groups.

Table 5.1 Bond strengths and exothermicities for hydrogen abstraction by fluorine atoms for various C–H bonds. The average F + squalane exothermicity has been estimated by weighting according to the number of C–H bonds (N_H) and functional groups (N_{CHx}) in squalane. Uncertainties in parenthesis are one standard deviation.

CH bond order	D_0 (kcal/mol)	ΔH_{rxn} (kcal/mol)[a]	N_H	N_{CHx}
Primary	99.6(4)[b]	-35.7(4)	24	8
Secondary	96.9(3)[b]	-38.4(3)	32	16
Tertiary	95.0(4)[b]	-40.3(4)	6	6
Squalane[c]	97.7	-37.5		
Squalane[d]	97.3	-38.1		

[a] D_0(HF) = 135.27(1) kcal/mol from Ref. 34
[b] Based on Ref. 35
[c] D_0 as average for equal probability abstraction of all H atoms
[d] D_0 as average for equal probability abstraction from all CH_x groups

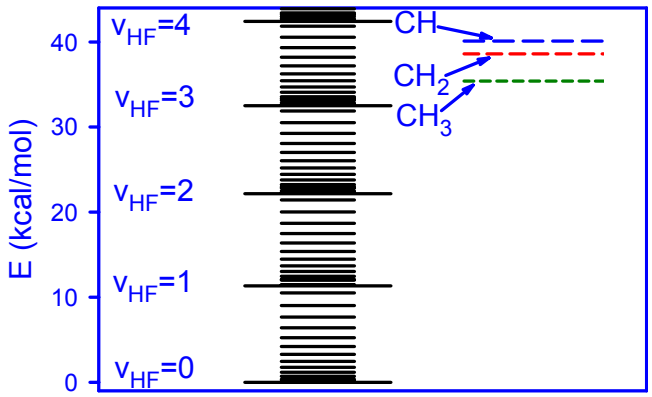

Figure 5.2 Energy level diagram for HF, along with the exoergicity for reaction of F atoms with different types of saturated hydrocarbon functional groups. Heterogeneous bond energies for the various C–H bonds result in approximately 5 kcal/mol uncertainty in the energy released following reaction of F with squalane. The 37–42 kcal/mol reaction energy is sufficient to access HF states with energy well above the $v = 3$, $J = 0$ level.

5.2 Static Liquid Experiment

The study employs the same high sensitivity IR laser spectrometer used in the previous two chapters and in other state resolved studies of gas-phase collision dynamics in crossed molecular jets.[37-42] As a first attempt to probe the interactions at the gas-liquid interface, a minimal alteration configuration was implemented by placing stagnant pool of liquid squalane (commercially purchased) under the F atom plasma jet source, as illustrated in Fig. 5.3.

At room temperature the vapor pressure of liquid squalane is $\approx 10^{-7}$ Torr, i.e., negligible compared to the $\approx 8\times10^{-7}$ Torr base pressure of the vacuum chamber. However, the chamber must be evacuated slowly (over the course of about one hour) from atmospheric pressure, in order to prevent rapid outgassing and consequent "bumping" of the liquid reactant. The F atom source is identical to that previously employed in crossed molecular jet studies, and described in detail in Ch. 2.3(A). During the experiment, the F atom source operates at 10 Hz, and the average chamber pressure rises to $\approx 1.0\times10^{-4}$ Torr. This low pressure prevents shocking in the supersonic expansion. The nascent nature of HF recoiling from the surface has also been directly verified, as discussed in more detail below.

A sample transient absorption waveform is shown in Fig. 5.4, recorded with an FCL frequency of approximately 3693.682 cm^{-1}, line center of the $v = 3\leftarrow2, J = 2\leftarrow1$ HF transition. The rising edge of the absorption occurs approximately 250 μs from the start of the F discharge (dotted line in Fig. 5.4), in excellent agreement with time of flight predictions based on the 14.5 cm nozzle-to-liquid path length and 5.73×10^4 cm/s supersonic expansion velocity. The inset of Fig. 5.4 emphasizes that the observed HF(v,J) signal duration is a convolution of the plasma current pulse duration (t_d) and the source-to-surface flight time spread due to the F atom velocity distribution. For short discharge pulses (< 250 μs), the peak HF absorption signal grows linearly with t_d. For longer discharge pulses (> 250 μs), the peak signals remain constant with a width of

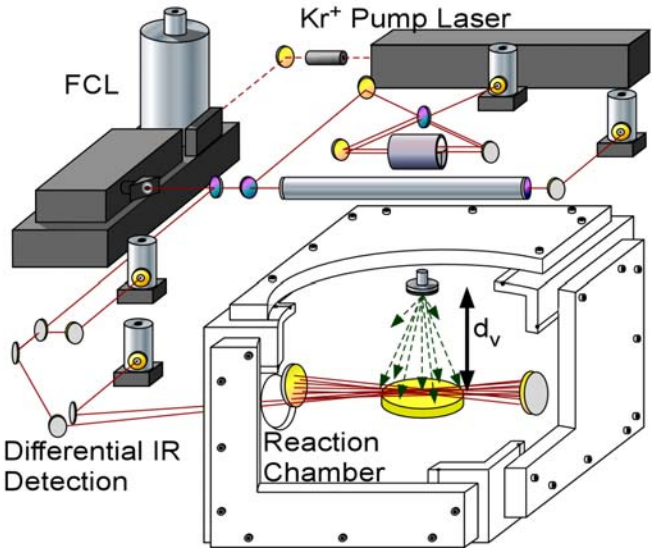

Figure 5.3 Schematic of the static liquid apparatus. A pulsed jet F atom source directs reactant at a shallow Pyrex container of squalane. The infrared laser multipass detects HF product 0.7 cm above the liquid surface with high resolution and ultra high sensitivity via direct absorption measurements.

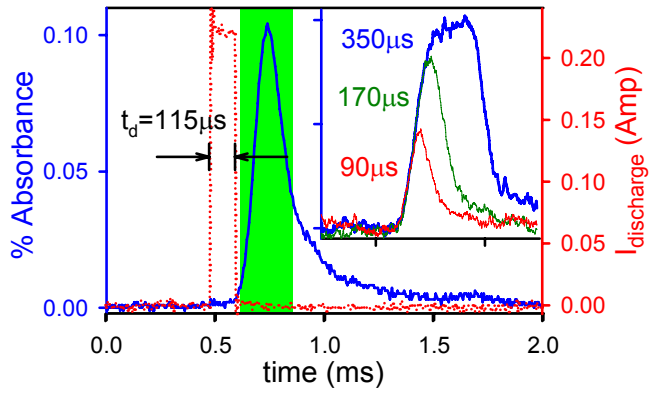

Figure 5.4 Representative transient IR absorption measurement of HF $v = 3 \leftarrow 2$, $J = 2 \leftarrow 1$, formed by reactive scattering of fluorine atoms from liquid squalane at 0.7(3) kcal/mol collision energy. The solid line is the measured absorption (left axis), and the dotted line is the plasma current in the F atom source (right axis), with duration t_d = 115 μs. Inset plots show the signal waveform as a function of t_d. The shaded region denotes the time domain of digital signal averaging used to construct HF absorption measurements.

approximately t_d. The limiting signal duration is readily anticipated from the 200(50) m/s FWHM of the F atom velocity distribution, measured separately using IR Doppler measurements of the F atom jet oriented nearly parallel the IR laser axis and doped with HF. A discharge width of t_d = 115 μs is utilized for the remainder of this study, corresponding to ≈ 70% of the maximum signal.

For the stagnant liquid surface study, the data is acquired in an identical fashion as in the gas-phase studies. Specifically, a transient recorder captures the time-dependent absorption and transfers it to a personal computer for analysis as described in Sect. 2.3(B). The signal under a 200 μs window centered on the peak HF signal, indicated by the shaded region in Fig. 5.4, is numerically averaged, and only this value is recorded as a function of laser frequency to construct the signal absorption profiles. Two such Doppler measurements, originating from different J states in the v = 2 manifold, are presented in Fig. 5.5.

Single-collision conditions at the gas-liquid interface are necessary for the determination of the nascent HF product state distribution. Placement of the nozzle orifice (≈ 0.01 cm^2) a large distance (14.5 cm) from the liquid ensures that the gas density is low at the surface. Under these conditions, secondary radical-radical interactions at the liquid surface are negligible due to an F atom coverage of approximately 0.001 monolayers per pulse. For these preliminary studies, reacted liquid molecules must diffusively mix into the bulk, a likely process on the macroscopic time scales for surface coverage. This concern is further allayed by the second-generation experiment, described in the following section, which employs an actively refreshed surface, for which similar results have been obtained, as discussed in Sect. 5.4. The experimental conditions are such that gas-phase interactions subsequent to reaction at the surface are also highly improbable, since the total gas density at the liquid surface is approximately 1.5×10^{13} #/cm^3, and the mean free path (≈ 10 cm) exceeds the 0.7 cm surface-probe distance by more than an order of magnitude.

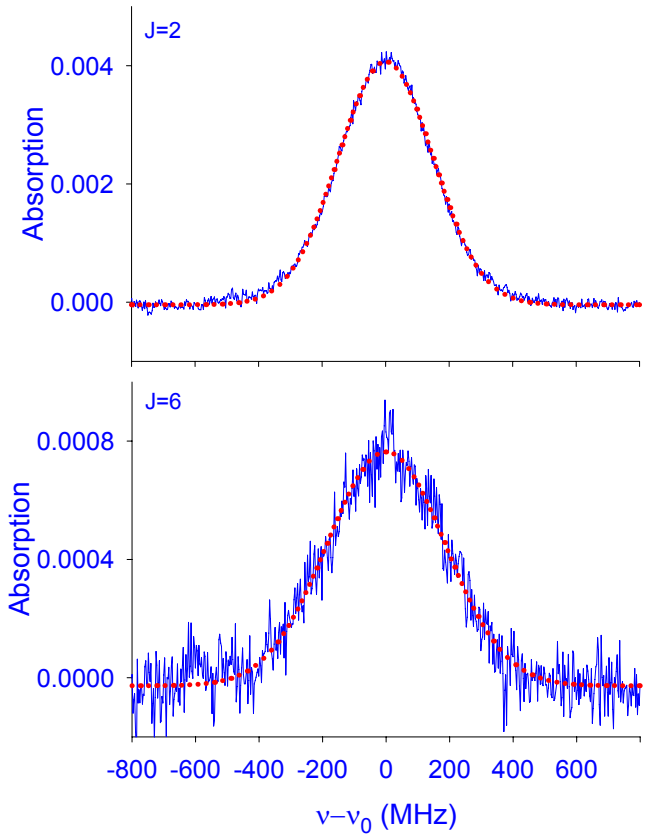

Figure 5.5 Representative HF Doppler measurements following reaction of F at a liquid squalane surface. Both lines are recorded on R-branch transitions originating from the v'' = 2 manifold, with J'' as indicated. Solid lines denote raw absorption measurements, and dotted lines are fits to Gaussian lineshape functions.

To establish nascent conditions unambiguously, the absorption profiles for transitions out of two rotational states shown in Fig. 5.5, the R-branch lines from J'' = 2 and 6 in v'' = 2, have been recorded at a series of nozzle-surface distances d_v, shown in Fig. 5.3. Since gas density varies with $1/d_v^2$, this quantity is used as the x-axis in Fig. 5.6. To quantify the HF translational energy, the measured profiles are fitted to a Gaussian function according to Eq. 2.20. The fitted widths $\Delta\nu$ are scaled to the transition frequency ν, yielding a quantity directly proportional to the velocity distribution's full width at half maximum (FWHM). This value remains constant over a ten-fold variation in the gas density, as shown in Fig. 5.6(a). Moreover, $\Delta\nu/\nu$ exceeds the value expected at the 300 K surface temperature, and the J = 6 state exhibits more translational excitation than J = 2. This trend for increasing translational energy release with increasing internal excitation is measured throughout and is discussed in more detail with the Doppler analysis presented in Sect. 5.5(B), where this correlation is further discussed. The density independence of these high-resolution Doppler widths confirms that the observed HF distributions are determined solely by nascent dynamics of the gas-surface reactive interaction and not by secondary gas-phase collisions.

The measured HF absorbance intensities corroborate this conclusion. As seen in Fig. 5.6(b), the integral signals grow linearly with $1/d_v^2$, as expected for signals linear in the F atom density. In particular, the maximally populated rotational state at 300 K is J = 2, and the signal from this state reveals no upward curvature with increasing density, which would be anticipated if thermal relaxation were significant. Furthermore, the relative intensity ratio of 0.23(3) between HF(v = 2, J = 6) and HF(v = 2 , J = 2) is significantly greater than the 0.07 value expected for a 300 K rotational distribution [dashed line in Fig. 5.6(b)], and the "hot" J = 6 density shows no evidence of decreasing with increasing gas density. The robust insensitivity of both translational and rotational energy distributions to the experimental conditions indicates that the measured HF state distributions can be confidently attributed to dynamics at the liquid surface. To be safe,

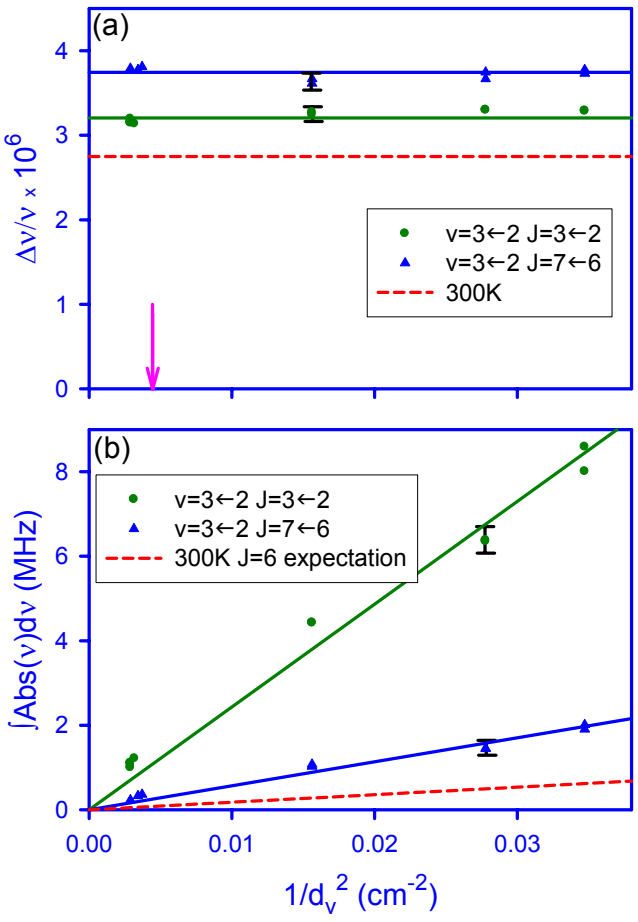

Figure 5.6 Jet density dependence of the observed HF absorption measurements, varied by changing the distance from the F source to the squalane surface, d_v. The total gas density scales with $1/d_v^2$, which is plotted along the abscissa. (a) Observed Doppler widths from Gaussian fits of the HF lines $v = 3 \leftarrow 2$, $J = 3 \leftarrow 2$ (circles) and $v = 3 \leftarrow 2$, $J = 7 \leftarrow 6$ (triangles). The FWHM of a 300 K distribution is plotted as a dashed line for comparison. The solid arrow indicates the density used for the remainder of this study. (b) HF integral absorption intensities for the same observations as in Fig. 5.5. Measured intensities scale linearly with gas density. The dashed line is the expected $J' = 6$ intensity relative to the measured $J' = 2$ slope for a 300 K rotational distribution. Error bars are representative of typical uncertainties.

however, the most conservative (i.e. lowest density) conditions are used for the remainder of the study, corresponding to $d_{v=}$ 14.5 cm, marked by arrow in Fig. 5.6(a), ≈ 1.5×10^{13} #/cm^3.

Nascent HF rovibrational quantum state distributions have been determined from Doppler profile measurements on all laser-accessible R and P branch rovibrational transitions connecting the $v + 1 \leftarrow v$ manifolds for v = 0,1,2,3. These measurements include a total of ≈ 300 Doppler scans, typically repeated at least three times for each line. Data are normalized to the HF(v = 3←2, J = 1←2) reference line to account for slowly drifting F atom production efficiency. As in previous studies, numerically integrating the Doppler profiles provides net absorption intensities for each spectral line, and the observed spectrum is fitted to obtain the HF(v,J) state resolved column densities. These nascent densities have been normalized and are displayed as populations in Fig. 5.7. Populations exhibit a simple rise and decay with increasing J state. However, closer inspection reveals a highly non-thermal HF distribution in J. More detailed analysis is delayed until Sect. 5.5, after the refreshed liquid surface experiment is described.

5.3 Continuously Refreshed Surface Experiment

Following the studies described in the previous section, a more sophisticated liquid surface has been implemented, as illustrated in Fig. 5.8. This renewed surface is based on the innovations of Fenn and co-workers[1,43] and the design has been taken from Perkins *et al.*[23] To continuously refresh the liquid interface, a 15 cm diameter glass disk rotates at 0.3 Hz through a copper reservoir containing 200 mL of commercially purchased squalane. The motion of the wheel viscously drags a layer of squalane from the reservoir, and a steel razor blade, mounted 0.5 mm from the glass disc surface, generates a uniform film of liquid while mechanically mixing the liquid at the surface. The IR probe passes ≈ 0.7 cm above the liquid 16 times via the Herriot multipass cell.[44]

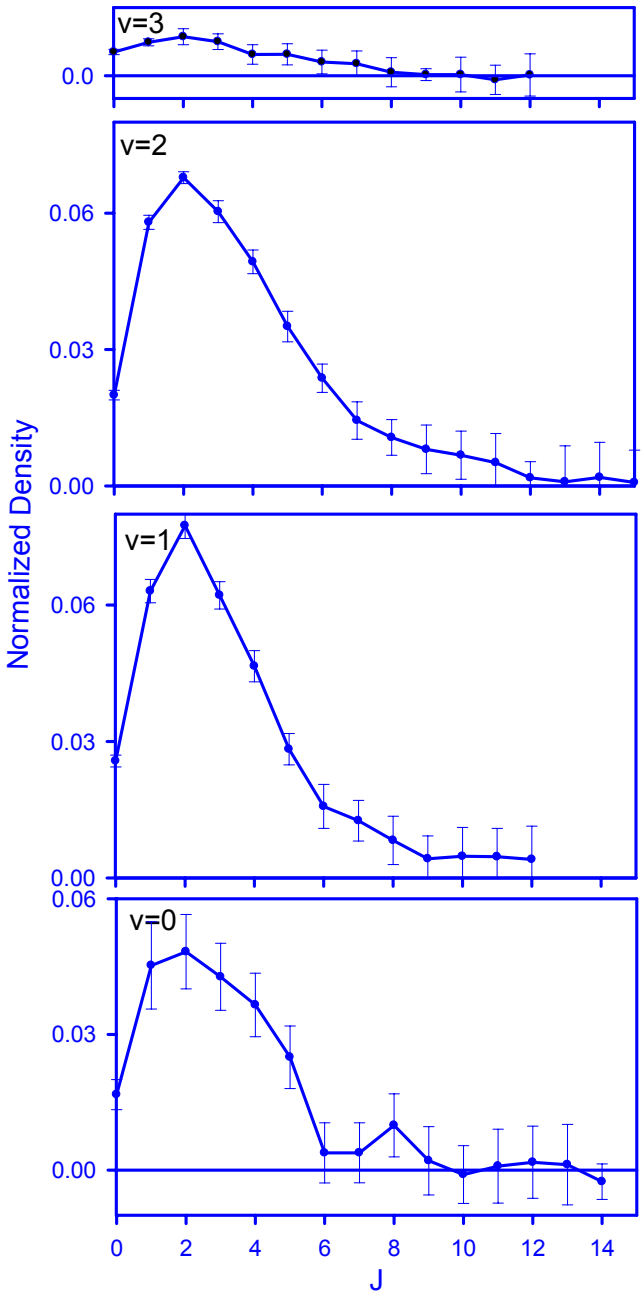

Figure 5.7 Normalized HF(*v,J*) density distributions, measured following reactive scattering of F atoms from a static liquid hydrocarbon surface.

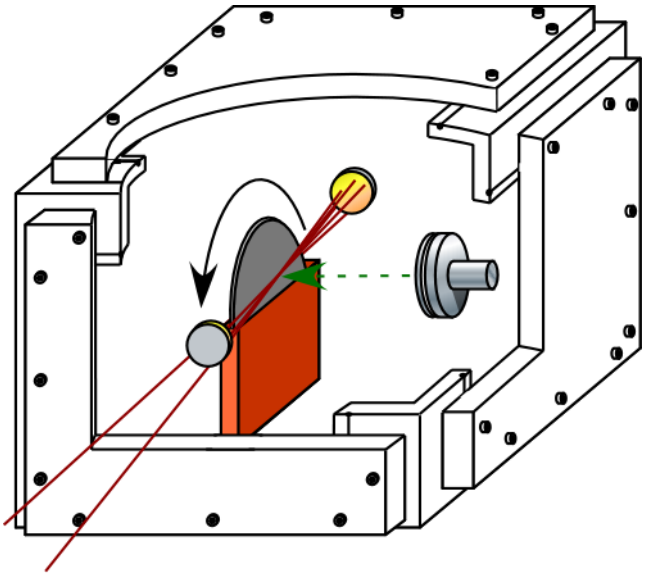

Figure 5.8 Schematic of the refreshed liquid apparatus. A rotating glass wheel is continuously recoated with liquid squalane as it passes through a trough of ≈ 100 mL liquid. The F source and IR detection are otherwise comparable to that depicted in Fig. 5.3.

Similar low-density conditions as used with the stagnant liquid studies ensure nascent HF populations scattering from the surface. Secondary radical-radical interactions at the liquid surface can be neglected due to the F atom coverage of approximately 0.001 monolayers per pulse. At the 0.3 Hz rotation rate of the wheel, the surface is exposed to < 2% of a monolayer of F prior to being mechanically mixed with the bulk in the liquid reservoir. Thus, the present results can be definitively attributed to the reactive scattering of isolated F atoms from squalane at the gas-liquid interface.

Sample absorption traces for detection of HF(v = 2,J = 1) product are presented in Fig. 5.9, along with the discharge current used for F atom generation. The 270 μs delay from the start of the discharge pulse to the rise of the HF absorption closely matches the expected 260(40) μs flight time for F atoms in a 573(85) m/s argon jet and the 15.0(1) cm valve-surface distance. The inset of Fig. 5.9 presents the time profiles for various t_d, comparable to those presented in Fig. 5.4. For the remainder of the present study, a discharge width of t_d = 200 μs is utilized, reflecting a compromise between signal intensity (≈ 70% of the long discharge maximum) and time resolution.

The fundamental experimental measurement consists of a series of IR absorption waveforms, such as those in the inset of Fig. 5.9, as a function of probe laser frequency. A fast digital acquisition card records the transient absorption waveform with a 500 kHz bandwidth, while the FCL tunes in 3 MHz steps through a ≈ 3 GHz window approximately centered on a given HF IR transition. Thus, raw data results in “three dimensional” measurement of absorption, as a function of laser frequency and time. 3D absorption profiles, such as the one presented in the false color intensity plot in Fig. 5.10, have been recorded for every HF transition probed, enabling reanalysis of various time windows to test for dynamical signatures as a function of time. For the majority of this study, the analysis has been performed on a 200 μs window located at the rising edge of the signal waveform, as shown in the shaded region of Fig. 5.9. However, alternative time

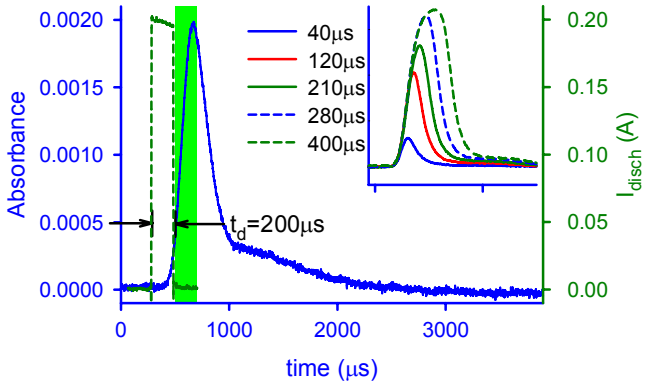

Figure 5.9 Transient IR absorption measurement of HF $v = 3 \leftarrow 2, J = 2 \leftarrow 1$, following reaction of fluorine atoms at the refreshed liquid surface. The solid line is the measured absorption (left axis), and the dashed line is the plasma current in the F atom source (right axis), with duration $t_d = 200$ ms. Inset plots show the signal waveform as a function of t_d. The shaded region denotes the time domain of digital signal averaging used to construct HF absorption measurements.

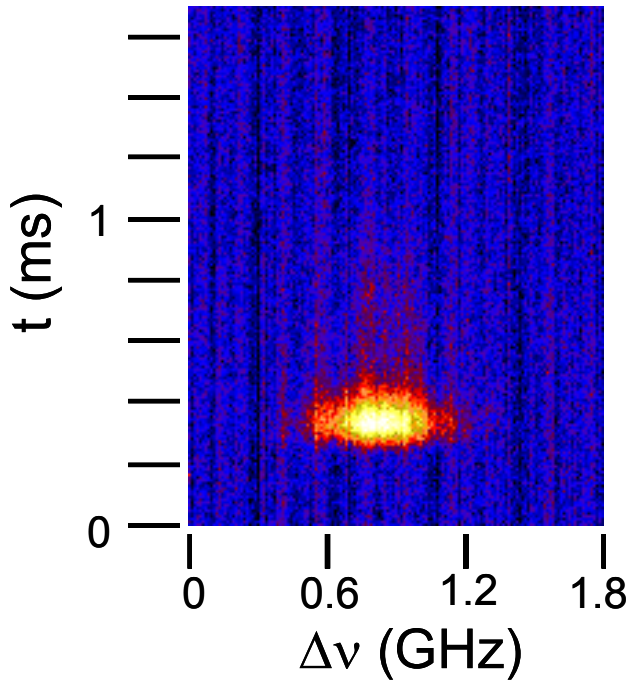

Figure 5.10 Sample 3D profile of the transition $v = 3 \leftarrow 2$, $J = 3 \leftarrow 2$ Infrared absorption is represented in false color, as a function of laser frequency (x axis) and time (y axis). Vertical line-outs result in waveforms such as those in Fig. 5.9, and time-domain averages produce Doppler profiles as in Fig. 5.1

windows were also considered and will be discussed in more detail in Sect. 5.4.

Representative Doppler measurements are presented in Fig. 5.11, from which certain features of the gas-liquid scattering experiment are immediately apparent. Many observed lines exhibit large intensities, with peak absorptions (Fig. 5.9) approaching 0.5%, or $\approx 10^{10}$ HF/cm^3 per quantum state. The rovibrational populations are broadly distributed in the $v = 0$–3 manifolds, with significant inversion in HF vibration. Since IR absorption directly measures population *differences* between upper and lower probed states, the HF lines can display either net absorption or gain, depending on whether absorption from the lower state or stimulated emission from the upper state is stronger. This competition is clearly illustrated in Fig. 5.11 by net *emission* signals observed for transitions involving the $v'' = 0$ lower level, as considered in more detail in Sect. 5.5. Nevertheless, the raw data illustrate that even with near-thermal collision energies, HF product does not remain trapped on the surface long enough to accommodate completely to the surface temperature, and a significant fraction of the reaction exothermicity remains in the recoiling gas-phase product.

Approximately 400 HF absorption profiles, such those shown in Fig. 5.11, have been observed, originating from all energetically accessible HF quantum states having transitions within the 2.5–3.3 μm tuning range of the FCL. In total, 87 transitions out of 59 quantum states have been probed, spanning $v = 0$–4 and J between 0 and 15. Integrating the Doppler measurements produces the "stick spectrum" of line intensities presented in Fig. 5.12(a). From the procedure detailed in Sect. 2.4(A), this spectrum is least squares fitted to obtain the HF(v,J) densities. The measured and fitted spectra agree within the 10 kHz experimental uncertainty of the measured intensities as shown in Fig. 5.12. The raw densities are presented in Table 5.2. These results are quite robust, as demonstrated in Fig. 5.13 and discussed next.

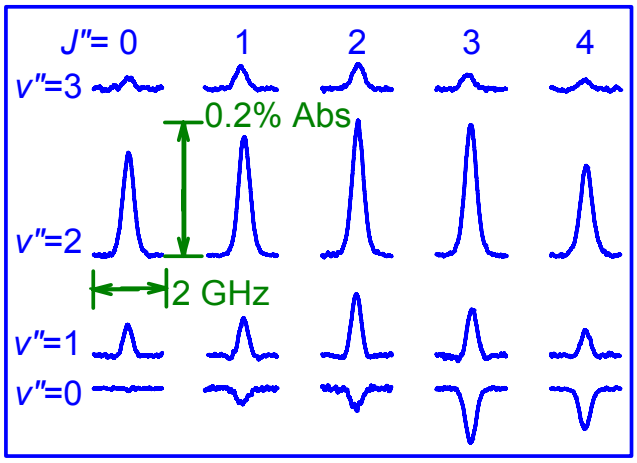

Figure 5.11 Sample Doppler resolved HF absorption measurements following reactive scattering from the liquid squalane surface.

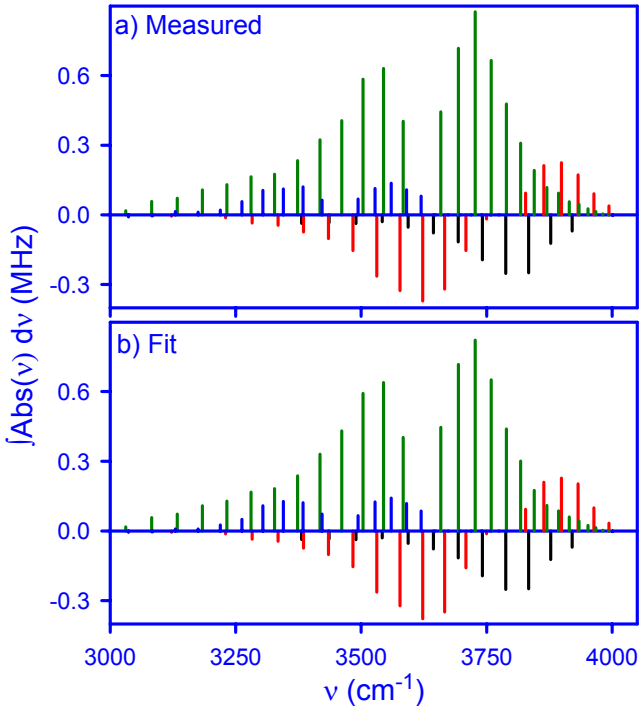

Figure 5.12 Stick spectrum of the measured (a) and fitted (b) HF spectral intensities following reaction of F at a liquid squalane surface. Shading indicates lower vibrational state as follows: blue (*v"* = 3), green (*v"* = 2), red (*v"* = 1), and black (*v"* = 0). Absorption features are plotted with positive amplitude, whereas net emission, created by population inversion on certain transitions, yields negative absorption.

5.4 Comparing Results

Three sets of normalized data for F + squalane are presented in Fig. 5.13. The dots with error bars are the "best set" data, i.e., the data acquired following scattering from the refreshed liquid surface, during the 200 μs rising edge of the transient absorption waveform, as described in detail in Sect. 5.3. The dashed line represents a reanalysis of the same raw data, where the time-averaging gate has been moved 100 μs later, to the peak of the transient absorption signal. This timing matches that used in the static liquid surface experiment, detailed in Sect. 5.2, the results of which are replotted as dotted lines.

Overall, remarkable agreement exists among the data in Fig. 5.13. Nearly identical results are obtained in both time windows, emphasizing that the observations are insensitive to this experimental choice for short time delays following the interaction of the F atom pulse with the liquid surface. Thus, the early portion of the time profiles likely can be attributed to the gas-liquid reaction dynamics, whose temporal signatures are blurred over the > 100 μs F atom arrival time, as shown in the insets of Fig. 5.9 and 5.4. The results obtained using the static liquid surface agree remarkably well with those from the refreshed surface. The only significant difference is the measured population in HF(v = 0, J = 2), the most populated state at room temperature. The origin of this discrepancy remains unclear, but the otherwise broad agreement between these studies justifies the early study's publication[45] and confirms that the static surface reveals similar dynamics as observed in the more rigorous study.

The falling edge of the absorption signal has also been analyzed to investigate the surprisingly slowly decay of signal evident in Figs. 5.4 and 5.9. Significant absorption is observed from various HF states for more than 1 ms after the rising edge, as shown in the sample time profiles in Fig. 5.14. In order to better understand the nature of these delayed signals, the data has also been analyzed using time gates located 250–3500 μs after the F atom plasma pulse, as marked in Fig. 5.14. The resulting HF rotational state distributions are 300 K within

Table 5.2 HF column-integrated densities [$\int dx\ \rho_{HF}(x)$] observed following the formation of HF(v,J) by reaction of F at the squalane surface. Values have been normalized to 100%. Uncertainties in parenthesis are one standard deviation from the least squares fit, in units of the least significant digit reported.

J	v = 0	v = 1	v = 2	v = 3
0	2.17 (18)	2.48 (6)	2.26 (4)	0.25 (2)
1	5.19 (51)	6.57 (11)	5.69 (7)	0.74 (5)
2	7.79 (42)	7.32 (15)	7.51 (8)	0.98 (6)
3	4.47 (40)	6.22 (15)	6.59 (10)	0.91 (6)
4	2.60 (30)	4.17 (16)	4.69 (9)	0.72 (6)
5	1.19 (36)	2.28 (16)	3.42 (9)	0.31 (7)
6	0.45 (34)	1.36 (18)	2.10 (10)	0.15 (6)
7	0.14 (29)	0.93 (15)	1.44 (10)	0.05 (7)
8	0.11 (31)	0.68 (14)	1.17 (11)	0.05 (6)
9	0.25 (30)	0.64 (15)	0.88 (11)	-0.02 (5)
10	0.10 (24)	0.58 (15)	0.64 (10)	-0.03 (7)
11	0.11 (29)	0.41 (14)	0.40 (11)	-0.05 (15)
12	-0.11 (22)	0.33 (15)	0.28 (17)	-0.03 (18)
13		0.32 (20)	0.07 (20)	
14		0.03 (24)	0.05 (35)	
ΣJ	24.46 (120)	34.33 (61)	37.17 (54)	4.04 (30)

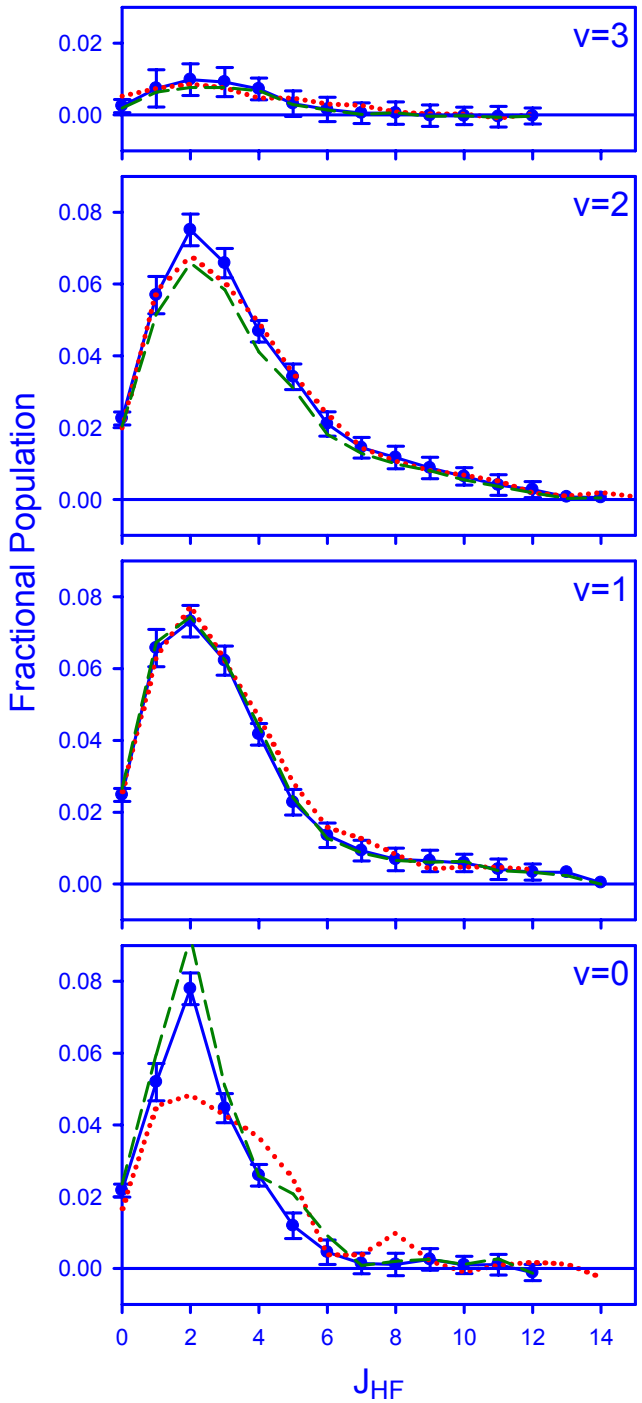

Figure 5.13 Comparison of the normalized HF(*v*,*J*) densities observed for the F + squalane reaction with the static surface (dotted line), and with the rising edge (solid lines, data points) and peak (dashed line) timing from the refreshed surface.

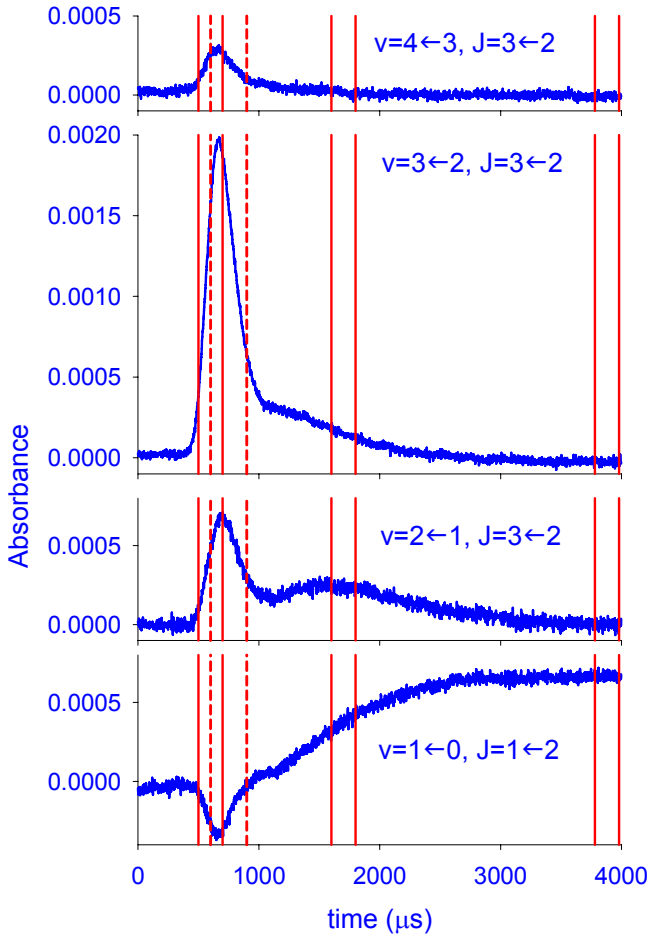

Figure 5.14 Sample time domain profiles for the indicated transitions originating from *v"* = 0–3. Pairs of vertical lines frame the timing domains used for temporal averaging. The first pair of solid lines and the adjacent pair of dotted lines frame the two time domains whose rovibrational state distributions are compared in Fig. 5.13.

uncertainty, while the shifting vibrational distributions are shown in Fig. 5.15. These data reveal a systematic shift toward a room-temperature HF internal state distribution with increasing time. Although these observations could, in principle, be caused by equilibration of HF product trapped on from the surface, the required sub-kilohertz thermalization rate is inconsistent with 10–100 ps vibrational relaxation times anticipated at the surface.[46-49] On the other hand, this slow decay does match that expected for product molecules reaching the edge of the vacuum chamber, relaxing upon contact with the room temperature surface, and returning to the probe region. This thermalization emphasizes the need to position the signal gate only 200 μs after the F atom pulse, insuring insufficient time for the thermally recoiling HF to return to the probe region following secondary collisions.

5.5 Analysis of Results

The high-resolution IR absorption measurements, such as those shown in Fig. 5.11, contain two independent pieces of information about each HF quantum state: the total (state resolved) transition intensity and detailed Doppler lineshape. Intensity information has been integrated and fitted to obtain the state resolved populations presented in Table 5.2 and Fig. 5.13. Additional information on the HF velocities, projected onto the probe axis, can also be obtained via fitting of the observed lineshape. These two methods of analysis will be considered separately in this section.

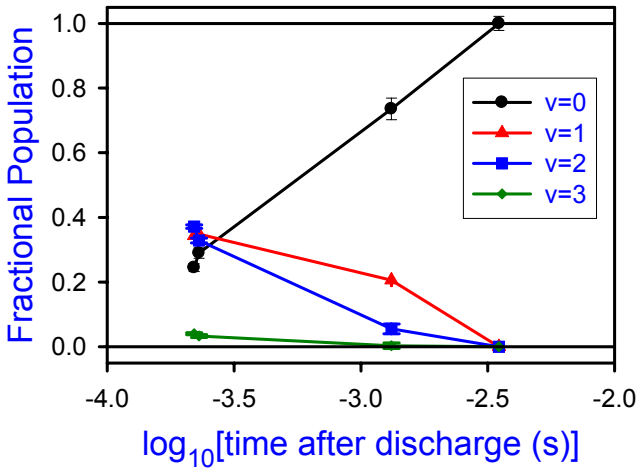

Figure 5.15 Vibrational distribution of HF product at three representative delay times, marked in Fig. 5.14. Populations are in good agreement between the first two gating windows, also compared in Fig. 5.13. After more than 1 ms delay, the apparent vibrational cooling appears to accelerate, as HF molecules relaxing at the sides of the vacuum apparatus have time to return to the probe region.

A. HF(v,J) state distribution

The "best set" HF rovibrational state distribution, defined in Sect. 5.4, for F + squalane has been obtained from the spectrum in Fig. 5.12(a), according the procedure in Ch. 2.4(A). The results appear in Table 5.2 and Fig. 5.13. In the least squares fit, the HF density in all unprobed states (generally with $J > 15$) and those in $v = 4$ is set to zero. Monotonically decaying intensities versus J in each band in Fig. 5.12 and the unobservable signals originating from $v = 4$ justify this approximation. As a result, the higher state populations are less correlated and determined with greater accuracy than those in lower vibrational manifolds, as can be seen by close inspection of derived densities, shown in Fig. 5.13. Nevertheless, even for the $v = 0$ manifold, the peak column-integrated rotational populations are determined to better than 5–10%, with precision improving to 1–2% for the higher vibrational manifolds.

We previously noted that that the $v = 4$ manifold, at 42.4 kcal/mol above the ground state, may be energetically accessible to F reacting with a tertiary C–H bond, within the certainty of the bond strength and possible thermal activation. However, direct measurements of transitions originating from the $v = 4$ manifold do not yield signals in excess of the $\leq 3\times10^{-5}$ absorbance noise limit, corresponding to less than 0.01% of the total HF population in any rotational state in this manifold. Since detailed modeling of the liquid surface indicates that tertiary CH bonds are accessible to impinging reactants,[21,50,51] the lack of HF population in the $v = 4$ manifold can be attributed to surface dynamics that do not favor extreme vibrational excitation, as also manifest in the relatively small branching into $v = 3$.

The average state resolved density of HF above the liquid surface can be obtained by scaling the column-integrated densities in Table 5.2 by the quantity $N\times x$, where $N = 16$ is the number of passes the probe laser makes through the Herriot cell and $x = 13(1)$ cm is the absorption path length of HF above the liquid surface. The most populated states have a density of approximately 1.2×10^{10} HF #/cm^3 per quantum state, and the total HF density is approximately

$1.5(2)\times10^{11}$ HF #/cm^3. Interestingly, this number is in excellent agreement with the estimated $1.5(3)\times10^{11}$ #/cm^3 F atom density impinging on the liquid surface, calibrated against the known F + H_2 rate constant,[42,52] as described in more detail in Ch. 2.4(C). This calibration utilizes a number of experimentally determined values, such that propagation of uncertainty results in the 20% fractional uncertainty in the predicted F atom density. However, within these error bars, it is clear that nearly all F atoms impinging on the surface react and return to the gas phase on the 200 μs time scale of the supersonic jet pulse. This analysis highlights a unique strength of high-resolution direct absorption methods, whereby *absolute* absorbances can be used to accurately infer *absolute* column-integrated densities of transient species.

Several interesting trends emerge from the HF state distributions following reaction with the liquid squalane interface, plotted in Fig. 5.13. Summation over rotational states (Fig. 5.16) reveals a rather broad distribution of vibrational state populations, with 25–35% of the total population residing in each manifold between v = 0–2, and significantly less population entering the v = 3 manifold. Also presented in Fig. 5.16 is the HF vibrational branching following gas-phase reaction with ethane (gas), which has similar H–C bond strength. The gas-phase reaction yields significantly more branching into v = 3, at the expense of v = 0–1.

The HF rotational state distributions for the reaction of F atoms with liquid squalane (see Fig. 5.13) appear nearly Boltzmann in nature, with maximum rotational population in each vibrational manifold occurring at J = 2, the maximum for a 300 K distribution. However, closer inspection reveals excess population formed in highly rotationally excited states, starkly evident in the v = 2 and v = 1 manifolds. Boltzmann plots of degeneracy-scaled populations versus rotational energy are presented in Fig. 5.17. These curves strongly deviate from the straight lines characteristic of a purely thermal distribution. Indeed, the observed rotational distributions show a significant kink at intermediate J values between two approximately linear regions. This observation has prompted analysis of these rovibrational manifolds by a “two-temperature”

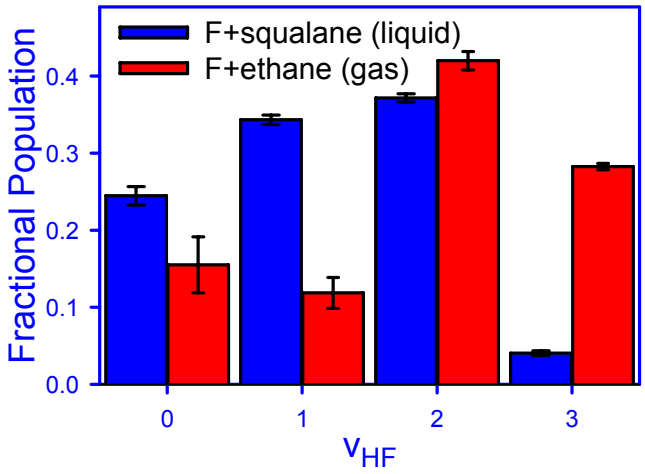

Figure 5.16 HF vibrational state distributions following the reaction of F atoms with hydrocarbons in the gas phase, and at the gas-liquid hydrocarbon surface, as indicated.

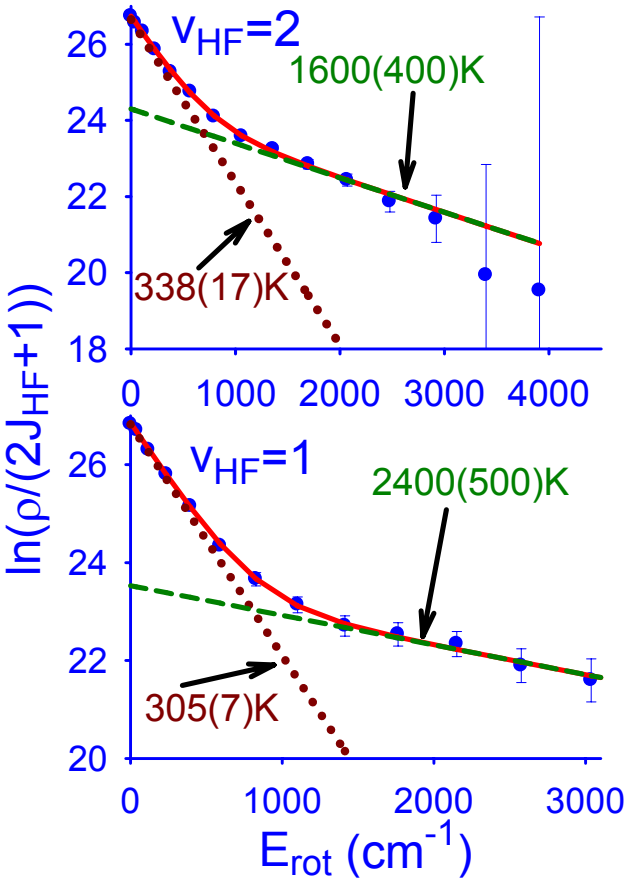

Figure 5.17 Boltzmann plots of the HF rotational state distributions in the $v = 1$ and $v = 2$ manifolds, as indicated. Measured populations are data points with error bars. The solid line is the result of the two-temperature fit, with the constituent high and low temperature thermal distributions plotted as the dashed and dotted lines, respectively.

model, also used extensively in the study of inelastic scattering of CO_2 from liquid surfaces.[23-26]

The two-temperature model describes the rotational populations as the sum of two thermal distributions:

$$\rho_v(J)/g(J) = A\{(\alpha/T_1)\exp(-E(J)/kT_1) + [(1-\alpha)/T_2]\exp(-E(J)/kT_2)\}, \qquad (5.1)$$

where $\rho_v(J)$ is the density of HF(v,J), $g(J)$ is the degeneracy, and $E(J)$ is the rotational energy of state J, α is the branching ratio between the two distributions, and A is an overall scaling factor. The present F + squalane reactive scattering data exhibit much more dramatic and obvious curvature than similar Boltzmann rotational state plots for gases inelastically scattered from liquids.[23-26] Of particular dynamical interest, the low temperature components in both HF(v = 1) and HF(v = 2) manifolds match the 300 K surface temperature (T_s), nearly within one standard deviation of the fit. In contrast, the curvature in the plots for v = 3 and v = 0 is much less dramatic, justifying fits to a simpler one-temperature Boltzmann distribution to reveal qualitative rotational energy trends. Such fits result in least squares values of 400(24) K and 315(30) K for v = 3 and 0, respectively.

Although there is no *a priori* reason to expect the dynamically determined rotational state distributions to approximate thermal distributions, this analysis does reveal qualitative features of the distribution that are likely to prove robust to detailed dynamical modeling. Specifically, lower vibrational manifolds, which may be strongly populated via longer lived trapping desorption (TD) dynamics at the gas-liquid interface, are characterized by rotational temperatures close to the surface temperature, T_s = 300 K. On the other hand, high vibrational excitation is correlated with hyperthermal rotations. This behavior is exactly opposite to trends observed in the gas phase,[38,41] where lower vibrational levels are generally accompanied by increasing rotational energy.

The v = 3 and v = 0 rotational state distributions readily conform to this picture. The v = 3 rotational "temperature" of about 400 K exceeds T_s, as expected because strongly accommodating TD interactions only serve to *depopulate* this high-energy manifold. Although

partial rotational relaxation is likely, the fully equilibrated molecules are simply missing from this distribution because they have also vibrationally relaxed. In contrast, the $v = 0$ population does not exhibit any significant hyperthermal rotational component. This observation is consistent with HF($v = 0$) being formed almost exclusively via strongly trapped interactions, and the 0.24(1) fractional vibrational branching into this manifold represents a clear upper limit for the HF population component that spends an appreciable time on the surface as compared with the time for vibrational energy transfer to the surface.

However, the $v = 0$ population represents only a relatively small fraction of the total population. Most of the nascent HF escapes with $v > 0$, and a significant amount does so while maintaining a nonthermal distribution of rotational energy. The simplest interpretation is that surface interactions can occur with varying degrees of accommodation, and higher energy states are selectively populated via processes that eject HF directly into the gas phase prior to complete thermalization.

The intermediate vibrational levels ($v = 1$–2) appear to have both thermally accommodated and rotationally hot signatures in their rotational distributions, motivating the two-temperature fit in Fig. 5.17. The TD fraction (α), defined in Eq. 5.1, comprises 0.78(2) and 0.69(4) of the $v = 1$ and $v = 2$ populations, respectively. A simple picture for the dynamics based on the rotational state analysis is that 70–80% of the HF product in the *vibrationally* excited ($v = 1, 2$) levels desorb after *rotationally* equilibrating with the liquid surface. However, these molecules have not interacted with the bulk 300 K squalane long enough to lose their high vibrational excitation, motivating their assignment to the DRS channel. Of course, this picture is likely to be an oversimplification of the true dynamics, as gas-phase reactions, analogous to the DRS component, have not been found to match the 2000 K Boltzmann distribution found for the high-temperature component of the rotational state distributions. Nevertheless, the $v = 1$ and $v = 2$ populations appear to have both rotationally excited components, created by the DRS channel, and 300 K components, from TD. More evidence for HF product-state-dependent residence times

on the liquid surface can be found from the observed absorption lineshapes, which we discuss next.

B. Doppler lineshape analysis

The measured Doppler lineshapes directly reveal the HF velocity distribution, projected along the laser axis, i.e., parallel to the liquid surface. Sample Doppler profiles are presented in Fig. 5.18 and fits have been obtained using the method described in this section.

Modeling of Doppler lineshapes is straightforward for transitions terminating in an unpopulated upper state, such as those originating in the $v = 3$ manifold and $v = 2$ with $J > 7$. In this case, only the velocity distribution in the lower state must be considered in the Doppler analysis. Such transitions have been fitted to a simple Gaussian lineshape:

$$A(\nu) = A_0 \exp(-4\ln(2)[(\nu-\nu_0)/\Delta\nu]^2) , \qquad (5.2)$$

where $\Delta\nu$ is the FWHM of the transition, A_0 is the peak absorbance, and ν_0 is the line center frequency. The choice of this functional form is arbitrary yet empirically justified by the robust agreement between the fitted to the observed measurements, such as that shown in the top trace in Fig. 5.18. Fits to Gaussian lineshapes are physically motivated by anticipated quasi-thermal Doppler measurements, and Boltzmann-like velocity distributions observed following inelastic scattering from liquid surfaces.[23-26]

For lower manifolds, emission from the upper state necessitates consideration of the velocity distributions of both the upper and lower levels simultaneously. Specifically, lineshapes can be expressed as a sum of two Gaussian components:

$$A(\nu) = A_l \exp(-4\ln(2)[(\nu - \nu_0)/\Delta\nu_l]^2) - A_u \exp(-4\ln(2)[(\nu - \nu_0)/\Delta\nu_u]^2) . \qquad (5.3)$$

The subscripts l and u indicate components used to describe the lower and upper state distributions, respectively. Correlations between A_l and A_u, and between $\Delta\nu_l$ and $\Delta\nu_u$ make a five-

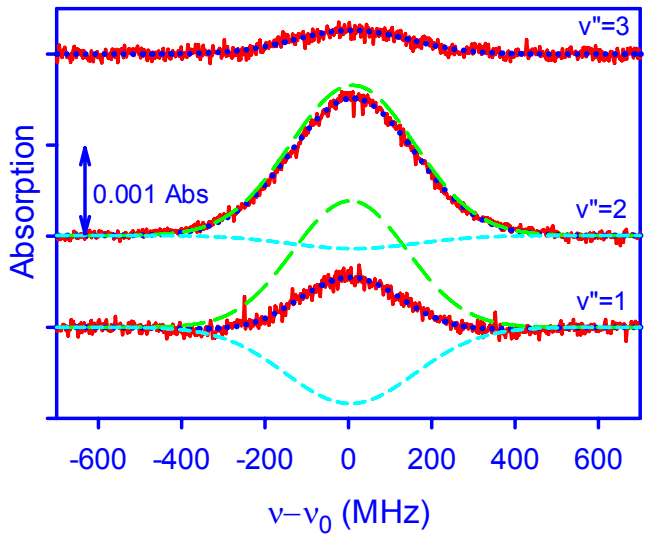

Figure 5.18 Representative Doppler resolved absorption data (solid lines) and fits (dotted lines) for several HF $J'' = 2$, $\Delta J = +1$ transitions. Vibrational manifolds are as indicated. Absorption originating from the $v'' = 3$ manifold is well represented by a single Gaussian fit, as no measurable population has been observed in the $v'' = 4$ manifold. Doppler modeling of the $v'' = 1$–2 levels includes contributions from absorbing molecules in the lower state (long dashes) and emission from the upper state (short dashes).

parameter least squares fit of individual Doppler profiles using Eq. 5.3 intractable. However, the correlation between the peak absorbances can be broken by using the column-integrated state densities shown in Fig. 5.13 to fix the ratio R_{EA} between the integrated emission and absorption components of the Doppler profiles, given by

$$R_{EA} = S_o^{v'J' \rightarrow v''J''} \int dx \int d\nu \, \rho_{v'J'}(\nu,x) \,/\, S_o^{v'J' \leftarrow v''J''} \int dx \int d\nu \, \rho_{v''J''}(\nu,x). \qquad (5.4)$$

Integration over the absorption and emission profiles in Eq. 5.3 relates the peak absorbances via $A_u = A_l R_{EA} \Delta\nu_l / \Delta\nu_u$. The correlation between $\Delta\nu_l$ and $\Delta\nu_u$ can be broken by simultaneously fitting the Doppler profiles of transitions in which a given level is both the upper and lower level, *e.g.* the $v + 2, J'' \leftarrow v + 1, J'$ and $v + 1, J' \leftarrow v, J$ lines, whose frequencies are denoted ν_0' and ν_0, respectively. In this case, $\Delta\nu_l$ of the former can be related to $\Delta\nu_u$ of the latter by scaling to the absolute frequencies via $\Delta\nu_l = \Delta\nu_u'(\nu_0/\nu_0')$.

These relationships are used in several ways. In the simplest approach, the Doppler fits using Eq. 5.2 are carried out for transitions out of the highest energy states, which only have an absorption component. The $\Delta\nu$ parameters obtained from these fits are then used to fix $\Delta\nu_u$ in Eq. 5.3 to obtain fits of transitions out of the next lower vibrational manifold, and the process is repeated for progressively lower levels. Uncertainties in the fitted Doppler widths are obtained by a propagation of errors analysis. Alternatively, Eq. 5.3 and 5.4 are employed to fit simultaneously sets of paired transitions. Similar widths are obtained within the derived uncertainties from both procedures.

The Gaussian nature of the Doppler lineshapes suggests converting the fitted widths $\Delta\nu$ to translational temperatures T_{trans}. Specifically, T_{trans} for a Maxwell-Boltzmann distribution is related to the Doppler FWHM $\Delta\nu$ and center frequency ν via

$$T_{trans} = (c\Delta\nu/\nu)^2 (m_{HF}/8k \ln 2), \qquad (5.5)$$

where m_{HF}, c, and k are the mass of the HF molecule, speed of light, and Boltzmann's constant, respectively. The results of the Doppler analysis are presented in Fig. 5.19, which shows

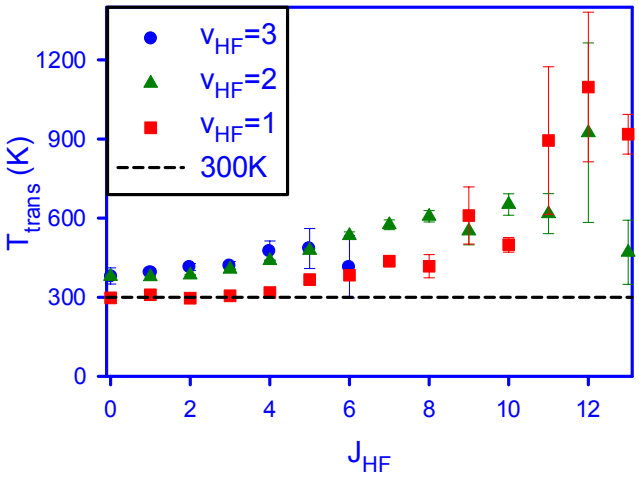

Figure 5.19 Results from the least squares fit to the measured absorption lineshapes originating from the $v = 3$ (circles), $v = 2$ (triangles) and $v = 1$ (squares) manifolds. Observed Gaussian linewidths have been converted to translational temperatures via Eq. 5.5. HF translational energy increases with increasing rovibrational energy. Such translational dynamics indicate strongly state-dependent surface residence times.

that the product HF translational degree of freedom is hotter than or equal to the 300 K surface temperature. Overall, the Doppler widths *increase* with rovibrational excitation, revealing a positive correlation between average translational energy and internal HF energy. This observation is most evident in the propensity for hotter translational temperatures as J increases within a given vibrational manifold. The translational temperature also increases with the product vibrational excitation, although this effect is less pronounced than the dependence upon the rotation state.

Doppler widths for the $v = 0$ manifold are not presented in Fig. 5.19 because they cannot be fitted reliably using the procedure detailed above. Careful inspection of the $v'' = 0$ Doppler measurements in Fig. 5.11 reveals less structure is this manifold than in the $v'' = 1,2$ manifolds. Specifically, the Doppler structure appears approximately Gaussian, because the Δv values in HF($v = 0$,$J < 6$) correspond to 300 K, i.e., nearly identical to those for the upper states, HF($v = 1$, $J < 5$). These similar Doppler widths result in strong parameter correlation through Eq. 5.3, which prevents reliable least squares fitting of the $v'' = 0$ manifold. Nevertheless, thermally equilibrated HF($v = 0$,J) Doppler profiles would be completely consistent the established trend for more accommodation with the surface as internal energy decreases.

The strong positive correlation between *increasing* HF Doppler widths and *increasing* internal HF rovibrational energy contrasts rather dramatically with that observed in previous studies of H atom abstraction in the gas phase, where energy sequestered into product internal energy necessarily reduces the amount available for recoil.[38] This effect was most convincingly demonstrated in studies of F + ethane, where the Doppler measurements of HF(v,J) translational energy proved to be linearly correlated with $E_{avail} = E_{tot} - E_{HF(v,J)}$ and therefore yielded a *negative* correlation with HF internal energy. Stated most simply, this trend results from energy conservation and insufficient time during the collisional event for energy flow into the isolated ethyl cofragment.

By way of contrast, the gas-liquid interface offers a quite different scenario for H atom extraction reaction dynamics. In particular, new correlations arise from quantum-state dependent residence times on the liquid surface. For example, translational energy is likely to be dissipated into the bulk liquid within one or two collisional interactions after the reaction event. Therefore, translationally hot HF might be expected to correlate with molecules that escape from the surface almost immediately following reaction (i.e., the DRS channel) and therefore retain a maximal amount of energy released during reaction.

Similarly, molecules that have lost translational energy from the reaction event through multiple collisions with the surface (i.e., the TD channel) may be linked with additional loss of internal energy as well. In particular, since rotations are expected to equilibrate with the surface almost as rapidly as translations, this consideration suggests a simple mechanism for a *positive* correlation between rotational and translational energies. Because of the large size of its quanta, vibrational energy transfer to the surface may be expected to occur much more slowly, explaining the much weaker trend in translational energies with respect to final vibrational state. From this perspective, the key difference between gas-phase (e.g. F + ethane) and gas-liquid (e.g. F + squalane) reaction dynamics is the presence of many additional channels for subsequent energy transfer after the primary reaction event. As one simple physical picture, the liquid surface offers a larger cross section for subsequent inelastic interactions with the nascent product and thus substantially restricts its ability to behave like a spectator.

5.6 Discussion

Following reaction of F atoms at the liquid squalane surface, HF desorbs into the gas phase with varying amounts of energy in vibrational, rotational, and translational degrees of freedom. High HF internal energy, particularly rotation, is strongly correlated with hot translational distributions. This observation suggests that reaction occurs via competing

dynamical pathways, by which product escapes with a large fraction of the reaction energy, the DRS channel, or partially accommodates with the room temperature surface via TD.

It is interesting to compare the present results with those reported by McKendrick and coworkers for H abstraction by O from squalane and other liquid hydrocarbon interfaces.[15-20,22] Such comparison is necessarily general because these two reactions are quite different. Specifically, O atoms react with a significantly higher (5–10 kcal/mol) barrier,[29] and the exothermicity is much less (≈ 5 kcal/mol). In addition to a single abstraction event, forming OH as probed my McKendrick and coworkers,[15,16,18-20,22,29,53] subsequent reaction events can lead to H_2O product.[7,9] Nevertheless, both HF and OH products are vibrationally excited following reaction at the liquid surface, although they retain less vibrational energy than observed from analogous gas-phase reactions. This result is consistent with the inefficient vibrational accommodation following inelastic scattering of CO_2[23-26] and I_2[11-14] from liquid interfaces. The OH and HF rotational distributions both closely match the surface temperature, but the fastest moving OH(v = 1) products mimic the sub-thermal distributions expected from gas-phase dynamics.[15] Similarly, in the present study the hottest Doppler widths are observed for high HF rotational levels; in this case hot rotations occur with rapidly recoiling molecules attributed to the DRS mechanism. Recent theoretical simulations of O + squalane reaction have found similar trends for increasing rotation and translational energy, though the much larger (> 100 kcal/mol) incident energies in these studies complicates more detailed comparison.[51]

Further insight into energy transfer into the liquid can be gained by comparing the results of F + hydrocarbon reactions at the liquid interface and in the gas phase. We focus on the F + ethane reaction system for this comparison because it has very similar energetics and has already been studied using high-resolution IR methods. However, similar conclusions would be expected for other F + hydrocarbon systems.[41,54] Fig. 5.20 presents detailed energetic branching analysis, in

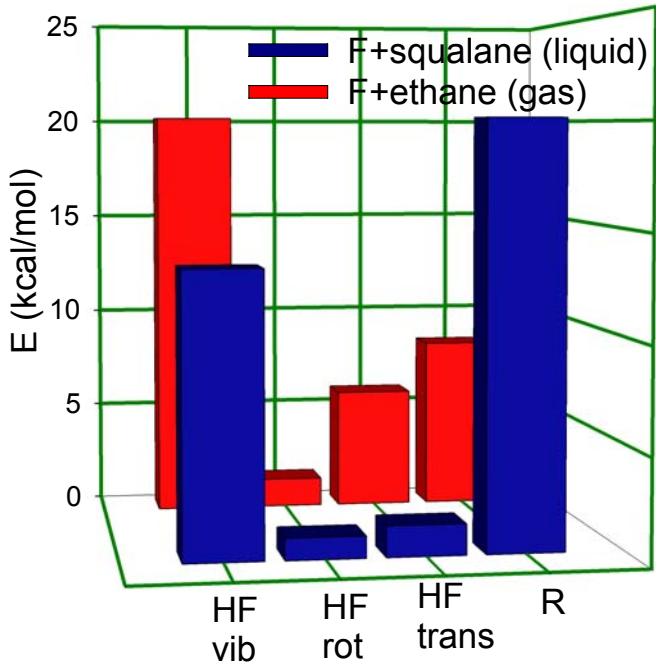

Figure 5.20 Energy partitioning following various F + hydrocarbon reactions in the gas phase and at the liquid interface. Expectation values for energy deposited in the indicated modes are evaluated according to Eq. 5.6. R denotes energy assumed to be sequestered in the unseen hydrocarbon radical.

which average values $\langle E_i \rangle$ of vibrational, rotational, or translational energy are presented. Here, $\langle E_i \rangle$ is computed as

$$\langle E_i \rangle = \Sigma_{v,J} P(v,J) E_i(v,J) \ , \qquad (5.6)$$

where $P(v,J)$ is the HF state distribution, and $E_i(v,J)$ is the energy (i = vibration, rotation, or translation), and E_{trans} is taken as $2kT_{trans}(v,J)$, the energy of an effusive source at temperature T_{trans}, as derived in the present study via Doppler data in Fig. 5.18. The most dramatic change in energy partitioning originates from the larger HF(v = 0,1) population formed via reaction at liquid interface, primarily at the expense of HF(v = 3). The energy partitioning analysis presented in Table 5.3 emphasizes this result. Approximately 60% of the available energy deposited in the HF vibrational coordinate for various gas-phase reactions, versus < 40% for F atom abstraction at the liquid squalane interface.

The presentation in Fig. 5.20 reveals that every HF mode retains less energy after reaction at the liquid interface than in the gas phase, resulting in larger energy branching into the unseen hydrocarbon, denoted R. In general, gas-phase halogen-alkane reactions result in modest (4–12%) energy transfer to internal modes of the hydrocarbon radical product, which acts mostly as a spectator to the reaction.[38,55] By comparison, the HF product recoils from the liquid surface after partial equilibration, during which the extent of relaxation in rotational, vibrational, and translational degrees of freedom relax according to the propensity for energy transfer based on the size of the energy quantum, i.e., larger quanta relax more slowly than smaller quanta. This trend results in the average HF translational energy of 1.47(3) kcal/mol being only 25% higher than the 300 K value of 1.18 kcal/mol. Rotations are also nearly equilibrated, with 1.04(8) kcal/mol average energy, nearly 75% larger than kT, as expected for a linear rotor at 300 K. With respect to surface residence time, the observation of rotationally and translationally excited HF clearly indicates fractional branching of HF into a channel that remains in contact with the

Table 5.3 Fractional energy partitioning (X) of reaction energy following reaction of fluorine with liquid squalane and several gas-phase hydrocarbons. Uncertainties in parenthesis are one standard deviation.

Reactant	X_{HFvib}	X_{HFrot}	$X_{Hftrans}$	$X_{cofragment}$
squalane[a]	37(3)	2.8(3)	4.1(3)	56(8)
ethane[b]	56(6)	3.9(4)	16(2)	23(2)
methane[c]	60.6(7)	4.4(6)		
neopentane[d]	64			
toluene[d]	55			
benzene[d]	63			

[a] Uncertainty dominated by the heterogeneous C–H bond strength in squalane
[b] From Ref. 38
[c] From Ref. 41
[d] From Ref. 54

surface for less than the sub-picosecond relaxation timescales for these modes. Finally, vibrational excitation remains extremely hot, with 13.3(2) kcal/mol average energy, and only partial relaxation occurs because of moderately slow (tens of ps) relaxation time on the liquid surface. Indeed, theoretical studies indicate that vibrational relaxation times are extended by a factor of only two to four by the partial caging present at the interface,[46-49] so even the TD channel is likely to be characterized by a ≈ 100 ps surface residence time.

Very recent computations of F + squalane by the Schatz group[50] have reproduced many of the general features of the experimental results, such as hotter rotational distributions in lower vibrational manifolds. At an even higher level of detail, this work has found that excited rotations are more likely to remain excited following scattering events that spend a relatively small time below the so-called Gibbs surface. Indeed, the predicted vibrational distributions strongly agree with measurements, though the theoretical rotational distributions are much more structured and less Boltzmann-like than those presented here. These differences may arise from the very high F atom translational energies (0.5, 1.0 eV) used in these studies, or the need for more accurate PES calculations to reliably predict rotational distributions. Nevertheless, the results of these landmark computational studies seem to confirm the present interpretation of the experimental results, and present the opportunity to begin developing more detailed physical pictures for gas-liquid scattering processes.

5.7 Conclusions

The reaction of fluorine atoms at the gas-liquid interface of squalane reveals a wide variety of surface energy exchange with recoiling HF products. Highly inverted vibrational populations indicate that a significant amount of the reaction energy remains sequestered in the diatomic fragment as it recoils from the surface, although significant branching into the ground vibrational manifold is also observed. In contrast, rotational and translational excitation of HF

product is moderate. At low *J*, population distributions closely resemble the 300 K surface temperature, though a slowly decaying tail in the rotational population results from hyperthermal populations. The observed rotational state populations are well described by either a thermal distribution or the sum of two such distributions, depending on the vibrational manifold. The v = 3 manifold is characterized by a hot (400 K) distribution, while the v = 0 rotational state distribution closely resembles a thermal distribution at the surface temperature, and intermediate (v = 1–2) levels have rotational state distribution components characterized by thermalized (300 K) and very hot (2000 K) temperatures. Doppler measurements reveal that the HF translational energy matches the liquid surface temperature for moderately excited states, whereas recoil energy increases with HF internal energy. These results indicate microscopic branching of HF interactions with the surface following the reactive event, with high energy components resulting from brief "direct reactive scattering" interaction with the liquid surface, contrasted with "trapped desorption" events during which the product may become translationally, rotationally, and even vibrationally accommodated with the surface. The contribution from each of these components varies with the resulting HF quantum state and is most readily deduced from the translational energy measurements. These observations match expectations for partial equilibration at the surface following an initial reaction event analogous to gas-phase F + hydrocarbon reactions. Results are also consistent with previous studies in which bifurcated dynamic pathways and relaxation rates were determined by energy gap expectations. Recent theoretical studies reproduce the general features observed experimentally, and increase confidence in the present interpretation.

References for Chapter V

1 S. L. Lednovich and J. B. Fenn, Aiche J. **23**, 454 (1977).

2 G. M. Nathanson, P. Davidovits, D. R. Worsnop, and C. E. Kolb, J. Phys. Chem. **100**, 13007 (1996).

3 M. E. Saecker and G. M. Nathanson, J. Chem. Phys. **100**, 3999 (1994).

4 M. E. Saecker and G. M. Nathanson, J. Chem. Phys. **99**, 7056 (1993).

5 M. E. Saecker, S. T. Govoni, D. V. Kowalski, M. E. King, and G. M. Nathanson, Science **252**, 1421 (1991).

6 G. M. Nathanson, Annu. Rev. Phys. Chem. **55**, 231 (2004).

7 J. M. Zhang, D. J. Garton, and T. K. Minton, J. Chem. Phys. **117**, 6239 (2002).

8 D. J. Garton, T. K. Minton, M. Alagia, N. Balucani, P. Casavecchia, and G. G. Volpi, J. Chem. Phys. **112**, 5975 (2000).

9 D. J. Garton, T. K. Minton, M. Alagia, N. Balucani, P. Casavecchia, and G. G. Volpi, Faraday Discuss.387 (1997).

10 J. M. Zhang, H. P. Upadhyaya, A. L. Brunsvold, and T. K. Minton, J. Phys. Chem. B **110**, 12500 (2006).

11 A. J. Kenyon, A. J. McCaffery, C. M. Quintella, and M. D. Zidan, Faraday Discuss. **96**, 245 (1993).

12 C. M. Quintella, A. J. McCaffery, and M. D. Zidan, Chem. Phys. Lett. **214**, 563 (1993).

13 A. J. Kenyon, A. J. McCaffery, C. M. Quintella, and M. D. Zidan, J. Chem. Soc.-Faraday Trans. **89**, 3877 (1993).

14 A. J. Kenyon, A. J. McCaffery, C. M. Quintella, and M. D. Zidan, Chem. Phys. Lett. **190**, 55 (1992).

15 S. P. K. Kohler, M. Allan, H. Kelso, D. A. Henderson, and K. G. McKendrick, J. Chem. Phys. **122**, 24712 (2005).

16 H. Kelso, S. P. K. Kohler, D. A. Henderson, and K. G. McKendrick, J. Chem. Phys. **119**, 9985 (2003).

17 F. Ausfelder, H. Kelso, and K. G. McKendrick, Phys. Chem. Chem. Phys. **4**, 473 (2002).

18 M. Allan, P. A. J. Bagot, R. E. Westacott, M. L. Costen, and K. G. McKendrick, J. Phys. Chem. C **112**, 1524 (2008).

19 M. Allan, P. A. J. Bagot, M. L. Costen, and K. G. McKendrick, J. Phys. Chem. C **111**, 14833 (2007).

20 M. Allan, P. A. J. Bagot, S. P. K. Kohler, S. K. Reed, R. E. Westacott, M. L. Costen, and K. G. McKendrick, Phys. Scr. **76**, C42 (2007).

21 S. P. K. Kohler, S. K. Reed, R. E. Westacott, and K. G. McKendrick, J. Phys. Chem. B **110**, 11717 (2006).

22 S. P. K. Kohler, M. Allan, M. L. Costen, and K. G. McKendrick, J. Phys. Chem. B **110**, 2771 (2006).

23 B. G. Perkins, T. Haber, and D. J. Nesbitt, J. Phys. Chem. B **109**, 16396 (2005).

24 B. G. Perkins and D. J. Nesbitt, J. Phys. Chem. B **110**, 17126 (2006).

25 B. G. Perkins and D. J. Nesbitt, J. Phys. Chem. A **111**, 7420 (2007).

26 B. G. Perkins and D. J. Nesbitt, J. Phys. Chem. B **112**, 507 (2008).

27 B. G. Perkins and D. J. Nesbitt, Proc. Natl. Acad. Sci. U. S. A. **105**, 12684 (2008).

28 B. G. Perkins and D. J. Nesbitt, J. Phys. Chem. A **112**, 9324 (2008).

29 F. Ausfelder and K. G. McKendrick, Prog. React. Kinet. Mech. **25**, 299 (2000).

30 A. Furlan, Chem. Phys. Lett. **309**, 157 (1999).

31 A. Furlan, J. Phys. Chem. B **103**, 1550 (1999).

32 A. Furlan and G. E. Hall, J. Chem. Phys. **109**, 10390 (1998).

33 A. Furlan, Chem. Phys. Lett. **275**, 239 (1997).

34 W. T. Zemke, W. C. Stwalley, J. A. Coxon, and P. G. Hajigeorgiou, Chem. Phys. Lett. **177**, 412 (1991).

35 S. J. Blanksby and G. B. Ellison, Accounts Chem. Res. **36**, 255 (2003).

36 J. C. Polanyi and W. H. Wong, J. Chem. Phys. **51**, 1439 (1969).

37 A. M. Zolot and D. J. Nesbitt, J. Chem. Phys. **127**, 114319 (2007).

38 E. S. Whitney, A. M. Zolot, A. B. McCoy, J. S. Francisco, and D. J. Nesbitt, J. Chem. Phys. **122**, 124310 (2005).

39 S. A. Nizkorodov, W. W. Harper, W. B. Chapman, B. W. Blackmon, and D. J. Nesbitt, J. Chem. Phys. **111**, 8404 (1999).

40 W. W. Harper, S. A. Nizkorodov, and D. J. Nesbitt, J. Chem. Phys. **116**, 5622 (2002).

41 W. W. Harper, S. A. Nizkorodov, and D. J. Nesbitt, J. Chem. Phys. **113**, 3670 (2000).

42 W. B. Chapman, B. W. Blackmon, S. Nizkorodov, and D. J. Nesbitt, J. Chem. Phys. **109**, 9306 (1998).

43 M. P. Sinha and J. B. Fenn, presented at the Proceedings of the 5th International Symposium on Molecular Beams, France, 1975 (unpublished).

44 D. Kaur, A. M. Desouza, J. Wanna, S. A. Hammad, L. Mercorelli, and D. S. Perry, Appl. Optics **29**, 119 (1990).

45 A. M. Zolot, W. W. Harper, B. G. Perkins, P. J. Dagdigian, and D. J. Nesbitt, J. Chem. Phys. **125**, (2006).

46 I. Benjamin, J. Phys. Chem. B **110**, 9375 (2006).

47 I. Chorny, J. Vieceli, and I. Benjamin, J. Phys. Chem. B **107**, 229 (2003).

48 J. Vieceli, I. Chorny, and I. Benjamin, Chem. Phys. Lett. **364**, 446 (2002).

49 J. Vieceli, I. Chorny, and I. Benjamin, J. Chem. Phys. **117**, 4532 (2002).

50 B. K. Radak, S. Yockel, D. Kim, and G. C. Schatz, J. Phys. Chem. A (in press) (2009).

51 D. Kim and G. C. Schatz, J. Phys. Chem. A **111**, 5019 (2007).

52 F. Dong, S. H. Lee, and K. Liu, J. Chem. Phys. **113**, 3633 (2000).

53 F. Ausfelder, H. Kelso, and K. G. McKendrick, Phys. Chem. Chem. Phys. **4**, 473 (2002).

54 D. J. Bogan and D. W. Setser, J. Chem. Phys. **64**, 586 (1976).

55 S. Rudic, C. Murray, J. N. Harvey, and A. J. Orr-Ewing, J. Chem. Phys. **120**, 186 (2004).

Bibliography

P. M. Aker, G. J. Germann, and J. J. Valentini, J. Chem. Phys. **96**, 2756 (1992).

M. Alagia, N. Balucani, P. Casavecchia, D. Stranges, G. G. Volpi, D. C. Clary, A. Kliesch, and H. J. Werner, Chem. Phys. **207**, 389 (1996).

M. H. Alexander, G. Capecchi, and H. J. Werner, Faraday Discuss. **127**, 59 (2004).

M. H. Alexander, D. E. Manolopoulos, and H. J. Werner, J. Chem. Phys. **113**, 11084 (2000).

W. A. Alexander, B. S. Day, H. J. Moore, T. R. Lee, J. R. Morris, and D. Troya, J. Chem. Phys. **128**, (2008).

M. Allan, P. A. J. Bagot, M. L. Costen, and K. G. McKendrick, J. Phys. Chem. C **111**, 14833 (2007).

M. Allan, P. A. J. Bagot, S. P. K. Kohler, S. K. Reed, R. E. Westacott, M. L. Costen, and K. G. McKendrick, Phys. Scr. **76**, C42 (2007).

M. Allan, P. A. J. Bagot, R. E. Westacott, M. L. Costen, and K. G. McKendrick, J. Phys. Chem. C **112**, 1524 (2008).

S. C. Althorpe, Chem. Phys. Lett. **370**, 443 (2003).

S. C. Althorpe and D. C. Clary, Annu. Rev. Phys. Chem. **54**, 493 (2003).

S. C. Althorpe, F. Fernandez-Alonso, B. D. Bean, J. D. Ayers, A. E. Pomerantz, R. N. Zare, and E. Wrede, Nature **416**, 67 (2002).

F. J. Aoiz, L. Banares, and V. J. Herrero, Int. Rev. Phys. Chem. **24**, 119 (2005).

F. J. Aoiz, L. Banares, B. MartinezHaya, J. F. Castillo, D. E. Manolopoulos, K. Stark, and H. J. Werner, J. Phys. Chem. A **101**, 6403 (1997).

V. Aquilanti, D. Cappelletti, F. Pirani, L. Y. Rusin, M. B. Sevryuk, and J. P. Toennies, J. Phys. Chem. **95**, 8248 (1991).

E. Arunan, D. W. Setser, and J. F. Ogilvie, J. Chem. Phys. **97**, 1734 (1992).

B. S. Ault, J. Chem. Phys. **68**, 4012 (1978).

F. Ausfelder, H. Kelso, and K. G. McKendrick, Phys. Chem. Chem. Phys. **4**, 473 (2002).

F. Ausfelder and K. G. McKendrick, Prog. React. Kinet. Mech. **25**, 299 (2000).

J. D. Ayers, A. E. Pomerantz, F. Fernandez-Alonso, F. Ausfelder, B. D. Bean, and R. N. Zare, J. Chem. Phys. **119**, 4662 (2003).

M. Baer, M. Faubel, B. Martinez-Haya, L. Y. Rusin, U. Tappe, and J. P. Toennies, J. Chem. Phys. **108**, 9694 (1998).

N. Balucani, G. Capozza, F. Leonori, E. Segoloni, and P. Casavecchia, Int. Rev. Phys. Chem. **25**, 109 (2006).

N. Balucani, D. Skouteris, G. Capozza, E. Segoloni, P. Casavecchia, M. H. Alexander, G. Capecchi, and H. J. Werner, Phys. Chem. Chem. Phys. **6**, 5007 (2004).

V. J. Barclay, B. A. Collings, J. C. Polanyi, and J. H. Wang, J. Phys. Chem. **95**, 2921 (1991).

R. J. Bartlett and G. D. Purvis, Phys. Scr. **21**, 255 (1980).

P. Beadle, M. R. Dunn, N. B. H. Jonathan, J. P. Liddy, and J. C. Naylor, J. Chem. Soc., Faraday Trans. II **74**, 2170 (1978).

P. Beadle, M. R. Dunn, N. B. H. Jonathan, J. P. Liddy, J. C. Naylor, and S. Okuda, J. Chem. Soc., Faraday Trans. II **74**, 2158 (1978).

I. Benjamin, J. Phys. Chem. B **110**, 9375 (2006).

I. Benjamin, M. Wilson, and A. Pohorille, J. Chem. Phys. **100**, 6500 (1994).

M. J. Berry, J. Chem. Phys. **59**, 6229 (1973).

R. P. A. Bettens, M. A. Collins, M. J. T. Jordan, and D. H. Zhang, J. Chem. Phys. **112**, 10162 (2000).

S. J. Blanksby and G. B. Ellison, Accounts Chem. Res. **36**, 255 (2003).

D. Bogan and D. W. Setser, in *Fluorine-containing free radicals: kinetics and dynamics of reactions: based on a symposium sponsored by the Division of Physical Chemistry at the 169th meeting of the American Chemical Society, Philadelphia, Pennsylvania, April 7-11, 1975*, edited by J. W. Root (American Chemical Society, Washington, 1978), pp. 237.

D. J. Bogan and D. W. Setser, J. Chem. Phys. **64**, 586 (1976).

K. Bolton, W. L. Hase, and G. H. Peslherbe, in *Modern Methods for Multidimensional Dynamics Computations in Chemistry*, edited by D. L. Thompson (World Scientific, River Edge, NJ, 1998), pp. 143.

S. B. M. Bosio and W. L. Hase, J. Chem. Phys. **107**, 9677 (1997).

S. E. Bradforth, D. W. Arnold, R. B. Metz, A. Weaver, and D. M. Neumark, J. Phys. Chem. **95**, 8066 (1991).

D. Brandt and J. C. Polanyi, Chem. Phys. **35**, 23 (1978).

D. Brandt and J. C. Polanyi, Chem. Phys. **45**, 65 (1980).

M. J. Bronikowski, W. R. Simpson, B. Girard, and R. N. Zare, J. Chem. Phys. **95**, 8647 (1991).

M. Brouard, I. Burak, S. Marinakis, L. R. Lago, P. Tampkins, and C. Vallance, J. Chem. Phys. **121**, 10426 (2004).

R. A. Brownsword, C. Kappel, P. Schmiechen, H. P. Upadhyaya, and H. R. Volpp, Chem. Phys. Lett. **289**, 241 (1998).

G. Capecehi and H. J. Werner, Phys. Chem. Chem. Phys. **6**, 4975 (2004).

P. Casavecchia, Rep. Prog. Phys. **63**, 355 (2000).

J. F. Castillo, F. J. Aoiz, L. Banares, E. Martinez-Nunez, A. Fernandez-Ramos, and S. Vazquez, J. Phys. Chem. A **109**, 8459 (2005).

J. F. Castillo, B. Hartke, H. J. Werner, F. J. Aoiz, L. Banares, and B. Martinez-Haya, J. Chem. Phys. **109**, 7224 (1998).

D. W. Chandler and P. L. Houston, J. Chem. Phys. **87**, 1445 (1987).

H. W. Chang, D. W. Setser, M. J. Perona, and R. L. Johnson, Chem. Phys. Lett. **9**, 587 (1971).

S. D. Chao and R. T. Skodje, J. Chem. Phys. **119**, 1462 (2003).

W. B. Chapman, B. W. Blackmon, and D. J. Nesbitt, J. Chem. Phys. **107**, 8193 (1997).

W. B. Chapman, B. W. Blackmon, S. Nizkorodov, and D. J. Nesbitt, J. Chem. Phys. **109**, 9306 (1998).

W. B. Chapman, M. J. Weida, and D. J. Nesbitt, J. Chem. Phys. **106**, 2248 (1997).

W. Chen, W. L. Hase, and H. B. Schlegel, Chem. Phys. Lett. **228**, 436 (1994).

I. Chorny, J. Vieceli, and I. Benjamin, J. Phys. Chem. B **107**, 229 (2003).

R. E. Continetti, B. A. Balko, and Y. T. Lee, J. Chem. Phys. **93**, 5719 (1990).

H. W. Cruse, P. J. Dagdigian, and R. N. Zare, Faraday Discuss. **55**, 277 (1973).

G. Czako, B. C. Shepler, J. B. Braams, and J. M. Bowman, J. Phys. Chem. A(in press) (2009).

S. Davis, D. T. Anderson, G. Duxbury, and D. J. Nesbitt, J. Chem. Phys. **107**, 5661 (1997).

B. S. Day, J. R. Morris, W. A. Alexander, and D. Troya, J. Phys. Chem. A **110**, 1319 (2006).

W. Demtroder, *Laser Spectroscopy*. (Springer, Berlin, 1996).

M. P. Deskevich, M. Y. Hayes, K. Takahashi, R. T. Skodje, and D. J. Nesbitt, J. Chem. Phys. **124**, 224303 (2006).

M. P. Deskevich, D. J. Nesbitt, and H. J. Werner, J. Chem. Phys. **120**, 7281 (2004).

A. M. G. Ding, L. J. Kirsch, D. S. Perry, J. C. Polanyi, and J. L. Schreiber, Faraday Discuss. **55**, 252 (1973).

F. Dong, S. H. Lee, and K. Liu, J. Chem. Phys. **113**, 3633 (2000).

F. Dong, S. H. Lee, and K. Liu, J. Chem. Phys. **115**, 1197 (2001).

V. Dribinski, A. Ossadtchi, V. A. Mandelshtam, and H. Reisler, Rev. Sci. Instrum. **73**, 2634 (2002).

M. L. Dubernet and J. M. Hutson, J. Phys. Chem. **98**, 5844 (1994).

W. H. Duewer and D. W. Setser, J. Chem. Phys. **58**, 2310 (1973).

T. H. Dunning, J. Chem. Phys. **90**, 1007 (1989).

A. Eppink and D. H. Parker, Rev. Sci. Instrum. **68**, 3477 (1997).

H. Eyring, J. Am. Chem. Soc. **54**, 170 (1932).

H. Eyring and M. Polanyi, Z. Phys. Chem. B-Chem. Elem. Aufbau. Mater. **12**, 279 (1931).

J. R. Fair, D. Schaefer, R. Kosloff, and D. J. Nesbitt, J. Chem. Phys. **116**, 1406 (2002).

M. Faubel, B. Martinez-Haya, L. Y. Rusin, U. Tappe, J. P. Toennies, F. J. Aoiz, and L. Banares, J. Phys. Chem. A **102**, 8695 (1998).

F. Fernandez-Alonso and R. N. Zare, Annu. Rev. Phys. Chem. **53**, 67 (2002).

A. V. Fishchuk, G. C. Groenenboom, and A. van der Avoird, J. Phys. Chem. A **110**, 5280 (2006).

A. V. Fishchuk, P. E. S. Wormer, and A. van der Avoird, J. Phys. Chem. A **110**, 5273 (2006).

A. A. Fokin and P. R. Schreiner, Chem. Rev. **102**, 1551 (2002).

From, pp. http://nobelprize.org/nobel_prizes/chemistry/laureates/1986/.

A. Furlan, Chem. Phys. Lett. **275**, 239 (1997).

A. Furlan, Chem. Phys. Lett. **309**, 157 (1999).

A. Furlan, J. Phys. Chem. B **103**, 1550 (1999).

A. Furlan and G. E. Hall, J. Chem. Phys. **109**, 10390 (1998).

D. J. Garton, A. L. Brunsvold, T. K. Minton, D. Troya, B. Maiti, and G. C. Schatz, J. Phys. Chem. A **110**, 1327 (2006).

D. J. Garton, T. K. Minton, M. Alagia, N. Balucani, P. Casavecchia, and G. G. Volpi, Faraday Discuss.387 (1997).

D. J. Garton, T. K. Minton, M. Alagia, N. Balucani, P. Casavecchia, and G. G. Volpi, J. Chem. Phys. **112**, 5975 (2000).

D. J. Garton, T. K. Minton, M. Alagia, N. Balucani, P. Casavecchia, and G. G. Volpi, J. Chem. Phys. **114**, 5958 (2001).

D. J. Garton, T. K. Minton, B. Maiti, D. Troya, and G. C. Schatz, J. Chem. Phys. **118**, 1585 (2003).

W. Gellermann, J. Phys. Chem. Solids **52**, 249 (1991).

D. Gerlich, E. Herbst, and E. Roueff, Planet Space Sci. **50**, 1275 (2002).

S. Ghosal and S. Mahapatra, J. Phys. Chem. A **109**, 1530 (2005).

J. L. Hall and S. A. Lee, Appl. Phys. Lett. **29**, 367 (1976).

S. A. Harich, D. W. H. Hwang, X. F. Yang, J. J. Lin, X. M. Yang, and R. N. Dixon, J. Chem. Phys. **113**, 10073 (2000).

W. W. Harper, S. A. Nizkorodov, and D. J. Nesbitt, J. Chem. Phys. **113**, 3670 (2000).

W. W. Harper, S. A. Nizkorodov, and D. J. Nesbitt, Chem. Phys. Lett. **335**, 381 (2001).

W. W. Harper, S. A. Nizkorodov, and D. J. Nesbitt, J. Chem. Phys. **116**, 5622 (2002).

J. G. Harris, J. Phys. Chem. **96**, 5077 (1992).

D. R. Hartree, Proc. Camb. Philol. Soc. **24**, 111 (1928).

D. R. Hartree, Proc. Camb. Philol. Soc. **24**, 89 (1928).

M. Y. Hayes, M. P. Deskevich, D. J. Nesbitt, K. Takahashi, and R. T. Skodje, J. Phys. Chem. A **110**, 436 (2006).

D. Herriot, H. Kogelnik, and R. Kompfner, Appl. Optics **3**, 523 (1964).

G. Herzberg, *Infrared and Raman Spectra of Polyatomic Molecules*. (D. Van Nostrand Company, New York, 1945).

R. C. Hilborn, Am. J. Phys. **50**, 982 (1982).

M. C. Hsiao, A. Sinha, and F. F. Crim, J. Phys. Chem. **95**, 8263 (1991).

N. Isa, K. D. Gibson, T. Yan, W. Hase, and S. J. Sibener, J. Chem. Phys. **120**, 2417 (2004).

Y. Ishikawa, T. Nakajima, T. Yanai, and K. Hirao, Chem. Phys. Lett. **363**, 458 (2002).

W. Jakubetz, D. Sokolovski, J. N. L. Connor, and G. C. Schatz, J. Chem. Phys. **97**, 6451 (1992).

S. Javoy, V. Naudet, S. Abid, and C. E. Paillard, Exp. Therm. Fluid Sci. **27**, 371 (2003).

N. Jonathan, Melliars.Cm, D. Timlin, and D. H. Slater, Appl. Optics **10**, 1821 (1971).

N. Jonathan, Melliar-Smith Cm, S. Okuda, D. H. Slater, and D. Timlin, Mol. Phys. **22**, 561 (1971).

J. V. V. Kasper, C. R. Pollock, R. F. Curl, and F. K. Tittel, Appl. Optics **21**, 236 (1982).

D. Kaur, A. M. Desouza, J. Wanna, S. A. Hammad, L. Mercorelli, and D. S. Perry, Appl. Optics **29**, 119 (1990).

H. Kelso, S. P. K. Kohler, D. A. Henderson, and K. G. McKendrick, J. Chem. Phys. **119**, 9985 (2003).

A. J. Kenyon, A. J. McCaffery, C. M. Quintella, and M. D. Zidan, Chem. Phys. Lett. **190**, 55 (1992).

A. J. Kenyon, A. J. McCaffery, C. M. Quintella, and M. D. Zidan, Faraday Discuss. **96**, 245 (1993).

A. J. Kenyon, A. J. McCaffery, C. M. Quintella, and M. D. Zidan, J. Chem. Soc.-Faraday Trans. **89**, 3877 (1993).

D. Kim and G. C. Schatz, J. Phys. Chem. A **111**, 5019 (2007).

L. J. Kirsch and J. C. Polanyi, J. Chem. Phys. **57**, 4498 (1972).

J. Klos, M. M. Szczesniak, and G. Chalasinski, Int. Rev. Phys. Chem. **23**, 541 (2004).

W. Koechner, (Springer, Berlin, 1999), pp. 232.

S. P. K. Kohler, M. Allan, M. L. Costen, and K. G. McKendrick, J. Phys. Chem. B **110**, 2771 (2006).

S. P. K. Kohler, M. Allan, H. Kelso, D. A. Henderson, and K. G. McKendrick, J. Chem. Phys. **122**, 24712 (2005).

S. P. K. Kohler, S. K. Reed, R. E. Westacott, and K. G. McKendrick, J. Phys. Chem. B **110**, 11717 (2006).

K. L. Kompa and G. C. Pimentel, J. Chem. Phys. **47**, 857 (1967).

H. Kornweitz and A. Persky, J. Phys. Chem. A **108**, 140 (2004).

C. Kreher, J. L. Rinnenthal, and K. H. Gericke, J. Chem. Phys. **108**, 3154 (1998).

O. D. Krogh, D. K. Stone, and G. C. Pimentel, J. Chem. Phys. **66**, 368 (1977).

K. Kudla and G. C. Schatz, Chem. Phys. **175**, 71 (1993).

P. J. Kuntz, E. M. Nemeth, J. C. Polanyi, S. D. Rosner, and C. E. Young, J. Chem. Phys. **44**, 1168 (1966).

S. R. Langhoff and E. R. Davidson, Int. J. Quantum Chem. **8**, 61 (1974).

I. Last and M. Baer, J. Chem. Phys. **80**, 3246 (1984).

R. B. Leblanc, J. B. White, and P. F. Bernath, J. Mol. Spectrosc. **164**, 574 (1994).

S. L. Lednovich and J. B. Fenn, Aiche J. **23**, 454 (1977).

Y. T. Lee, Science **236**, 793 (1987).

Y. T. Lee, J. D. McDonald, P. R. Lebreton, and D. R. Herschbach, Rev. Sci. Instrum. **40**, 1402 (1969).

E. B. W. Lerch, X. C. Dai, S. Gilb, E. A. Torres, and S. R. Leone, J. Chem. Phys. **124**, (2006).

R. D. Levine and R. B. Bernstein, *Molecular Reaction Dynamics and Chemical Reactivity*. (Oxford University Press, New York, 1987).

R. D. Levine and S. F. Wu, Chem. Phys. Lett. **11**, 557 (1971).

G. Li, S. B. M. Bosio, and W. L. Hase, J. Mol. Struct. **556**, 43 (2000).

G. S. Li and W. L. Hase, J. Am. Chem. Soc. **121**, 7124 (1999).

J. J. Lin, J. G. Zhou, W. C. Shiu, and K. P. Liu, Rev. Sci. Instrum. **74**, 2495 (2003).

J. J. M. Lin, J. G. Zhou, W. C. Shiu, and K. P. Liu, Chin. J. Chem. Phys. **17**, 346 (2004).

F. Lique, M. H. Alexander, G. L. Li, H. J. Werner, S. A. Nizkorodov, W. W. Harper, and D. J. Nesbitt, J. Chem. Phys. **128**, (2008).

J. B. Liu, B. Van Devener, and S. L. Anderson, J. Chem. Phys. **119**, 200 (2003).

K. P. Liu, Phys. Chem. Chem. Phys. **9**, 17 (2007).

F. London, Z. Elektrochem. Angew. Phys. Chem. **35**, 552 (1929).

D. E. Manolopoulos and M. H. Alexander, Phys. Chem. Chem. Phys. **6**, 4984 (2004).

U. Manthe, G. Capecchi, and H. J. Werner, Phys. Chem. Chem. Phys. **6**, 5026 (2004).

M. M. Maricq and J. J. Szente, J. Phys. Chem. **98**, 2078 (1994).

J. D. D. Martin and J. W. Hepburn, J. Chem. Phys. **109**, 8139 (1998).

E. Martinez-Nunez, A. Rahaman, and W. L. Hase, J. Phys. Chem. C **111**, 354 (2007).

J. M. Merritt, J. Kupper, and R. E. Miller, Phys. Chem. Chem. Phys. **7**, 67 (2005).

R. B. Metz, J. D. Thoemke, J. M. Pfeiffer, and F. F. Crim, J. Chem. Phys. **99**, 1744 (1993).

M. Meuwly and J. M. Hutson, J. Chem. Phys. **119**, 8873 (2003).

D. R. Miller, in *Atomic and molecular beam methods*, edited by G. Scoles (Oxford University Press, New York, 1988), pp. 14.

L. F. Mollenauer, Rev. Sci. Instrum. **49**, 809 (1978).

C. M. Moore, I. W. M. Smith, and D. W. A. Stewart, Int. J. Chem. Kinet. **26**, 813 (1994).

G. B. Moore and I. W. M. Smith, J. Phys. Chem. **100**, 12848 (1996).

J. R. Morris, P. Behr, M. D. Antman, B. R. Ringeisen, J. Splan, and G. M. Nathanson, J. Phys. Chem. A **104**, 6738 (2000).

J. T. Muckerman, J. Phys. Chem. **93**, 179 (1989).

C. Murray, A. J. Orr-Ewing, R. L. Toomes, and T. N. Kitsopoulos, J. Chem. Phys. **120**, 2230 (2004).

G. M. Nathanson, Annu. Rev. Phys. Chem. **55**, 231 (2004).

G. M. Nathanson, P. Davidovits, D. R. Worsnop, and C. E. Kolb, J. Phys. Chem. **100**, 13007 (1996).

C. Naulin, M. Costes, A. Benseddik, and G. Dorthe, Laser Chem. **8**, 283 (1988).

D. A. Neufeld, J. Zmuidzinas, P. Schilke, and T. G. Phillips, Astrophys. J. **488**, L141 (1997).

D. M. Neumark, A. M. Wodtke, G. N. Robinson, C. C. Hayden, and Y. T. Lee, J. Chem. Phys. **82**, 3045 (1985).

S. A. Nizkorodov, W. W. Harper, W. B. Chapman, B. W. Blackmon, and D. J. Nesbitt, J. Chem. Phys. **111**, 8404 (1999).

J. H. Parker and G. C. Pimentel, J. Chem. Phys. **51**, 91 (1969).

B. F. Parsons and D. W. Chandler, J. Chem. Phys. **122**, 174306 (2005).

B. F. Parsons, K. E. Strecker, and D. W. Chandler, Eur. Phys. J. D **38**, 15 (2006).

J. K. Pearce, B. Retail, S. J. Greaves, R. A. Rose, and A. J. Orr-Ewing, J. Phys. Chem. A **111**, 13296 (2007).

B. G. Perkins, T. Haber, and D. J. Nesbitt, J. Phys. Chem. B **109**, 16396 (2005).

B. G. Perkins and D. J. Nesbitt, J. Phys. Chem. B **110**, 17126 (2006).

B. G. Perkins and D. J. Nesbitt, J. Phys. Chem. A **111**, 7420 (2007).

B. G. Perkins and D. J. Nesbitt, J. Phys. Chem. B **112**, 507 (2008).

B. G. Perkins and D. J. Nesbitt, Proc. Natl. Acad. Sci. U. S. A. **105**, 12684 (2008).

B. G. Perkins and D. J. Nesbitt, J. Phys. Chem. A **112**, 9324 (2008).

D. S. Perry, Private Communication (2006).

G. H. Peslherbe and W. L. Hase, J. Chem. Phys. **100**, 1179 (1994).

J. M. Pfeiffer, R. B. Metz, J. D. Thoemke, E. Woods, and F. F. Crim, J. Chem. Phys. **104**, 4490 (1996).

A. S. Pine, J. Opt. Soc. Am. **66**, 97 (1976).

J. C. Polanyi, Accounts Chem. Res. **5**, 161 (1972).

J. C. Polanyi and D. C. Tardy, J. Chem. Phys. **51**, 5717 (1969).

J. C. Polanyi and W. H. Wong, J. Chem. Phys. **51**, 1439 (1969).

J. C. Polanyi and K. B. Woodall, J. Chem. Phys. **57**, 1574 (1972).

W. H. Press, S. A. Teukolsky, W. T. Vetterling, and B. P. Flannery, *Numerical recipes in C: the art of scientific computing*, 2 ed. (Cambridge University Press, New York, 1992).

D. Proch and T. Trickl, Rev. Sci. Instrum. **60**, 713 (1989).

M. H. Qiu, Z. F. Ren, L. Che, D. X. Dai, S. A. Harich, X. Y. Wang, X. M. Yang, C. X. Xu, D. Q. Xie, M. Gustafsson, R. T. Skodje, Z. G. Sun, and D. H. Zhang, Science **311**, 1440 (2006).

G. Quemener and N. Balakrishnan, J. Chem. Phys. **128**, (2008).

C. M. Quintella, A. J. McCaffery, and M. D. Zidan, Chem. Phys. Lett. **214**, 563 (1993).

B. K. Radak, S. Yockel, D. Kim, and G. C. Schatz, J. Phys. Chem. A (in press) (2009).

B. Retail, J. K. Pearce, C. Murray, and A. J. Orr-Ewing, J. Chem. Phys. **122**, (2005).

S. Rogers, D. S. Wang, A. Kuppermann, and S. Walch, J. Phys. Chem. A **104**, 2308 (2000).

S. Rudic, C. Murray, J. N. Harvey, and A. J. Orr-Ewing, J. Chem. Phys. **120**, 186 (2004).

L. Y. Rusin and J. P. Toennies, Phys. Chem. Chem. Phys. **2**, 501 (2000).

M. E. Saecker, S. T. Govoni, D. V. Kowalski, M. E. King, and G. M. Nathanson, Science **252**, 1421 (1991).

M. E. Saecker and G. M. Nathanson, J. Chem. Phys. **99**, 7056 (1993).

M. E. Saecker and G. M. Nathanson, J. Chem. Phys. **100**, 3999 (1994).

S. Sato, J. Chem. Phys. **23**, 2465 (1955).

S. Sato, J. Chem. Phys. **23**, 592 (1955).

R. Sayos, J. Hernando, R. Francia, and M. Gonzalez, Phys. Chem. Chem. Phys. **2**, 523 (2000).

R. Sayos, J. Hernando, J. Hijazo, and M. Gonzalez, Phys. Chem. Chem. Phys. **1**, 947 (1999).

A. Schiffman, W. B. Chapman, and D. J. Nesbitt, J. Phys. Chem. **100**, 3402 (1996).

B. Scott Day, J. R. Morris, and D. Troya, J. Chem. Phys. **122**, (2005).

W. Shiu, J. J. Lin, K. P. Liu, M. Wu, and D. H. Parker, J. Chem. Phys. **120**, 117 (2004).

A. Simoes and K. Gavroglu, Stud. Hist. Philos. Mod. Phys. **31B**, 511 (2000).

A. Sinha, M. C. Hsiao, and F. F. Crim, J. Chem. Phys. **92**, 6333 (1990).

A. Sinha, M. C. Hsiao, and F. F. Crim, J. Chem. Phys. **94**, 4928 (1991).

M. P. Sinha and J. B. Fenn, presented at the Proceedings of the 5th International Symposium on Molecular Beams, France, 1975 (unpublished).

R. T. Skodje, Annu. Rev. Phys. Chem. **44**, 145 (1993).

R. T. Skodje, D. Skouteris, D. E. Manolopoulos, S. H. Lee, F. Dong, and K. Liu, J. Chem. Phys. **112**, 4536 (2000).

R. T. Skodje, D. Skouteris, D. E. Manolopoulos, S. H. Lee, F. Dong, and K. P. Liu, Phys. Rev. Lett. **85**, 1206 (2000).

D. Skouteris, H. J. Werner, F. J. Aoiz, L. Banares, J. F. Castillo, M. Menendez, N. Balucani, L. Cartechini, and P. Casavecchia, J. Chem. Phys. **114**, 10662 (2001).

J. J. Sloan, D. G. Watson, J. M. Williamson, and J. S. Wright, J. Chem. Phys. **75**, 1190 (1981).

I. W. M. Smith and D. J. Wrigley, Chem. Phys. Lett. **70**, 481 (1980).

D. M. Sonnenfroh and K. P. Liu, Chem. Phys. Lett. **176**, 183 (1991).

K. Stark and H. J. Werner, J. Chem. Phys. **104**, 6515 (1996).

P. S. Stevens, W. H. Brune, and J. G. Anderson, J. Phys. Chem. **93**, 4068 (1989).

B. P. Stoicheff, Can. J. Phys. **79**, 165 (2001).

B. R. Strazisar, C. Lin, and H. F. Davis, Science **290**, 958 (2000).

R. A. Sultanov and N. Balakrishnan, Astrophys. J. **629**, 305 (2005).

Z. G. Sun, S. Y. Lee, and D. H. Zhang, Chin. J. Chem. Phys. **20**, 365 (2007).

J. P. Sung and D. W. Setser, Chem. Phys. Lett. **48**, 413 (1977).

K. Tamagake, D. W. Setser, and J. P. Sung, J. Chem. Phys. **73**, 2203 (1980).

B. Y. Tang, B. H. Yang, K. L. Han, R. Q. Zhang, and J. Z. H. Zhang, J. Chem. Phys. **113**, 10105 (2000).

E. Tannenbaum, K. J. Higgins, W. Klemperer, B. Segev, and E. J. Heller, J. Phys. Chem. B **106**, 8100 (2002).

L. M. Tashiro, W. Ubachs, and R. N. Zare, J. Mol. Spectrosc. **138**, 89 (1989).

E. H. Taylor and S. Datz, J. Chem. Phys. **23**, 1711 (1955).

J. D. Thoemke, J. M. Pfeiffer, R. B. Metz, and F. F. Crim, J. Phys. Chem. **99**, 13748 (1995).

R. L. Toomes and T. N. Kitsopoulos, Phys. Chem. Chem. Phys. **5**, 2481 (2003).

R. L. Toomes, A. J. van den Brom, T. N. Kitsopoulos, C. Murray, and A. J. Orr-Ewing, J. Phys. Chem. A **108**, 7909 (2004).

D. Townsend, M. P. Minitti, and A. G. Suits, Rev. Sci. Instrum. **74**, 2530 (2003).

D. Troya, J. Chem. Phys. **123**, 214305 (2005).

D. Troya and G. C. Schatz, J. Chem. Phys. **120**, 7696 (2004).

D. Troya and G. C. Schatz, Int. Rev. Phys. Chem. **23**, 341 (2004).

D. G. Truhlar and Kupperma.A, J. Chem. Phys. **56**, 2232 (1972).

Y. R. Tzeng and M. H. Alexander, J. Chem. Phys. **121**, 5183 (2004).

E. Uggerud and T. Helgaker, J. Am. Chem. Soc. **114**, 4265 (1992).

J. J. Valentini, J. Phys. Chem. A **106**, 5745 (2002).

S. A. Vazquez, J. R. Morris, A. Rahaman, O. A. Mazyar, G. Vayner, S. V. Addepalli, W. L. Hase, and E. Martinez-Nunez, J. Phys. Chem. A **111**, 12785 (2007).

J. T. Verdeyen, *Laser Electronics*, 3rd ed. (Prentice Hall, Upper Saddle River, NJ, 1995).

J. Vieceli, I. Chorny, and I. Benjamin, J. Chem. Phys. **115**, 4819 (2001).

J. Vieceli, I. Chorny, and I. Benjamin, Chem. Phys. Lett. **364**, 446 (2002).

J. Vieceli, I. Chorny, and I. Benjamin, J. Chem. Phys. **117**, 4532 (2002).

R. von Glasow and P. J. Crutzen, in *Treatise on Geochemistry*, edited by R. F. Keeling, H. D. Holland, and K. K. Turekian (Elsevier Pergamon, Amsterdam, 2003), Vol. 4, pp. 347.

I. M. Waller, T. N. Kitsopoulos, and D. M. Neumark, J. Phys. Chem. **94**, 2240 (1990).

P. F. Weck and N. Balakrishnan, J. Chem. Phys. **123**, 144308 (2005).

H. J. Werner and P. J. Knowles, J. Chem. Phys. **89**, 5803 (1988).

E. S. Whitney, A. M. Zolot, A. B. McCoy, J. S. Francisco, and D. J. Nesbitt, J. Chem. Phys. **122**, 124310 (2005).

C. D. Wick, J. I. Siepmann, and M. R. Schure, Anal. Chem. **74**, 3518 (2002).

M. A. Wickramaaratchi, D. W. Setser, H. Hildebrandt, B. Korbitzer, and H. Heydtmann, Chem. Phys. **94**, 109 (1985).

K. R. Wilson, G. H. Kwei, D. R. Herschbach, J. A. Norris, J. H. Birely, and R. R. Herm, J. Chem. Phys. **41**, 1154 (1964).

N. Winter and I. Benjamin, J. Chem. Phys. **121**, 2253 (2004).

S. H. Wu, P. Dupre, and T. A. Miller, Phys. Chem. Chem. Phys. **8**, 1682 (2006).

Y. S. M. Wu, A. Kuppermann, and J. B. Anderson, Phys. Chem. Chem. Phys. **1**, 929 (1999).

E. Wurzberg, A. J. Grimley, and P. L. Houston, Chem. Phys. Lett. **57**, 373 (1978).

E. Wurzberg and P. L. Houston, J. Chem. Phys. **72**, 5915 (1980).

C. X. Xu, D. Q. Xie, and D. H. Zhang, Chin. J. Chem. Phys. **19**, 96 (2006).

S. Yan, Y. T. Wu, and K. P. Liu, Phys. Chem. Chem. Phys. **9**, 250 (2007).

T. Y. Yan and W. L. Hase, Phys. Chem. Chem. Phys. **2**, 901 (2000).

T. Y. Yan and W. L. Hase, J. Phys. Chem. B **106**, 8029 (2002).

T. Y. Yan, W. L. Hase, and J. R. Barker, Chem. Phys. Lett. **329**, 84 (2000).

T. Y. Yan, W. L. Hase, and J. C. Tully, J. Chem. Phys. **120**, 1031 (2004).

T. Y. Yan, N. Isa, K. D. Gibson, S. J. Sibener, and W. L. Hase, J. Phys. Chem. A **107**, 10600 (2003).

M. H. Yang, D. H. Zhang, M. A. Collins, and S. Y. Lee, J. Chem. Phys. **115**, 174 (2001).

X. Yang, X. B. Wang, and L. S. Wang, J. Chem. Phys. **115**, 2889 (2001).

X. M. Yang and D. H. Zhang, Accounts Chem. Res. **41**, 981 (2008).

R. N. Zare and Dagdigia.Pj, Science **185**, 739 (1974).

W. T. Zemke, W. C. Stwalley, J. A. Coxon, and P. G. Hajigeorgiou, Chem. Phys. Lett. **177**, 412 (1991).

D. H. Zhang, J. Chem. Phys. **125**, 133102 (2006).

D. H. Zhang, M. H. Yang, and S. Y. Lee, Phys. Rev. Lett. **89**, 283203 (2002).

D. H. Zhang and J. Z. H. Zhang, J. Chem. Phys. **99**, 5615 (1993).

J. M. Zhang, D. J. Garton, and T. K. Minton, J. Chem. Phys. **117**, 6239 (2002).

J. M. Zhang, H. P. Upadhyaya, A. L. Brunsvold, and T. K. Minton, J. Phys. Chem. B **110**, 12500 (2006).

J. G. Zhou, J. J. Lin, and K. P. Liu, J. Chem. Phys. **121**, 813 (2004).

J. G. Zhou, J. J. Lin, W. C. Shiu, S. C. Pu, and K. P. Liu, J. Chem. Phys. **119**, 2538 (2003).

C. Zhu, R. Krems, A. Dalgarno, and N. Balakrishnan, Astrophys. J. **577**, 795 (2002).

M. Ziemkiewicz and D. J. Nesbitt, manuscript in preparation.

M. Ziemkiewicz, M. Wojcik, and D. J. Nesbitt, J. Chem. Phys. **123**, 224307 (2005).

A. Zolot, M., P. Dagdigian, J., and D. Nesbitt, J., J. Chem. Phys. **129**, 194705 (2008).

A. Zolot, M. and D. Nesbitt, J., J. Chem. Phys. **129**, 184305 (2008).

A. M. Zolot, W. W. Harper, B. G. Perkins, P. J. Dagdigian, and D. J. Nesbitt, J. Chem. Phys. **125**, (2006).

A. M. Zolot and D. J. Nesbitt, J. Chem. Phys. **127**, 114319 (2007).

Appendices

Appendix A: F Center Laser Realignment

The FCL used in the present work was manufactured by Burleigh Instruments as part of their commercial color center laser line developed in the early 1980s. The FCL was discontinued in 1996 and Burleigh was subsequently purchased by EXFO, who does not support any Burleigh electro optics products. This situation strongly compromises the ability to service and maintain the FCL, and suggests that more robust modern technology, such as quantum cascade lasers, CW optical parametric oscillators, and difference frequency generation, will be more suitable for this type of apparatus in the future. Particular complications with using discontinued equipment arose after an unfortunate series of events necessitated the complete factory alignment of the FCL. Based on these experiences, I strongly advise FCL users to always fill the Dewar by hand, and NEVER use an automated filling mechanism, which is prone to fail and freeze the exterior of the crystal chamber, creating vacuum leaks. After such an o-ring freezing and vacuum failure, critical alignment of mirrors mounted on the base plate was lost. Specifically, the mounting of the cavity end mirror using a single set screw on a post has been found to be a critical design flaw of the current version of the FCL, and accidental perturbation of this and other optical elements necessitated the extensive efforts described below.

Although Burleigh Instruments no longer exists, a company founded by former Burleigh engineers, Bristol Instruments, does provide expert assistance on many of their former employer's devices. Unfortunately, they do not have any expertise in the FCL field. However, through contacts at Bristol instruments, I was able to talk to the retired Burleigh engineer who was primarily responsible for the FCL assembly and alignment, and with his help I was able to recreate the FCL factory adjustments. This alignment used to be performed at the Burleigh

factory with specially machined alignment jigs that no longer exist, meaning a number of the factory alignments had to be recreated. The details of this process follow in this appendix, to assist other workers who may want to resurrect a Burleigh FCL.

To aid the current discussion, Fig. A.1 provides a sketch of the FCL's optical elements. In regular operation, the krypton ion pump laser is guided into the cavity through input irises (IIa, and IIb), reflects off the input steering mirror (ISM), enters the crystal vacuum chamber through a vacuum window, and is reflected from a dichroic beam splitter (DBS). The folding mirror (FM) focuses the pump beam onto the gain medium, mounted at Brewster's angle. Finally, the pump beam retroreflects from the cavity end mirror (CEM), which is mounted on a gear-driven translation stage to enable adjustments while under vacuum. The IR laser cavity follows the pump laser path between the CEM and FM, but the DBS efficiently transmits the IR light. The beam then passes through a Brewster window forming the vacuum seal into the tuning arm, and through the center of the cavity iris (CI), located close to the tuning arm input. An approximately 30 cm gap between the CI and the output coupling grating provides space for additional cavity elements, i.e., the galvo plates and thick etalon. Two interchangeable gratings provide coarse frequency selection and are blazed to couple either 10% (the B grating) or 1.5% (the A grating) of the light out of the chamber in zeroth order with high retroreflection in first order. The gratings are mounted on a right angle corner mount with a high reflector, such that tilting the grating tunes the cavity wavelength without displacing the output laser beam. A final output-coupling mirror (OCM) steers the beam out of the cavity and through the final window, which forms the tuning arm vacuum seal.

The only benchmark for the alignment that was left unperturbed was the CI, though even this position could be recreated, if necessary, by carefully positioning it 3.4 cm above the laser base plate and centering it on the tuning arm axis. To assist alignment, an output iris (OI) was added in front of and centered on the output window. The OI and CI define the laser oscillation

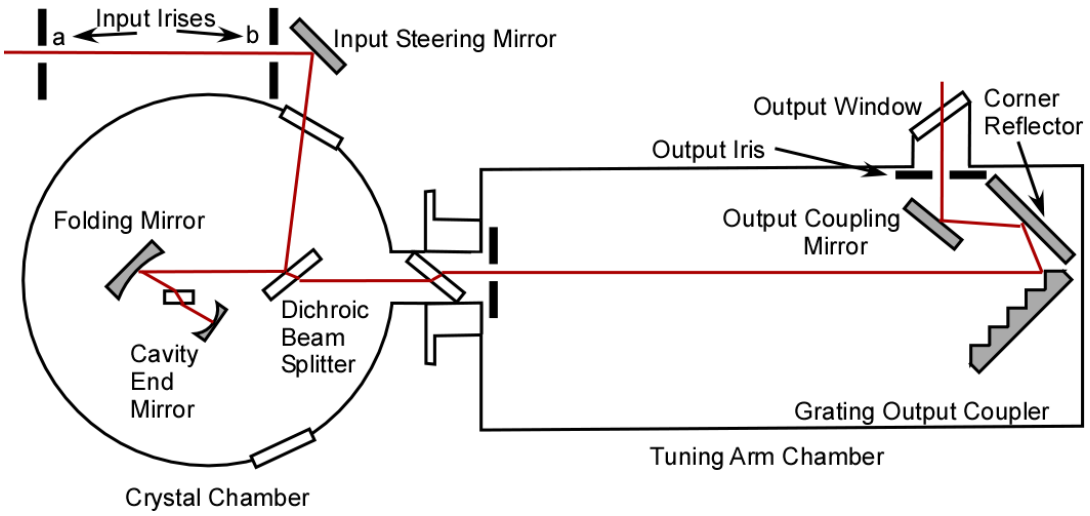

Figure A.1 Essential elements of the FCL laser cavity. Abbreviations for optical elements are as follows. Input Iris (IIa and IIb), Dichroic Beam Splitter (DBS), Folding Mirror (FM), Cavity End Mirror (CEM), Cavity Iris (CI), Output Coupling Mirror (OCM), Output Iris (OI).

path, along with the OCM and grating. However, the position of the OCM is not critical, since it is after the output coupler, so this element is coarsely positioned in the middle of its adjustment range and bolted firmly in place for the remainder of the alignment. Similarly, the horizontal tilt of the grating is not critical, as it simply determines the frequency of the laser oscillation. However, the vertical adjust on the grating should be selected such that the grating does not produce a dramatic vertical tilt in the beam height. It must therefore be readjusted as the alignment proceeds and beam path is optimized, as described next.

To perform the alignment, the round trip oscillator path is defined by directing a HeNe beam into the laser *output*. Two steering mirrors define this beam path, which must be centered on the CI and OI. Next, the grating vertical tilt must be optimized. By turning the grating horizontal tilt (via the sine bar drive), one grating reflection can be directed approximately backwards along the incoming HeNe path. Adjusting the grating vertical tilt enables this beam to be perfectly retroreflected into the incoming beam, but displaces the alignment onto the CI. Thus, the CI, OI, and grating retroreflection adjustments must be iterated until the beam is centered on both irises and retroreflected along the HeNe input. Adequate positioning of the irises and OCM can be checked, as it results in the tracer beam being level in the tuning arm and parallel to the long edge of the laser base plate.

Next, the crystal chamber optics are coarsely positioned. To attain the needed displacement from going through an Brewster window, the vacuum coupling between the crystal chamber and tuning arm must be unbolted from the chamber housing and attached to the tuning arm bellows, such that it occupies the position it would with the crystal chamber in place. After bolting the DBS and FM onto the base plate, correct angular positioning may be verified using a plumb bob measurement device or similar contraption to measure the HeNe path relative to some reference point. Such measurements can be used to verify that the DBS is at Brewster's angle relative to the alignment beam (56.3°), and the FM bends the beam by 18.4° toward the CEM, the angle at which the FM astigmatism compensates for the astigmatism induced by focusing the

laser light on the crystal at Brewster's angle.[1] Next, the CEM translation stage may be attached, and its tilt coarsely adjusted. The tilt of the stage can be observed by affixing a card to the stage and observing any apparent "walk" of the HeNe spot on the card as the stage translates. Properly angling the stage minimizes such walk, as achieved by loosening the bolts attaching the stage to the base plate and gently moving the stage in its slotted boltholes.

To replicate the beam displacement by the gain medium, a 2.0 mm thick quartz (or similar material with index of refraction of ≈ 1.5, close to that of KCl and RbCl) dummy crystal should be placed in the crystal cassette holder. Positioning the crystal cassette mount is the most problematic procedure without the Burleigh alignment jigs, due to translational and angular freedom provided in bolting it to the base plate. Acceptable positioning can be found by expanding the HeNe tracer in a telescope and finding the location of its focus after reflecting from the 3 cm focal length FM. This position defines the location of the beam waist between the two curved mirrors, which should be the center of the F center crystal. Angular positioning of the cassette holder requires reflecting an additional HeNe beam from the lower right side of the crystal (as drawn in Fig. A.1) and measuring the angle of the dummy crystal's face in order to verify that it is close to 56.3° from the tracer beam, i.e., Brewster's angle at 3 μm in the salt crystals. The angular adjustment needs to only be *close* to Brewster's angle, since the reflection is a slowly increasing function and actually varies a bit between the different F center crystals and operating wavelengths.

After the crystal cassette position is approximately correct, the CEM translation stage to gain medium distance must be optimized, such that the middle of the CEM translation stage motion corresponds to a CEM – crystal distance of ½ the CEM focal length (f = 7.1 mm). Burleigh did this adjustment using an alignment jig, equipped with a special crystal marked with a "cross-hair", which could be illuminated and re-imaged on itself from the CEM. I recreated this crystal by gluing a thin piece of paper, etched with a cross-hair, between two 1 mm microscope

slides, cut to match the desired crystal dimensions. The cross-hair crystal is best illuminated from behind, as achieved by removing the FM in a reproducible manner, i.e., by screwing it out of its mount and counting how many turns are needed for it to be released. Then, the inverted image of the cross hair can be focused on itself by careful CEM positioning. At this point the worm screw, which enables CEM translation while in vacuum, should be adjusted such that the focusing position approximately corresponds to the center of the translation range.

After replacing the FM and quartz dummy crystal, the unexpanded HeNe alignment beam can be retroreflected along its incoming path by carefully positioning the CEM. A card with a small hole centered on the incoming beam can be placed in the tuning arm to facilitate this adjustment. However, the CEM mount consists of a post with a setscrew to hold it in place, so it is difficult to get the alignment perfect using only the CEM. For small angular displacements, the FM mount angular adjust knobs can be used without significantly perturbing the earlier alignments. Once adequate alignment has been obtained, the CEM should be translated on its stage and any walking of the retroreflected beam observed. For the greatest sensitivity to walk, observe the beam reflected off the DBS and toward the pump laser. Beam translation indicates that the CEM translation is not perfectly parallel the alignment beam because perfect retroreflection has only been attained for one CEM position. Changing the CEM stage angle can largely eliminate horizontal motion, but small horizontal walk and vertical displacements may be corrected by changing the FM angular adjust knobs and compensating with the CEM position. The process of retroreflecting the beam and checking for walk must be repeated until perfect.

Once the CEM and FM have been positioned, the cavity has been aligned and the pump laser beam path must be defined. The alignment beam's reflection off the DBS can be centered on IIa and IIb by adjusting the DBS and ISM. The ISM is readily adjusted to center the beam on IIa. At this point, the beam should be close to centered on IIb. Viewing the closer iris is difficult and best done by peering into the bulky ISM mount and looking at the inner surface of IIb in the reflection off the ISM. Horizontal DBS adjustment is performed by slightly loosening the bolts

attaching its mount to the base plate and using a screwdriver to pry this mount and angle it. Vertically adjust the DBS by firmly placing a finger on the top of the optic, which is only held by its base, and gently pressing it forward or back. After iterating the DBS and ISM adjustments and perfecting the iris alignment, a weak krypton ion pump beam can be used to check the cavity alignment. Center the pump beam on the input irises and verify that the remnant of the pump beam that exits the FCL output follows the incoming alignment beam. Note the retroreflected pump beam may not be perfectly aligned with its incoming path, which may require slight adjustments to the ISM to obtain. This slight fudging of the beam path is necessary because the close (14 cm) spacing of the input irises is not sufficient to perfectly define the incoming beam path. However, translation of the CEM should not produce significant walk of the reflected beam, compared to the change in the beam divergence. Additionally, motion of the CEM should be sufficient to change the retroreflected beam from somewhat diverging (at the closest crystal distance), to collimated, to diverging again as the CEM is translated.

Following these adjustments, the cavity is ready to receive the crystal, and lasing attempted. However, one more adjustment may be needed – perfecting the FM to crystal spacing, which centers the waist of the stable cavity in the gain medium. Unfortunately, this can only be optimized via the long process of inserting the crystal, pumping down and cooling the chamber, testing the laser performance, then warming up the Dewar, removing the crystal, translating the FM in its threaded mount, re-perfecting the alignment (all of the preceding paragraphs in this subsection), and going through the whole process again. I found that the laser output characteristics (particularly threshold) changes with as little as $1/8^{th}$ of a turn of the FM in its mount. It is critical to follow the proper crystal handling procedures described in Sect. 2.2(A), particularly not exposing the warm crystal to white light and never letting the cold crystal condense moist air. If properly aligned and using a good KCl crystal, with the 10% output coupler, the FCL should have a threshold of about 0.5 W 647 nm pump power and output more than 10 mW at 2.0 W pump power. (Note: it is important to be aware of possible “rollover” when

pumping the laser at high power, during which the gain medium heats to the point where its output power fails to increase as expected, or even decreases with higher pump power. The rollover power for the KCl crystal occurs above 2.0 W and above 1.0 W for the RbCl crystal.) Other characteristics of a well-aligned, functional cavity are the beam waist (ω_0 = 0.63 mm 1/*e* electric field radius) and divergence (z_0 = 48 cm) on the output grating, as inferred from measurements further downstream. In fact, using a fresh crystal, multi-mode powers of more than 20 mW may be obtained with pump power of 2.0 W of 647 nm light. The methods and equipment for making more color center crystals are described by Mollenauer.[2] The difficulties in handling and producing the gain media are the primary handicap with this IR source. Although this realignment has been an unfortunate diversion from my graduate studies, it has been a valuable learning experience as I have become fearless with respect to aligning complex optical systems.

Appendix B: Ion Imaging Apparatus

A great deal of effort has gone into the design and construction of a new experimental apparatus for studying reactive scattering dynamics. Specifically, a velocity mapped ion imaging (VMII) apparatus, based on the experimental innovations of Houston,[3] Parker,[4] Suits,[5] Kitsopolous,[6] Liu,[7] and others, has been designed to enable crossed molecular jet studies to be performed. The implementation of this new experimental technique was motivated by the unique results obtained in the F + HCl reactive scattering dynamics, described in detail in Ch. III. The VMII technique's strength lies in measuring the angular distribution of products and the state of spectroscopically ionizable species, such as Cl atoms. The details of this experimental apparatus are presented in this section.

The key features of the experimental apparatus are schematically presented in Fig. A.2. The frequency doubled output of an yttrium aluminum garnet (YAG) laser pumps a dye laser, which is frequency tripled to provide tunable UV pulses with about 10 ns duration. A prism filter separates the tripled light, at about 235 nm, from the lower harmonics. About 1 mJ of light at this wavelength, focused via a 50 cm calcium fluoride lens, passes into the vacuum chamber. The resulting intense UV field enables resonantly enhanced multiphoton ionization (REMPI) of atomic and molecular species. The main advantage of REMPI is that ionization of chemical species occurs state selectively, when the UV photon energy is one half of an electronically excited state of the neutral. These excited states are readily ionized, so the two-photon transition limits the detection process, which scales with the square of the laser intensity. In contrast, analogous non-resonant multi photon ionization would not be state selective, and signal scales with intensity to the third power.

Once the ions have been created, they accelerate toward a position sensitive detector, in this case a microchannel plate (MCP) with phosphorescent output. Chandler and Houston pioneered this ion imaging technique.[3] Eppink and Parker[4] introduced the velocity map

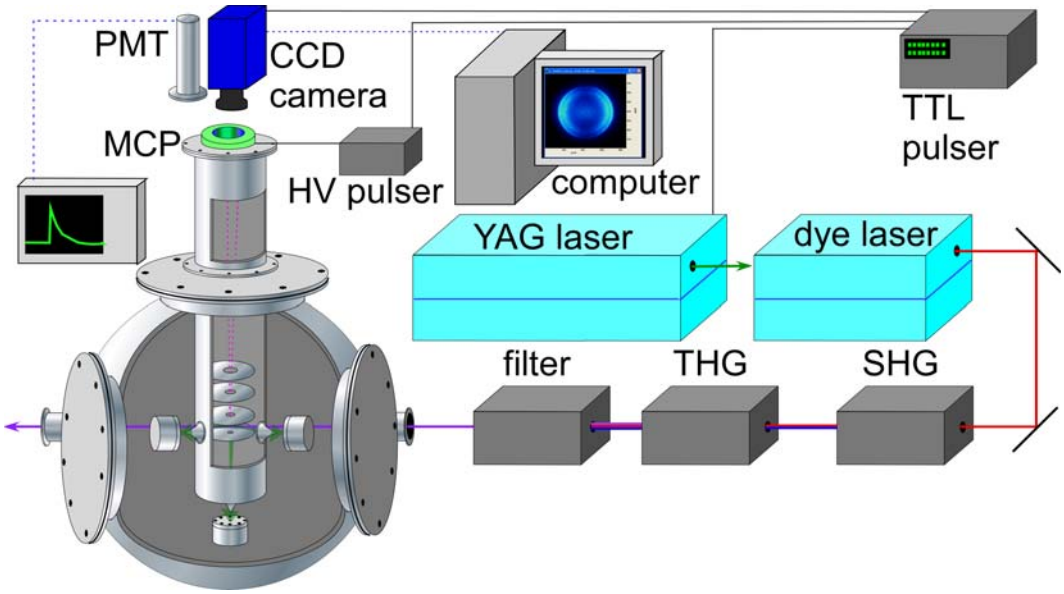

Figure A.2 Schematic of the ion imaging apparatus. Skimmed molecular beams intersect in a differentially pumped vacuum chamber at a 90° angle. Resonantly enhanced multiphoton ionization (REMPI) detection of collision products is achieved via intense tunable UV laser pulses, generated from third harmonic generation (THG) of a yttrium aluminum garnet (YAG) pumped dye laser. Ions are detected on a spatially sensitive microchannel plate (MCP) detector with phosphorescent optical output coupling. Accelerating electrode geometries produce velocity map ion imaging conditions, such that the location at which ions are detected on the MCP directly correlate to the product's velocity projection in the plane of the detector. A charge coupled device (CCD) yields spatially resolved detection, and a PMT provides time domain measurements. HV pulsing of the MCP enables precise time of flight selection of ions, and a TTL pulse delay generator synchronizes the experimental timing and data acquisition.

improvement, which enables higher resolution using ion optics (and not just flat electrodes) to remove most blurring introduced by the spatial distribution of the ions prior to acceleration, providing higher resolution velocity measurements.

The high gain provided by the MCP detector enables individual ion detection events to be recorded by the charge coupled device (CCD) camera focused on the phosphor screen. Selective detection of the ion of interest results from the time of flight (TOF) spectrum of the accelerated ions. A fast (τ = 60 ns) phosphor decay disperses the mass spectrum in real time, which can be monitored using a photomultiplier tube (PMT) directed at the MCP output. A high voltage (HV) pulser switches the MCP bias from about 2 kV (high gain $\approx 10^7$) to 1.5 kV (low gain $\approx 10^5$), such that time of flight selection images only the species of interest. Additional experimental resolution enhancement results from "centroiding" individual ion detection events, i.e., analyzing the photon distribution on the CCD from a single event and finding the "center of intensity", and assigning the detection event to that location.

The details of the crossed jet apparatus are as follows. A 3.5 inch inner diameter tube forms the differentially pumped chamber and ion flight tube, in the center of a 55 L vacuum chamber, pumped by a 1250 L/s turbo pump. Three skimmed Proch-Trickl[8] valves are positioned around the flight tube, one centered on and directed along the TOF axis, and two others at 90° to this axis and each other. At the top of the flight tube, a gate valve opens to expose the MCP to ions and differentially pump the inner region of the flight tube via two 250 L/s turbo pumps. The focus of the UV laser lies at the intersection of the three molecular beams, and the UV laser axis is oriented at 45° and 135° to the two non-axial beams.

The intersection of the molecular beams and laser defines the region where ions are created. This location is centered between the first two ion optics electrodes, separated from the MCP detector by a 55.4 cm ion flight distance. The electrodes are a series of 1/16th inch thick stainless steel disks with a 2.75 inch diameter. Each disk has a central hole with diameter *d* for the

passage of ions and bending of electric field lines to create the ion lenses. Table A.1 summarizes the spacing between the electrodes, and the electrode disk hole diameters. The VMII and TOF conditions have been modeled using the Simion electrostatic modeling package (version 7.0), the results of which are summarized in Fig. A.3. Velocity mapping conditions are demonstrated in Fig. A.3(a), where the trajectories of several 1 eV Cl^+ ions are presented. The ions begin at three locations along the laser axis, and with initial velocities oriented in 45° increments away from the TOF axis. Varying the ratio of voltages between the repeller plate and first ion lens changes the lens' focal distance. Thus, ions created at different locations, but with the same initial velocity component parallel the detector plane are detected at the same position on the MCP. Distances in the image plane are directly proportional to this same velocity component, giving rise to the term "velocity mapping." The insensitivity to spatial origin when measuring velocities is what is meant by VMII conditions.

An intuitive picture of the ion lens behavior can be gained by considering the surfaces defined by the curved potential lines illustrated in Fig. A.3(b). Since the electrostatic forces bend the ion velocities toward the surface normal, i.e., toward the field gradient, equipotential surfaces play a role analogous to interfaces between regions with different indices of refraction in ray optics – they bend diverging rays and enable the possibility of focusing optics.

Elementary electrodynamical considerations can be used to anticipate scaling of the VMII conditions with respect to ion mass. Specifically, the local trajectory taken by an ion with a given velocity vector can be described by the radius of curvature (r_n) caused by the velocity component normal to the local force (v_n), according to

$$r_n = v_n^2/a, \qquad \text{(A.1)}$$

where a is the acceleration caused by the applied force. In this case, the acceleration is simply $q|E|/m$, where q is the ion's charge, $|E|$ is the magnitude of the electric field, and m is the ion

Table A.1 Geometry of the ion optics electrodes used in the ion imaging device.

Electrode	H (mm)[a]	d (mm)[b]
Repeller[c]	0.0	0 , 2.0 , 4.0
Lens 1	13.4	12.0
Lens 2	31.8	24.0
Lens 3	60.2	30.0

[a] Height of electrode above the bottom, repeller plate.
[b] Diameter of the central aperture in each lens.
[c] Repeller plate also acts as collimator for the on-axis molecular beam, necessitating several interchangeable electrodes to match beam dimensions.

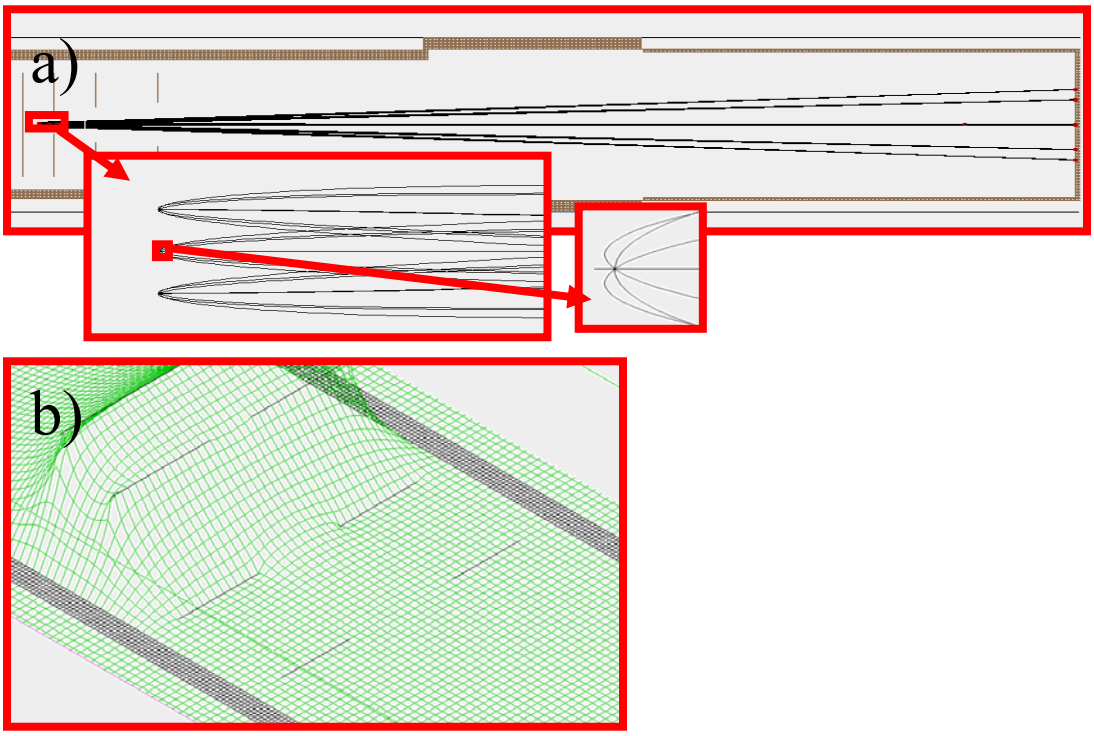

Figure A.3 a) Simulated ion trajectories illustrating the velocity map ion imaging technique in the experimentally used, cylindrically symmetric flight tube geometry. As shown in the inset magnifications, 1 eV Cl^+ ions with initial velocities progressively angled by 45° in the plane of the trajectory diagram. Initial ion positions are displaced by 1 mm from each other perpendicular to the flight tube. The velocity mapping conditions illustrated result in ions landing on the detector at nearly the same location if they have the same velocity projection, regardless of the start location. b) Equipotential lines between the accelerating electrodes. Curved field lines in the vicinity of the central holes in the electrodes bend the trajectories and act as ion lenses.

mass. Thus, the local radius of curvature becomes

$$r_n = mv_n^2 / q|E|. \qquad \text{(A.2)}$$

The numerator in this equation is proportional to the ion's kinetic energy, T, and otherwise only depends upon the direction of the initial velocity vector in the constant $\boldsymbol{E}$ filed. Thus, ions formed at the same position and with parallel velocity vectors will follow the same three-dimensional path through the electric field if they also have the same *kinetic energy*. Note that this result is completely general, and applies to ions in electrostatic fields. The additional advantage of VMII is that, to a very good approximation, the end point of the trajectories is also independent of position in the vicinity of the region the ion lenses are mapping onto the detector plane. Thus, ions with mass m and velocity components (v_x, v_y, v_z) striking a given detector position all have the same $\sqrt{(mv_x^2 + mv_y^2)}$, where the z-axis is the direction perpendicular to the detector axis. Under most conditions only a single mass is selected and so this conditions produces a map of the ions' velocities projected onto the xy plane.

Careful inspection of Fig. A.3(a) reveals that VMII cannot distinguish between velocities with the same vector component in the plane of the detector, but different absolute velocities. Traditionally, this problem was resolved by studying systems with an axis of cylindrical symmetry parallel to plane of the detector, such that the two dimensional information recorded in x, z directions could be converted to cylindrical polar coordinates (r, z) via the inverse Abel transformation or similar mathematical methods.[9] The two non-axial molecular beams in Fig. A.2 produce a relative velocity vector in the plane of the jets, satisfying such a condition. However, new VMII experimental techniques have made such symmetry considerations and data transformation unnecessary. By turning on the MCP HV pulse for a very short time period (≈ 10 ns) compared to the spread of ion velocities perpendicular to the detector (≈ 200–400 ns) one can select the ion velocities along the TOF axis. Such "slicing" of the velocity map was first implemented by the Suits and Kitsopoulos groups.[5,6] For optimal slicing resolution, it is therefore

useful to maximize the spread of the ions along the TOF axis, which can be practically expanded to several hundred nanoseconds by lowering the electric field strength between the repeller and first ion lens. Thus, 5–10% of the ion cloud can be sliced, avoiding the need for inverse Abel transformation. Changing the lens voltage necessarily alters the ion focusing conditions, requiring the use of a second lens to restore VMII conditions. For this reason, the current design was built with a second variable electrode (lens 2) in addition to the final, grounded one (lens 3).

Following the construction of such a complicated device as the VMII apparatus, each component was carefully characterized. In particular, many of the components shown in Fig. A.2 detect individual particles, such as photons on the PMT and CCD camera, and ion, electron, or photon events on the MCP. These devices are characterized by measuring the gain G (or calibration on the CCD analog to digital conversion) to verify proper functioning. Such calibration is performed by measuring two independent quantities that are related to G, i) the device output and ii) the noise on the output. Mathematically, the device output signal S when N events are detected is given by

$$S = GN. \tag{2.23}$$

Under the same shot noise limited conditions, repeat measurements of S result in a standard deviation σ_S according to

$$\sigma_S = G\sqrt{N}. \tag{2.24}$$

Thus, when both signal and noise are measured under shot noise limited conditions, a plot of σ_S^2 versus S will yield a linear plot with a slope of G. Such calibrations result in the following. The Lavision FlowMaster 3S CCD camera has a calibration of 2.15 photoelectrons (e^-) per analog to digital unit (ADU), very close to the factory specified 2 e^-/ADU. Similarly, the Burle PS33189 MCP detector with 2.0 kV bias and 5.0 kV phosphor potential exhibits 29 ADU/event when calibrated with the CCD camera. The MCP gain increases with the applied bias according to an exponential curve with 120 V characteristic voltage. Finally, the electron tubes 9924QB PMT

gain was also calibrated, and fitted to the form $G = Ae^{-V/V'}$ with $A = 4500$, and characteristic voltage $V' = 143$ V.

The ultimate velocity resolution of the VMII experiment may be limited by several different factors. The translational temperature of the jet determines the spread of the unionized species velocities parallel the jet direction, and for a helium carrier gas with a $v/\Delta v \approx 3$, the limiting resolution is about 300 m/s. However, perpendicular to the jet axis, the skimmer geometry determines the velocity resolution, and for the on-axis valve, velocity spreads as small as 10 m/s may be obtained. This value is sufficiently low that the recoil kinematics of the ionization event also become significant. For Cl atoms ionized by three photons at 235 nm, the electron recoils from the Cl with 2.8 eV excess energy, imparting a kick of 16 m/s to the Cl^+ ion. In the limit that the electron recoils isotropically, this recoil produces an effective blurring of the Cl atom's initial velocity.

The REMPI spectral resolution has also been measured in two ways. Firstly, a jet of Cl or HCl is introduced to the chamber, and the laser is scanned through a transition. The measured ≈ 0.5 cm^{-1} linewidth exceeds the 0.04 cm^{-1} expected from Doppler broadening and the 0.1 cm^{-1} laser linewidth. This measurement is confirmed by imaging Cl_2 photolysis with the doubled 353 nm dye laser light. This process produces Cl atoms with 1660 m/s laboratory-frame velocities, and resulting in atoms with a maximum 0.47 cm^{-1} Doppler shift. At line center, the edges of the image have about ½ the center's intensity, again revealing a homogeneous width of about 0.5 cm^{-1}. These measurements indicate that power broadening dominates, and the time a Cl atom spends in the upper state is about 60 ps before a third photon ionizes it. This observation makes sense, as the REMPI process is limited by the two-photon transition, and the final ionization step strongly saturated.

The detection efficiency has also been calibrated by measuring the number of ions generated with a known gas density in the ionization region. Bleeding gas into the source

chamber produces a constant density of molecules in the ionization region, and the absolute density can be measured directly on ion gauges in the source chamber and the detector chamber. However, neither of these gauges directly measures the pressure in the ionization region of the flight tube, which can only be inferred via conductance measurements of the intervening vacuum components. Such measurements are performed by measuring the throughput between the source and differentially pumped vacuum regions via ion gauge readings as a function of gas bleed. Removing a single element (e.g., the ion lens stack) changes the conductance between the two measured regions and provides a relative measure of that element's conductance. Absolute conductance values can be obtained via a region with known throughput, for example the specified pumping speed of the detection region's turbo pumps. Conductances measured this way agree to within a factor of three to the infinitely thin "effusive source" expectation. More importantly, the relative conductance provides an accurate measure of the pressure drop between regions, and the ionization region has been calibrated to have 6% of the gas density produced by the bleed in the source chamber, which is measured directly. Thus, the absolute density of molecules in the ionization region can be known.

Next, the volume in which the UV laser ionizes 100% of the REMPI active species, i.e., the effective ionization volume can be inferred and calculated. Estimates of this volume can be made from first principles considerations. For a Gaussian laser beam with 2.5 mm 1/*e* electric field radius (ω), a 45 cm focal length lens (measured at 235 nm) produces a waist with $\omega_0 = 24$ μm. If the laser saturates the two-photon transition at the beam waist, the effective ionization region can be calculated as 5.4×10^{-7} cm^3, or about 20% of the focal volume, $2\pi\omega_0^2 z_0$, where z_0 is the confocal beam parameter. This estimate anticipates about 14 ions being produced per pulse with an HCl density of 2.5×10^7 #/cm^3 of HCl($J = 0$) in the ionization region, very close to the 10–20 ions observed with about 1.3 mJ pulse energy.

After completing construction and calibration of the VMII apparatus, we attempted to study the reaction F + HCl via velocity map imaging the product Cl atoms. Unfortunately, unanticipated background from the photo fragmentation/ionization process,

$$HCl + 3h\nu \rightarrow Cl^{+} + H, \qquad (A.3)$$

which occurs resonantly with the Cl transitions, swamps the signal. Indeed, a jet of 10% HCl in He should produce about ten Cl^{+} ions per shot under favorable reaction and detection conditions. However, these ten ions are outnumbered by the 30–1200 ions per shot produced from the process in Eq. 2.25, as shown in background the spectrum presented in Fig. A.4. Consequently, any measured reaction dynamics would be masked by background at least three times higher than the anticipated signal. Subtracting the background with only the HCl jet present from the reactively produced "signal" with both reactants was attempted, but did not reveal any meaningful structure within uncertainty. Thus, this project has been sidelined while seeking methods to surmount this hurdle. Despite such difficulties, VMII presents a powerful new technique for the study of state resolved reaction dynamics, and one on which we anticipate fruitful results in the areas of photolysis and collision dynamics in the near future.

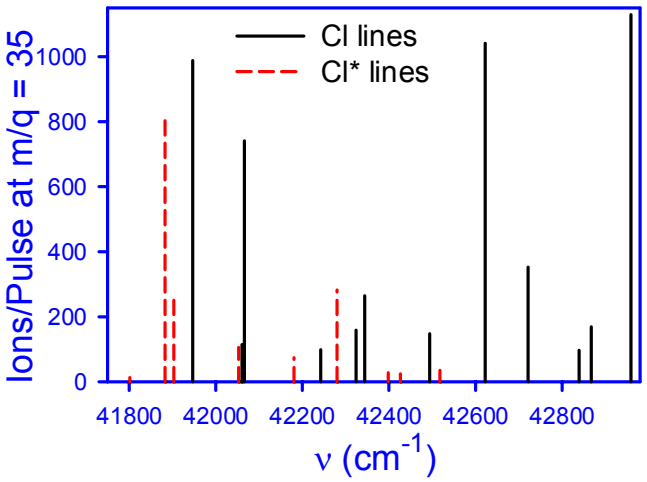

Figure A.4 Background ion spectrum of the 10% HCl jet in He, resulting in ions with mass to charge ratio equal to 35. Measurements have been made at frequencies corresponding to resonant ionization of ground state Cl (solid lines) and spin orbit excited Cl^* ($^2P_{1/2}$) (dashed lines).

Appendix C: F + HCl Quasi-classical Trajectory Simulations

We have performed a QCT study of the reaction F + HCl → HF + Cl using the DHSN surface and a fourth-order Runge-Kutta integration method.[10] Varying the time step for numerical integration produces a very rapid change in the energy conservation, found to scale with approximately the 5th power of the step size, as shown in Fig. A.5. Yet, the computational cost scales inversely with the step size, as shown in Fig. A.6, such that the choice of integration parameters is a compromise between accuracy and computer cost. Reasonable accuracy is readily obtained by choosing a time step of 5 atomic units = 0.12 fs, which conserves energy to better than 0.03 and 0.0002 kcal/mol for reactive and non-reactive events, respectively, for typical 1–2 ps trajectories which require about 10 seconds of CPU time. Such fast calculations enable many thousand trajectories to be run for various starting conditions in order to obtain reasonable statistics.

Trajectories were started in the entrance channel with an initial distance of ≈ 10 Å between the F atom and the HCl center of mass, and stopped when the F–Cl distance again exceeded 10 Å. At this distance, the potential energy between the reactants/products is less than 0.001 kcal/mol and completely negligible. 4–10 kcal/mol collision energies were utilized in order to simulate experimental conditions. Impact parameters of 0–4 Å were explored, though the probability for reaction approached zero above 2 Å. The HCl reactant's zero point energy was explicitly included by beginning the trajectory with the H–Cl distance stretched to the zero point level's outer classical turning point. In order to randomly sample the phase of the HCl vibration during the collision, the F–HCl distance was varied by 1 Å. The relative orientation of the products was also randomly sampled.

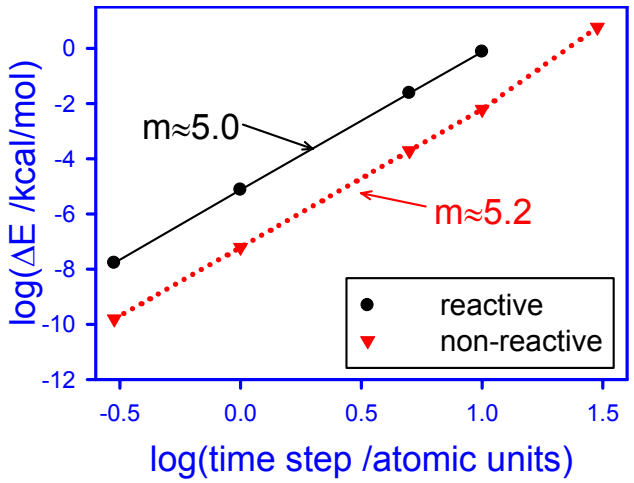

Figure A.5 The scaling of energy conservation (ΔE) versus the size of the integration time step used for QCT calculations. Very rapid scaling (t^5) is anticipated from the 4th order Runge-Kutta integration method.

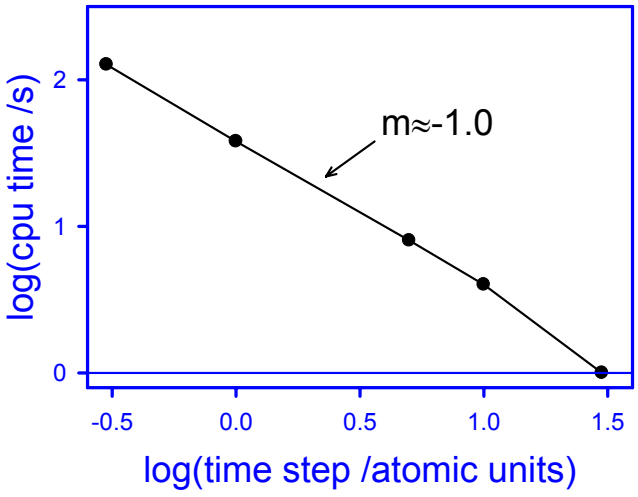

Figure A.6 Simple reciprocal scaling of the CPU time required to compute a single QCT trajectory as a function of the integration step size.

The calculated of reaction cross sections σ shown in Fig. A.7 are 2–3 orders of magnitude smaller than anticipated from experiment at all collision energies studied. Modest increases in reaction probability are obtained for higher collision energies and for rotationally excited HCl, as noted by Hayes and Sun.[11,12] Significantly, the reaction cross section remains negligible at the experimental collision energy, which is above the classical barrier to reaction. The low probability for reaction is discussed in more detail, below.

Following each reactive trajectory, the HF product is calculated using quasi-classical approximation. The results of many such calculations are histogrammed and representative results from 50,000 trajectories starting in the F + HCl channel at E_{com} = 7 kcal/mol and J_{HCl} = 2 are plotted in Fig. A.8. Although collision energy and HCl rotation enhance reaction probability, the qualitative aspects of the HF product quantum-state distributions for reactive events prove relatively insensitive to collision conditions. Specifically, for all initial conditions studied, product HF forms exclusively in the v = 3 and v = 2 manifolds, with high energy rotational states primarily correlating with v = 2, as anticipated from conservation of energy. The results are qualitatively similar to those reported by Sayos *et al*.,[13] who also found only rotationally excited HF in v = 2. Sayos *et al*.'s results are less vibrationally excited than the present DHSN calculations, but were performed on the SHHG PES, which has an empirically lowered barrier that enabled study at lower collision energies. Nevertheless, trajectories on both surfaces predict high vibrational excitation and, more specifically, only high rotational excitation in v = 2. Thus, full trajectory QCT methods do not qualitatively reproduce the observed HF state distributions. Very recent wave packet calculations on the DHSN surface have been performed at substantially lower energy than used in the present study, also resulting in branching primarily into high J in v = 2.[14] Thus, the DHSN surface reproduces the propensity for high J HF(v = 2) and lower J HF(v = 3) products first observed on older surfaces.

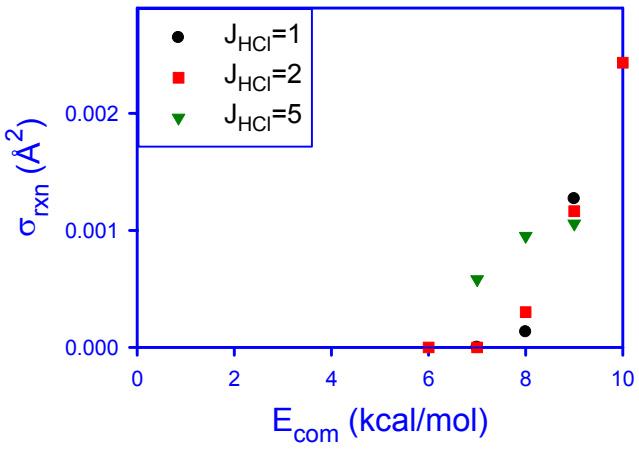

Figure A.7 Theoretical F + HCl reaction cross section from QCT calculations on the DHSN surface for reaction with HCl in the rotational states indicated. Reaction events are not observed until the center of mass collision energy well exceeds the 4 kcal/mol barrier. Modest rotational enhancement is evident, though computed cross sections remain nearly 1000 times smaller than experimentally determined.

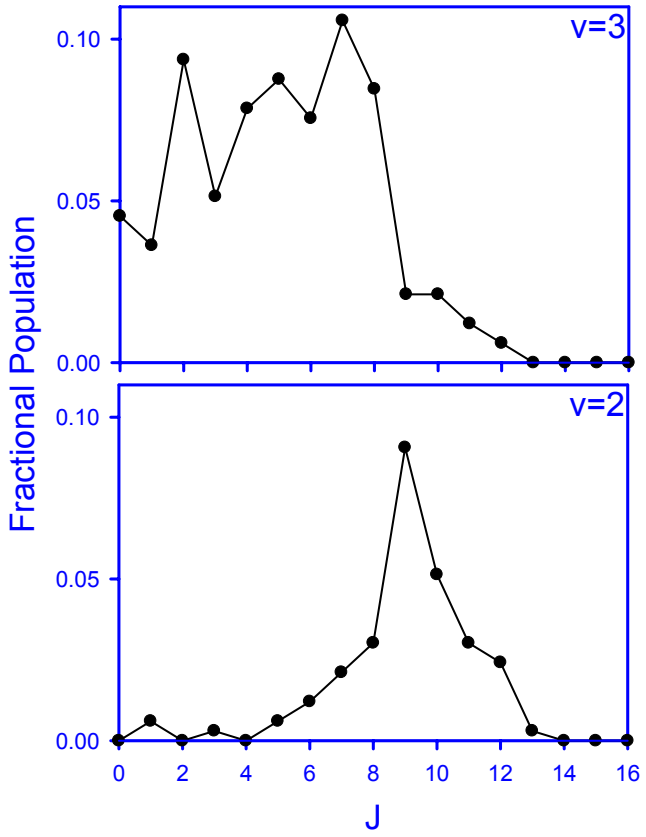

Figure A.8 HF product state distribution for QCT scattering calculations on the DHSN potential energy surface. Initial conditions are E_{com} = 7 kcal/mol, J_{HCl} = 2. These results were obtained following 50,000 scattering trajectories.

In order to test the validity of the full collision calculations, a second set of trajectories has been performed, starting simply in the transition state (TS) region of the DHSN surface with total energy 0.2 kcal/mol above the classical barrier. Although these TS calculations have not been chosen to reflect accurately a distribution of reactive trajectories, they should represent the type of distributions obtained for reactive trajectories that surmount the classical barrier. As shown in Fig. A.9, trajectories starting near the transition state and proceeding to the HF + Cl channel exhibit similar features as the full trajectory results, i.e., population forms exclusively in highly vibrationally excited states ($v = 2$ in this case), and high J state rotational excitation is favored. Thus, the full trajectory results are indicative of the qualitative features of general trajectories traversing the transition state.

We have also used QCT methods to explore briefly the possible influence of deep van der Waals well in the HF + Cl exit channel. These trajectories are motivated by the wealth of vibrational predissociation studies of van der Waals complexes, as well as the possibility of long-lived resonance states that explore portions of the exit well not extensively visited by classical reaction path. Exit-well trajectories are started in the vicinity of the HF–Cl van der Waals minimum, in an initial distribution of HF rovibrational states obtained from full trajectory calculations shown in Fig. A.8 and with zero kinetic energy in the HF–Cl coordinate. The starting position is chosen to be within 0.5 kcal/mol of the bottom of the van der Waals minimum, and the total energy varies by this amount. In essence, these conditions mimic what might be expected if nascent reactive products were to become trapped in the HF–Cl van der Waals well following reaction. The trajectories with non-rotating but vibrationally excited HF were nondissociative on the time scales explored; roughly corresponding to vibrational predissociation, which is known to be exquisitely sensitive to the hard inner wall of the PES and poorly modeled by QCT.[15] However, the dissociation probability of the HF–Cl complex does rise rapidly with HF rotation, in effect rotationally predissociating to yield HF with reduced internal energy. The results shown

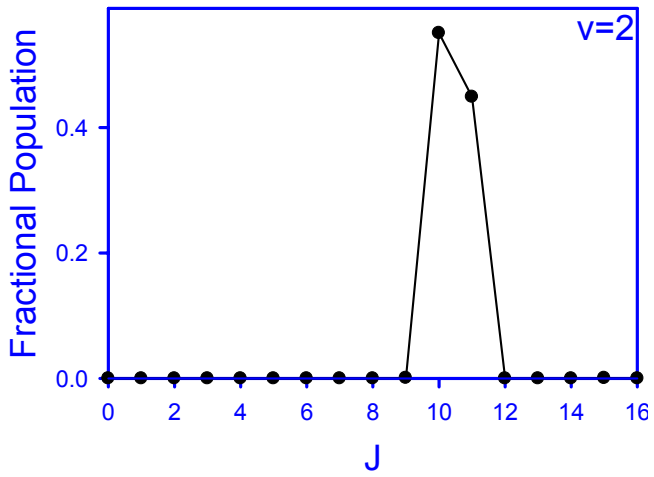

Figure A.9 HF distribution for trajectories started in the transition state region. Total energy is constrained to exceed the classical barrier by 0.2 kcal/mol and initial kinetic energy is randomly distributed. All reactive trajectories correspond to population in the v = 2 manifold.

in Fig. A.10 reveal that product HF fragments retain most of their vibrational energy while being "cooled" into lower angular momentum states. Such relaxation suggests the Van der Waals exit well may play a significant role in the formation of the low *J* HF observed experimentally and may even contribute to HF population in lower vibrational manifolds. Indeed, previous studies of exit-channel dynamics by Orr-Ewing and coworkers in reactive trajectories found that rotationally cold products with strong dipole moments can torque on recoiling fragments and thereby rotationally "heat up" in the exit channel.[16] It would seem equally dynamically plausible in the F + HCl system for highly rotationally excited HF to be "cooled" by angular forces in the van der Waals exit channel, which would be an interesting direction for further theoretical exploration.

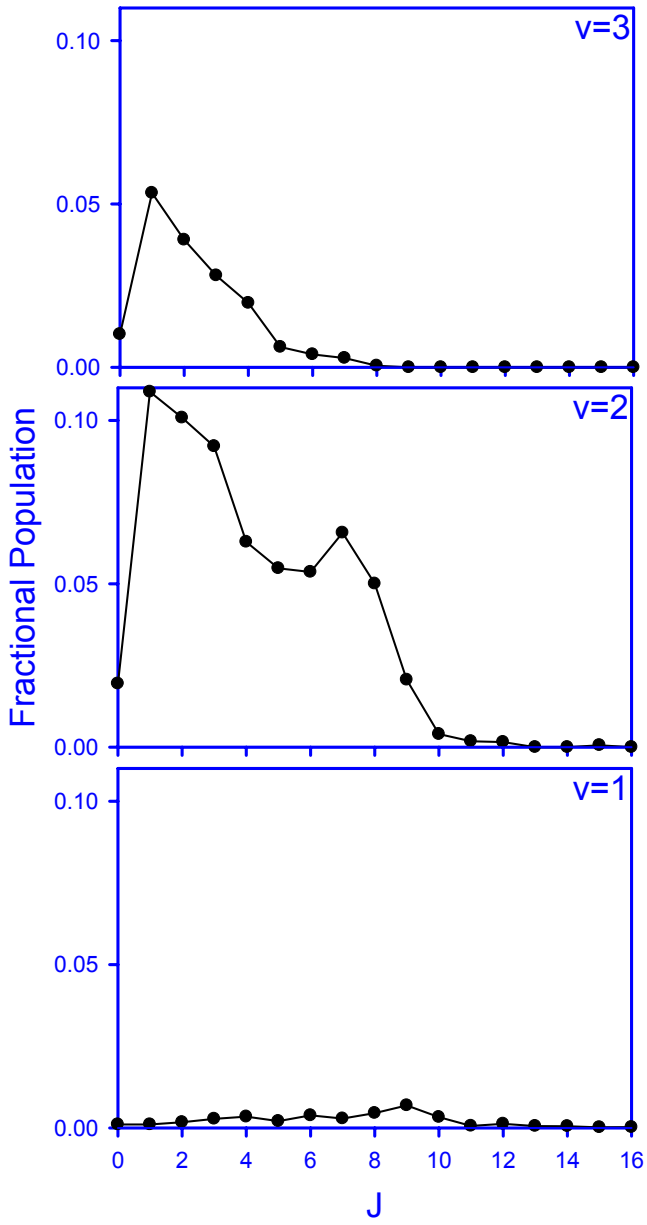

Figure A.10 Quantum state distribution obtained by starting trajectories in the HF–Cl van der Waals well. Initial HF rovibrational energy distribution is that plotted in A.8, and initial HF–Cl kinetic energy is fixed at zero.

Appendix D: Surprisal Analysis of HF State Distributions Produced By F + H_2O

The surprisal analysis works as follows. The "prior" distribution P_{prior} is defined as the one with maximum entropy, the case where all states (described by the rotational, vibrational, and translational states of the products) that are energetically accessible are equally likely to be populated. Thus, the prior distribution is related to the degeneracy $g(\boldsymbol{N})$ of each level $\boldsymbol{N}$, according to

$$P_{prior}(\boldsymbol{N}) = g(\boldsymbol{N})/\Sigma_{\boldsymbol{N}} g(\boldsymbol{N}), \quad \text{(A.4)}$$

for N such that the energy of state N is less than the total energy. From information theory, the surprisal[17,18] $I(\boldsymbol{N})$ is generated by comparing the calculated $P_{prior}(\boldsymbol{N})$ to the observed distribution, $P_{obs}(\boldsymbol{N})$, via

$$I(\boldsymbol{N}) = -ln[P_{obs}(\boldsymbol{N})/ P_{prior}(\boldsymbol{N})]. \quad \text{(A.5)}$$

A linear plot of $I(\boldsymbol{N})$ versus a quantity f_N indicates a "constraint" on the quantity f_N over the course of reaction. Likely constraints are energy $E(\boldsymbol{N})$ or the HF angular momentum J_{HF}. The nearly collinear surprisal plot in Fig. A.11 reveals that vibrational branching matches a simple one-parameter surprisal model that is nearly the same at all studied energies.

Unlike the vibrational populations, statistical analysis fails to even qualitatively describe the measured rotational distributions. Surprisal analyses of the $v = 1$ rotational distributions are presented in Fig. A.12, using J_{HF} and $E(\boldsymbol{N})$ as f_N, defined in the discussion of Eq. A.5. These plots are constructed by summing over the unseen parameters in the state indicator $\boldsymbol{N}$, such as the OH rovibrational quanta. Neither of the plots in Fig. A.12 is linear over the entire range of HF rotational states probed, and recently proposed modified surprisal analyses[21] result in similarly non-linear trends. Thus, simple statistical considerations are not sufficient to explain the observed rotational distributions, even if they do match the vibrational trends in Fig. A.11 reasonably well. Since no physical mechanism has been proposed to predict the slope of such surprisal plots from first principles, even in when observed trends exhibit linear surprisals, they shed little insight.

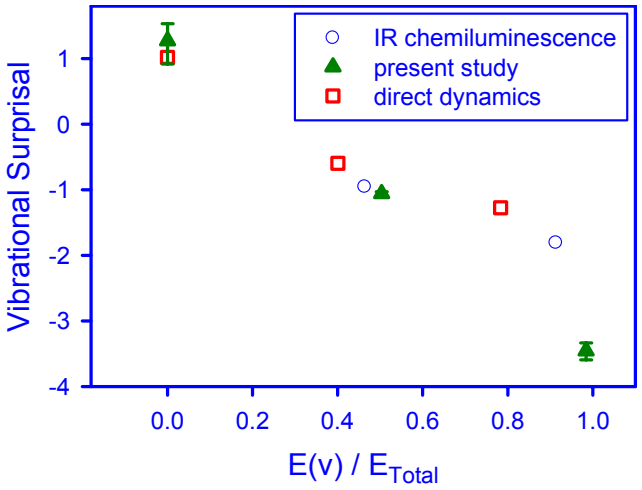

Figure A.11 Surprisal analysis of HF vibrational partitioning observed in the present F + H_2O study, inferred from comparison to F + D_2O chemiluminescence in Ref. 19, and computed in the theoretical study in Ref. 20.

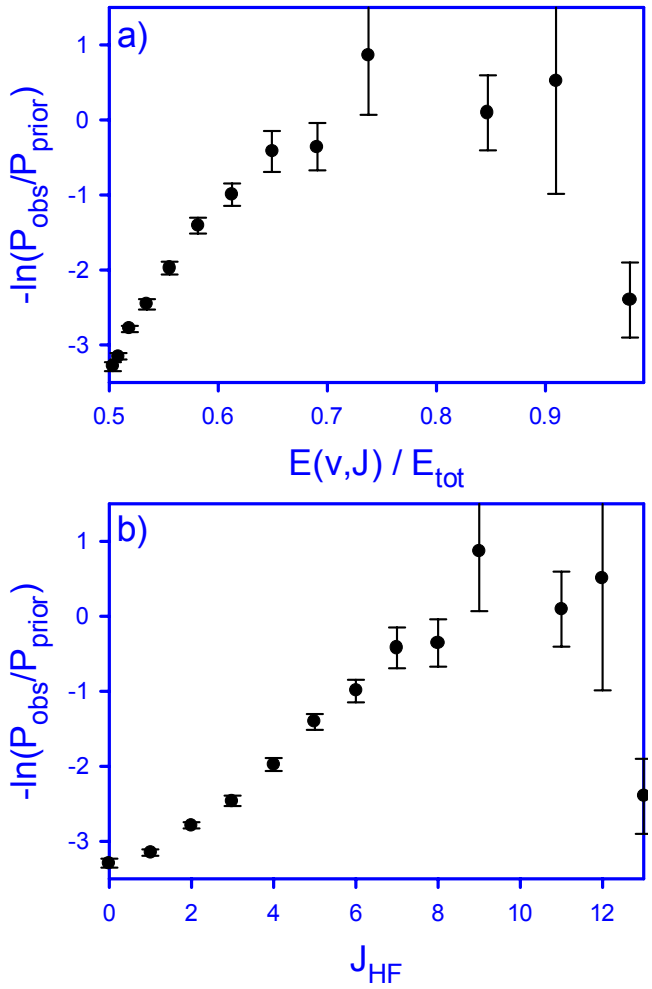

Figure A.12 Surprisal plots of the $v_{HF} = 1$ rotational distribution, plotted as a function of (a) fractional energy deposited in the HF product, and (b) HF angular momentum quantum number , J_{HF}.

Appendix E: Estimated State Resolved Branching Ratios

The precise HF branching ratios are obtained following the density-to-flux conversion, and performed via Monte Carlo modeling of the crossed jet conditions, as described in detail in Chapter 2.4(B) This model produces the average residence time, $\langle \tau \rangle$, for product HF in each (v,J) state, which varies with the assumed differential scattering distribution. The calculated $\langle \tau \rangle$ values for HF formed in the reaction F + HCl are presented in Fig. A.13(a) and Table A.2 for several differential scattering cross section limits. Defining θ as the angle between the F and HF velocities in the center of mass frame, the limiting cases considered here are defined as follows: isotropic ($-1 \le \cos(\theta) \le 1$), forward ($0.33 \le \cos(\theta) \le 1$), side ($-0.33 \le \cos(\theta) \le 0.33$), and backward ($-1 \le \cos(\theta) \le -0.33$). Although $\langle \tau \rangle$ varies by a factor of 0.57–1.7, depending on the unknown differential scattering limit, angular measurements on similar reactions have not found this quantity to vary rapidly between adjacent product rotational states.[22] Essentially, the reactions tend to proceed through one or more mechanisms that do not turn on and off abruptly between product states, such that the entire HF population distribution may be obtained using one universal differential cross section assumption.

The density-to-flux analysis has been performed for each of the angular scattering limits presented in Table A.2, resulting in the normalized fluxes in Fig. A.14. This presentation reveals that the uncertainty in the branching ratio introduced by the assumed differential cross section is smaller than the experimental uncertainty in the measured HF densities, at least to the extent that the differential cross section ($d\sigma/d\Omega$) does not vary with HF state. This insensitivity largely arises from the similar shape of the curves in Fig. A.13 and is explained by substantial blurring of the angular resolution of the experiment caused by spatial averaging within the unskimmed jets. Therefore the exact choice of scattering limit is arbitrary, and for the analysis that follows, the isotropic limit has been used, as presented in Fig. A.14 and Table 3.1.

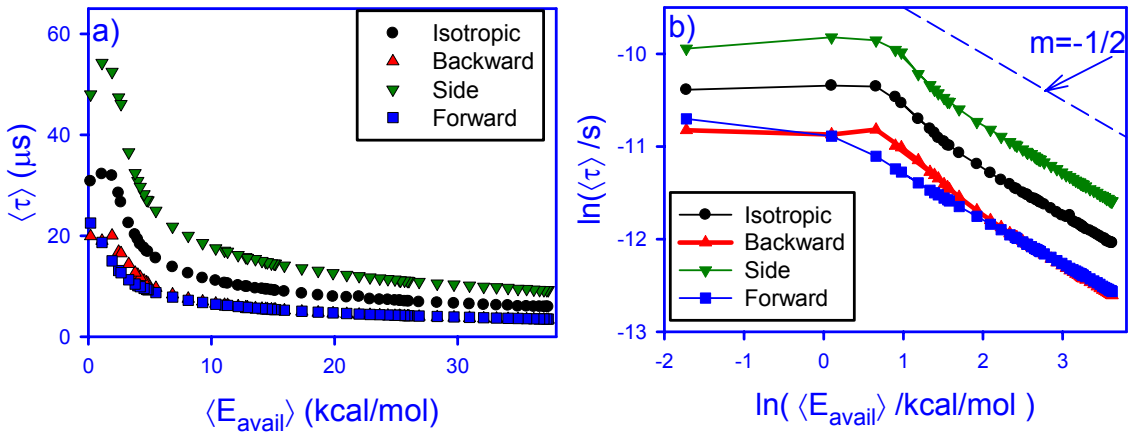

Figure A.13 a) Calculated HF residence times from Monte Carlo simulation of the F + HCl crossed jet experiment. Computed values are shown for four limiting cases of differential scattering cross section, as discussed in the text. b) Log-log plot of the same data. For sufficiently high recoil energy, $\langle \tau \rangle$ scales with available energy (E_{avail}) to the -½ power, i.e., with the inverse of the recoil speed.

Table A.2 HF(v,J) state resolved residence times in the probe region following the reaction F + HCl → HF + Cl, as calculated via Monte Carlo simulation of the crossed jet conditions. The crossed jet conditions are as described in Ch. III. Average residence times are presented for the isotropic differential cross section limit$\langle \tau_i \rangle$. Ratio of residence times to this value are also provided for the other three differential scattering limits, backward scattering $\langle \tau_b \rangle$, side scattering $\langle \tau_s \rangle$, and forward scattering $\langle \tau_f \rangle$, as defined in the text.

v	J	$\langle \tau_i \rangle$(μs)	$\langle \tau_b \rangle/\langle \tau_i \rangle$	$\langle \tau_s \rangle/\langle \tau_i \rangle$	$\langle \tau_f \rangle/\langle \tau_i \rangle$	V	J	$\langle \tau_i \rangle$ (μs)	$\langle \tau_b \rangle/\langle \tau_i \rangle$	$\langle \tau_s \rangle/\langle \tau_i \rangle$	$\langle \tau_f \rangle/\langle \tau_i \rangle$
0	0	5.89	0.57	1.57	0.59	2	0	9.12	0.59	1.59	0.59
	1	5.91	0.57	1.56	0.59		1	9.16	0.58	1.58	0.59
	2	5.90	0.57	1.57	0.60		2	9.25	0.58	1.57	0.59
	3	5.93	0.57	1.56	0.59		3	9.36	0.58	1.58	0.59
	4	5.93	0.57	1.58	0.60		4	9.49	0.58	1.58	0.59
	5	6.01	0.57	1.58	0.59		5	9.58	0.59	1.61	0.59
	6	6.01	0.58	1.58	0.60		6	9.90	0.59	1.58	0.59
	7	6.17	0.57	1.57	0.59		7	10.13	0.59	1.60	0.59
	8	6.21	0.57	1.58	0.59		8	10.52	0.59	1.60	0.59
	9	6.33	0.57	1.57	0.60		9	11.10	0.59	1.58	0.58
	10	6.45	0.57	1.57	0.60		10	11.63	0.60	1.60	0.58
	11	6.59	0.57	1.57	0.59		11	12.54	0.60	1.60	0.58
	12	6.73	0.57	1.57	0.59		12	13.80	0.61	1.58	0.57
	13	6.85	0.58	1.59	0.60		13	15.56	0.62	1.60	0.56
	14	7.14	0.57	1.57	0.59		14	19.31	0.63	1.60	0.52
1	0	7.00	0.57	1.58	0.59		15	28.48	0.59	1.66	0.46
	1	7.00	0.57	1.58	0.60	3	0	16.85	0.62	1.60	0.55
	2	7.01	0.57	1.59	0.59		1	16.93	0.63	1.60	0.55
	3	7.10	0.57	1.57	0.60		2	17.60	0.63	1.61	0.54
	4	7.16	0.58	1.59	0.59		3	18.32	0.64	1.62	0.54
	5	7.29	0.57	1.57	0.59		4	20.23	0.63	1.60	0.52
	6	7.33	0.58	1.58	0.59		5	22.50	0.64	1.62	0.50
	7	7.44	0.58	1.58	0.59		6	26.64	0.62	1.73	0.48
	8	7.94	0.55	1.51	0.57		7	31.90	0.63	1.65	0.47
	9	7.81	0.58	1.57	0.59		8	32.21	0.59	1.68	0.58
	10	7.94	0.58	1.59	0.60		9	30.78	0.65	1.56	0.73
	11	8.20	0.58	1.60	0.59		10	36.48	0.54	1.37	0.73
	12	8.55	0.58	1.59	0.59		11	43.18	0.53	1.21	0.75
	13	8.94	0.58	1.58	0.59		12	45.55	0.57	1.26	0.83
	14	9.36	0.58	1.58	0.59						
	15	9.91	0.59	1.59	0.59						
	16	10.62	0.59	1.61	0.59						

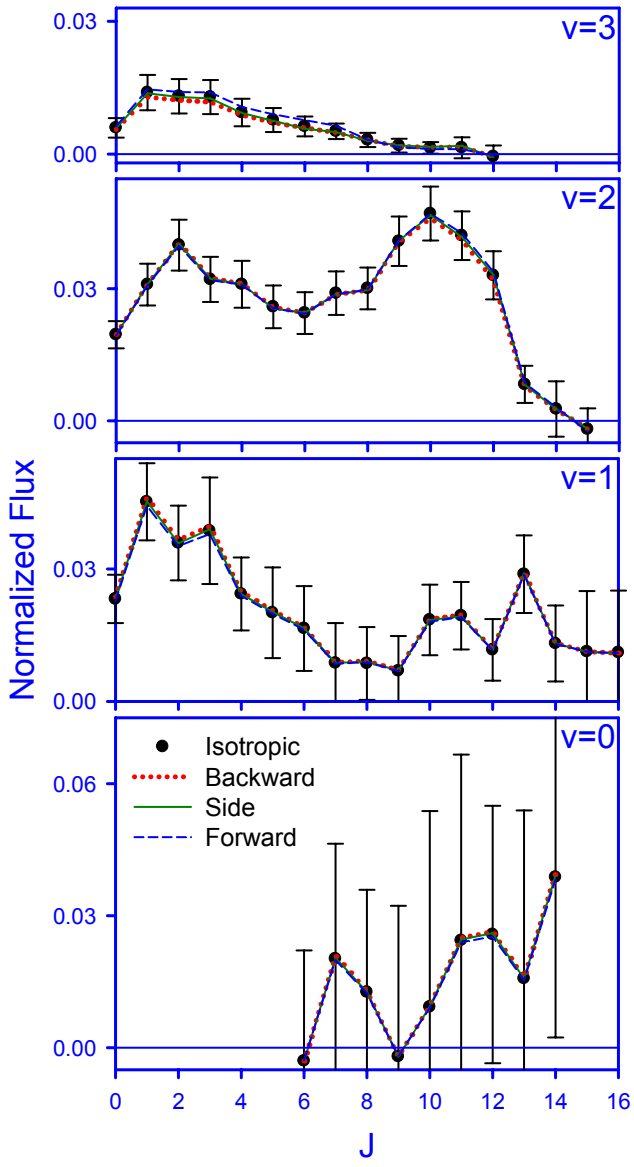

Figure A.14 Calculated HF state resolved flux following the reaction F + HCl → HF + Cl for four limiting cases of reactive differential cross section. All data have been normalized such that they sum to 1. The agreement shown here reveals the high confidence in the present results, limited by the unknown state-dependent differential cross sections.

It is important to note that the structured rotational distributions in Fig. 3.6 cannot be ascribed to varying detection sensitivity. With the present scaling, the local maxima at low and high J in the $v = 1$ and $v = 2$ manifolds have comparable magnitudes. Thus, even if the dynamical processes leading to these features are correlated with radically different differential cross sections, the detection sensitivity changes by at most a factor of about 2.7 between the largest and lowest $\langle \tau \rangle$ values presented in Fig. A.13. Thus, for the most extreme case, any portion of the results in Fig. A.14 cannot change by more than three-fold, which is insufficient to mask the relevant bimodal structure. Additionally, if such extreme differential scattering structure were present, it would further support bifurcated dynamics in the F + HCl reaction event.

Similar Monte Carlo modeling of the F + H_2O experiment provides the $\langle \tau \rangle$ values for each HF(v,J) state for that system. In order to model the F + H_2O reaction kinematics, the recoil energy, and thus the HF *and* OH internal states, must be specified. Although the OH state distribution is not explicitly measured in the current experiment, it has been found to be a small heat sink (with respect to the total energy),[23,24] consistent with the spectator bond approximation. Indeed, varying the energy deposited in the OH fragment between zero and 1 kcal/mol (the average rotational energy observed in the OH product in Ref. 23) changes the density-to-flux results by a completely negligible amount.

The resulting residence times are presented in Table A.3, for limiting cases of the differential cross section ($d\sigma/d\Omega$). Since $d\sigma/d\Omega$ as a function of HF state is unknown, it is not possible to perform the transformation with 100% certainty. However, in the limit that all product states are formed with similar angular scattering dependence – consistent with the monotonic distribution of product states and measurements of $d\sigma/d\Omega$ on other reactive systems – the choice of $d\sigma/d\Omega$ does not significantly alter the results. This insensitivity is exploited in Fig. A.15, which presents the normalized flux for each limiting case of $d\sigma/d\Omega$. In $v = 0$ and $v = 1$, each of

Table A.3 HF(v,J) state resolved residence times (μs) in the probe region following the reaction $F + H_2O \rightarrow HF + OH$, as calculated via Monte Carlo simulation of the crossed jet conditions. The crossed jet conditions are as described in Ch. IV. Data are organized as in Table A.2.

v	J	$\langle\tau_i\rangle$(μs)	$\langle\tau_b\rangle/\langle\tau_i\rangle$	$\langle\tau_s\rangle/\langle\tau_i\rangle$	$\langle\tau_f\rangle/\langle\tau_i\rangle$	v	J	$\langle\tau_i\rangle$ (μs)	$\langle\tau_b\rangle/\langle\tau_i\rangle$	$\langle\tau_s\rangle/\langle\tau_i\rangle$	$\langle\tau_f\rangle/\langle\tau_i\rangle$
0	0	8.86	0.53	3.03	0.36	1	0	13.45	0.49	3.35	0.35
	1	8.87	0.54	3.02	0.36		1	13.53	0.49	3.38	0.35
	2	8.93	0.53	3.03	0.36		2	13.81	0.49	3.38	0.35
	3	9.02	0.53	3.04	0.36		3	14.08	0.48	3.43	0.34
	4	9.08	0.53	3.05	0.36		4	14.59	0.47	3.49	0.34
	5	9.29	0.53	3.04	0.36		5	15.26	0.47	3.56	0.34
	6	9.44	0.53	3.05	0.36		6	16.42	0.45	3.72	0.33
	7	9.63	0.53	3.06	0.36		7	18.03	0.43	3.90	0.33
	8	9.90	0.53	3.08	0.36		8	19.94	0.41	4.29	0.30
	9	10.25	0.52	3.09	0.36		9	23.18	0.37	4.48	0.30
	10	10.64	0.52	3.13	0.36		10	24.82	0.37	4.70	0.30
	11	11.21	0.51	3.17	0.36		11	26.02	0.39	4.38	0.31
	12	11.83	0.51	3.22	0.36		12	25.17	0.43	3.81	0.36
	13	12.75	0.50	3.30	0.35		13	22.04	0.53	3.02	0.46
	14	14.23	0.48	3.42	0.35		14	25.60	0.54	2.72	0.49
	15	16.31	0.45	3.71	0.33		15	29.34	0.61	2.51	0.56
	16	20.56	0.40	4.28	0.30	2	0	22.20	0.56	2.71	0.48
	17	26.04	0.35	4.61	0.30		1	23.56	0.54	2.79	0.48
	18	25.60	0.41	4.08	0.33		2	22.93	0.59	2.71	0.47
							3	23.27	0.58	2.62	0.51
							4	25.10	0.58	2.55	0.52
							5	25.37	0.62	2.48	0.73
							6	28.20	0.63	2.36	0.59
							7	31.83	0.64	2.17	0.67

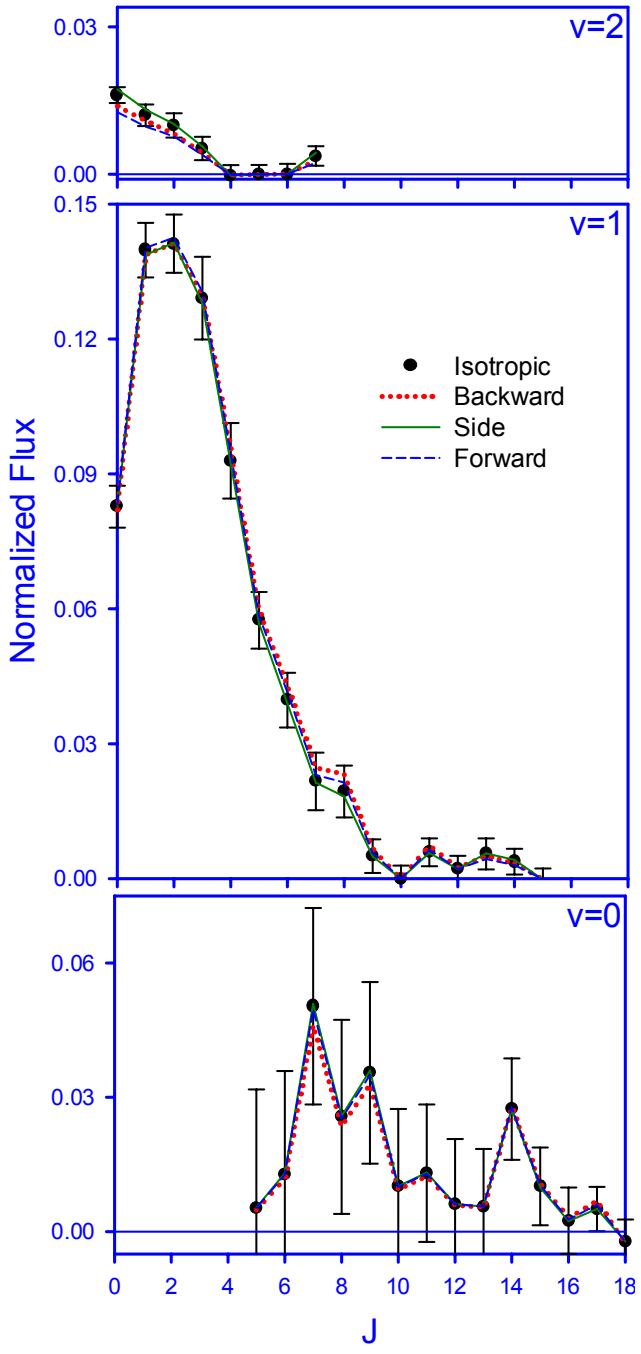

Figure A.15 Observed nascent HF(*v,J*) populations produced by the F + H_2O reaction, obtained from the measured densities via the density-to-flux transformation. Data points, and dotted, solid, and dashed lines indicate the results from various assumed differential cross section scattering limits used in the density-to-flux conversion, as defined in the text.

these limiting cases results in rovibrational population distributions that agree well within the reported experimental error bars, and the $v = 2$ populations are only slightly shifted by the chosen angular scattering limit. The F + H_2O results are particularly insensitive to changes in $d\sigma/d\Omega$ because of i) the large amount of spatial averaging in the unskimmed jet geometry, ii) the relatively small reaction exoergicity, compared to reactions such as F + HCl,[25] or F + CH_4,[26] and iii) the narrow distribution of HF states populated, primarily $v = 1$, $J < 5$. Thus, for the bulk of Ch. IV, the results obtained assuming isotropic differential scattering have been discussed, as presented in Table 4.2.

In the gas-phase studies in Ch. III and IV, Monte Carlo simulations of the recoil dynamics enabled the *density-to-flux* transformation to be performed and state resolved branching ratios to be estimated. In Ch. V, the reaction at the gas-liquid interface may have similar state-dependent sensitivities. However, complications arise at the liquid interface because the dynamics of the highly exothermic reaction event and subsequent interactions at the liquid interface completely determines the state-dependent HF velocities in the laboratory frame. Thus, any prediction of recoil velocities necessitates detailed dynamical commutation of the gas-liquid scattering event. However, the Doppler measurements do provide direct experimental information about the HF recoil velocities. As discussed in more detail in the next Chapter 5.5, the HF velocities are quite close to thermal, and only change slowly with quantum state. Although Doppler measurements in the current experimental arrangement only reveal velocities parallel the liquid surface, a physically motivated $\cos(\theta)$ angular distribution of HF velocities escaping the surface can be used to infer residence times in the probe volume and compute the state resolved HF flux. Fig. A.16 presents the normalized flux values, along with the normalized column-integrated densities from Table 5.2. This presentation reveals that the fluxes and densities agree nearly quantitatively in the present study. Thus, any flux correction results in only a slight increase of the fractional branching into $v = 3$ and $v = 2$, at the expense of the slowly moving

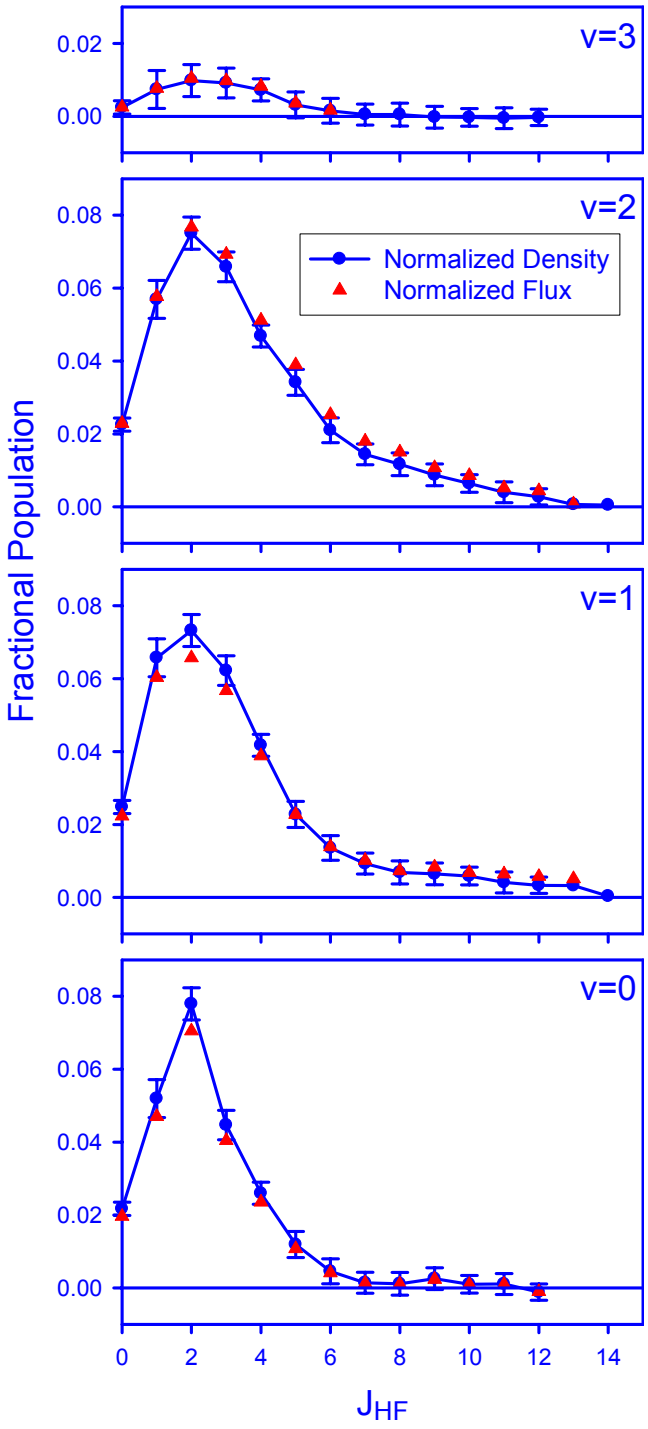

Figure A.16 Normalized HF densities and inferred fluxes following reactive scattering of F from a liquid squalane surface.

(nearly translationally equilibrated) molecules in $v = 0$ and $v = 1$. Since the effect of such weighting does not change the populations within the experimental uncertainty, we have focused our attention on interpreting the measured densities. This approximation is complicated by recent theoretical work by Schatz and coworkers,[27] revealing a propensity for recoiling HF to be directed along the surface normal. However, the high F atom translational energy used in this theoretical study (0.5, 1.0 eV) makes direct comparison to the present study difficult.

References for Appendices A–E

1 W. Koechner, (Springer, Berlin, 1999), pp. 232.

2 L. F. Mollenauer, Rev. Sci. Instrum. **49**, 809 (1978).

3 D. W. Chandler and P. L. Houston, J. Chem. Phys. **87**, 1445 (1987).

4 A. Eppink and D. H. Parker, Rev. Sci. Instrum. **68**, 3477 (1997).

5 D. Townsend, M. P. Minitti, and A. G. Suits, Rev. Sci. Instrum. **74**, 2530 (2003).

6 R. L. Toomes and T. N. Kitsopoulos, Phys. Chem. Chem. Phys. **5**, 2481 (2003).

7 J. J. Lin, J. G. Zhou, W. C. Shiu, and K. P. Liu, Rev. Sci. Instrum. **74**, 2495 (2003).

8 D. Proch and T. Trickl, Rev. Sci. Instrum. **60**, 713 (1989).

9 V. Dribinski, A. Ossadtchi, V. A. Mandelshtam, and H. Reisler, Rev. Sci. Instrum. **73**, 2634 (2002).

10 W. H. Press, S. A. Teukolsky, W. T. Vetterling, and B. P. Flannery, *Numerical recipes in C: the art of scientific computing*, 2 ed. (Cambridge University Press, New York, 1992).

11 M. Y. Hayes, M. P. Deskevich, D. J. Nesbitt, K. Takahashi, and R. T. Skodje, J. Phys. Chem. A **110**, 436 (2006).

12 Z. G. Sun, S. Y. Lee, and D. H. Zhang, Chin. J. Chem. Phys. **20**, 365 (2007).

13 R. Sayos, J. Hernando, R. Francia, and M. Gonzalez, Phys. Chem. Chem. Phys. **2**, 523 (2000).

14 G. Quemener and N. Balakrishnan, J. Chem. Phys. **128**, (2008).

15 E. Tannenbaum, K. J. Higgins, W. Klemperer, B. Segev, and E. J. Heller, J. Phys. Chem. B **106**, 8100 (2002).

16 S. Rudic, C. Murray, J. N. Harvey, and A. J. Orr-Ewing, J. Chem. Phys. **120**, 186 (2004).

17 R. D. Levine and R. B. Bernstein, *Molecular Reaction Dynamics and Chemical Reactivity*. (Oxford University Press, New York, 1987).

18 J. T. Muckerman, J. Phys. Chem. **93**, 179 (1989).

19 M. A. Wickramaaratchi, D. W. Setser, H. Hildebrandt, B. Korbitzer, and H. Heydtmann, Chem. Phys. **94**, 109 (1985).

20 Y. Ishikawa, T. Nakajima, T. Yanai, and K. Hirao, Chem. Phys. Lett. **363**, 458 (2002).

21 J. J. Valentini, J. Phys. Chem. A **106**, 5745 (2002).

22 X. M. Yang and D. H. Zhang, Accounts Chem. Res. **41**, 981 (2008).

23 M. Ziemkiewicz and D. J. Nesbitt, manuscript in preparation.

24 M. Ziemkiewicz, M. Wojcik, and D. J. Nesbitt, J. Chem. Phys. **123**, 224307 (2005).

25 A. M. Zolot and D. J. Nesbitt, J. Chem. Phys. **127**, 114319 (2007).

26 W. W. Harper, S. A. Nizkorodov, and D. J. Nesbitt, J. Chem. Phys. **113**, 3670 (2000).

27 B. K. Radak, S. Yockel, D. Kim, and G. C. Schatz, J. Phys. Chem. A (in press) (2009).